High-Speed Videography of Submerged Arc Welding

by

Vivek Sengupta

A thesis submitted in partial fulfillment of the requirements for the degree of

Master of Science

in

WELDING ENGINEERING

Department of Chemical and Materials Engineering
University of Alberta

Abstract

In submerged arc welding (SAW), the welding takes place under a flux bed. The physical phenomena taking place under the flux bed is crucial in determining the quality of the final weld. The presence of the flux layer prevents the direct visibility of the weld zone during welding; this limitation has prevented a lot of research in SAW. The thesis presents a technique to visualize the weld zone of SAW. The technique involves penetrating the flux bed with a tunnel made up of thin sheet steel. The tunnel provides an opening of the arc cavity and allows to capture the physical phenomena taking place under the flux bed into videos at 10,000 frames per second. With the developed technique the present work explores for the first time the effect of current on metal transfer in SAW between 500 A and 1000 A both DCEP and AC polarities. Additionally, the work explores for the first time the effect of fluxes on metal transfer and arc length in SAW between 500 A and 1000 A in both DCEP and AC polarities.

The existing research in SAW is scattered among researchers from different places, times, and languages. The thesis presents an exhaustive literature review of the research done in the metal transfer, arc length, arc cavity and slag shell and dynamics of the weld pool in SAW. The review summarizes all the work done related to the physical phenomena in the weld zone of SAW from 1892 to present day.

For the effect of current on metal transfer in DCEP-SAW experiments, analysis of the videos at 500 A, shows an irregular shaped droplet with chaotic, non-axial metal transfer. Between 600 A and 1000 A, a new mode of metal transfer based on electromagnetic kink instability is observed. The detachment frequency between 500 A and 1000 A increased from approximately 9 Hz to 82 Hz. The metal transfer observed at 500 A is in good agreement with five different researchers. The metal transfer observed at 800 A is also in good agreement with one more researcher. The weld pool was significantly depressed

under the arc pressure and at 800 A and above the meniscus was not visible any more consistent with a change in penetration mode from recirculating flow to the gouging region.

For the effect of current on metal transfer in AC-SAW experiments, the metal transfer shows many similar features as observed for DCEP experiments. The key feature in AC is the electrode negative (EN) cycle with mobile cathode area on the droplet surface. At 500 A, the detachment takes place without forming a molten metal tail. Between 600 A and 1000 A, the detachment morphology is often different in EP and EN cycle. The detachment in the EP cycle is based on electromagnetic kink instability. The detachment in the EN cycle takes place by explosions. Most of the detachments (approximately 72%) are in the EP cycle. The detachment frequency increases with increasing current and is higher than DCEP experiments at lower currents. The weld pool flows are found to be consistent with previous experiments done with radioactive tracer techniques.

For the effect fluxes on metal transfer and arc length in SAW experiments, five different fluxes (Lincolnweld 760M, Lincoln ES200, Lincolnweld 980, Lincolnweld 880M, and an experimental flux with 85% CaF_2) are tested with a 3.2 mm wire. Analysis of the videos shows, at 500 A, an irregular shaped droplet under all the fluxes for both DCEP and AC polarities. Frequent explosions at the droplet surface are seen under the oxide fluxes compared to fluoride fluxes. Between 600 A and 1000 A, the metal transfer observed under all the fluxes is based on electromagnetic kink instability in DCEP and EP cycle of AC polarities. In EN cycle of the AC, the detachments take place by explosions. The detachment frequency increases with the increase in current for both DCEP and AC polarities. In DCEP, a higher detachment frequency is observed under the oxide fluxes compared to the fluoride fluxes. In AC, a noticeable trend in detachment frequency is not observed among the different fluxes. The arc length observed under the fluoride fluxes is shorter compared to the oxide fluxes.

Preface

The material presented in this thesis comprises the author's research project under the supervision of Prof. Patricio Mendez. This work has been funded by Natural Sciences and Engineering Research Council (NSERC) of Canada, Wilkinson Steel (CRDPJ 470231), and Apollo Laser Clad (CRDPJ 462535).

Chapter 2 of this work is to be submitted as Sengupta, V., Havrylov, D., Mendez, P.F., 2017 "Physical Phenomena in the Weld Zone of Submerged Arc Welding - A Literature Review", *Welding in the World.* Dmytro Havrylov's role was to review some of the papers necessary to conduct this study. Prof. Patricio Mendez was the supervisory author. The paper to be submitted will be a slightly altered version of the chapter.

Chapter 3 of this work has been submitted as Sengupta, V., Mendez, P.F., 2016 "Effect of Current on Metal Transfer in SAW. Part 1: DCEP", *Welding Journal.* Prof. Patricio Mendez was the supervisory author. A slightly altered version of the work presented in Chapter 3 has been submitted to the journal.

Chapter 4 of this work has been submitted as Sengupta, V., Mendez, P.F., 2016 "Effect of Current on Metal Transfer in SAW. Part 2: AC", *Welding Journal.* Prof. Patricio Mendez was the supervisory author. A slightly altered version of the work presented in Chapter 4 has been submitted to the journal.

Chapter 5 of this work is to be submitted as Sengupta, V., Mendez, P.F., 2017 "Effect of Fluxes on Metal Transfer and Arc Length in SAW.", *Welding Journal.* Prof. Patricio Mendez was the supervisory author. A slightly altered version of the work presented in Chapter 5 will be submitted to the journal.

As the supervisor in all the work presented in this thesis, Prof. Patricio Mendez provided advice in designing the experimental matrix and analysis of the results. Prof. Patricio Mendez also reviewed and revised all publications before submission.

To my mother, for her love, support, and sacrifices.

"I was born not knowing and have had only a little time to change that here and there."

- Richard Feynman

Figure 1: The picture is taken at my room and shows a collection of literature on SAW from different parts of the world in primarily four languages (English, Russian, Japanese, and German). I dedicate this picture to everyone who helped me to collect the papers needed for the review. Thank you to all who helped me in collecting all the papers related to SAW and fluxes from 1892 to present day.

Acknowledgements

It all began on June 20^{th}, 2014 with Prof. Mendez's email saying:
"I'm glad to say I will sponsor you."

I will be forever indebted to my supervisor Prof. Patricio F. Mendez for giving me this opportunity. Time flies and the day of my arrival to Edmonton feels like yesterday. Prof. Mendez treated all of his students as his family. He showed a lot of confidence in me. He showed a lot of confidence in me. Thank you for maintaining an enormous patience and forgiving me for my mistakes. Sometimes, times were tough and lonely, Prof. Mendez took out time from his work and spent time with me and listened to my problems. Working with him was an inspiration in itself, many times we bounced back emails at 2.00 am! He spent a lot of time in reviewing my papers suggesting meaningful changes and improving my writing style. He is a great teacher I can proudly say that I took the most number of classes under him. His lectures on foundry technology were mesmerizing. I will never forget that time. He is a true leader and encourages everyone to do a better job. But most importantly he is an amazing human being with an awesome heart. I became a better human being working with him!

I am very grateful to Prof. Jean-Luc Fihey of École de technologie supérieure for showing his interest in my project. Thanks for your help with high-temperature thermodynamics. With your help, we will better understand welding fluxes. Thanks for visiting our lab and discussing the project. I hope this is just a beginning of a life long relationship!

Natural Sciences and Engineering Research Council (NSERC) of Canada, Wilkinson Steel, and Apollo Laser Clad is gratefully acknowledged for funding this project.

I would like to thank Satya Gajapathi, without his high recommendation Dr. Mendez would not have considered my application. Satya did not even knew me personally but

said good things to Dr. Mendez. Thanks for your recommendation, company, and advice during my stay in Edmonton.

The thesis would not have been same without the people who helped me to collect literature from different parts of the world in different times and languages. Thank you, Randy Reichardt, librarian, Cameron Library, UofA, the people from Interlibrary Loan UofA for their endless support, discussions and exuberance in searching literature. I would like to especially thank Dmytro Havrylov for all the literature from the Paton Welding Institute. Gregor Goett, INS Greifswald for a crucial thesis required for this work. Johannes Schaefer, RWTH Aachen, for sharing their work and some key papers. Alexander Maslennikov, RWTH Aachen for sharing their work with us. Prof. YuMing Zhang, University of Kentucky and Jun Xiao, Beijing University of Technology, for an exhaustive search in Chinese databases for literature relevant to the topic and providing some key papers. Hillary Barton from CWB group for an important paper needed for this research. Kevin Lyttle, Praxair for some good insights on the work done in SAW in the 1980s. Douglas Steyer and his team from Praxair for looking into a document.Niko Wolf for his help with the German translations. It seems like a dream that we have collected documents related to SAW from 1892 to present day across the world in all possible languages! I dedicate Picture. 1 to everyone who helped me to collect the papers needed for the review.

I would like to thank each and every member associated with the lab for their contribution to this project and beyond. Thank you Ata Kamayabi for picking me up from the airport on my arrival to Edmonton and helping me out whenever I needed help. Special thanks to Cory McIntosh for the help with experiments, theory, and discussions on metal transfer. Cory, it was great working with you! We really learned a lot working and failing together! Thank you! Goetz Dapp for helping with everything from the initial days till this day. Gentry, thanks for all the help with experiments, analysis of the

weld samples, and inviting me to visit Apollo Clad, Nairn for the insightful discussions on advanced ceramics, metallurgy, and metal transfer. Mitch for interesting ideas on my project and other projects related to welding, Rebekah for helping me with ordering materials and making the lab a more awesome place, Ying and Louie for the help with MATLAB and company for Indian and Chinese lunches, Rangasayee for company, Jason for inviting me to his place for dinner and company during my initial days in the lab. I would like to thank Forest Liu, Qing Yao, and Garrett Eleniak for their help with conducting experiments, I owe a lot of Saturday's to you guys! Adam Ostashek for his help on metallographic sample preparation.

I would like to thank the welding communities who welcomed us for their respective conferences. Thanks to the members associated with CWA, AWS, and IIW, it was an amazing experience to participate and present at the conferences. Special thanks to Samuel Wilkinson Steel for providing steel plates. Lincoln Electric for providing welding equipment and consumables. Praxair for CO_2 gas used for the experiments. Raheel Khan, Lincoln Electric for helping me by arranging all the welding supplies and consumables. Jack Tracy-Roth for welcoming me several times to Wilkinson Steel and providing me with an opportunity to present my work and a tutorial on welding fluxes.

I would like to thank people from ESAB, India where I started my welding career. I learned a lot about manufacturing welding electrodes and SAW fluxes during my stay there. It was great working with you guys. I will never forget the great time I spent at the factory. A special thanks go to my school teachers Sunita Rao madam, Upendra Verma sir for providing me excellent fundamentals to things. I can not believe that I used those concepts of ionization potentials to understand arc stability and in designing fluxes!

I want to thank my mother for her love, support, and sacrifices. Together we have come a long way!

Table of Contents

List of Tables

List of Figures

Chapter 1

Introduction

1.1 Introduction

Submerged arc welding (SAW) has been around for more than 80 years. It is an important arc welding process. It is a highly efficient process and is used to weld thick plates. The key feature of this process is the use of a flux covering. The welding takes place under this flux bed. The flux is a highly engineered product with a lot of functions including protection of the weld from the atmosphere, providing arc stability, alloying, etc.. The physical phenomena taking place under the flux bed is crucial in determining the quality of the final weld. For instance, metal transfer alone affects the weld width, weld penetration, alloy recovery, fume generation etc.. The presence of the flux prevents the visualization of the weld zone in SAW; this limitation has prevented exhaustive research for this welding process. The present day SAW machines are capable of producing more sophisticated waveforms. However, due to the lack of understanding of the metal transfer in SAW, this capability is seldom used. The thesis presents a technique to visualize the weld zone of SAW. The technique involves inserting a tunnel made up of thin sheet steel into the flux bed. This provides an opening of the arc cavity and thus, making it possible to capture the physical phenomena going inside it in videos.

The existing research in SAW is scattered among researchers from different places,

times, and languages. The distribution, timeline, and languages of the publications made it difficult for a consolidated review of the available literature on the topic. Need for a consolidated review led to research in the available literature on the physical phenomena of the weld zone of SAW. The work presented in Chapter 2 of this thesis explores the available literature of over 80 years related to the physical phenomena in the weld zone of SAW. Papers from North America, former Soviet Union, Germany, and Japan have been searched and found. Many papers were unearthed in this process and cited for the first time. Publications in Russian, German, Japanese, and, English are searched and important aspects related to the topic are summarized. Interestingly, the connection with SAW is not only scientific but also patriotic and is noted in Chapter 2. The research on the weld zone in SAW is divided into research into the metal transfer, arc length, arc cavity and slag shell, and dynamics of the weld pool. The review focuses on the important questions asked for each segment of the weld zone, the different techniques used for answering these questions and the summary of the findings.

The effect of current on metal transfer is not thoroughly studied among researchers. Welding current has a significant effect on the metal transfer in gas metal arc welding (GMAW). The effect of current on metal transfer in SAW is unknown due to the presence of the flux covering. Early attempts to understand the physical phenomena in SAW used two main approaches: X-ray videography and optical videography. The X-ray videography did not disrupt the welding process. However, with X-ray imaging, it is difficult to get a good contrast between the metal and surrounding slag. Thus, visualizing phenomena like droplet detachment becomes challenging. Refs. [2–4] used X-ray imaging to observe the physical phenomena in the weld zone of SAW.

Optical videography provides a clear view of the wire and droplet; so detachment events can be easily studied. However, the optical techniques disrupt the flux cover thus making the validity of the observations questionable. Franz [5] used a ceramic tube to

penetrate the flux bed and visualized the metal transfer. The metal transfer was captured in videos at 3000 f/s. Adrichem [6] did similar experiments as Ref. [5] with a glass tube. Both the researchers reported spherical droplets at low current and fine droplets at high currents. Recently, Mendez et al. [7] developed a technique to visualize metal transfer in SAW. They used a tunnel made of thin-sheet and inserted it perpendicular to the welding direction. The metal transfer was captured in high-speed videos at 10,000 f/s. They reported that at 500 A, a non-axial metal transfer was observed for both DCEP and AC. At 1000 A DCEP, a tapering electrode with a buried arc was observed.

A modified technique of Ref. [7] is used in this research. A thinner sheet is used to make the tunnel. The technique is used to study for the first time the effect of current on metal transfer for a 3.2 mm wire in SAW for both DCEP and AC polarities. The high-speed videos are captured at 10,000 f/s. The results of metal transfer observed is compared with the results of previous researches done with both non-invasive and other optical techniques.

In addition, the developed technique is used to study the effect of fluxes on metal transfer and arc length in SAW for both DCEP and AC polarities. It has been reported in literature [8, 9] that the components of the flux vaporizes and decomposes under the arc temperatures. The gases generated from the fluxes may have an effect on the metal transfer and arc length during SAW. Whether the welding in SAW takes place forming an arc or through the slag shell has to be investigated. The study in Chapter 5 presents for the first time the effect of five fluxes on metal transfer and arc length in SAW. The fluxes consisted of three commercial SAW fluxes (Lincolnweld 760 M, Lincolnweld 980, and Lincolnweld 880 M), one commercial electroslag welding flux (Lincoln ES200), and an experimental flux wit 85% CaF_2. The electroslag welding flux and high CaF_2 flux were chosen to see whether the welding takes place without forming an arc.

1.2 Objectives

The main objective of this research project is to develop a technique to capture the physical phenomena like metal transfer and arc length etc. taking place in SAW into high-speed videos. Additionally, the project aims to carry out an exhaustive literature review on the physical phenomena in the weld zone of SAW. The following objectives are established to achieve the goal:

- Carry out an exhaustive literature review of the work done on the physical phenomena in the weld zone of SAW.
- Capture the effect of current on metal transfer in SAW in both DCEP and AC polarities into high-speed videos.
- Capture the effect of fluxes on metal transfer and arc length in SAW in both DCEP and AC polarities into high-speed videos.

1.3 Thesis Outline

The thesis consists of 6 chapters aiming to achieve the above objectives. After the Introduction chapter, in Chapter 2, an exhaustive literature review of the research done on the physical phenomena in the weld zone of SAW is established. The review summarizes the work done on the metal transfer, arc length, arc cavity and slag shell, and weld pool of SAW.

Chapter 3 focuses on the development of a technique to capture the physical phenomena in the weld zone of SAW. The chapter also studies the effect of current on metal transfer in DCEP-SAW using the developed technique. In this chapter, the metal transfer at currents between 500 A and 1000 A, DCEP has been recorded in high-speed videos. The

results presented in this chapter will show that current has a significant effect on the metal transfer in DCEP-SAW. At high currents, a new mode of metal transfer has been established for the first time in SAW. The results obtained for the metal transfer are consistent with past researchers.

Chapter 4 focuses on the effect of current on metal transfer in AC-SAW. In this chapter, the metal transfer at currents between 500 A and 1000 A, AC has been recorded in high-speed videos. The results presented in this chapter will show that the metal transfer in AC-SAW is similar to DCEP-SAW with mobile cathode area on the droplet surface in the electrode negative cycle.

Chapter 5 focuses on the effect of fluxes on metal transfer and arc length in SAW. The results presented in this chapter will show that the fluxes have a minimal effect in determining the mode of metal transfer in SAW. However, fluxes had a significant effect on the arc length in SAW.

Finally, Chapter 6 concludes and summarizes the findings.

1.4 References

[1] Slavyanov N.G. Electric casting of metals, a guide for equipment and practical application (Russian). Technical report, St. Petersburg, 1892.

[2] N.G. Ostapenko and B.I. Medovar. X-ray analysis of submerged arc zone (Russian). *Avtogennoe Delo*, (11):16–20, 1947.

[3] P.G. Grebelnik. X-ray study of the process of automatic submerged arc welding (Russian). *Avtomatich. Svarka*, (6):18–29, 1950.

[4] I.K. Pokhodnya. A method of investigating the processes of melting and transfer of electrode metal during welding. *Automatic Welding*, (2):1–10, 1964.

[5] U. Franz. Vorgänge in der Kaverne beim UP-Schweißen, Teil I (Processes in the cavern during submerged arc welding, Part I). *Schweisstechnik*, 15(4):145–150, 1965.

[6] Van Th. J. Adrichem. Metal transfer in submerged-arc welding. In *International Institute of Welding Document Number 212-78-66*, Nijmegen, Holland, 1966.

[7] Patricio F. Mendez, Gregor Goett, and Stuart D. Guest. High Speed Video of Metal Transfer in Submerged Arc Welding. In *International Institute of Welding Document Number 212-1345-14*, Seoul, South Korea, 2014.

[8] T .W. Eagar. Sources of Weld Metal Oxygen Contamination During Submerged Arc Welding. *Welding Journal research supplement*, 2(March):76–80, 1978.

[9] E.O. Paton. *Automatische LichtbogenschweiSSung*. VEB Carl Marhold Verlag, Halle (Saale), 1958.

Chapter 2

Physical Phenomena in the Weld Zone of Submerged Arc Welding - A Literature Review

2.1 Introduction

Submerged arc welding (SAW) is an important welding process and has been there for more than 80 years. It is used to achieve high deposition rates. It is a highly efficient process and is used to weld thick plates. SAW differs from other wire-based welding processes by the use of flux. The research in SAW witnessed a significant growth during the Second World War in both Allies and Axis powers. SAW played a pivotal role in the engineering during the Second World War. The significance was not only scientific but also patriotic. A patriotic connection is seen from the article from Irving [1] where he reported during the war the then US President Roosevelt wrote to UK Prime Minister Winston Churchill,

"Here there had been developed a welding technique which enables us to construct standard merchant ships with a speed unequaled in the history of merchant shipping."

According to Irving, the welding reported in the letter was SAW. The former Soviet Union also felt the patriotic connection with this welding. The web page of Paton Welding

Institute [2] noted that with the development of SAW the USSR manufactured more tanks than all other countries at war combined. The famous T-34 tanks played a pivotal role in winning the war for USSR against invading Nazi Germany. Jargon like 'Great Patriotic War' is common in the literature related to SAW from the former Soviet Union [3, 4]. The research in SAW has continued to grow in the years after the war. Present day SAW is the backbone of many major industries like pipelines, shipbuilding, structural, boiler, and pressure vessels. Its importance as a welding process is paramount and can not be ignored.

In 1892, Russian scientist Slavyanov [5] introduced fluxes (crushed glass) to metal casting. Crushed glass was used to protect the molten metal from the atmosphere by forming a layer of slag. Paton B.E. [6] and Paton E.O. [7] accredits Slavyanov's for the idea behind modern day SAW. Paton E.O. further reported that the technology developed by Slavyanov got lost in time under Tsarist Russia until 1929 when Dulchavsky [8] utilized this technology to weld copper under fluxes and received the first patent on welding under fluxes. In 1930, Robinoff et al. [9] obtained a patent for SAW. In 1936, Kennedy et al. [10] was granted a patent related to SAW. Truyk and Grobosz [11] shed light on the beginnings of SAW in Poland and the worldwide.

In his book, Simonson [12] mentions SAW as the greatest advancement in automatic arc welding. He recollects the use of SAW in the welding of large vessels of all types, shipbuilding, and later war tanks. Simonson [12] further reported that in 1935, Kennedy [10] and Linde introduced SAW as a commercial name under the name "Union Melt" process. Simultaneously, Lincoln Electric Co. came up with a process called "Hidden Arc" process. The typical names associated with SAW are: Unionmelt Welding Process (Linde welding group, North America), Submerged Melt Welding (North America), Hidden Arc (Lincoln Electric Co.), Ellira Verfahren (Elektro Linde Rapid process, Germany), Submerged Arc Welding (North America), Unter-Pulver-Schweissen (Germany), and Welding Under Flux

(in Russian) (Russia).

In SAW, the arc is not directly visible during the welding; this has prevented exhaustive research of this process. The existing research on the weld zone of SAW is scattered among researchers from different places, times, languages and techniques. The timeline and languages of the publications made it difficult for a consolidated review of the available literature on the topic. The work presented here aims to summarize all the existing literature available on weld zone of single arc SAW for over 80 years and among 81 researchers.

The research on the weld zone in SAW is subdivided into:

- Research into metal transfer in SAW.
- Research into the arc length in SAW.
- Research into arc cavity and slag shell in SAW.
- Research into dynamics of the weld pool in SAW.

Over the years, a lot of research is done in this process, but the available literature lacks a consolidated review of the physical phenomena going on in the process. Lancaster [13,14] does an excellent review of the physics of fusion welding. The papers bring insights on the available literature in SAW but lack an in-depth discussion. Natalie et al. [15] reviews the work done on welding fluxes, but the work lacks on connecting it to the physical phenomena going on in the weld zone of SAW.

Fig. 2.1 and Table 2.1 encapsulates the different research areas and methodologies utilized to study the weld zone in SAW. Table A2.1 shows the composition of the fluxes used by different researchers. The composition of some of the fluxes could not be retrieved from the literature.

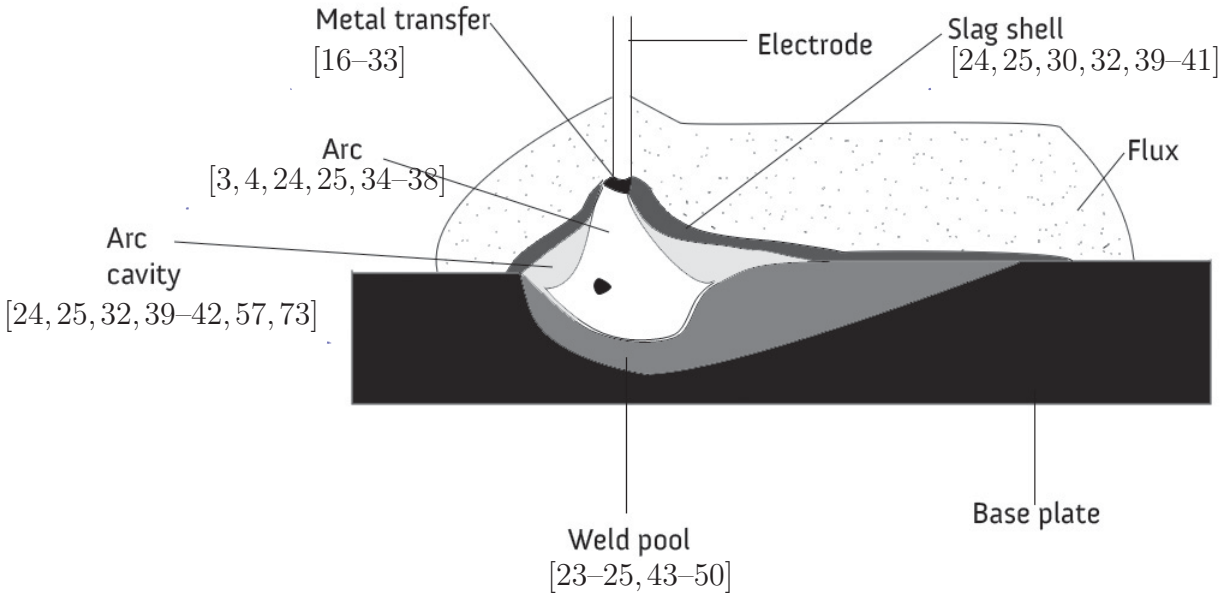

Figure 2.1: A schematic of weld zone of SAW. The research into the weld zone in SAW focused on the metal transfer, the arc, the arc cavity and the slag shell, and the weld pool dynamics.

2.2 Metal transfer in SAW

The metal transfer is one of the most important phenomena in wire-based processes. The metal transfer determines the weld quality, weld width, weld penetration, fume emission, recovery of alloying elements, etc. In SAW, the presence of fluxes has restricted the study of these phenomena. Since the invention of the process very few researchers successfully studied of the metal transfer in SAW. Table 2.2 summarizes the research into the metal transfer.

The research on metal transfer in SAW mainly focused on answering the following questions:

- What is the metal transfer in SAW; is it free flight or short-circuit?
- What is the effect of welding current, voltage on the metal transfer?

Table 2.1: Distribution of the research on physical phenomena in weld zone of SAW among researchers

Focus of research	Methodology	References
Metal Transfer	X-rays	[16–18, 23–25]
	Optical observations	[19, 21, 22, 26, 28–31, 42, 48, 52–54, 57]
Arc length	X-rays	[3, 4, 24, 25, 34–37]
Arc cavity and slag shell	X-rays	[24, 25, 34, 55]
	Optical observations	[29, 30, 32, 41, 42, 57]
	Rapid ejection of the weld pool	[39–41]
	Using piezoelectric sensor, water manometers, and gas sampler	[41, 42, 73]
	Spectroscopy	[57]
Dynamics of weld pool	X-rays	[43, 45, 46, 56]
	Tracer techniques	[23–25, 44]
	Computational	[47–50]

- What is the effect of welding flux on the metal transfer?
- What are the reactions that take place at the droplet?

2.2.1 Methodologies utilized for research in metal transfer in SAW

The methodologies used to answer the questions related to the metal transfer in SAW are:

- Investigation using X-ray photography.
- Investigation using optical techniques.
- Investigation using collecting droplets and weld chemical analysis.

Table 2.2: Details of research into the metal transfer in SAW

Reference	Methodology	Frame rate (f/s)	Wire diameter (mm)	Current (A)	Voltage (V)	Polarity
Pokhodnya [16]	X-rays accompanied with high-speed cinematography	750-900	6	470	29	DCEP
Eichhorn [23]	X-rays accompanied with high-speed cinematography	500-2000	-	-	-	-
Franz [19–21]	High-speed video	3000	3, 4, 5	210 - 810	27 - 43	DCEP
Adrichem [22]	High-speed video	3000	3.2	300 - 600	25 - 40	DCEP, AC
Gupta et al. [26]	High-speed video	3000	1.6, 3.0	210 - 600	25 - 36	Pulsed DC
Mendez et al. [28, 54]	High-speed video	10000	3.2	500, 1000	30, 38	DCEP, AC
Sengupta, Mendez [33]	High-speed video	10000	3.2	500 - 1000	30 - 42	DCEP, AC
Reisgen et al. [30]	All mentioned above	10000	2	435, 350 - 550 (Pulsed)	28, 18 - 32 (Pulsed)	DCEP, Pulsed DC
Gött et al. [57]	High-speed video	5000	4	600, 1000	30, 34	DCEP, DCEN, AC

2.2.1.1 Investigation using X-ray photography

In X-ray photography, the SAW weld zone is exposed to X-rays. The X-rays transmitted through the weld zone can be captured with single-frame photography or high-speed photography. Most of the researchers [3, 4, 27, 34, 35, 38], used X-rays accompanied with single-frame photography to study the phenomena in SAW. The use of single-frame photography made the study of the fast phenomena almost impossible. Different aspects of the arc are studied using this technique. X-rays with high-speed photography was introduced to overcome this drawback. Radiography with high-speed photography of up to 1500 frames per second was used to record the phenomena of metal transfer. Oscillographic information of welding current and voltage was synchronized with the information from the X-rays. Table 2 shows the typical parameters of the X-ray and cinematography setup used to capture the phenomena of metal transfer.

Fig. 2.2 shows a typical setup to capture metal transfer in SAW using X-rays and cinematography. The process of capturing the metal transfer, in a nutshell, is as follows: X-rays pass through the arc gap; the image obtained is amplified by an electron-optical amplifier and then photographed by the high-speed cine camera. Ref. [16] describes the setup as follows:

- **The X-ray apparatus:** Table 2.2 gives the details of the X-ray apparatus used. Pokhodnya concluded the quality of the X-ray image depends on the characteristics of the X-ray beam source, the image amplifier, and on the X-raying conditions. The X-ray exposure time should be as short as possible. The intensity of the X-rays is proportional to the product of the square of the anode voltage and the anode current of the X-ray tube. Ref. [16] further reported that everything else kept constant; the contrast of the pictures was proportional to the cube of anode voltage. Keeping the anode voltage constant, increasing the anode current does not lead to any

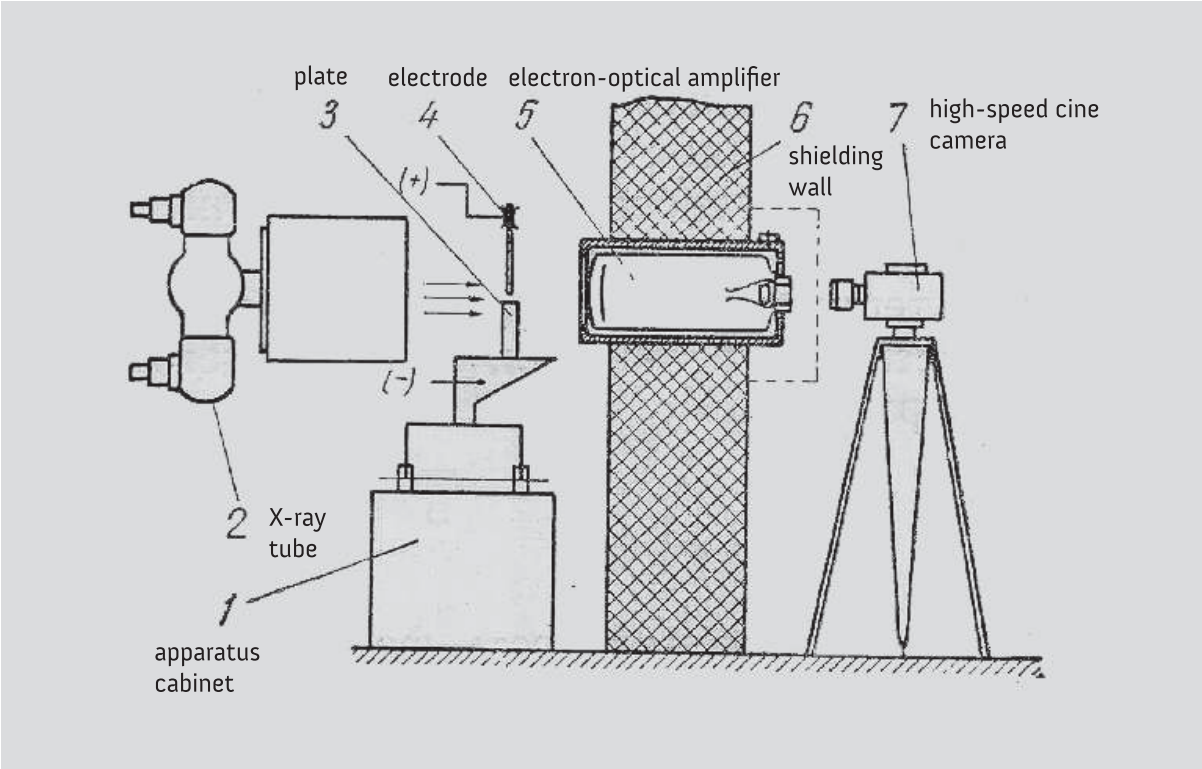

Figure 2.2: An experimental setup schematic used by Ref. [16] for filming X-ray pictures of metal transfer in SAW.

deterioration of the image contrast.

- **The electron-optical amplifier:** Ref. [16] recommended for studying a process happening at a high-speed, the brightness, contrast, and sharpness of the image must be impeccable. Ref. [16] chose an amplifier with a high brightness amplification factor for the experiments. The brightness of the X-ray picture was amplified by an electron-optical device (URI-60). The equipment was capable of resolving droplets with diameter 0.5 mm or higher.

- **The optical system and high-speed camera:** The electron-optical amplifier gave an inverted and reduced size image. An optical system was developed comprising of a mirror prism, a long focus object telescope. The optical system re-inverts and magnifies the image. An SKS-1M cine camera was used at frame rates of 750-900 frames per second (f/s) to record the images.

Eichhorn and Dilthey [23] carried out high-speed X-ray photography for SAW. Ref. [23] reported that the quality of images obtained by Pokhodnya [16] as unsatisfactory. The technique used by Ref. [23] is similar to Pokhodnya [16]. Table 2.2 compares the setups used by Ref. [23] and Ref. [16]. The minimum observable resolution was reported as 0.3 mm at 1000 f/s and 0.16 mm at 2000 f/s. One of the key features of the setup was the X-ray image intensifier. Ref. [23] put a lot of emphasis on the importance of the X-ray image intensifier and claim it to be essential for high-quality images.

2.2.1.2 Investigation using optical techniques

In optical techniques researchers have perturbed the flux bed of SAW in some way to directly observe the phenomena taking place in the arc cavity and capture it in videos using a high-speed camera. Table 2.1 summarizes the researchers involved in studying metal transfer in SAW using the optical techniques.

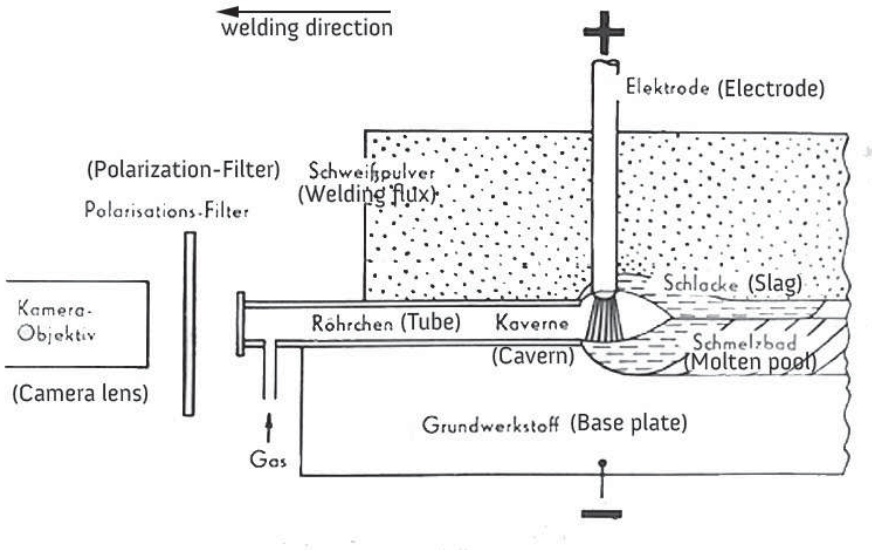

Figure 2.3: Schematic and actual experimental setup used by Franz [19]. The key feature about these experiments was the use of the "ceramic tube". The "ceramic tube" provided a view of the weld cavity in SAW. The videos are recorded at 3000 f/s.

In 1965, Franz [19–21] published the first work on studying metal transfer in SAW using an optical technique. Franz inserted a glass tube in the flux bed. The glass tube was placed parallel, coinciding with the welding direction. The tube penetrated the flux bed and provided a view of the weld cavity. The composition of the tube was chosen similar to the flux; so to minimize the effect of the tube on the slag composition. The tube eventually became the part of the cavity wall. The tube diameter and thickness was chosen based on the welding parameters and wire diameter.

The observation was recorded in videos at 3000 f/s using a high-speed camera. Fig. 2.3 shows the schematic of the experimental setup used by Ref. [19]. While penetrating the tube the slag shell gets broken thus, releasing the internal pressure of the cavity. A gas was injected from side to keep the cavity open.

Following Franz, Adrichem [22] carried out work on metal transfer in SAW using a similar setup. A ceramic tube was used to penetrate the flux and provide a view of the weld cavity. The tube material was chosen in a way that it gets easily melted. The

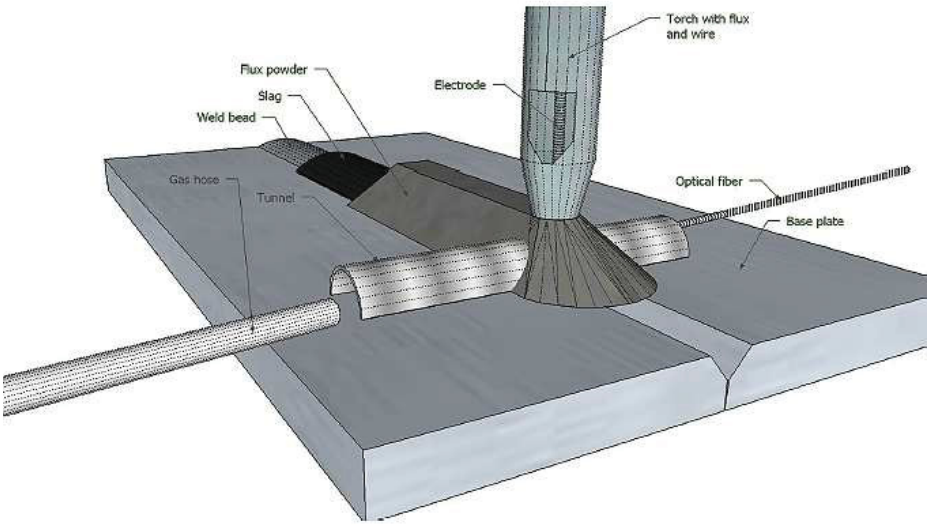

Figure 2.4: Experimental setup used to capture high-speed video of metal transfer in SAW by Mendez et al. [54]. The key feature of the setup is a "tunnel" made of thin-gauge steel. The videos are recorded at a rate of 10,000 f/s.

melting temperature of the tube was higher than the melting temperature of the slag; the tube will pierce through the cavity walls. The dimensions of the tube were chosen according to the welding parameters so that it melts off without hampering the electrode movement. The tube opening on the camera side was sealed off with a glass plate. Argon was blown into the tube to keep the cavity open. The Argon flow rate used was 0.3 l/min. Gupta et al. [26] used an identical technique to Franz [19] and recorded metal transfer in pulsed current SAW.

Recently, Mendez et al. [28, 54], has captured metal transfer in SAW in videos at a rate of 10,000 f/s by inserting a thin-gauge steel tunnel along the welding path. The thickness of the sheet was 0.5 mm. The tunnel had a semi-circular cross-section. The tunnel was placed perpendicular to the welding direction, and the camera was focused on one end. An external gas was blown in from one end to maintain the internal pressure of the cavity and blow away stray flux when the wire is penetrating the tunnel. Mendez concluded that the choice of making a tunnel out of thin sheet steel over a glass or ceramic

tube has its advantages. The thin sheet steel is easier to melt by heat from the wire and the arc than a glass tunnel; thus avoiding situations when the wire mechanically pushes the tunnel.

Sengupta and Mendez [33] used a similar setup to Mendez et al. [54] with a modified tunnel design. The tunnel was made up of very thin-sheet having a thickness of 0.10 mm and had a square cross-section. The thin-sheet was used to minimize the effect of the tunnel on the welding process and avoid stray arcs between the wire and the tunnel. Reisgen et al. [30] has compared all the techniques discussed above.

Gött et al. [57] carried out experiments by penetrating the flux bed using a thin-gauge steel tunnel. The experiments were conducted in DCEP (600 A, 1000 A), DCEN (600 A), and AC (600 A). The work primarily focused on the spectroscopic study of the atmosphere of arc cavity.

Mendez et al. [28], Sengupta and Mendez [33] and Reisgen [30] recorded the videos at a very fast rate of 10,000 f/s. The process of metal transfer is very chaotic and fast and hence using a high frame rate facilitates to capture better videos and post analysis. Ref. [54] and Ref. [33] chose a tunnel perpendicular to the welding direction compared with a longitudinal arrangement as chosen by Ref. [19] and Ref. [22]. The choice of a tunnel perpendicular to welding was to reduce the amount of ejected debris generated ultimately blocking the camera view.

2.2.1.3 Investigation using collecting droplets and weld chemical analysis

Researchers have collected the droplets during the SAW and analyzed the chemistry to understand the reactions taking place at the droplet. North [58] used a water cooled rotating copper cylinder (rotating at 540 r.p.m.), the droplets ejected from the disk were collected in a water tray. The unit to catch the droplets was moved in a transverse direction at a speed of 224 mm/min. The flux was fed past the electrode tip. North

comments that the flux swept past the electrode tip in the same way gas moves past the electrode tip in GMAW. The collected droplets were covered with slag. The droplets were mounted in bakelite and polished to expose their mid-section. The analysis of the droplets was done with an electrode probe microanalyser. Mitra [59] analyzed the weld metal compositions made by different wires and base plates and proposed the theory of slag-metal reactions in SAW. Lau et al. [60] collected and analyzed the electrode tips after stopping the welding machine; also the droplets were collected by a similar procedure as North. Potapov [61] used similar techniques to North to collect droplets during SAW.

2.2.2 Summary of findings on metal transfer in SAW

The present section will summarize all the findings on the metal transfer in SAW, thus, aiming to answer all the questions regarding metal transfer in SAW. The findings on the metal transfer in SAW are as follows:

2.2.2.1 Free flight or short-circuiting metal transfer in SAW?

For decades the question, "what is the metal transfer in SAW?" has kept researchers interested in SAW. The lack of visibility of the arc zone due to the flux cover has added to the mystery. The question whether the metal transfer is similar to other wire-based processes or not is of utmost importance. Researchers have tried to understand whether the metal transfer is free flight or short-circuit for typical SAW parameters. Pokhodnya [16] reported the observation of formation and detachment of droplets for all currents in SAW. Franz [19, 21] reported similar observation as Pokhodnya with no observation of any short-circuit transfer. The voltage readings recorded by Franz [20] does not show data related to short-circuit transfer.

Adrichem [22] agrees with previous researchers and reported absence of short-circuiting

transfer for the parameters used in SAW. Recently, Mendez et al. [54] reported free-flight transfer in SAW for a current of 500 A, voltage 30 V and a wire diameter of 3.2 mm. For 1000 A, 38 V, a buried arc with a tapered electrode ejecting a tail of molten metal was observed. Mendez [28] reported the observation of a fluid bridging the electrode and the weld pool momentarily in the experiment 1000 A, 38 V; this fluid is believed to be slag as the data acquisition does not show any event related to short-circuit transfer. Reisgen [30] also reported free flight transfer in SAW for a 2 mm wire at currents 435 A to 550 A, both in pulsed and non-pulsed SAW. Sengupta and Mendez [33] explored the effect of current on metal transfer in SAW between 500 A and 1000 A and reported free flight transfer without any observation of short-circuiting. It can thus be concluded that the mode of metal transfer in SAW is based on free flight and not short-circuit.

2.2.2.2 Effect of current on metal transfer in SAW

Current plays an important role in determining the metal transfer in SAW. Pokhodnya [16] used X-rays accompanied with high-speed cinematography to observe the metal transfer in SAW. Fig. 2.5a shows the metal transfer observed by Pokhodnya at 470 A, 29 V for a 6 mm wire. It was reported that the droplets often transfer through the slag. At times the droplet traveled through the arc. Kostenko and Pokhodnya [18] observed small droplets for a positive electrode. When the electrode is negative, large shapeless droplets were observed.

Fig. 2.5b shows the metal transfer observed by Franz [19]. Franz observed a large globular droplet at low welding currents and small droplets at high currents. The welding current was found to have a strong influence on the metal transfer. The transition current for a 3 mm wire was about 400 A. A transition current was established for metal transfer by the transition from a globular (large) droplet to small droplets. Above 450 A, a tapered electrode tip was observed. The small drops formed have the spherical shape.

An increase in current leads to increased melting of the wire giving a higher detachment frequency. At high currents, fewer eruptions of the molten metal are observed.

Adrichem [22] reported similar findings as Franz. Adrichem concluded two different metal transfer in SAW; transfer through the slag (at low arc current and high arc voltage) and free droplet transfer through the arc zone (at high arc current and low arc voltage). Under the welding conditions used, short-circuit transfer was not observed in both films and oscillograms. Adrichem reported the total transfer frequency increases with increasing welding current. With increasing current the ratio slag/free transfer decreases. The increase in electromagnetic forces at high current leads to projected spray type of transfer.

Mendez et al. [28, 54] reported the observation of a large globular droplet at 500 A for both polarities AC and DC. At 1000 A, a tapering electrode tip with a buried arc was observed ejecting a molten tail through a mechanism resembling an electromagnetic kink instability.

Sengupta and Mendez [33] observed a large irregular shaped droplet at 500 A for both polarities AC and DCEP. Between 600 A and 1000 A, a tapered electrode tip was observed ejecting a molten tail through a mechanism resembling an electromagnetic kink instability in both DCEP and EP, AC.

Fig. 2.5 summarizes the metal transfer observed among six different researchers. A large irregular shaped droplet is observed having a diameter similar to the wire diameter. Fig. 2.6 displays the metal transfer at 800 A. A new mode of metal transfer based on electromagnetic kink instability is observed for this current. Chapter 3 discusses more on this new mode of metal transfer.

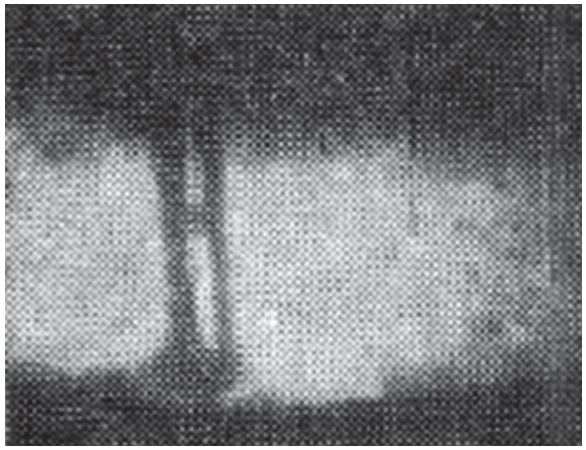

(a) 1964, Pokhodnya [16], 6 mm wire 470 A, 29 V

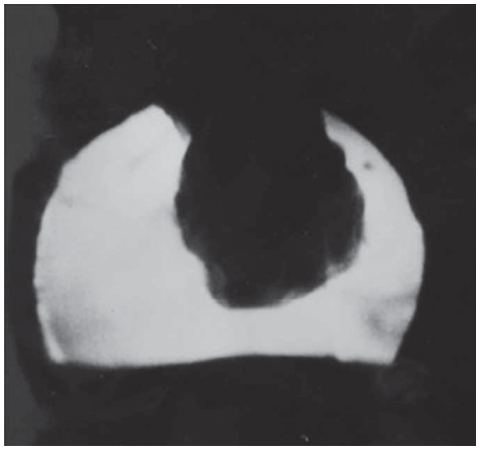

(b) 1965, Franz [19], 3 mm wire 470 A, 31 V

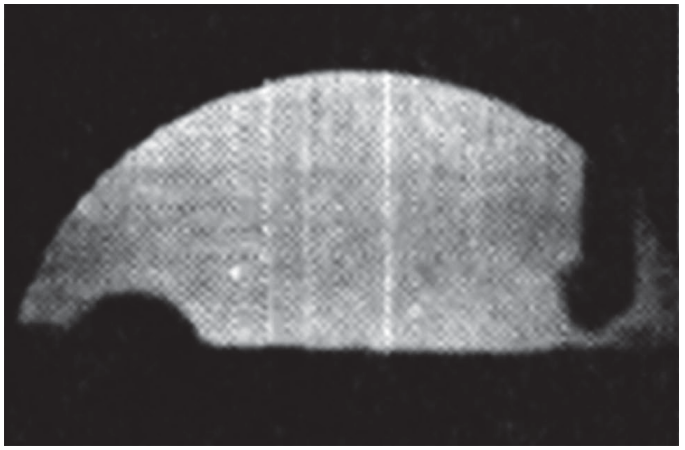

(c) 1981, Akahide et al. [27], 4.8 mm wire 500 A, 40 V

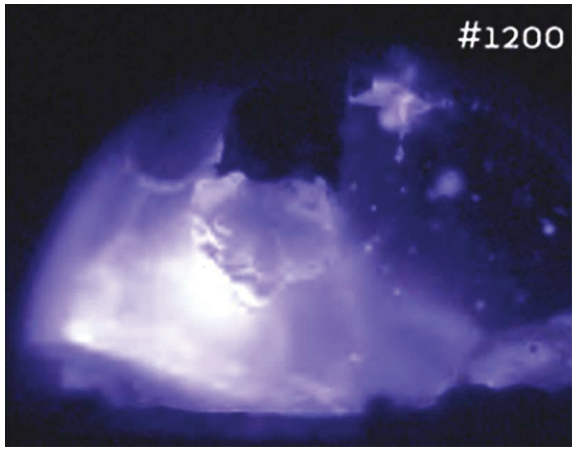

(d) 2013, Mendez et al. [28], 3.2 mm wire 500 A, 30 V

(e) 2015, Reisgen et al. [30], 2 mm wire 435 A, 28 V

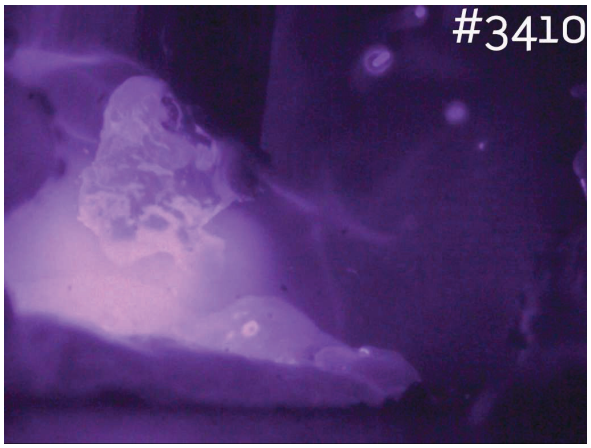

(f) 2015, Sengupta and Mendez [33], 3.2 mm wire 500 A, 30 V

Figure 2.5: Summary of metal transfer in SAW observed done by several researchers at around 500 A. A characteristic large droplet is observed having an irregular shape. Reprinted from Sengupta and Mendez [33]

(a) 1950, Grebelnik [4], 800 A, 38 V, 41.6 cm/min **(b)** 1950, Grebelnik [4], 800 A, 38 V, 66.6 cm/min **(c)** 2016, Sengupta and Mendez [33], 800 A, 38 V, 91.4 cm/min (flipped image)

Figure 2.6: Summary of the metal transfer at 800 A with Ref. [4]. A characteristic "whipping tail" (indicated by arrows) observed.

2.2.2.3 Effect of welding voltage on metal transfer in SAW

Welding voltage was found to be less significant in affecting the metal transfer in SAW [16, 19]. Pokhodnya [16] reported that with an increase in voltage, there was the increase in droplet mass and decrease in detachment frequency. But at very high voltages, droplets were observed to be smaller.

Franz reported with the increased voltage more flux gets melted and thus loss of current through slag increases; this is shown by the decrease in detachment frequency at higher voltages. The transition current for transfer through slag to transfer through the arc is affected by the voltage. For instance, the transition current for transfer through slag to transfer through arc increased from 260 A to 460 A for an increase in voltage from 26 V to 32 V.

Adrichem reported with increasing voltage at constant current, the ratio slag/free transfer increases. The increase in arc length leads to erratic movement of the molten wire tip.

2.2.2.4 Effect of welding flux on metal transfer in SAW

Researchers [19, 22] suggested that the welding flux has a minimal role in determining the metal transfer in SAW. According to Franz [19], the two important properties of the flux to be considered are the surface tension and the resistance of the molten flux. A proportion of the current goes through the slag; basic slags are a better conductor than acid slags considering the same temperature and FeO content. Franz stated that a flux with high CaF_2 is a good conductor in the molten state. The current conducted through the molten flux is not used to melt the wire hence decreases the detachment frequency. It was reported that the flux bed density was higher for a fused welding flux compared to a sintered flux. The sintered flux will have a larger cavity than a fused flux. The droplet

will transfer only through the slag in a case of a fused flux.

Adrichem reported with the increase of activity of the flux, the slag/free transfer ratio decreases. The increased activity of the slag will decrease the surface tension of the liquid metal and hence, increase free transfer through the arc zone. The movement of a cavity wall is determined by the viscosity of the slag that forms it. For instance, a less viscous slag will lead to an intensive movement of the cavity wall. The movement results in frequent contact of the wire tip with the cavity wall.

2.2.2.5 Reactions taking place at the droplet in SAW

Reactions with the gas/plasma

Researchers have proposed several arguments regarding the reactions at the droplet in SAW. Franz [21] reported the high temperature and large surface area of the droplet favors reaction of the droplet with the surrounding gas. Franz concluded the oxidation of carbon to carbon monoxide as the most important reaction at the droplet surface. Pokhodnya and Kostenko [17, 18] reported that the droplet before detachment from the wire is constantly in contact with the slag and the gas generated by the flux; this interaction time of the droplet with the slag/gas phase is of utmost importance. The time which the droplet spends after detachment till it meets the weld pool is of secondary importance.

Ref. [17] further reported that the welding current determines the time the droplet spends at the wire tip hence, influencing the extent of the reactions. Voltage has a minimal effect on the detachment frequency and hence, it was concluded that voltage has minimal effect on the reactions taking place at the droplet. Pokhodnya did not experimentally analyze the chemical composition of the electrode tip or the droplets. Also, the inference of the current and voltage on the reactions was deduced based on the reaction time and not an actual measurement of any chemical analysis.

Potapov and Lyubavskii [61] collected droplets after welding and carried out chemical analysis to understand the chemical reactions taking place at the droplet. The droplets were collected over a water cooled copper cathode and then screened and were subjected to chemical analysis. Potapov agrees with Pokhodnya and Kostenko [17, 18] on the dependence of reaction times at the droplet with the welding current. However, with the voltage the reaction time observed by Potapov was much higher than Pokhodnya; Potapov reported the use of a high CaF_2 flux by Pokhodnya restricted him in achieving a stable process with high voltages. Nevertheless, Potapov reported the reaction times at the electrode tip are important and decisive in determining the overall weld metal chemistry.

The time when the droplet passes through the gas to the weld pool is of secondary importance. Potapov and Lyubavskii [62] reported that the droplet at the electrode tip undergoes vigorous chemical and slag-metal reactions and by the time the droplet reaches the weld pool there is a very limited scope of any further reactions. Based on the experimental data Potapov developed regression equations to predict the change in the Mn, Si, S and P content of the weld metal.

North et al. [63] collected the electrode tip and droplets and measured the oxygen content to predict the reaction at the droplet during SAW. North reported at the droplet temperatures of 2400 C, all of the oxygen gets dissolved in liquid iron. In another work, North [58] reported that the Mn loss takes place at the droplet/slag interface at the electrode tip.

Lau et al. [64] conducted experiments with CaO-Al_2O_3 flux. Lau collected the electrode tips and detached droplets after they passed through the arc and studied its composition. Lau reported that the droplet is a site of oxygen absorption. The oxygen was produced from the breakdown of the involved fluxes. A large amount of Al was found in the droplets, showing the extent of decomposition of the flux. Lau et al. [65] found

on increasing welding current there was an increase in oxygen content at the electrode tip and detached droplet. Increasing current increases arc temperature and hence, more decomposition of the fluxes. The oxygen from the decomposed fluxes get absorbed at the droplet surface.

Mitra [59] and Mitra and Eagar [66] reviewed all the previous work on reaction time theories at the droplet. Mitra [67] proposed that oxygen from the breakdown of the fluxes is transferred to the droplet and the exchange of alloying element is minimal. The oxygen rapidly builds at the surface and prevents carbon and other elements from reaching the surface and reacting; thus, contradicting the conclusions from Franz [20, 21] and Potapov [61].

Electrochemical reactions

Kim et al. [68] reported the possibility of electrochemical reactions are the droplet in SAW. It was proposed that the electrochemical reactions take place between the droplet and the surrounding slag. In DCEP welding, the reaction 2.1 was proposed to take place at the droplet (anode) and in DCEN welding, reactions 2.2, 2.3, and 2.4 are proposed to take place at the droplet (cathode). Kim reported that in SAW, both the thermochemical reactions mentioned previously and electrochemical reactions are important. In DCEP, the electrochemical reactions are responsible for Oxygen anion pick up from the flux to the droplet.

$$M(metal) + nO^{2-}(slag) = MO_n(slag) + 2ne^- \tag{2.1}$$

$$M^{2+}(slag) + 2e^- = M(metal) \tag{2.2}$$

$$Si^{4+}(slag) + 4e^- = Si(metal) \tag{2.3}$$

$$O(metal) + 2e^- = O^{2-}(slag) \tag{2.4}$$

M is iron or any other alloy element in consideration.

Table 2.3: Summary of research done in metal transfer in SAW

Focus of research	**Conclusions**
Mode of metal transfer	a) Free flight transfer either through the arc or slag b) No evidence of short-circuit transfer observed
Effect of welding current	a) Current is of significant importance in determining the metal transfer in SAW b) A large irregular shaped droplet is observed at low current in DCEP c) Refs. [16, 19] reported that at high currents, a tapered electrode is observed spraying small droplets d) Refs. [28, 33, 54, 57] reported at high currents, a tapered electrode was observed ejecting a molten metal tail based on electromagnetic kink instability
Effect of welding voltage	a) Voltage is of less significance in determining the metal transfer in SAW b) A decrease in droplet frequency on increasing voltage at same currents [16, 19] c) Increasing voltage the ratio of slag/free transfer increases [22]
Effect of welding flux	Flux is of less significance in determining the metal transfer in SAW
Reactions at the droplet	a) Ref. [59] concluded that elemental oxygen from the fluxes gets adsorbed on the droplet surface and prevent any further reaction at the droplet. b) Ref. [68] proposed possibilities of electrochemical reactions between the flux and droplet. The type of reaction will depend on the polarity of the electrode

2.3 Arc length in SAW

Arc length plays an important role in determining the quality of the weld in arc-welding processes. It is extensively studied in other arc-based systems like gas metal arc welding. In the beginning, there was a debate on whether there is an arc or no arc in SAW. The Welding Handbook from 1942 [69] describes this process as "Submerged Melt Welding", where the welding takes place without an arc and the current is carried through the molten flux. The subsequent experimental and oscillographic analysis have shown that there is an arc in SAW. However, the possibility of no arc can not be ignored with the use of high conductive fluxes, as used in electroslag welding. In SAW, the arc is hidden under the flux bed and not visible to the sight. In addition, the composition of the gas forming plasma in SAW is complex. Peshak [36] mentions that Webb indicated the SAW plasma to be constituting primarily of iron vapors and elements from the flux and electrode. Table 2.4 summarizes the researchers involved in the investigation of the arc length in SAW.

Focus of research in arc length in SAW The research in arc length and plasma composition in SAW mainly focused on answering the following questions:

- Is there an arc during SAW?
- What is the effect of welding voltage, current and travel speed and on the arc length in SAW?
- What is the effect of the type of welding flux on the arc length in SAW?

2.3.1 Methodologies utilized for research in arc length in SAW

The methodology used to answer the questions related to the arc length is:

- Investigation using X-ray photography.

2.3.1.1 Investigation using X-ray photography

In X-ray photography, X-rays are directed on the SAW arc zone. The X-rays transmitted are then captured using a camera. In 1942, Tannheim [34] published work on observation of phenomena in SAW using X-ray photography. The X-ray photographs were accompanied by current and voltage readings obtained from an oscillogram. Tannheim's work focused on investigating whether an arc is present or not in SAW. In 1947, Ostapenko and Medovar [3] used X-rays to investigate the different aspects of the arc zone in SAW. They concluded that the arc length in SAW consists of two parts: a) the part below the base metal and not visible in the radiographs, b) the part between the wire and the base metal.

In 1949, Paton B.E. [35] used X-ray techniques to understand the phenomena in SAW. The quality of the radiographs is not very good to draw conclusions regarding the shape of the arc. In 1961, Tikhodeyev [70] used a very thin base metal (0.7 cm) so that the X-rays can penetrate the base metal and the part of the arc below the base metal can be seen on the radiographs. Peshak [36] used X-ray technique and investigated different aspects of the arc in SAW.

The X-ray setups used to radiograph the arc zone in SAW are similar among researchers. The setup used by Peshak [36] will be used to describe a typical X-ray setup used for observing the arc zone in SAW. Fig. 2.7 shows a typical X-ray setup to visualize the arc in SAW. The setup consisted of an X-ray unit. The X-ray film was placed in a cassette which was held in place with a cassette holder located just behind the welding tip. The welding head was stationary, and the plate was moved. Most of the radiographs generated were at an exposure time of 6s (for Kodak Type AA X-ray film). Some were generated at exposure times of 3s (for Type KK film). Finally, the films are developed and printed for subsequent analysis.

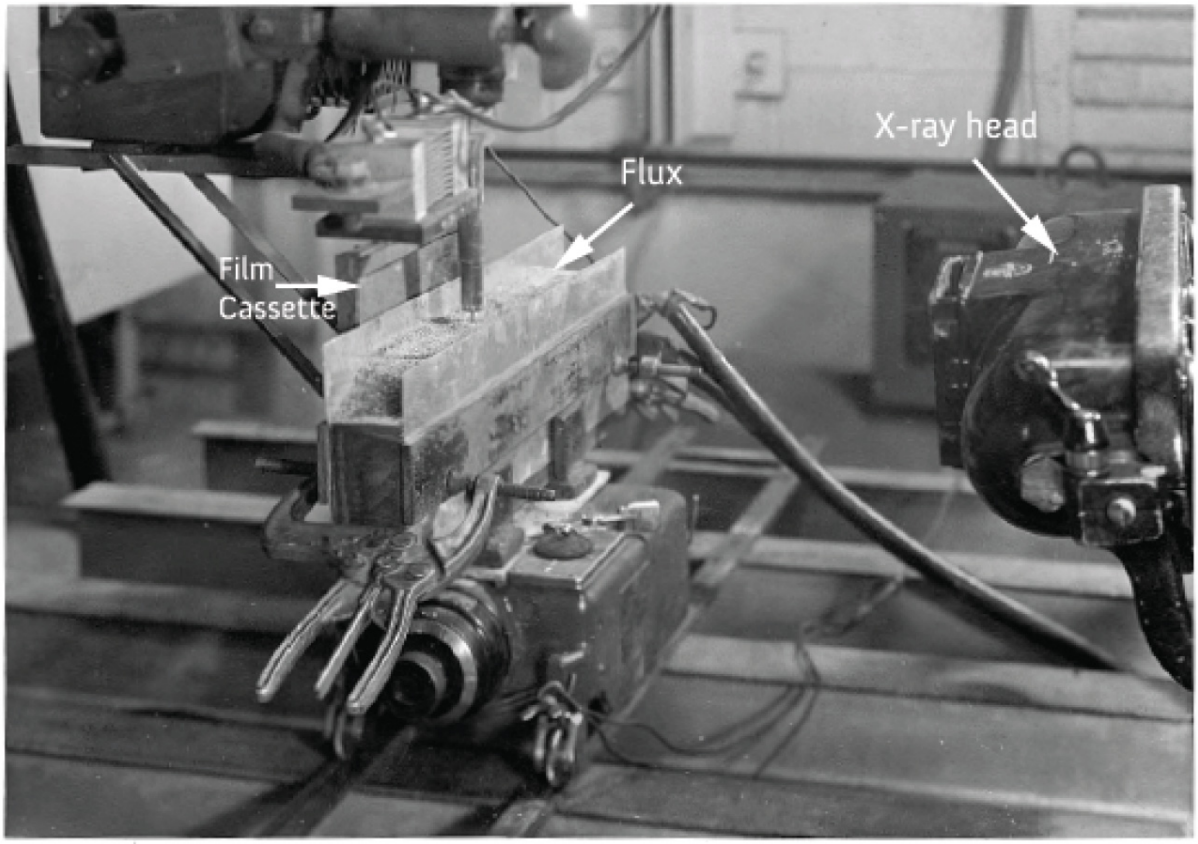

Figure 2.7: An experimental setup for filming X-ray pictures of the arc in SAW. Reprinted from Ref. [36].

Table 2.4: Details of research into the arc length in SAW

Researcher	Methodology	Frame rate (f/s)	Wire diameter (mm)	Flux*	Current (A)	Voltage (V)	Travel speed (cm/min)
Tannheim [34]	X-rays	1	6.35	Ellira powder	1100, 1200	40, 45, 55	30, 35, 50
Ostapenko, Medovar [3]	X-rays	1	5	AN-3, OSC-45 (Russian)	800, 1400	25, 30, 38, 48	41.67, 100
Paton B.E. [35]	X-rays	Multiple frames	4.0,5.0	AN-3 (Russian)	500 - 1000	27 - 55	-
Grebelnik [4]	X-rays	1	5	GAZ-1, ASH (Russian)	600, 800	24, 38	25, 41.67, 66.67
Tikhodeyev [70]	X-rays	1	2.4	ADW-500, AN-348 (Russian)	150 - 2200	15 - 48	-
Peshak [36]	X-rays	-	2.4, 3.2, 4.0	A - G	200-600	20 - 45	25.4 - 101.6
Engel [24], Eichhorn and Engel [25]	X-rays	500	1.6	-	190	43	20

* Composition of the fluxes are presented in Table A2.1

2.3.2 Summary of findings on the arc in SAW

The present section will summarize all the findings on the arc in SAW, aiming to answer all the questions regarding the arc in SAW. The findings on the arc in SAW are as follows:

2.3.2.1 Is there an arc during SAW?

The early attempts of investigation in SAW weld zone aimed to settle the debate on whether an arc exists during welding under the fluxes. In 1942, Tannheim [34] led an investigation of the arc zone in SAW using X-ray radiography. Tannheim reported that the welding in SAW (Ellira Verfahrens) is by the formation of an arc. Fig. 2.8 shows the formation of an arc inside a cavity. The formation of an arc is confirmed by the lighter contrast of the region (arc zone) compared to the molten flux, base metal, and electrode. Tannheim reported the X-rays are more permeable through the gaseous region of the arc and hence result in a bright spot; the base metal, slag, and electrode contains elements with high atomic numbers and thus the X-rays are less penetrable through them giving a dark contrast on the radiographs.

Ostapenko and Medovar [3] and Grebelnik [4] observed an arc during SAW similar to Tannheim. Ref. [3, 4] defines the arc length between the two electrodes (wire and base metal) as an external component of the arc length and arc below the base metal as the hidden component of the arc length. Similar observations are reported in Ref. [71]. Paton E.O. [71] reported that the amount of current going through the molten flux is extremely low.

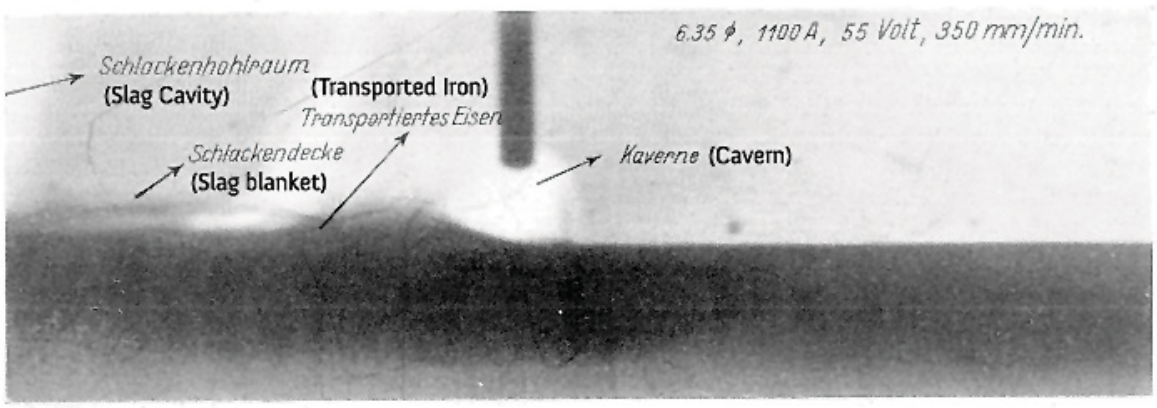

Figure 2.8: X-ray picture of arc zone in SAW. Reprinted from Tannheim [34]. Current used is 1100A, voltage is 55V, and travel speed is 35 cm/min for a 6.35 mm diameter wire. The images show the presence of an arc in SAW. The arc burns in a cavity and is represented by the bright spot between the electrode and base metal.

2.3.2.2 Effect of welding voltage on arc length in SAW

Welding voltage has an effect on the arc length in open arc welding processes. Investigations were carried out using X-ray photography to understand the effect of voltage on arc length in SAW. Ostapenko and Medovar [3] reported the arc length increases with increasing voltage. The increase in arc length with voltage is reported to be linear. Fig. 2.9 shows the influence of voltage on the arc length in SAW. Grebelnik concludes similar observations as Ref. [3] for the effect of welding voltage on the arc length. Paton [35] proposed a linear relationship between the external component of the arc length the voltage at constant current; the theory was experimentally verified using X-ray photography of the arc zone; Fig. 2.10 shows the X-ray images obtained by Paton B.E. and the relationship between voltage and arc length in SAW. Peshak [36] reported the arc length to increase with the increase in voltage. The curves between arc length are fairly linear with occasional departure from linearity. Fig. 2.11 shows the effect of voltage on arc length for three different fluxes. Tikhodeyev [70] reported an increase in arc length

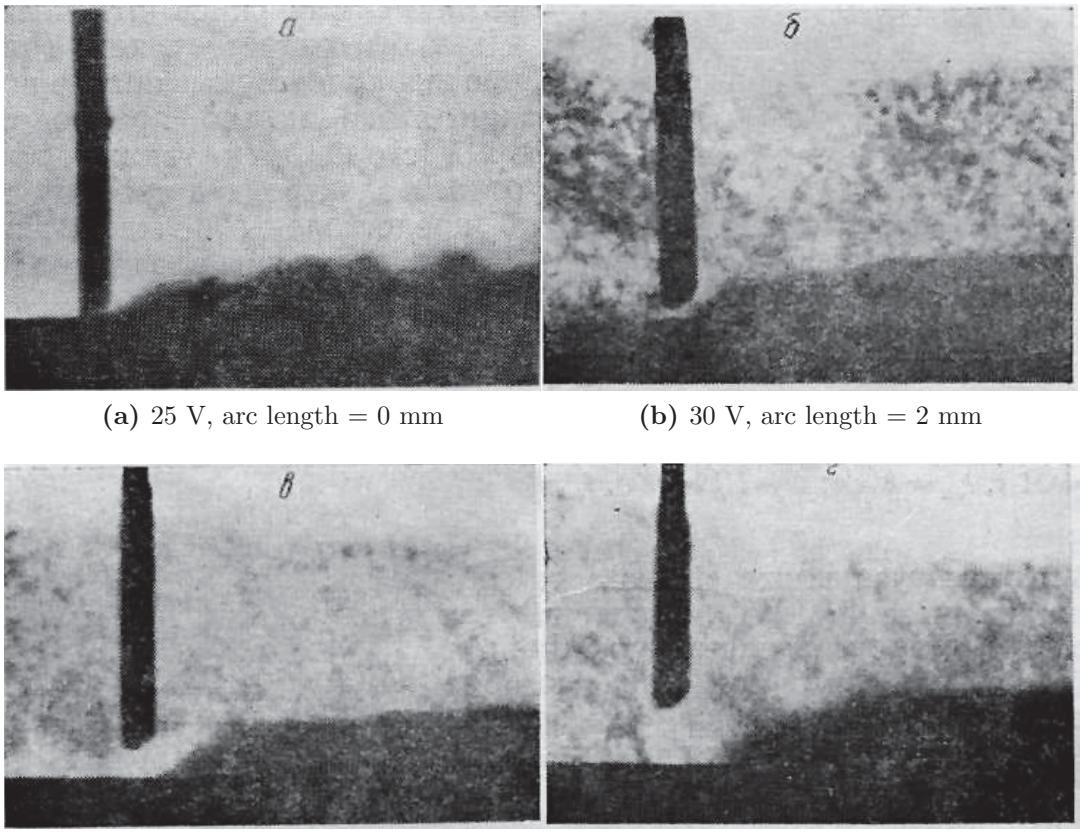

(a) 25 V, arc length = 0 mm **(b)** 30 V, arc length = 2 mm

(c) 38 V, arc length = 5 mm **(d)** 48 V, arc length = 9 mm

Figure 2.9: X-ray pictures of arc zone in SAW. Reprinted from Ostapenko and Medovar [3]. The wire diameter is 5 mm and current is 800 A. The electrode is traveling from right to left and travel speed is 41.66 cm/min. The flux used is AN-3 with primary composition as silicon dioxide. The images show the influence of voltage on the arc length in SAW. An increase in voltage leads to an increase in the external length of the arc.

with the increase in voltage for SAW.

2.3.2.3 Effect of welding current on arc length in SAW

Welding current has an effect on the arc length in SAW. Researchers have conducted experimental investigations to study this effect. Ostapenko and Medovar reported a decrease of 6 mm in the arc length with an increase of current from 800 A to 1400 A. Fig. 2.12 shows the effect of current on arc length as observed by Ref. [3]. Ref. [3] reported

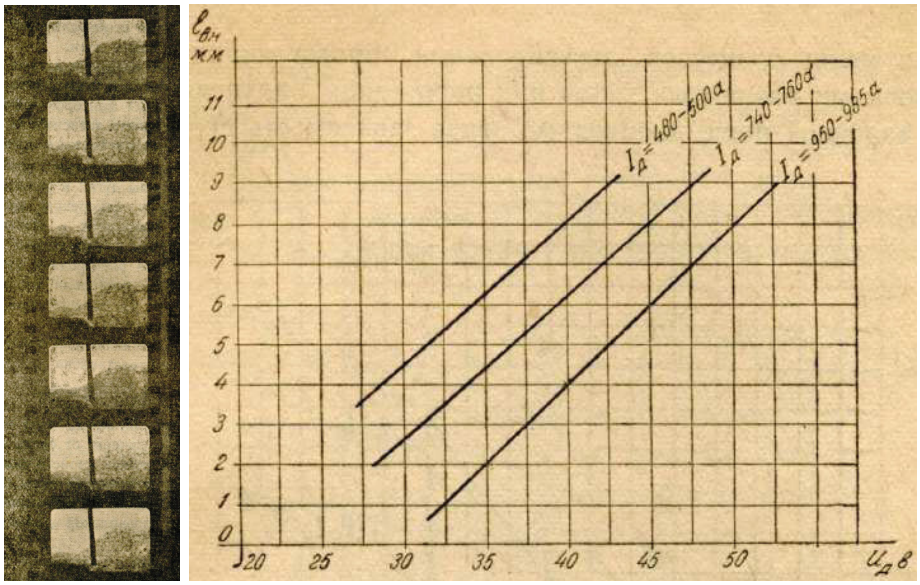

Figure 2.10: Left image: X-ray pictures of arc zone in SAW. Reprinted Fig. 1 from Paton B.E. [35]. Right image: arc length vs voltage. Reprinted Fig. 2 from Paton B.E. [35].

a decrease of 1 mm in arc length for every 100 A increase in current. Peshak [36] reported a decrease in arc length for an increase in current at a constant voltage.

Fig. 2.13 shows the effect of current on the arc length as observed by Peshak [36]. Peshak reported that with an increase in current under same voltage, the corresponding wire feed speed will increase and the wire tip will be drawn more into the plasma region. The anode and cathode fall voltages will increase with an increase in current and plasma length have to decrease in order to maintain the same total arc voltage.

Eichhorn and Engel [25] report the change in arc length was due to the movement of the weld pool. Fig. 2.14 shows the dependence of the arc length on the movements of the weld pool. The current is responsible for these weld pool movements.

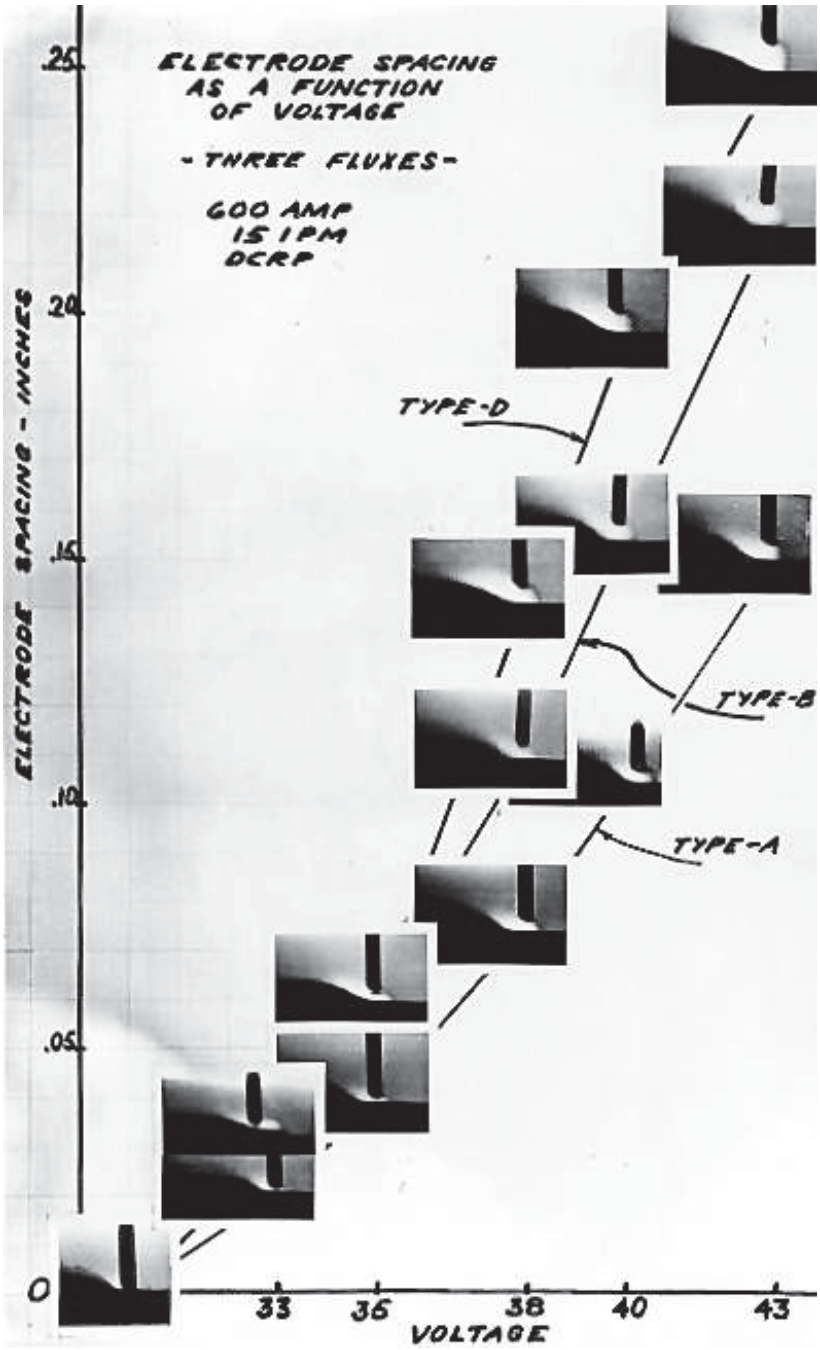

Figure 2.11: Radiographs of SAW weld zone. Reprinted Fig. 40 from Peshak [36]. The current used is 600 A, the wire diameter is 5/32 in., and travel speed is 38.1 cm/min from left to right. Figures summarize the effect of voltage on arc length in SAW for fluxes A, B, and D.

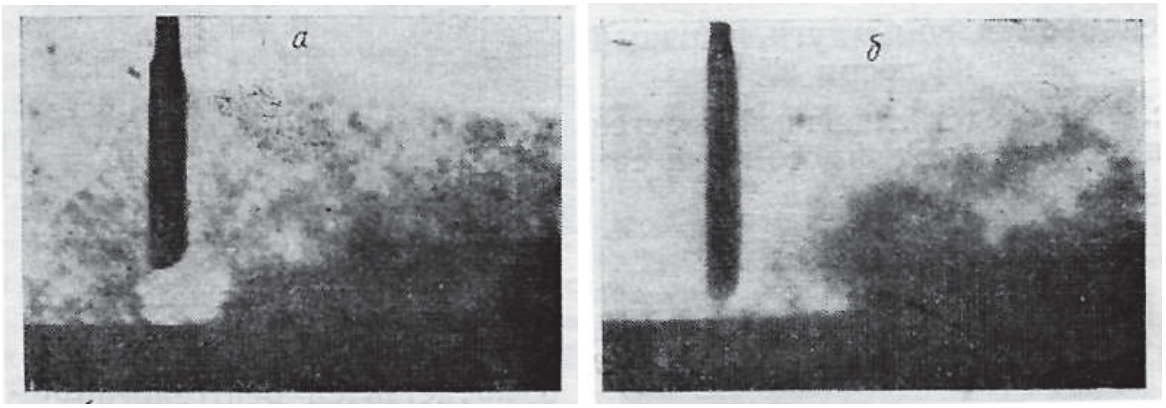

(a) 800 A, arc length = 9 mm **(b)** 1400 A, arc length = 3 mm

Figure 2.12: X-ray pictures of arc zone in SAW. Reprinted from Ostapenko and Medovar [3]. The wire diameter is 5 mm and voltage is 48 V. The electrode is traveling from right to left and travel speed is 41.66 cm/min. The flux used is AN-3 with primary composition as silicon dioxide. The images show the influence of current on the arc length in SAW. An increase in current leads to a reduction in external length of the arc.

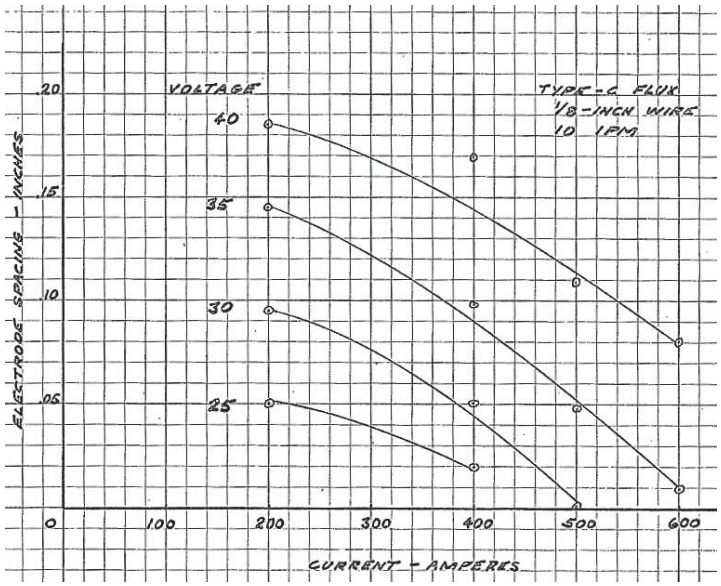

Figure 2.13: Effect of current on arc length in SAW. Reprinted Fig. 44 from Ref. [36]. The arc length decreases with an increase in current at a constant voltage.

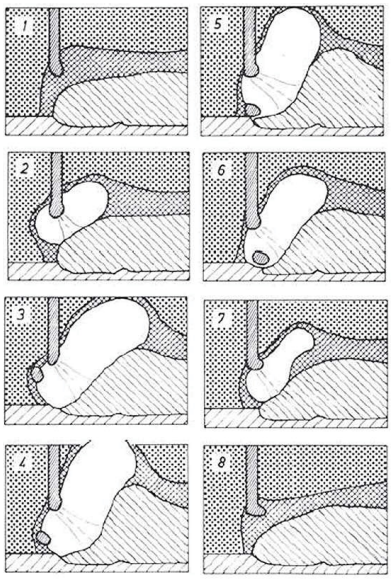

Figure 2.14: Images from high-speed X-ray film of weld zone of SAW. Reprinted from Eichhorn and Engel [25], and Engel [24]. Current used is 190 A, the voltage used is 43 V, travel speed is 20 cm/min. The electrode is moving from right to left. The images show the dependence of the arc length on the weld pool movements.

2.3.2.4 Effect of travel speed on arc length in SAW

The effect of travel speed on the arc length has not been well understood among researchers. Ostapenko and Medovar [3] reported that the arc length does not change with travel speed. However, Grebelnik [4] reported a decrease in the arc length with increasing travel speed. Fig. 2.17 summarizes observations of Grebelnik [4]. Peshak [36] reported that travel speed has a significant impact on the arc length in SAW. Fig. 2.15 shows the effect of travel speed on the arc geometry. The arc length is seen to decrease with an increase in the travel speed and ultimately reaches minima at about 20 inches per min (ipm); this trend is consistent with all fluxes. Peshak notes that at slower travel speeds, the arc is vertically symmetrical and the molten metal tends to flow under and ahead of the wire tip. At high travel speeds, the arc is forced downward and backward because of the higher travel speeds and mechanical resistance of the flux.

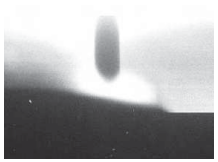

(a) Travel speed = 25.4 cm/min

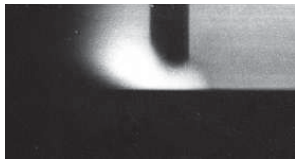

(b) Travel speed = 38.1 cm/min

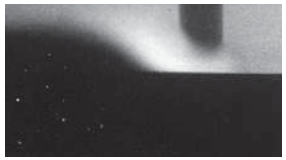

(c) Travel speed = 63.5 cm/min

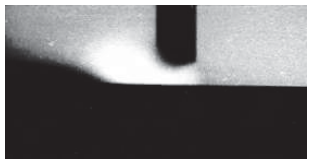

(d) Travel speed = 76.5 cm/min

(e) Travel speed = 101.6 cm/min

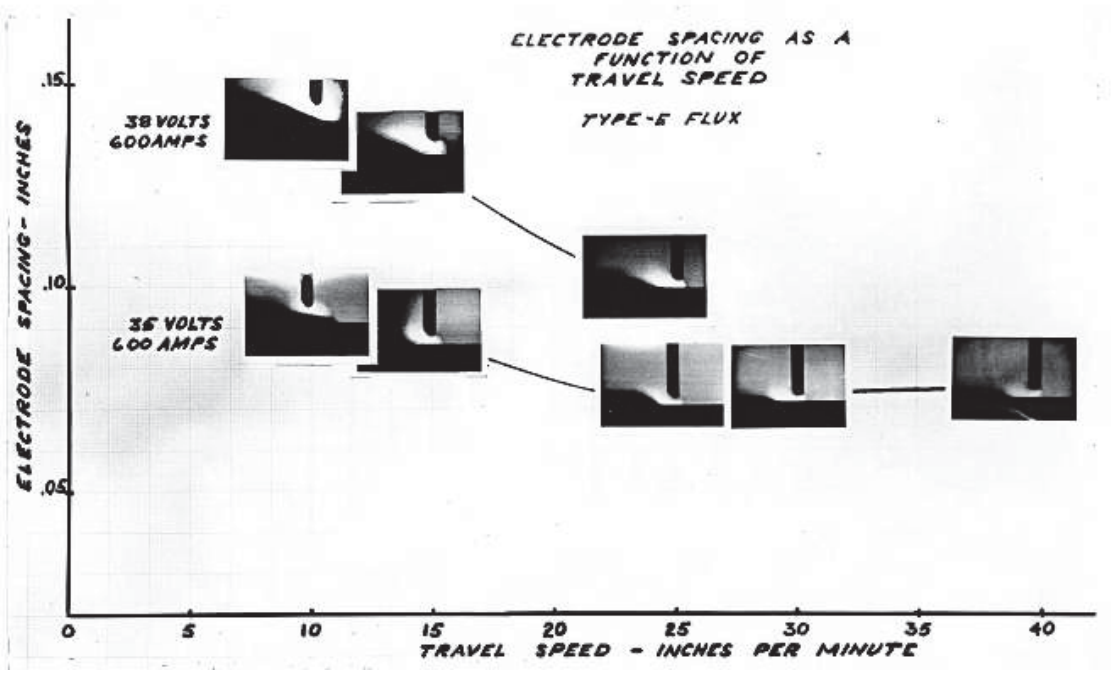

(f) Electrode spacing as function of travel speed.

Figure 2.15: Radiographs of SAW weld zone. Reprinted from Peshak [36]. The flux used is Flux E. Figures summarize the effect of travel speed on arc length in SAW.

2.3.2.5 Effect of welding fluxes on arc length in SAW

Welding fluxes provide a unique atmosphere in the arc cavity of SAW. The properties of the gas forming the plasma determines the shape of the arc. Researchers tried to study the effect of different fluxes on the shape of the arc. Ostapenko and Medovar [3] reported that the arc length under different fluxes depends on the stabilizing properties of the flux. The fluxes with lower stabilizing properties (flux OSC-45 in this case) have a shorter arc length. Fig. 2.16 shows the effect of two different flux on the arc length as observed by Ref. [3]. Grebelnik [4] tried two fluxes and did not obtain a lot of change in the arc length with the flux composition for low travel speeds; the results are shown in Fig. [4].

Peshak [36] reported that the constituent of the plasma determined the electrical characteristics of the arc and the plasma composition will be determined by the composition of the flux. In case two fluxes produce different arc length for same welding parameters, then two changes might have occurred: a) thermal conductivity of the plasma b) anode and cathode fall voltages. If the thermal conductivity of the arc under two different fluxes is same, then the arc length will be determined by the anode and cathode fall voltages under these fluxes or vice versa. Peshak reported that most of the fluxes give different plasma conductivity and anode and cathode fall voltages; the dominant factor amongst the two will determine the arc length. Fig. 2.11 summarizes the effect of voltage on arc length for three different fluxes. Peshak further reported the arc length increased on adding CaF_2 up to 5% by weight then decreases when CaF_2 is increased further; an initial decrease and then an increase in the plasma conductivity was reported for this type behavior of arc length.

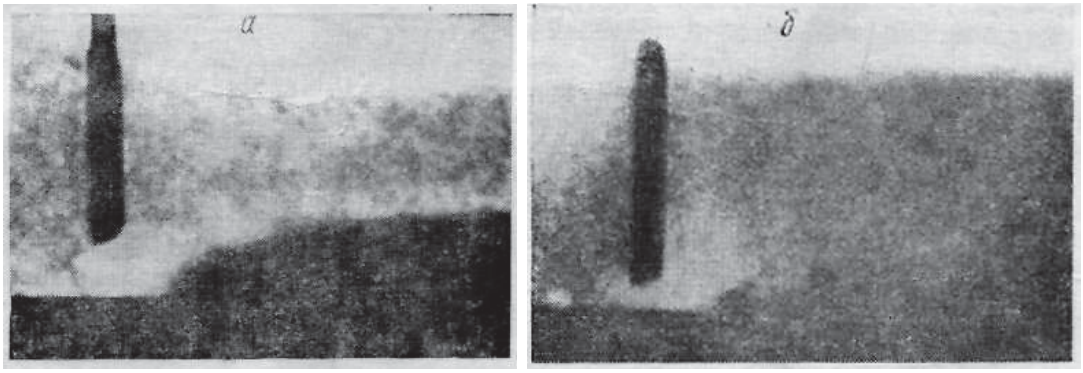

(a) Flux AN-3 (Russian), arc length = 9 mm **(b)** Flux OSC-45 (Russian), arc length = 3 mm

Figure 2.16: X-ray pictures of arc zone in SAW. Reprinted from Ostapenko and Medovar [3]. The wire diameter is 5 mm, current is 800 A, and voltage is 48 V. The electrode is travelling from right to left at 41.66 cm/min. The images show the influence of flux on the arc length in SAW.

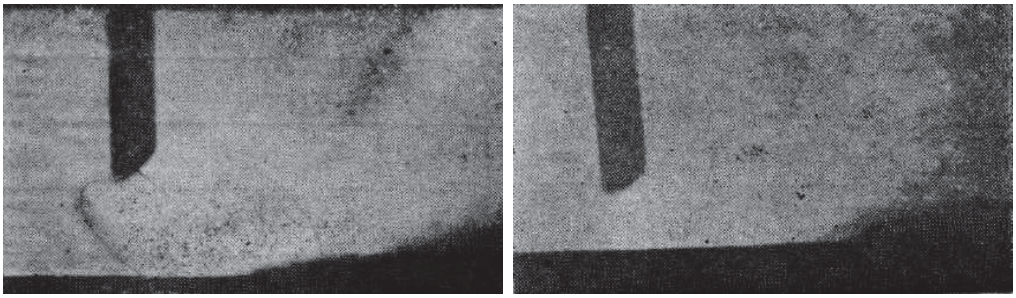

(a) Flux GAZ-1 (Russian), travel speed = 41.66 cm/min, arc length = 13 mm

(b) Flux GAZ-1 (Russian), travel speed = 66.66 cm/min, arc length = 7 mm

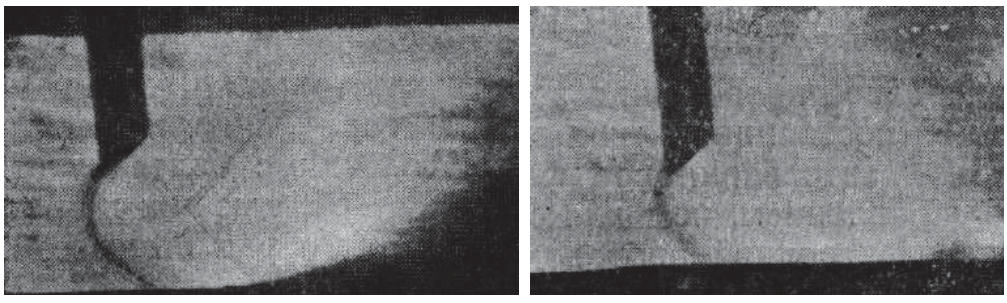

(c) Flux ASH (Russian), travel speed = 41.66 cm/min, arc length = 14 mm

(d) Flux ASH (Russian), travel speed = 66.66 cm/min, arc length = 11 mm

Figure 2.17: X-ray pictures of arc zone in SAW. Reprinted from Grebelnik [4]. The wire diameter is 5 mm, current is 800 A, and voltage is 38-40 V. The welding direction is from right to left. The images show the influence of flux and travel speed on the arc length in SAW.

Table 2.5: Summary of research done in arc length of SAW

Focus of research	**Conclusions**
Is there an arc during SAW?	An arc is present during SAW
Effect of welding voltage	Keeping other parameters constant, arc length increases with increasing welding voltage
Effect of welding current	Keeping other parameters constant, arc length decreases with increasing welding current
Effect of travel speed	No unanimous conclusion on the effect of travel speed on arc length. Ref. [36] reported a decrease in the arc length with increase in travel speed, other researchers did not found change in arc length with travel speed
Effect of welding fluxes	a) The flux composition has an effect on the arc length b) Ref. [36] concluded that the flux composition could affect the plasma conductivity and anode and cathode fall voltages The dominant factor among the two will determine the arc length c) Ref. [3] found a shorter arc with a less stabilizing flux (flux with no arc stabilizers)

2.4 Arc cavity and slag shell in SAW

The arc in SAW burns in a cavity. The cavity is believed to be surrounded by a slag shell, however, the presence of the shell has been debated among researchers. The shell is believed to prevent atmospheric contamination in SAW. The present section aims to summarize the work done on the arc cavity and slag shell in SAW.

The research in arc cavity and slag shell in SAW mainly focused on answering the following questions:

- What is the typical nature of the arc cavity in SAW?
- What is the pressure and atmosphere in the arc cavity in SAW?
- Is there a slag shell present in SAW?

2.4.1 Methodologies utilized for research in arc cavity and slag shell in SAW

The methodologies used to answer the questions related to the arc cavity and slag shell are:

- Investigation using X-rays.
- Investigation using optical techniques.
- Investigation using a piezoelectric sensor, water manometer, and gas sampler.
- Investigation using rapid ejection of the weld pool technique.
- Investigation using spectroscopy.

2.4.1.1 Investigation using X-rays

X-rays are directed to the arc cavity in SAW. The cavity in SAW is dynamic in nature. The X-rays directed to the cavity is mostly transmitted through the lower density gases that fill the cavity. The boundary of the cavity with the flux is indicated by darker contrast. Thus, the position of the cavity can only be approximated using this process.

A typical X-ray setup to capture arc cavity dynamics in SAW is shown in Fig. 2.18. The X-rays penetrate the welding zone and strike the phosphor screen of the X-ray image intensifier. The phosphor screen emits electrons depending on the intensity and brightness of the X-ray shadow image. The photocathode electrons are accelerated at a voltage of 25 kV and focused on a small observing screen; this creates an image eleven times smaller and 3000 times brighter. The image is then captured using a high-speed camera. Due to the strong absorption of the X-rays by the welding flux and the slag, the frame rates could not be increased more than 500 f/s. The width of the welding zone was limited to 20 mm. To avoid overheating of the base material it was pierced in the longitudinal direction and cooled with cooling water. Simultaneously with the filming, the current-voltage readings were recorded with an oscillogram; it was synchronized with the images in the film. Eichhorn et al. [72] has reported X-ray videography of SAW of Aluminium. The frame rates used were 800 f/s.

Table 2.6: Details of research in visualizing the arc cavity

Researcher	**Methodology**	**Key feature of the methodology**
Eichhorn and Engel [25]	X-rays	Operating voltage = 40 kV
Eichhorn et al. [72]	X-rays	High-speed radiography and recording the image with a high-speed camera at 800 f/s
Reisgen et al. [29, 30, 32]	Optical	a) Using a ceramic tube perpendicular to welding direction b) Using a longitudinal glass sheet parallel to the welding direction
Kuzmenko [39–41]	Optical	Using a glass sheet parallel to welding direction
Gött et al. [57]	Optical	High-speed videos at 5000 f/s synchronized with high-speed spectra using a spectrometer

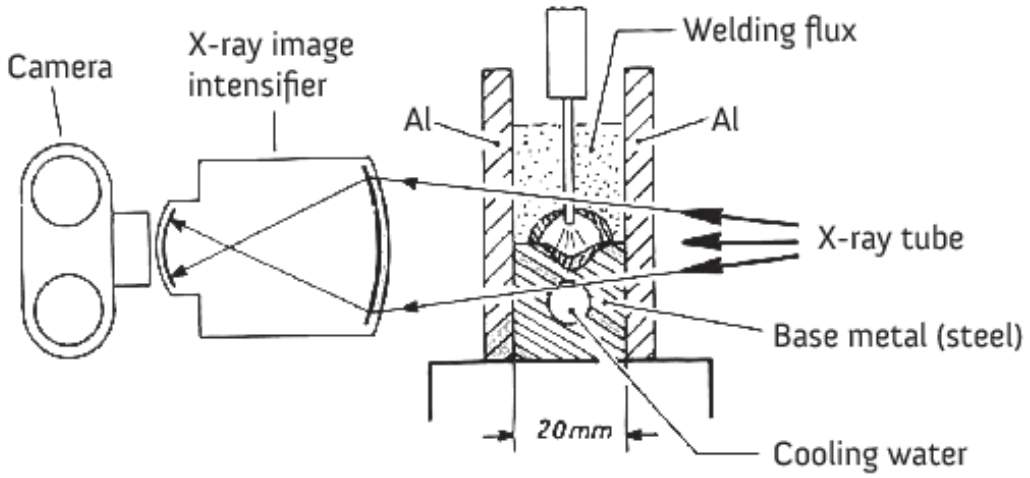

Figure 2.18: An experimental setup schematic used for filming X-ray pictures of arc cavity in SAW. Reprinted from Ref. [25].

2.4.1.2 Investigation using optical techniques

Optical techniques provide direct visualization of the arc cavity in SAW. Reisgen et al. [29, 30, 32] used different optical techniques to obtain the view of the weld zone in SAW. Fig. 2.19 shows the experimental setup by Reisgen to observe the arc cavity in SAW. In the first method, a ceramic tube is placed perpendicular to the welding direction and is shown in Fig. 2.19a. The tube is placed in such a way that the cavity wall and the ceramic tube forms a single component during welding. The tube is very small in size and the cavity is opened only from one end. An optimized gas flow is used in this method to avoid the overstretching of the arc cavity. In the second method, a glass pane is placed longitudinally to the welding direction. The phenomena in the cavity are captured into videos from the view provided by the glass pane.

Kuzmenko [39–41] carried out experiments in SAW using a window glass pane parallel to the welding direction to obtain a view of the cavity in SAW. The setup is similar to the one used by Reisgen and is displayed in Fig. 2.19b. The research focused especially

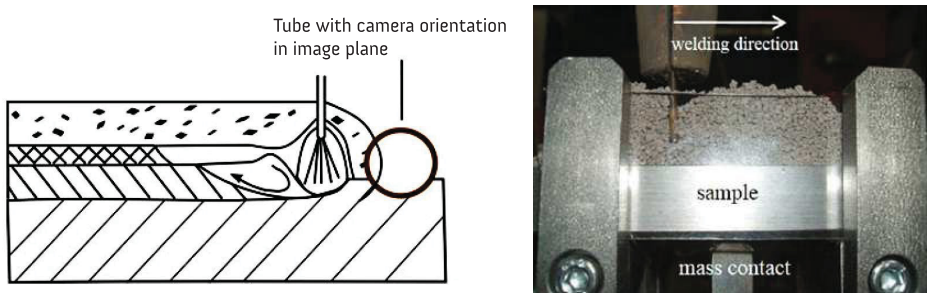

(a) Observation of SAW arc cavity using a perpendicular ceramic tube to the welding direction.

(b) Observation of SAW arc cavity using a longitudinal glass sheet parallel to the welding direction.

Figure 2.19: Schematic of the experimental setup to observe arc cavity in SAW by Reisgen et al. [30, 32].

on the presence of slag shell in SAW.

Recently, Gött et al. [57] used a thin-gauge steel tunnel to penetrate the flux bed. The opening in the flux bed provided an opportunity to record the phenomena going in the arc cavity of SAW. The videos are recorded at 5000 f/s. A shielding gas was blown in from side to prevent the arc cavity from collapsing.

2.4.1.3 Investigation using a piezoelectric sensor, water manometer and gas sampler

The present section incorporates the various techniques used to measure the pressure and the atmosphere of the arc cavity in SAW. The pressure and atmosphere of the arc cavity influence the reactions in SAW and are significant in determining the final weld metal composition. The cavity is not visible during the welding and the processes taking place in the cavity are very complex and difficult to quantify. Researchers have utilized unique techniques to understand the cavity pressure and atmosphere of SAW. The techniques used are as follows:

Pressure measurements using a piezoelectric sensor

Schaefer et al. [42], Reisgen et al. [30, 32] reported the measurement of relative pressure in the arc cavity in SAW pulsed and non-pulsed state using a piezoelectric sensor. Fig. 2.20 shows the schematic of the experimental setup. A glass pipe is inserted into the cavity during the welding process; this pipe is connected to a pressure measuring piezoelectric sensor. A tube made of quartz with a 2 mm internal diameter was used. The tube has to be continuously pushed into the arc cavity as it melts under the high temperatures. The possibility of the tube getting closed after melting is not reported.

Pressure measurements using a water manometer

Kuzmenko [39, 40] reported the measurement of the gas pressure in the arc cavity in SAW. A water manometer accompanied with a steel pipe having an internal diameter of 4 mm was used to quantify the pressure of the gases in the arc cavity. Fig. 2.21 shows the schematic of the setup.

Collection of gases from arc cavity using a gas sampler

Terashima et al. [73] conducted experiments to collect gas from the arc cavity of SAW. Fig. 2.22 shows the gas sampler used by Terashima to collect gas from the arc cavity in SAW. The front end of the sampler is made up of quartz glass which gets melted in the heat of the arc and gases enter the sampler to the soft glass. The cock is closed to avoid any interference from the atmosphere. A microsyringe is used to extract the gas from the soft glass through the vacuum hose. Gas chromatography is used to obtain the composition of the gas. Fig. 2.23 shows the schematic of the operation The gas sampler is pushed rapidly under the arc when the distance between the cavity and the sampler is less than 30 mm. The fluxes used for this study were fluxes G1, G4, and G7. The composition of these fluxes are noted in Table A2.1.

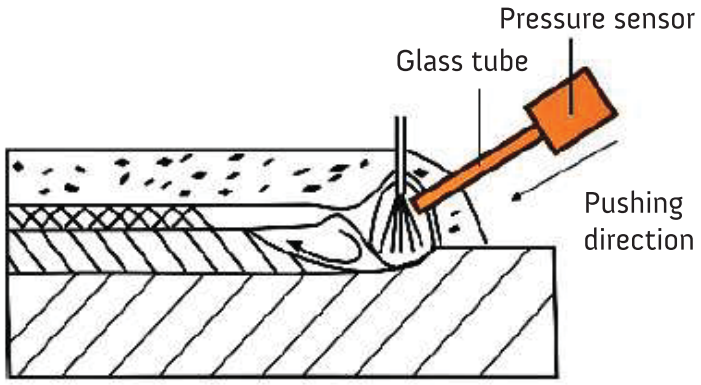

Figure 2.20: An experimental setup used for measuring arc cavity pressure in SAW. Reprinted Fig. 5 from Reisgen et al. [32]. The figure shows the use of a piezoelectric sensor to measure the pressure in arc cavity in SAW.

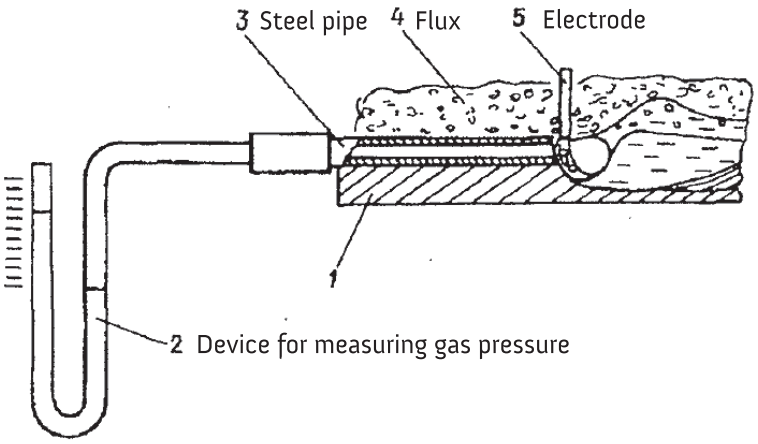

Figure 2.21: An experimental setup to measure arc cavity pressure in SAW. Reprinted Fig. 2 from Kuzmenko [39, 40]. A water based manometer is used to measure the pressure in arc cavity in SAW.

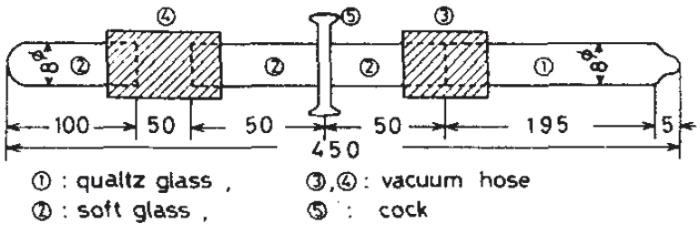

Figure 2.22: A gas sampler used to collect gas from the arc cavity of SAW. Reprinted Fig. 10 a from Terashima et al. [73].

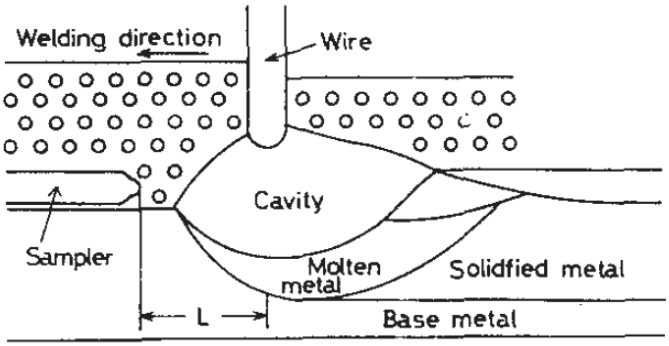

Figure 2.23: An experimental setup to collect gas from the arc cavity in SAW. Reprinted Fig. 10 b from Terashima et al. [73]. The sampler is pushed rapidly under the arc when L is 30 mm.

2.4.1.4 Rapid ejection of the weld pool

Kuzmenko [39–41] theoretically and experimentally investigated the presence of slag shell in SAW. Kuzmenko reported conducting of special experiments to understand the distribution of mass of liquid slag along the length of the weld pool. Fig. 2.24 shows the setup used by Kuzmenko for these experiments. The setup consists of a tilting platform; this platform is tilted during the welding, the molten metal, slag and unmelted flux flows out of the weld zone to the containers. The liquid components were ejected during welding when the front edge of the electrode reaches the outer edge of the first container (leftmost container in Fig. 2.24). The length of the weld pool is also recorded for all the experiments. The slag is carefully separated from the metal and unmelted flux and weighed.

2.4.1.5 Investigation using spectroscopy

Gött et al. [57] penetrated the flux bed of SAW with a thin-gauge steel tunnel. A spatially resolved high-speed spectrometer was focused on the opening of the cavity. The chosen spectrometer had a high resolution so that it can indicate the elements present in the arc. The observations from the spectrometer were synchronized with images obtained

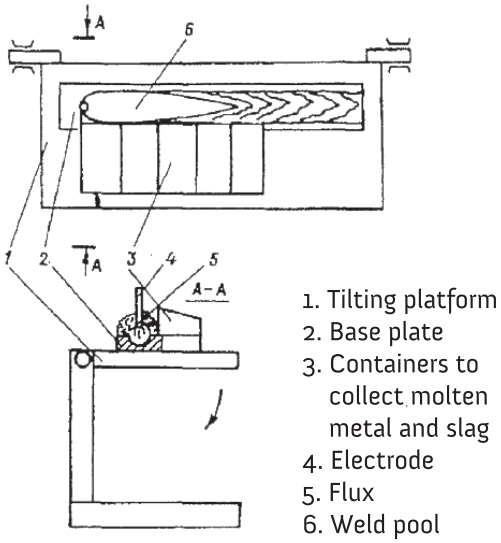

Figure 2.24: An experimental setup to investigate the presence of slag shell in SAW. Reprinted from Ref. [39, 40]. The welding was done on a tilting platform which was tilted during welding to collect molten slag and metal from different places of the weld into containers.

from a high-speed camera. Ref. [57] reported that with the setup used it was possible to distinguish the different areas of the arc cavity and location of the different elements.

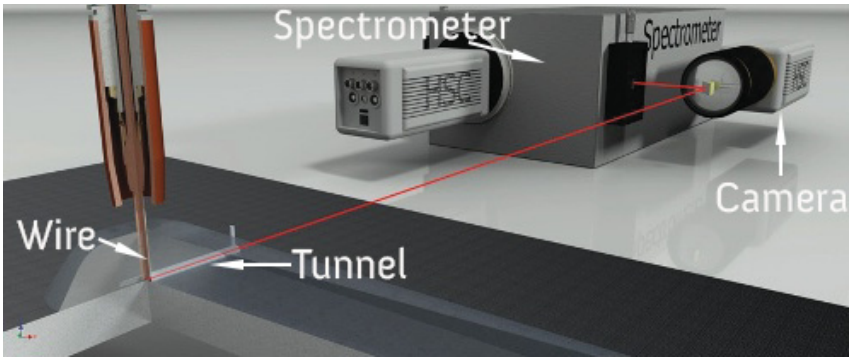

Figure 2.25: Spectroscopic study of SAW the arc cavity. Reprinted Fig. 1 from Gött et al. [57]. The spectroscopy images were synchronized with high-speed images.

2.4.2 Summary of findings on arc cavity and slag shell in SAW

Submerged arc welding (SAW) takes place by formation of an arc cavity/cavity. The arc cavity can be surrounded by a slag shell or not. Summary of findings on arc cavity and slag shell in SAW:

2.4.2.1 Typical nature of the arc cavity in SAW

The arc in SAW burns in a cavity surrounded by a slag shell. The presence or absence of slag shell in SAW will be discussed shortly. Eichhorn [25] concludes the process of cavity formation and collapse in SAW. Eichhorn reported the cavity in SAW is dynamic in nature. As the arc current increases the arc cavity length increases from thermal expansion of the gases generated from the fluxes. After reaching a maximum size, depending on the surface tension of the fluid slag the cavity collapses and arc current decreases and slag current increases. Following this event, there is again evaporation and ionization of the flux particles and the cycle repeats. The cycle is periodic in nature with the periodicity of few tenths of a second. When there is no arc, the magnitude of the slag current is much smaller to the arc current (around 20% of arc current).

Eichhorn et al. [72] showed that in SAW of Aluminium (Al) with a nondehydrated flux, a degassing cavity is present in addition to the arc cavity. Fig. 2.26 shows the arc cavity and degassing cavity that exists in SAW Al. Eichhorn reported that in welding Al, the cavity exhibits less pulsation in the vertical direction. The degassing takes place through the degassing cavity; it is separated from the welding cavity by the slag. When using an anhydrous flux, a small closed arc cavity is observed which pulsates violently at 50 Hz. Eichhorn further reported that the moisture content of the flux increases the pressure in the arc cavity; thus enlarging its volume.

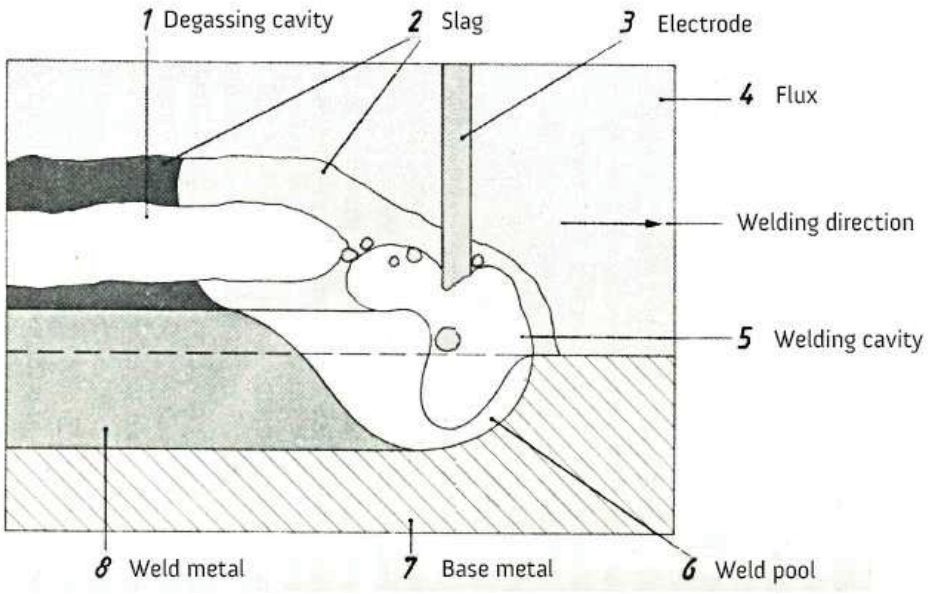

Figure 2.26: Arc cavity and a degassing cavity in SAW of Aluminum as observed by Eichhorn et al. [72].

2.4.2.2 Pressure and atmosphere in the arc cavity of SAW

The arc in SAW burns in a cavity. The pressure and atmosphere of the cavity depend on its constituents. As there is no direct way of estimating the gases present and the pressure generated by them in the arc cavity, researchers have developed unique experiments to understand the pressure and atmosphere in the arc cavity. These experiments were discussed in section 2.4.1.3. The present section summarizes the findings related the pressure and atmosphere in the arc cavity of SAW.

Arc cavity pressure in SAW

Schaefer et al. [42] and Reisgen et al. [30,32] studied pressure in arc cavity in pulsed-SAW. Schaefer et al. [42] and Reisgen et al. [30,32] reported an increase in cavity pressure under pulsed phase compared to the ground phase of SAW in pulsed-SAW. The pressure obtained was between 0-0.075 bar (0-7500 Pa). The data for pressure in cavity reported by Kuzmenko [39,40] is much lower than the one observed by Schaefer et al. [42] in pulse

phase of pulsed-SAW. Kuzmenko reported a pressure of 500 Pa in the arc cavity.

Arc cavity atmosphere in SAW

The arc cavity atmosphere is determined by the electrode, base plate, and flux compositions. The gases involved are high-temperature gases and can be complex in nature. Terashima et al. [73] reported in situ collection of gases from the arc cavity using a gas sampler; the experimental procedure is discussed in section 2.4.1.3. Researchers have theoretically, and from weld metal composition inferred the presence of different gases in SAW cavity. For the present section, a unanimous conclusion is absent among researchers.

Fluxes with halides

Often halides mainly in the form of fluorides are added to SAW fluxes to reduce the oxygen content in the weld metal. CaF_2 is the most common fluoride which is added to the flux for welding steels. In SAW of Titanium, the whole flux is halide based as a mixture of fluorides and chlorides [74]. The research was carried out to understand the formation of different gases in the SAW cavity.

Podgaetskii [75] and Podgaetskii and Novikova [76] propose possible reactions in the arc atmosphere of SAW. The proposals are based on thermodynamic calculations. Podgaetskii proposes the following reactions for fluxes containing CaF_2:

$$2CaF_2 + 3SiO_2 = 2CaSiO_3 + SiF_4 \uparrow \tag{2.5}$$

The SiF_4 evolved can react with nascent H or H_2O to give HF; CaF_2 can also react with the same and produce HF. Table 2.7 shows the possible reactions and the corresponding reaction constant at different temperatures calculated thermodynamically by Podgaetskii. Podgaetskii concludes that hydrogen is removed from the SAW plasma by reactions involving SiF_4 and not CaF_2.

Paton E.O. [71] proposed the reaction 2.6 in the arc atmosphere of fluxes consisting

of fluorides. Paton E.O. further proposed that at low silica levels in the flux, due to the tetrahedron structure of the SiO_4^{4-}, the oxygen atom protects the central silicon atom from the incoming fluorine ion. However, at high silica contents in the flux, the silica structure is complex, and the fluorine ions can attack the silicon atom and form SiF_4. Paton E.O. reported that at the arc temperatures, molecules could break down to individual atoms, e.g., reaction 2.7; almost all the gaseous molecules can break down into individual gaseous atoms. At such high temperatures, HF was proposed to be the most stable compound and reactions in Table 2.7 are possible.

Further, it was proposed that in the arc cavity, in addition to the atoms of the elements, which are present in the composition of the flux, even charged particles (ions) can be present. They may be the compound of hydrogen atoms with the fluorine; these ions include potassium, sodium, and calcium.

$$Si^{4+} + 4F^{-} = SiF_4 \tag{2.6}$$

$$SiF(g) = Si(g) + F(g) \tag{2.7}$$

Table 2.7: Thermodynamic calculations summary for possible reactions in SAW arc. Reprinted Table 4 from Podgaetskii [75]

Reaction	**The value of equilibrium constant (k) with temperature (K)**		
	2000	**3000**	**4000**
SiF_4+3H=SiF+3HF	2.36	182	1600
SiF_4+2H_2O=SiO_2+4HF	16.2	$1.38.10^5$	$1.48.10^7$
CaF_2+2H=CaF+2HF	$4.5.10^{-10}$	$1.1.10^{-6}$	$6.8.10^{-5}$
CaF_2+H_2O=CaO+2HF	$7.3.10^{-7}$	$5.6.10^{-3}$	0.49

Kuzmenko [39, 40, 77] similar to Podgaetskii, proposes the formation of SiF_4 gas with fluxes containing CaF_2 by reaction of CaF_2 with SiO_2. Chai and Eagar [78] contradicts

the conclusions of Podgaetskii and Kuzmenko of the formation of a significant amount of SiF_4 in fluxes containing CaF_2. There was no decrease in weld metal Si by formation of SiF_4 gas under CaF_2 + SiO_2 flux or pure CaF_2 flux suggesting the formation of SiF_4 is minimal. Eagar [79] proposes that the reaction of CaF_2 with H_2O is responsible for a loss of fluorine than by the formation of SiF_4 again contradicting the works of Podgaetskii and Kuzmenko.

Hunter et al. [74] carried out SAW of Titanium (Ti). Special fluxes were developed to carry out the welding. The fluxes used were a mixture of fluorides and chlorides with optical quality to minimize the moisture in these fluxes. CaF_2 was used as the fluoride. The chlorides used were NaCl and KCl. Hunter proposed that welding under CaF_2 flux there will be only fluorine atoms in the plasma which will combine with the electrons from the cathode thus constricting the plasma; this resulted into narrow weld beads. With the addition of the chlorides, the plasma will become wider. Hunter further proposed that the use of chlorides produced strong fumes around the electrode.

Fluxes with oxides

Oxides form a major part of the raw materials that goes into welding fluxes, especially used for steels. All the reactions when using an oxide flux are considered here. Podgaetskii [75] and Paton E.O. [71] reported that at high temperatures, the oxygen or oxides, and hydrogen in the flux can react and form hydroxyl groups. Terashima [73] reported the presence of significant values of carbon monoxide (CO) compared to carbon dioxide (CO_2) and oxygen (O_2) in the arc cavity for different fluxes. The P_{CO_2}/P_{CO} in the atmosphere is decreased with increasing slag basicity. Paton E.O. [71] also reported the presence of significant amount (83%) of CO in the arc atmosphere in SAW, H_2 was also reported in the arc atmosphere up to 9%, N_2 was minimal.

Kuzmenko [39] reported the formation of CO_2 from the breakdown of $CaCO_3$; this conclusion is in contradiction with Terashima [73]. Eagar [80] reported that at welding

temperatures the oxides like SiO_2 (l) decomposes into suboxides and are responsible for weld metal oxygen in SAW. SiO vapors must be present in the welding arc of SAW under fluxes high in silica. The decomposition reaction proposed by Eagar [80] is given by reaction 2.8. Eagar [80] further proposed that the flux should contain volatile substances in order to maintain the arc during SAW. Paton E.O. [71] agrees with Eagar [79] on the breakdown of oxides, and proposed reaction 2.9 in the arc atmosphere.

$$SiO_2(l) = SiO(g) + 1/2O_2(g) \tag{2.8}$$

$$MnO(g) = Mn(g) + O(g) \tag{2.9}$$

Zhdanov et al. [81] reported that the oxides present in the flux sublimate under the action of the arc and carries out thermodynamic calculations for the breakdown of oxides in SAW fluxes. Zhdanov reported all oxides breakdown to give molecular or atomic oxygen. The breakdown of the oxides with the temperature of total dissociation are determined and reported as FeO (6000 K), TiO2 (4600 K), CaO (4500 K), MgO (4500 K), SiO2 (3700 K), MnO (3500 K) and Al2O3 (3500 K).

Gött et al. [57] did the spectroscopic study of the SAW cavity and reported the presence of iron (Fe), calcium (Ca), self-reversed sodium (Na) lines and manganese (Mn) in the arc cavity for the flux Lincolnweld 8500 with Lincolnweld L50M wire. The spectra indicated a Fe dominated arc. Fig. 2.27 shows the spectra obtained during welding with AC 600 A, 30 V by Ref. [57]. It clearly shows the atmosphere of the cavity is dominated by Fe vapors, Ca, Mn, and self-reversed Na lines.

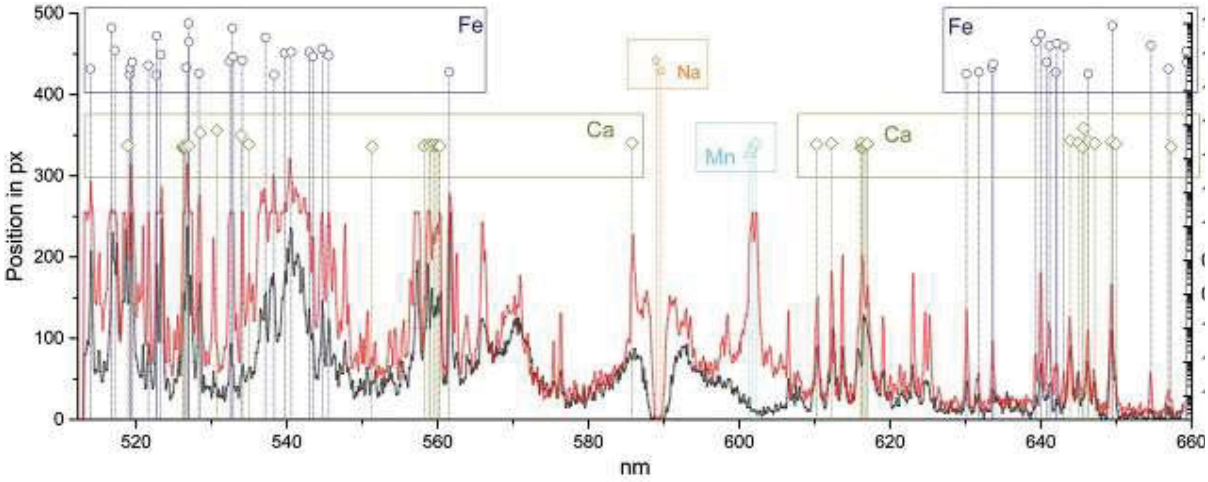

Figure 2.27: Spectra of the arc cavity for Lincolnweld 8500 flux and Lincolnweld L50M wire welded in AC at 600 A, 30 V. Reprinted Fig. 9 from Gött et al. [57]. The spectra indicate the cavity atmosphere is dominated by Fe vapors, Ca, Mn, and self-reversed Na lines. Red lines represent electrode positive cycle, and black lines represent electrode negative cycle of AC.

2.4.2.3 Slag shell surrounding the arc cavity in SAW

Researchers have reported the presence of a slag shell surrounding the arc cavity in SAW. The slag shell is believed to protect the arc zone in SAW from atmospheric contamination. Using X-ray photography of the arc zone in SAW, Refs. [3, 4, 34] reported the presence of a slag shell; the slag shell is characterized by a dark region surrounding the bright arc region. Fig 2.6a shows such a slag shell surrounding the arc. Eichhorn [25] also reported the presence of a slag shell surrounding the arc cavity and is shown in Fig. 2.28. Fig. 2.29 showed the presence of a molten slag shell surrounding the arc cavity. Ref. [32] reported the thickness of the slag shell fluctuating between 0.5 mm to 2 mm.

Kuzmenko [39–41] carried out experimental investigations to prove the absence of a slag shell in SAW. Kuzmenko reported that the impact of the arc and disturbances in the slag prevent the formation of a slag shell. Kuzmenko reported that the arc was visible throughout the welding process and the window glass used never got melted; this shows the surrounding flux never gets melted in SAW.

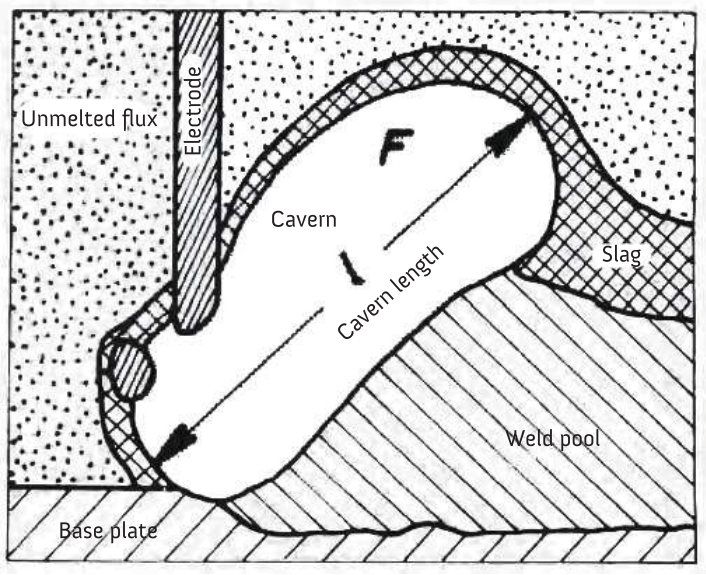

Figure 2.28: Definition of arc cavity and cavity length in SAW. Reprinted from Eichhorn [25].

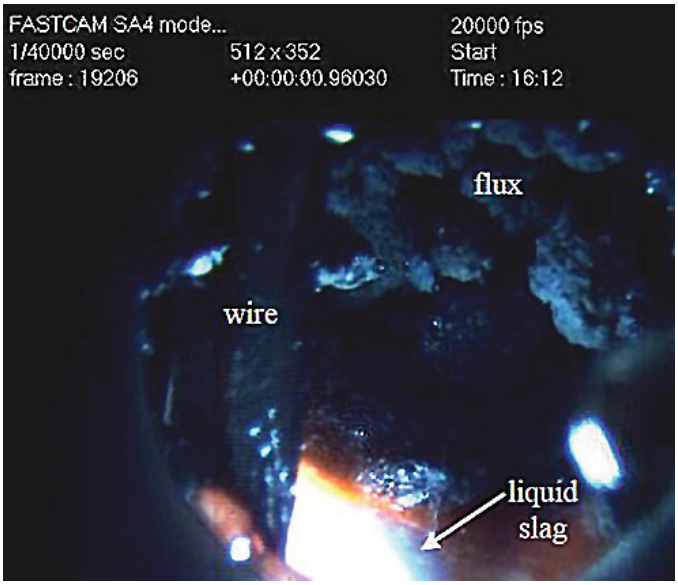

Figure 2.29: The arc cavity and surrounding slag shell in SAW. Reprinted from Ref. [32].

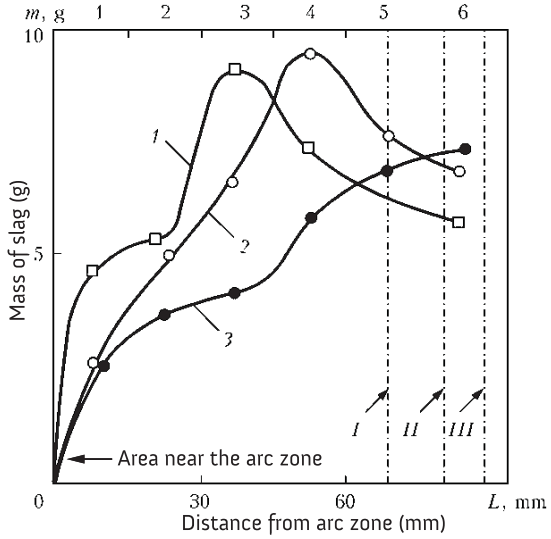

Figure 2.30: Distribution of slag in SAW using a rapid ejection technique explained in 2.4.1.4. Reprinted from Ref. [41]. The mass of slag obtained near the arc zone is very small compared to the mass of slag obtained away from the arc zone.

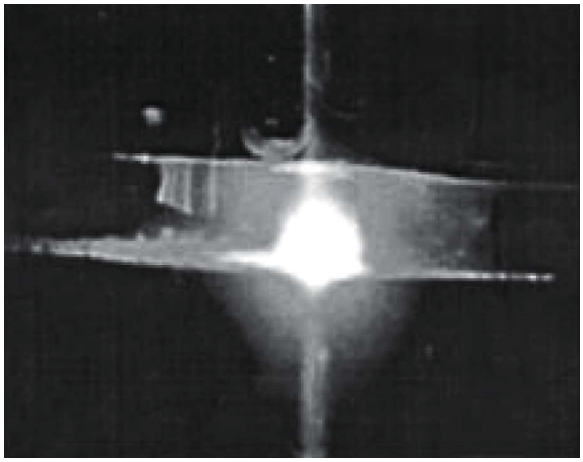

Figure 2.31: Experimental investigation of slag shell in SAW. Reprinted from Ref. [41]. The glass placed longitudinally to the weld area never got melted during the welding process showing that the flux near the arc region never gets melted during SAW.

Table 2.8: Summary of research done in arc cavity and slag shell in SAW

Focus of research	**Conclusions**
Typical nature of the arc cavity	a) SAW takes place by forming an arc cavity. b) The arc cavity in SAW is dynamic in nature. c) With the increase in current, the arc cavity expands with the thermal expansion of the gases present in the cavity. d) The cavity reaches a maximum size and then collapses.
Pressure in the arc cavity	a) Ref. [42] reported that an increase in cavity pressure under pulsed phase compared to ground phase in pulsed-SAW b) A pressure between 0-7500 Pa was reported by Ref. [42]. Ref. [39] reported a pressure of 500 Pa in the arc cavity.
Atmosphere in the arc cavity	a) The composition of the flux influences the arc cavity atmosphere. b) No unanimous conclusion is made on the composition of the atmosphere in the arc cavity of SAW. c) Refs. [71, 75–77] proposed the formation of SiF_4 gas in fluoride based fluxes. However, Ref. [78] reported SiF_4 gas does not get formed in calcium fluoride based fluxes. d) For oxide based fluxes, the presence of gases like CO (g), SiO (g), Mn (g) and O (g) are proposed in the arc cavity. It is reported that under welding temperatures, most of the oxides breakdown by forming suboxides [79]. e) Gött et al. [57] reported the presence of Fe vapors, Ca, Mn, and self-reversed Na lines in the arc cavity of SAW for Lincolnweld 8500 flux, and Lincolnweld L50M wire.
Slag shell surrounding the arc cavity	Many researchers except Ref. [39] have suggested the presence of a slag shell surrounding the arc cavity in SAW.

2.5 Dynamics of weld pool in SAW

The weld pool flows to determine the bead width and reinforcement and penetration in SAW. The dynamics of a weld pool in SAW takes place under a flux bed and is not visible directly. To overcome this challenge researchers have utilized unique techniques to study the dynamics of the weld pool in SAW. The present section explores the research in weld pool flows in SAW involving different researchers and techniques. Table 2.9 shows the researchers and details of the research in weld pool of SAW.

2.5.1 Focus of research in dynamics of weld pool in SAW

The research in the dynamics of weld pool of SAW mainly focused on answering the following questions:

- What is the flow mode and velocity of the molten metal in the weld pool in SAW?
- What is the degree of mixing of the molten metal in SAW?

The methodologies used to answer the questions related to the dynamics of weld pool are:

- Investigation using tracer techniques
- Investigation using computational simulations
- Investigation using X-rays

2.5.1.1 Investigation using tracer techniques

In tracer techniques, a small test piece (tracer) with some characteristic property like radioactivity is used. The tracer forms the part of the weld. The tracer movement is

Table 2.9: Details of research into weld pool in SAW

Researcher	Methodology	Details
Mori and Horii [44]	Tracer technique	Radioactive tracers (^{198}Au, ^{140}La) were used
Engel [24] and Eichhorn and Engel [25, 82]	Tracer technique	Metallographical contrast tracers (Zr, FeS) were used
Kuzmenko et al. [83]	Tracer technique	Using FeS tracers
Cho et al. [47]	Computational simulations	Energy balance equations related to heat transfer and fluid dynamics are solved using Flow-3D software
Nishi et al. [45]	X-rays	X-ray setup rated at 150 kV, 12 mA
Nomura et al. [84]	X-rays	X-ray setup rated at 300 kV, 10 mA

analyzed, and information about the weld pool flows is determined accordingly. In the tracer techniques the following procedures have been utilized by researchers:

- Using radioactive tracers (^{198}Au, ^{140}La) techniques by Mori and Horii [44].
- Using metallographical contrast tracers (Zr, FeS) techniques by Engel [24], Eichhorn and Engel [25, 82].
- Using FeS tracer by Kuzmenko et al. [83].

Mori and Horii [44] used ^{198}Au, as a tracer as it forms a solid solution with iron and has very low affinity for oxygen; thus, it will not get into the slag. ^{140}La was used to study the deoxidation process, as it has low solubility in steel and a strong affinity for slag and will get absorbed into the slag. The ^{198}Au was added to the molten metal pool by inserting it into the welding wire, or the groove, or it was brazed on a tungsten (W) rod with an Ag solder and directly inserted in the weld pool. After welding, the radioactivity was measured along the bead using a collimate; autoradiographs were taken on the vertical and horizontal cross section of the bead.

Eichhorn and Engel [25, 82] used similar procedures as Mori and Horii [44] with using metallographic contrast materials as Zr and FeS. The materials were embedded into the base plate surface. For some experiments, a copper wire was also used as a tracer and incorporated into the welding wire by resistance butt welding. The welding wire

was pulled out instantaneously from the welding slag to avoid fusion of electrode in the molten slag after switching off the current.

Kuzmenko et al. [83] cut a groove of 1 mm wide in the base plate (a low carbon steel sheet 16 mm thick). FeS was used as the tracer, and it was placed in the groove. Six welds were done in identical plates, and conditions. The welding was stopped at different intervals after the wire crossed the tracer. Fig. 2.32 shows the setup used by Kuzmenko.

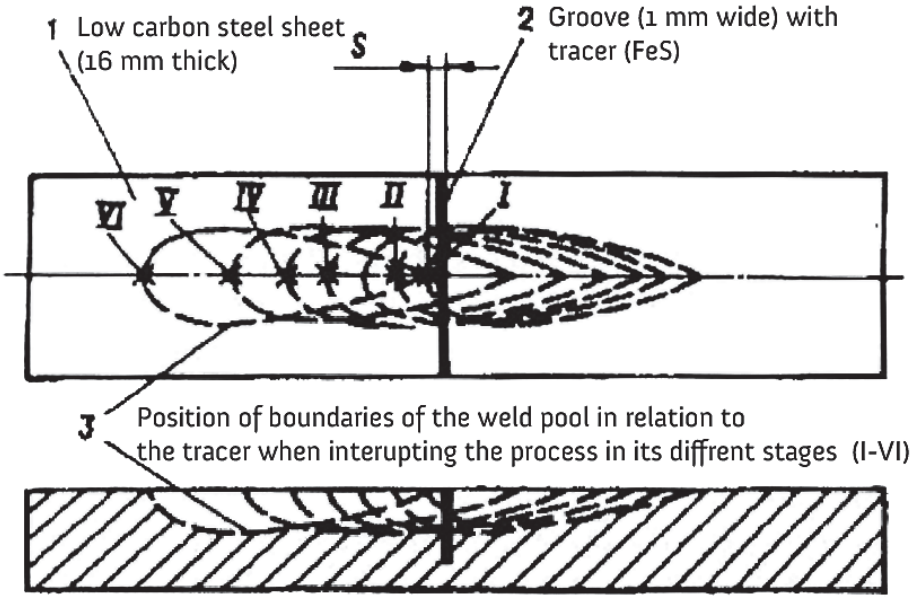

Figure 2.32: Experimental setup for determining molten metal flows in the weld pool of SAW. Reprinted Fig. 1 from Kuzmenko et al. [83].

2.5.1.2 Investigation using computational simulation techniques

In computational simulation techniques, the simulations of the weld pool can be carried on solving the equations involving mass transfer, heat transfer, and fluid dynamics. Cho et al. [47] simulated the weld pool in SAW by solving the energy balance equation, the momentum conservation equation, and the mass balance equation. Flow-3D was used to solve these equations. Ref. [47] reported the effect on the torch angle on the weld pool dynamics in SAW. The torch angles used were -20 degrees (pull) and +20 degrees (push).

Sudnik et al. [50] developed a physical-mathematical model of the SAW, taking into account the formation of the arc cavity. For their model, they considered the equation of heat of conduction and deformation of the weld pool surface. The system of equations was solved numerically, and the results were compared with experimental data. The electric arc was taken as the main heat source other heat sources included shunting current flowing through the molten flux.

2.5.1.3 Investigation using X-rays

X-rays are directed to the weld pool and arc cavity of SAW. Thin plates are often chosen so the X-rays directed at the pool gets transmitted and can be captured in a film. The pool appears as a bright area on a darker background of the plate. The main objective of these studies was to understand the phenomenon of undercutting in SAW.

A typical X-ray setup schematic to capture weld pool in SAW is shown in Fig. 2.33. The setup is used by Nishi et al. [45]. The X-rays are focused on the test piece and then the transmitted rays are passed through an image intensifier, and then to a tv camera, and finally displayed on a tv screen. Similar setups were used by Refs. [46, 84, 85]. Some of the work involve multi-electrode SAW. Eichhorn and Engel [24] also investigated the weld pool dynamics in SAW. However an aluminum base plate was used with a steel wire so the X-rays can completely penetrate the base plate, and the weld pool movements can be easily recorded.

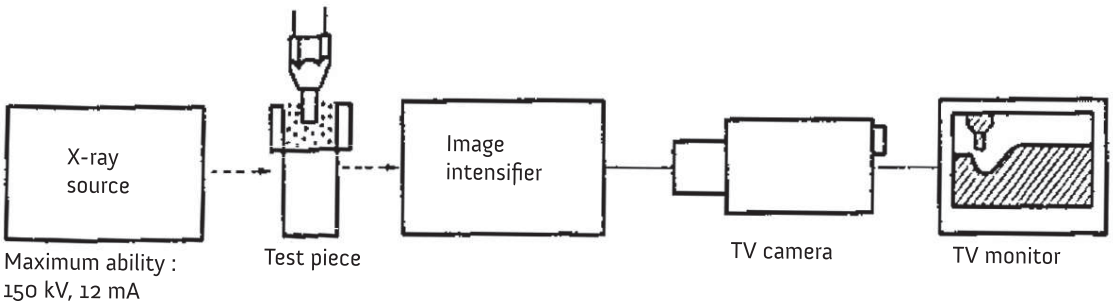

Figure 2.33: An experimental setup to observe dynamics of weld pool using X-rays. Reprinted Fig. 1 from Nishi et al. [45].

2.5.2 Summary of findings on the dynamics of weld pool in SAW

2.5.2.1 Flow mode and velocity of molten metal in weld pool of SAW

Mori and Horii [44] used radioactive tracers (^{198}Au) to study the flow patterns in SAW weld pool. Fig. 2.34 shows the radioactivities measured along the bead by the addition of ^{198}Au by Mori and Horii [44]. The origin on the X-axis represents the location of addition of the ^{198}Au. On adding ^{198}Au to the bottom of the secondary pool, a sharp peak was observed behind the origin. On adding the ^{198}Au on the surface of a secondary pool or the wire rounded curves were observed. The peak positions were different for both cases, in the front of the origin when added to the surface of the secondary pool and behind for the wire. The radioactivities decreased at a constant slope towards the welding direction for all the methods. The characteristic length defined as the length where the intensity becomes $1/e$ was found to be same irrespective of the method chosen; indicating that the added ^{198}Au went into the region of stirring and mixing of the weld pool.

Fig. 2.36a shows autoradiographs of the welds moments after adding ^{198}Au; this picture confirms the flow mode in high heat input SAW. Fig. 2.35a shows the bottom

flow in SAW; the molten metal can be seen to flow towards the tail of the pool with the brightest spot at the bottom corresponds to the peak in Fig. 2.34. The bottom flow was thought to be caused by the arc force and impact force from the transferred droplets. Fig. 2.35b confirms the surface flow in SAW. It can be seen that all the ^{198}Au added to the weld pool is not condensed to the tail end of the pool and the bright area was observed near the wire, showing that the surface flows are towards the welding direction.

The velocity of the bottom flow was found to be about 10 times than that of the welding travel speed. Fig. 2.36a summarizes the flow patterns observed in high heat input SAW as estimated by Ref. [44]. Fig. 2.36a shows two parts of the bottom flow, one flowing upward forming the primary molten pool with violent whirl flow, and another flowing to the tail and later forming the surface flows.

Mori and Horii [44] further suggested that during high-speed SAW (travel speed 100 - 200 cm/min), both the surface and the bottom flows are directed towards the end of the pool. Fig. 2.38 shows the flow pattern in the high-speed SAW. It was reported that the metal flows did not reach the pool end. The bottom flows turned upwards, and the surface flows turned downwards to combine into one center flow.

Engel [24] and Eichhorn and Engel [25, 82] studied the molten metal flows in weld pool of SAW using metallographic contrast materials (Zr, FeS). The contrast materials were embedded in the base plate, and their initial position was marked.

It was found that the contrast materials moved 50 mm away from their initial position in a direction opposite to the welding direction. The problem with this approach was that the exact time of admission of the contrast material was not known, as the position of the arc cannot be specified in advance. In order to overcome this challenge, the contrast material was incorporated in the wire. Ref. [82] suggested that as the arc covers the whole wire the exact time of the input of the contrast material can be known.

The conclusion made by Eichhorn on the flow of the molten metal in the weld pool of

SAW is presented in Fig. 2.36b. The flow of molten metal is similar to the one observed by Mori and Horii [44]. However, the velocity of the flow recorded was around 10 times than measured by Ref. [44]. Eichhorn further reported the possibility of reverse movements of the basic flow are possible as suggested by Mori and Horii, but these are limited by the cavity pressure. The reverse flows could also be limited due to solidification of the molten pool.

Kuzmenko et al. [83] reported that the flow in the front part of the weld pool is more turbulent under the force from the high plasma flows than its tail part. Fig. 2.36c shows the flow pattern as observed by Kuzmenko. Kuzmenko used the displacement of the FeS tracer as an indicator of the movement of the molten metal. Fig. 2.37 shows the distribution of FeS under the action of the arc. The first sulphur imprint shows the movement of the molten metal formed over a very small period, within less than 1s. From second to sixth sulphur imprints, shows results of experiments stopped at increasing distance from the position of the tracer. The flows show that the tail part of the weld pool moved a lot less. Kuzmenko concludes that the movement under the arc is turbulent and farther away from the arc is laminar. Towards the tail of the weld pool, the molten metal is stationary. Kuzmenko's conclusion about the tail part of the weld pool differs from as observed by Mori and Horii [44] and Eichhorn and Engel [25, 82] where a reversal of flows was observed.

Cho et al. [47] studied the flow patterns of the molten metal in the weld pool using computational fluid dynamics (CFD) simulations. The momentum transfer from the detached droplets to the weld pool was also considered. The droplet impingement angles to the weld pool are assumed to be same as the torch angles. For the torch angle of -20 degrees (pull), the direction of droplet impingement is similar to the molten pool flow direction. Thus, the molten pool flows in downward and backward as suggested by previous researchers. This type of flow leads to a deeper penetration. For the torch

angle of +20 degrees (push) the direction of droplet impingement does not match with the molten pool flow direction. Thus, less momentum is transferred to the pool. This type of flow leads to shallower penetration.

Sudnik et al. [50] reported that in SAW, the main source of heat is the electric arc and this is much greater than the heat generation by the shunting current flowing through the liquid flux layer. The high efficiency of the process is ensured by the formation of a deep crater and by immersing the arc in the crater so that the metal absorbs a large part of arc radiation. Their model predicted very large dimensions of the weld pool compared to the experimental result.

The work done with X-rays in SAW mainly focused on understanding the phenomenon of undercutting. Nishi et al. [45] and Ohara et al. [46] reported that two factors are responsible for undercutting. First one is a displacement of molten metal, and the other is a solidification point along a toe of the weld pool. When the displacement in the molten metal is more than the solidification point undercutting takes place. Nomura et al. [84] discussed the digging action of the arc in SAW. They reported that under the condition of undercut or humping bead, a solid surface instead of a molten layer was observed under the electrode.

2.5.2.2 Mixing in the weld pool of SAW

Mori and Horii [44] studied the mixing in the weld pool of SAW. The degree of mixing of the molten metal was studied by comparing the experimental results obtained by the radioactive tracers with the theoretical model of ideal mixing. The amount of Au added was very small compared to the solubility limit of Au in molten iron; this resulted in the partition coefficient in the direction of solidification to be 1. It was assumed that the ^{198}Au traces the behavior of molten iron. The two key parameters defined in their work are the mixing ratio (R) and the effective mean stay time (t_{eff}) in molten pool. The

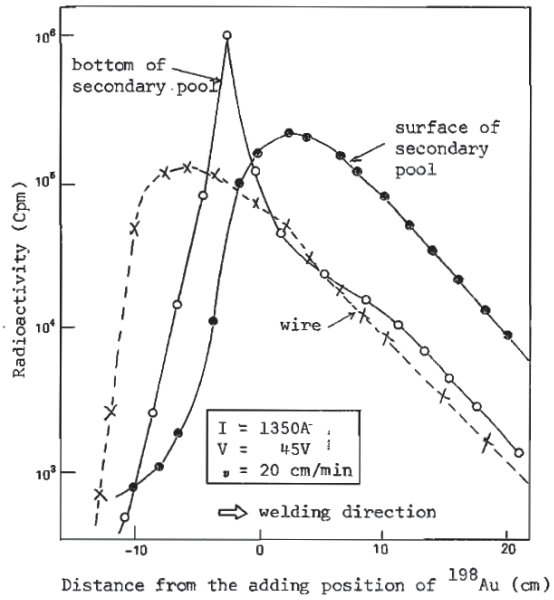

Figure 2.34: Radioactivities measured along the weld bead for different methods by ^{198}Au additions. Reprinted Fig. 2 from Mori and Horii [44].

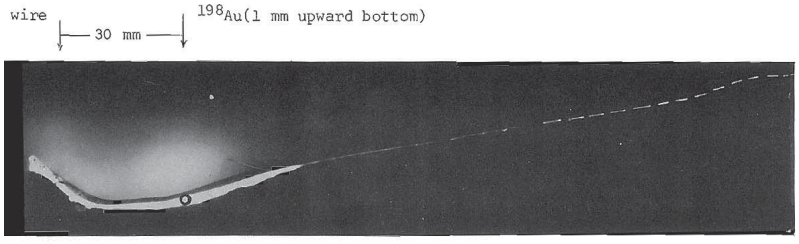

(a) Autoradiograph of the weld pool after 1.5 s of the addition of ^{198}Au showing bottom flow in SAW.

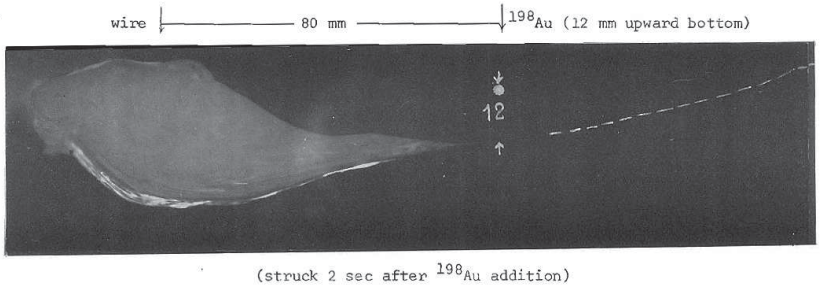

(b) Autoradiograph of the weld pool after 2 s of addition of ^{198}Au showing surface flow in SAW.

Figure 2.35: Confirmation of flow modes in high heat input SAW. Reprinted Photo 3 from Mori and Horii [44].

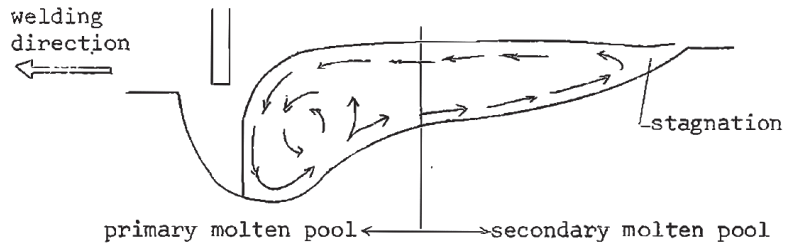

(a) Radioactive (^{198}Au) tracer techniques. Reprinted Fig. 3 from Mori and Horii [44]. Current = 1350 A, voltage = 45 V and travel speed = 20 cm/min.

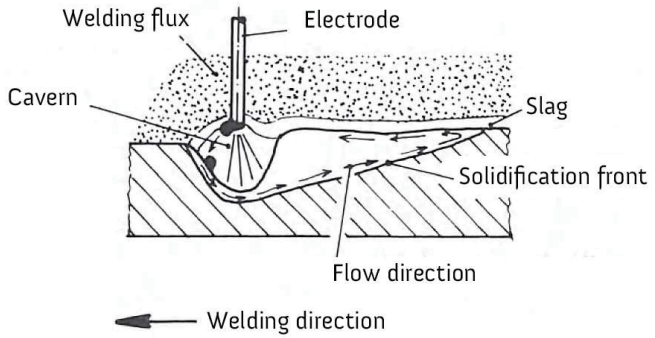

(b) Metallographical contrast tracers (Zr, FeS) techniques. Reprinted Fig. 23 (flipped) from Eichhorn and Engel [25]. Current = 740 A, voltage = 32 V and travel speed = 30 cm/min.

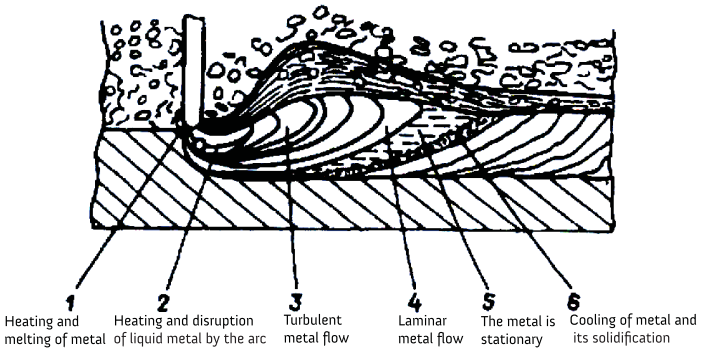

(c) FeS tracer techniques. Reprinted Fig. 4 from Kuzmenko et al. [83].

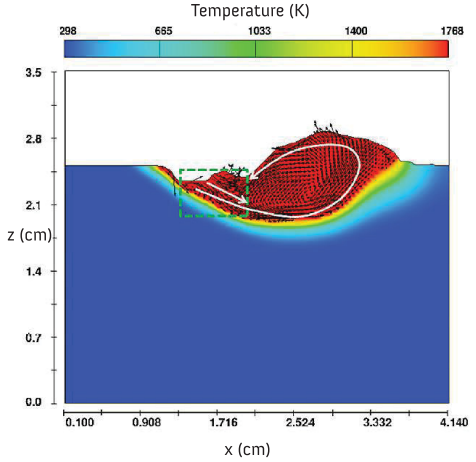

(d) Computational Fluid Dynamics Simulations techniques. Reprinted Fig. 12(b) (flipped) from Cho et al. [47]. The torch angle is -20 degrees (pull), current is 1000 A, voltage is 32 V, welding speed is 140 cm/min.

Figure 2.36: Flow mode of molten metal in weld pool of SAW using different techniques.

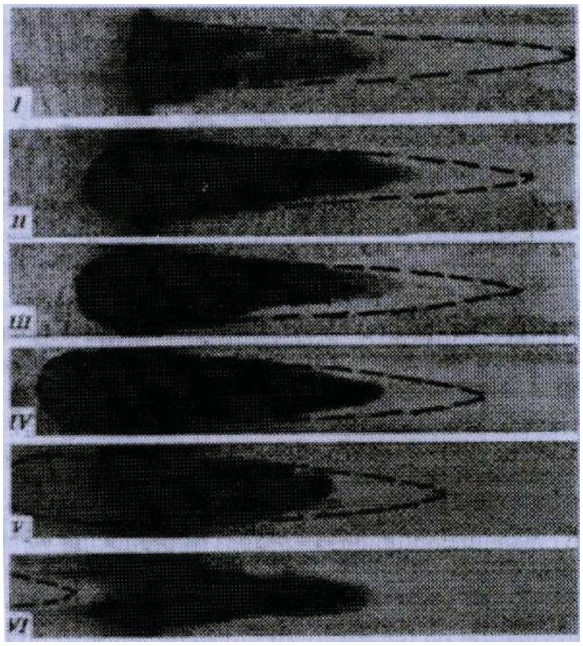

Figure 2.37: Distribution of tracing substance (FeS) in the weld pool of SAW. Reprinted Fig. 3 from Kuzmenko et al. [83].

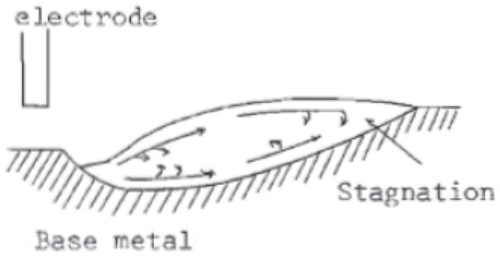

Figure 2.38: Flow pattern in the high-speed SAW. Reprinted Fig. 9 from Mori and Horii [44].

effective mean stay time in the molten pool is defined as the ratio of the characteristic distance of decrease of ^{198}Au to the welding speed. The mixing ratio is defined as the ratio between the characteristic distance of decrease of ^{198}Au to the characteristic distance of decrease in the complete (ideal) mixing molten pool.

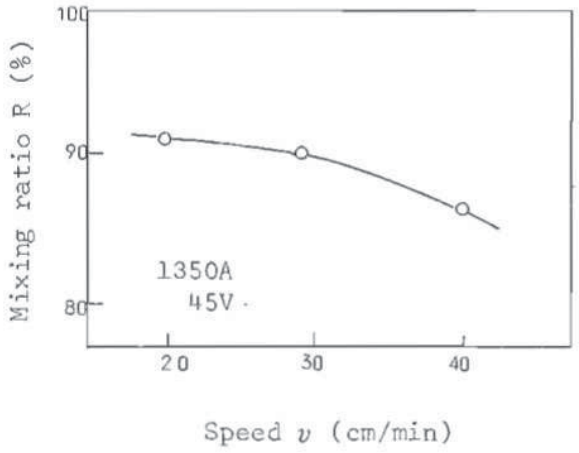

Figure 2.39: Effect of welding speed on mixing ratio in SAW. Reprinted Fig. 4 from Mori and Horii [44].

In the experiments with high heat inputs, a high mixing ratio of about 80% was obtained for all the experiments. The concentration of ^{198}Au was found to be almost constant along the segregation line. Additionally, ^{198}Au distributed symmetrically to the right and the left side for all the experiments. The mixing ratio was found to decrease with the increase in welding speed; this phenomenon is due to the decrease in the mean stay time in the pool. Fig. 2.39 shows the effect of welding speed on the mixing ratio in SAW. For high-speed SAW (travel speed of 100 - 200 cm/min), the mixing ratios obtained were very low of around 50% or lower. The mixing ratio was found to decrease with the decrease in current and increase in voltage; it was concluded that the decrease in arc force and electromagnetic force resulted in this trend. The variation with the current was found to be minimal.

Table 2.10: Summary of research done in dynamics of weld pool in SAW

Focus of research	**Conclusions**
Flow mode of molten metal in the weld pool	a) For high input welding, the molten metal flows towards the tail of the pool and turns back to form a secondary surface flow towards the welding direction. b) For high-speed SAW, both the surface and the bottom flows are directed towards the end of the weld pool.
Flow velocity of the molten metal in the weld pool	a) No consistent conclusion is reported on the magnitude of the flow velocity of the molten metal. b) Ref. [44] reported the flow velocities to be ten times the welding speed. c) Ref. [82] reported the flow velocities to be hundred times the welding speed.
The degree of mixing	a) A high mixing ratio was observed for high heat input SAW compared to high-speed SAW. b) The mixing ratio was found to decrease with increase in welding speed and voltage.

2.6 Summary of physical phenomena in weld zone of SAW

An exhaustive review of existing literature on weld zone of SAW was carried out. The review focused on the research into the metal transfer, the arc length, the arc cavity and slag shell, and the dynamics of the weld pool in SAW.

Metal transfer

The metal transfer in SAW was found to be in free flight mode. A short-circuiting transfer was not observed. Current has a significant effect on the metal transfer. At low current, the metal transfer was found to be chaotic globular. At high currents, a metal transfer based on electromagnetic kink instability was reported. The voltage was found to have minimal effect on the metal transfer. It was found that on increasing voltage, the ratio of slag/free transfer increases. Also, the fluxes were found to have minimal effect on determining the metal transfer. Fluxes with high CaF_2 showed a lower detachment frequency compared to fluxes with oxides.

The reactions at the droplet attached to the wire were also studied. It was concluded that due to the high temperature of the droplet, the oxygen from the flux gets adsorbed at the droplet. The adsorbed oxygen prevents carbon and other elements from reaching the surface and react. Possibilities of electrochemical reactions at the droplet and the weld pool were also suggested.

Arc length

SAW takes place by forming an arc. The increase in current was found to decrease the arc length for the same voltage. The increase in voltage was found to increase the arc length. The composition of the fluxes was found to have an effect on the arc length. A flux providing arc stabilizers were found to increase the arc length. A definite answer on the effect of travel speed on arc length was not reported; some researchers found that

the travel speed didn't have an effect on the arc length while other reported that the arc length decreased for high travel speeds. The arc was found to be axisymmetric for slow travel speeds.

Arc cavity and slag shell

SAW takes place by forming an arc cavity which is surrounded by a slag shell. The cavity has a pressure which is higher than the atmospheric pressure. The atmosphere of the arc cavity is determined by the composition of the fluxes used. Gases like SiO, MnO, SiF_4, CO, HF, H_2, etc. has been reported. A unanimous conclusion on the atmosphere of the arc cavity is absent. Most of the researcher except one believed that there is a slag shell surrounding the arc cavity.

Dynamics of weld pool

The flow of molten metal in the weld pool of SAW has been studied. For high heat input welding, the molten metal was seen to flow towards the tail of the pool and then turn back to form a secondary surface flow towards the welding direction. For high-speed SAW, both the surface and the bottom flows were found to be directed towards the end of the pool. The bottom flows turned upwards and the surface flows turned downwards to combine into one center flow. There was no consistency on the magnitude of the velocity of the flows reported among the different researchers.

A high mixing ratio was observed for high heat input SAW compared to high-speed SAW. The mixing ratio was found to decrease with increase in welding speed and voltage.

2.7 References

[1] Bob Irving. Blockbuster Events (Welding's vital part in major American historical events). *Welding Journal*, 1999.

[2] http://paton.kiev.ua/en/about-us/history/884-gody 1934-1950.

[3] N.G. Ostapenko and B.I. Medovar. X-ray analysis of submerged arc zone (Russian). *Avtogennoe Delo*, (11):16–20, 1947.

[4] P.G. Grebelnik. X-ray study of the process of automatic submerged arc welding (Russian). *Avtomatich. Svarka*, (6):18–29, 1950.

[5] Slavyanov N.G. Electric casting of metals, a guide for equipment and practical application (Russian). Technical report, St. Petersburg, 1892.

[6] B.E. Paton. State of the art of automatic submerged arc welding as the result of development of N.G. Slavyanov's ideas (Russian). In *Sci.-Techn. Conf. of Welders, Dedicated to the 100th Anniversary of N.G. Slavyanov.*, Kiev, 1955. Mashgiz.

[7] E.O. Paton. Development of automatic submerged arc welding during 10 years (Russian). *Avtogennoe Delo*, (2):1–3, 1951.

[8] DA Dulchevskogo. Method of electric arc welding of copper, Soviet patent no. 10578, 1929.

[9] Boris S. Robinoff, Sumner E. Paine, and Wringnol E. Quillen. Method of welding, US Patent 1,782,316, 1930.

[10] Jones Lloyd Theodere, Kennedy Harry Edward, and Maynard Arthur Rotermund. Electric Welding US patent 2,043,960, 1936.

[11] Eugeniusz Turyk and Wojciech Grobosz. Beginnings of submerged arc welding. *Biuletyn Instytutu Spawalnictwa*, (3):15–24, 2014.

[12] R D Simonson. *The history of welding.* 1969.

[13] J F Lancaster. The physics of fusion welding Part 1 : The electric arc in welding. *IEE Proceedings*, 134(5):233–254, 1987.

[14] J F Lancaster. The physics of fusion welding Part 2 : Mass transfer and heat flow. *IEE P*, 134(6):297–316, 1987.

[15] Charles A Natalie, David L Olson, and Milton Blander. Physical and Chemical Behavior of Welding Fluxes. *Annual Review of Materials Science*, 16:389–413, 1986.

[16] I.K. Pokhodnya. A method of investigating the processes of melting and transfer of electrode metal during welding. *Automatic Welding*, (2):1–10, 1964.

[17] BA Pokhodnya, IK and Kostenko. Fusion of electrode metal and its interaction with the slag during submerged arc welding. *Automatic Welding*, (10):16–22, 1965.

[18] BA Pokhodnya, IK and Kostenko. Research into kinetics of electrode melting during welding. *Automatic Welding*, (4):11–14, 1965.

[19] U. Franz. Vorgänge in der Kaverne beim UP-Schweißen, Teil I (Processes in the cavern during submerged arc welding, Part I). *Schweisstechnik*, 15(4):145–150, 1965.

[20] U. Franz. *Vorgänge in der Kaverne beim UP-Schweißen, Dipl.-Ing. dissertation*. PhD thesis, Technischen Hochschule Otto von Guericke, Magdeburg, 1965.

[21] U. Franz. Vorgänge in der Kaverne beim UP-Schweißen, Teil II (Processes in the cavern during submerged arc welding, Part II). *Schweißtechnik*, 16(9):400–404, 1966.

[22] Van Th. J. Adrichem. Metal transfer in submerged-arc welding. In *International Institute of Welding Document Number 212-78-66*, Nijmegen, Holland, 1966.

[23] Eichhorn F. and U. Dilthey. High-speed X-ray photography for submerged arc welding. *Metal Construction and British Welding journal*, 3(12):453–456, 1971.

[24] Arnold Engel. *Beitrag zur Prozeßanalyse beim Unterpulverschweißen mit Drahtelektrode*. PhD thesis, RWTH, Aachen, 1972.

[25] Friedrich Eichhorn and Arnold Engel. *Dynamisches Verhalten der Unterpulver-Schweißzone*. Number 2391. VS Verlag für Sozialwissenschaften, Wiesbaden, 1974.

[26] P. C. Gupta, D. Rehfeldt, and F. Erdmann-Jesnitzer. Influence of Current Pulses During Submerged Arc Welding. *Welding Research Supplement*, (November):377–380, 1976.

[27] Kozo Akahide, Teruo Ukibe, and Junichiro Tsuboi. Correlation between Arc Phenomena and Welding Parameters in Submerged-Arc Welding. *Journal of the Japan Welding Society*, 50(5):520–524, 1981.

[28] Patricio F. Mendez, Gregor Goett, and Stuart D. Guest. High Speed Video of Metal Transfer in Submerged Arc Welding. *Welding Journal*, 94(October):326–333, 2015.

[29] U. Reisgen. Unterpulver-Impulsschweißen zur Reduzierung des Wasserstoffeintrages beim Schweißen hochfester Feinkornbaustähle. *DVS, Annual Report 2014 Innovations*, pages 40–41, 2014.

[30] Uwe Reisgen, Konrad Willms, Rahul Sharma, and Johannes Schaefer. Diagnostic process analysis of the submerged-arc by welding high-strength fine-grained structural steels. In *International Institute of Welding Document Number 212-2205-15*, Helsinki, Finland, 2015.

[31] Gregor Goett, Andreas Gericke, and Dirk Uhrlandt. Optical study of a SAW cavern. In *IIW Doc. 212-1387-15*, Helsinki, Finland, 2015.

[32] U Reisgen, J Schäfer, and K Willms. Analysis of the submerged arc in comparison between a pulsed and non-pulsed process. *Welding in the World*, 2016.

[33] V. Sengupta and P.F. Mendez. Effect of Current on Metal Transfer in Submerged Arc Welding. Part 1: Technique and DCEP polarity. *Unpublished research work*, 2016.

[34] H Tanheim. Die physikalisch-chemischen Grundlagen des Ellira-Verfahrens. *Elektroschweißung*, 2:17–24, 1942.

[35] B.E. Paton. The process of melting the electrode in the automatic submerged arc welding (Russian). 1949.

[36] Gary Martin Peshak. *A radiographic study of the plasma geometry in submerged arc process*. PhD thesis, The Ohio State University, 1965.

[37] R. Hazzard. Continuous radiography of the submerged arc welding process. *Research Bulletin of The Welding Institute (Cambridge)*, page 295, 1968.

[38] L.A. Gobarev, A.G. Mazel, and I.A. Shmeleva. Research into the submerged welding arc. *Automatic Welding*, (2):69–70, 1973.

[39] V .G. Kuzmenko. Continuity of slag shell in submerged arc welding. *Avtomatich. Svarka*, 3:14–19, 1998.

[40] V .G. Kuzmenko. Integrity of the slag envelope in submerged-arc welding. *The Paton Welding Journal*, 10(3):119–124, 1998.

[41] V .G. Kuzmenko. On the Subject of Electric Submerged-Arc Welding. *The Paton Welding Journal*, (5):8–12, 2011.

[42] Johannes Schäfer, Konrad Willms, and Uwe Reisgen. Pulsed submerged arc welding in order to reduce the hydrogen input during the welding of high-strength fine-grained structural steels. *Welding and Cutting*, 14(4):228–233, 2015.

[43] Von G. Tybus. Farbige Zeitlupenaufnahmen zur Beobachtung des Schweißbades beim UP-Schwhweißen. *Schweisstechnik*, 7(Hefte 3):68–71, 1957.

[44] Naomichi Mori and Yukihiko Horii. Molten pool phenomena in Submerged Arc Welding. In *IIW Doc. 212-188-70*, 1970.

[45] Takeshi Nishi, Haruo Fujita, Sumichika Haseba, and Masahiro Ohara. Study on High Speed Submerged Arc Welding (Report 1) (Japanese). *Journal of the Japan Welding Society*, 51(8):686–692, 1982.

[46] Masahiro Ohara, Haruo Fujita, Sumichika Haseba, and Takeshi Nishi. Study on High Speed Submerged Arc Welding (Report 2) Effect of Arc Heat Source Shape on the Occurrence of Undercutting. *Quarterly Journal of The Japan Welding Society*, 1(2):133–138, 1983.

[47] Dae-Won Cho, Woo-Hyun Song, Min-Hyun Cho, and Suck-Joo Na. Analysis of submerged arc welding process by three-dimensional computational fluid dynamics simulations. *Journal of Materials Processing Technology*, 213(12):2278–2291, dec 2013.

[48] U. Reisgen, O. Mokrov, O. Lisnyi, and R. Sharma. Investigation of a welded seam formation of submerged arc welding by CFD simulation of heat-mass transfer, electromagnetic and hydrodynamics processes supported with experimental researches. In *IIW Commission IV, XII / SG 212, Intermediate Meeting*, pages 1–30, Fronius, Wels, Austria, 2014.

[49] U Reisgen, A Schiebahn, O Mokrov, O Lisnyi, and R Sharma. The experimental analysis of the influence of submerged arc welding parameters on weld bead geometry formation. Technical report, RWTH Aachen University, ISF – Welding and Joining Institute, Aachen, Germany.

[50] V.A. Sudnik, V.A. Erofeev, A.V. Maslennikov, D.V. Slezkin, and R.V. Tsvelev. A mathematical model of the submerged-arc welding process and phenomena in the arc cavity. *Welding International*, 27(8):629–637, 2013.

[51] R.V. Tsvelev V.A. Sudnik, V.A. Erofeev, A.V. Maslennikov. Modelling Submerged Arc Welding Process. Research of Arc Voltage and Electrode Diameter Influence.

[52] Kasano Kazuki, Matsunobu Shingo, Uchihara Masato, Hirata Hiroyuki, and Ogawa Kazuhiro. Study on Arc Phenomena of Submerged Arc Welding with Observation Method in Flux (Japanese). *Preprints of the National Meeting of JWS*, 2012s:102–103, 2012.

[53] Rahul Sharma and Johannes Schäfer. Diagnosewerkzeuge Für Das Unterpulverschweissen. In *ISF, Welding and Joining Institute, RWTH Aachen University*, pages 19–22. Alpha Informationsges, Aachen, Germany, 2013.

[54] Patricio F. Mendez, Gregor Goett, and Stuart D. Guest. High Speed Video of Metal Transfer in Submerged Arc Welding. In *International Institute of Welding Document Number 212-1345-14*, Seoul, South Korea, 2014.

[55] Manabu Tanaka, Masaya Shigeta, Fumikazu Miyasaka, and Kazuki Kasano. A Simplified Numerical Model of Submerged Arc Welding. *Preprints of the National Meeting of JWS*, 2014f:192–193, 2014.

[56] S. I. Rokhlin, A. C. Guu, and D. E. Applegate. In-Process Radiography of ARC Weld. In Donald O. Thompson and Dale E. Chimenti, editors, *Review of Progress in Quantitative Nondestructive Evaluation*, volume 7B, pages 1581–1588. Springer US, Boston, MA, 1988.

[57] G. Gött, A. Gericke, K.M. Henkel, and D. Uhrlandt. Optical and Spectroscopic Study of a Submerged Arc Welding Cavern. *Welding Journal*, (December):491–499, 2016.

[58] T.H. North. The Distribution of Manganese between Slag and Metal during Submerged Arc Welding. *Welding Research Abroad*, 23(March):2–40, 1977.

[59] U. Mitra. *Kinetics of slag metal reactions during submerged arc welding of steel*. PhD thesis, MIT, 1984.

[60] T. Lau. *Oxygen contamination in submerged arc welding, PhD thesis*. PhD thesis, University of Toronto, 1983.

[61] N.N Potapov and K.V. Lyubavskii. Interaction between the metal and slag in the reaction zone during submerged arc welding. *Welding Production*, 18(July):9–11, 1971.

[62] N.N Potapov and K.V. Lyubavskii. Oxygen content of weld metal deposited by automatic submerged arc welding. *Welding Production*, 18(January):11–13, 1971.

[63] T.H. North, H.B. Bell, A. Nowicki, and I. Craig. Slag / Metal Interaction , Oxygen and Toughness in Submerged Arc Welding. *Welding Journal's Research Supplement*, 24(March):63–75, 1978.

[64] T. Lau, C. Weatherly, and A. Mc Lean. Gas/Metal/Slag Reactions in Submerged Arc Welding Using CaO-Al2O3 Based Fluxes. *Welding Journal's Research Supplement*, (February):31–38, 1986.

[65] T. Lau, G C Weatherly, and A. MC Lean. The Sources of Oxygen and Nitrogen Contamination in Submerged Arc Welding Using CaO-Al2O3 Based Fluxes. *Welding Journal's Research Supplement*, (December):343–347, 1985.

[66] U Mitra and T W Eagar. Slag-Metal Reactions during Welding : Part I . Evaluation and reassessment ofa existing theories. *Metallurgical Transactions*, 22B(February):65—-71, 1991.

[67] U Mitra and T W Eagar. Slag-Metal Reactions during Welding : Part II. Theory. *Metallurgical Transactions*, 22B(February):65—-71, 1991.

[68] J.H. Kim, R H Frost, D L Olson, and M Blander. Effect of Electrochemical Reactions on Submerged Arc Weld Metal Compositions. *Welding Journal*, (December):446–453, 1990.

[69] American Welding Society. *The welding handbook*. 1942.

[70] G.M. Tikhodeyev. Energy properties of the electric welding arc. *Izdatel'stvo Akademii Nauk USSR Moskva*, pages 1–254, 1961.

[71] E.O. Paton. *Automatische LichtbogenschweiSSung*. VEB Carl Marhold Verlag, Halle (Saale), 1958.

[72] F. Eichhorn, P. Hirsch, and Holbach P. Physical and chemical processes taking place in the arc cavity and weld pool during the submerged arc welding of aluminium materials. In *International Conference London*, pages 311–321, London, 1980.

[73] Nishiyama Noboru-Junichiro Tsuboi Terashima, Hisaei. Influence of Slag Basicity on Deoxidation in Submerged-Arc Welding. *Journal of the Japan Welding Society*, 46(3):57–63, 1977.

[74] G Hunter, G. B. Kenney, M Ring, B.A. Russell, and T.W. Eagar. Submerged arc welding of Titanium. Technical report no. 3. Technical report, 1978.

[75] V.V. Podgaetskii. Reactions in arc atmosphere in submerged arc welding. *Avtomatich. Svarka*, (1):10–12, 1953.

[76] V.V. Podgaetskii and T.P. Novikova. About emission of silicon fluoride in heating of flux during welding and drying. *Avtomatich. Svarka*, 87(6):19–22, 1960.

[77] V .G. Kuzmenko. Special features of the interaction between calcium fluoride and silicon dioxide at 800-1900 C. *Avtomatich. Svarka*, (6):33–35, 1980.

[78] C. S. Chai and T.W. Eagar. Slag Metal Reactions in Binary CaF2 -Metal Oxide Welding Fluxes. *Welding Journal*, 61(7):S229–S232, 1982.

[79] T .W. Eagar. Sources of Weld Metal Oxygen Contamination During Submerged Arc Welding. *Welding Journal research supplement*, 2(March):76–80, 1978.

[80] T W Eagar. Oxygen and Nitrogen Contamination during Arc Welding. In *Proc. of Weldments:Physical Metallurgy and Failure Phenomena*, pages 31–42, Bolton Landing, Lake George; N.Y, 1979.

[81] Leonid Zhdanov, Vladyslav Kovalenko, Nataliya Strelenko, and Yevgenia Chvertko. Peculiarities of thermal dissociation of oxides during submerged arc welding. *Soldagem & Inspeção*, 18(4):314–321, dec 2013.

[82] F. Eichhorn and A. Engel. Mass Transfer in the Welding pool. In *International Institute of Welding Document Number 212-201-70*, 1970.

[83] V .G. Kuzmenko, V.I. Galinich, and Tokarev V.S. Characteristic zones of the weld pool in submerged arc welding. *The Paton Welding Journal*, 9(5):24–27, 1997.

[84] H Nomura, Y Sugitani, and H Nakagawa. Magnetic force in multi-electrode submerged-arc welding. In *International conference proceedings of Arc Physics and Weld Pool Behavior, London*, pages 311–323, 1979.

[85] H. Kihara, K. Masubuchi, Y. Ogura, O. Takagi, and M. Hamazaki. As to Arc Phenomenon of Multiple Electrode Submerged Arc Welding (Japanese). *Journal of the Japan Welding Society*, 27(11):647–652, 1958.

2.8 Appendix 2.1: Composition of the fluxes used by different researchers

The table is presented in the next page.

Table A2.1: Composition of the fluxes used by different researchers*

Fluxes	%SiO_2	%MnO	%MgO	%CaF_2	%CaO	%Na_2O	K_2O	%Al_2O_3	TiO_2	Fe_2O_3	FeO	ZrO_2	% Metal Alloys	Other oxides
AN-3	51	17	9.5	3	17	-	-	-	-	-	-	-	-	4
OSC-45	41	46.5	-	9.5	1.5	-	-	-	-	-	1.5	-	-	-
GAZ-1	46	14.5	-	7.2	18.5	1.3	-	12.5	-	-	-	-	-	-
AN-348	42	32	7	4.5	12	-	-	1	-	1.5	-	-	-	-
A	52	-	9	4	28	-	-	4	-	-	-	-	-	-
B	38	7	11	5	22	-	-	14	-	-	-	-	-	-
C	42	40	-	5	-	-	-	5	-	-	-	-	-	-
D	35	-	-	6	15	-	-	20	5			15		
E	33	8	22	5	-	1.75	-	20	-	-	-	-	4	
F	-	-	10	-	-	-	-	35	55	-	-	-	-	-
G	41.7	-	-	-	26.9	-	-	-	31.4	-	-	-	-	-
G1	42.6	-	0.5	-	30.8	3.5	-	20.3	-	-	-	-	-	-
G4	24.5	-	16.9	-	16.3	3	-	37.4	-	-	-	-	-	-
G7	21.9	-	38.8	-	13.2	3	-	18.2	-	-	-	-	-	-

* All values are in weight percentage

Chapter 3

Effect of Current on Metal Transfer in Submerged Arc Welding. Part 1: Technique and DCEP Polarity

3.1 Introduction

In submerged arc welding (SAW), the arc is submerged under the flux and can not be observed directly; this limitation has prevented from understanding the mode of metal transfer. Experience from gas metal arc welding (GMAW) indicates current plays a significant role in determining the mode of metal transfer. The lack of understanding of the effect of current on metal transfer has limited the use of complex waveforms for the process.

Early attempts to understand the phenomena in SAW used two main approaches: X-ray videography and optical videography (which disrupted the flux cover). The advantages of using X-ray videography is that it does not affect the welding process. The main disadvantage of using this method is that it provides low contrast, low resolution, and slow frame rates. X-ray imaging also capture only a shadow of the metal, with no information of surface features such as ripples or silicate islands on the surface of the melting wire. Optical videography overcomes this drawback and provides a clear

view of the wire and droplet; so detachment events can be studied easily. However, the optical techniques disrupt the flux cover thus making the validity of the observations questionable.

In 1950, Grebelnik [1] used X-ray imaging to investigate the SAW process. The research mainly focused on the welding arc and distance travelled by the ejected molten metal. For all the experiments, a wire diameter of 5 mm was used. The experiments were conducted at current 600 A with a voltage of 24 V to 26 V and at 800 A with 38 V to 40 V. In 1964, Pokhodnya [2] used X-ray cinematography at 1500 frames per second (f/s) accompanied by an image amplifier and a high-speed cine camera to capture images of metal transfer during welding. The paper focuses mostly on the newly developed method of high-speed X-ray cinematography and its advantages on the previous methods to study metal transfer in welding. Ref. [2] reports that with the use of high-speed X-ray cinematography shorter exposure times can be achieved compared to Ref. [1]. Ref. [2] studied metal transfer for a 6 mm wire at a current of 470 A and voltage of 29 V.

In 1957, Tybus [3] published work on optical observation in SAW by using a glass sheet parallel to welding direction. The work focused on the weld pool in SAW. Videos produced had a frame rate of 750 f/s. Metal transfer was not captured properly at such low frame rates.

In 1965, Franz [4,5] used a ceramic tube with its axis parallel to the welding direction. The tube penetrated the fluxes and provided a view of the weld cavity. The composition of the ceramic tube was chosen identical to the flux used so to minimize the influence of the tube on the composition of the slag. The videos produced had a frame rate of 3000 f/s. Carbon dioxide (CO_2) and Argon (Ar) was injected into the weld cavity with the intention of preventing its collapse. Experiments were carried out for currents ranging from 210 A to 510 A for 3 mm wire, 400 A to 700 A for 4 mm and 590 A to 800 A for 5 mm. Two types of metal transfer were concluded for SAW: one through slag and

the other through free flight transfer. Franz reported observation of both big and small droplets. The interaction of electromagnetic forces with arc forces was considered to be the primary influence in droplet detachment. The present work explores similar current and wire diameter as Franz [5], but with higher voltages. The choice of a higher voltage at high currents was made to see the electrode tip above the original plate surface. In 1966, Adrichem [6] also used a similar setup as Franz [4] and conducted experiments both with DCEP and AC for 3.2 mm wire with currents ranging from 300 A to 600 A and concluded similar observations as Ref. [4, 5].

Recently, Mendez et al. [7, 8] reported optical observations of metal transfer in SAW for 500 A DCEP and AC and 1000 A DCEP by placing a tunnel made of steel thin-sheet perpendicular to the welding direction. The metal transfer in SAW was captured in videos at a rate 10000 f/s. The videos had excellent image resolution and quality compared to previous researchers. At 500 A, a non-axial globular metal transfer was observed for both DCEP and AC. At 1000 A DCEP, a tapering electrode tip with a buried arc was observed. Gött et al. [9] carried out experiments using a thin-gauge steel tunnel. The experiments were conducted in DCEP (600 A, 1000 A), DCEN (-600 A), and AC (600 A). The work primarily focused on the spectroscopic study of the atmosphere of arc cavity. Ref. [9] reported that the metal transfer was erratic with a lot of spatter. Ref. [9] further notes that the droplet transfer at DCEP 600 A, switches between short-circuiting, exploding and repelling mode of metal transfer. The work presented by Mendez et al. [8] and Gött et al. [9] are revolutionary in the field of SAW but lacks in a complete study on the effect of current on the metal transfer over a large current range.

The present work explores the effect of current on the metal transfer mode in SAW between 500 A and 1000 A with the use of high-speed videos captured at 10000 f/s for a 3.2 mm wire in DCEP.

3.2 Experimental Setup

The experimental setup is illustrated schematically in Fig. 3.1. The setup is similar to the one used by Mendez et al. [8] with a modified tunnel design and higher voltages to avoid the conditions of a buried arc. The tunnel was made of carbon steel sheet of thickness 0.10 mm. The tunnel is given a rectangular cross-section with sides of length 12 to 15 mm as compared to a tunnel made by steel sheet of thickness 0.5 mm having a semicircular cross-section with radius 6 to 10 mm in Ref. [8]. The thin-sheet of steel was chosen to easily melt the tunnel and thus avoiding sustained stray arcs as observed in experiments done in Ref. [8]. A rectangular cross-section of the tunnel was chosen to match the rectangular shape of the videos. The advantages of choosing a steel sheet over a ceramic tube have been discussed previously in Ref. [8]. The tunnel is placed perpendicular to the welding direction. The far end of the tunnel from the camera was closed to prevent gases from escaping when wire cuts through the tunnel. Before the run of experiments, the camera was focused on the wire and plate. The tunnel was placed and aligned with the camera. An external stream of CO_2 was injected from the open end of the tunnel to blow away stray flux blocking the view of the cavity when the wire is cutting through the tunnel. This gas might also help maintain the cavity pressure; preventing the cavity from collapsing. The effect of the blown gas on metal transfer is believed to be minimal based on the Ne experiments reported in Ref. [8].

The welding power supply used was Lincoln AC/DC 1000 SD (WeldSet Name Z123334) running Powerwave Manager 1.0.1.209. The wire used was Lincolnweld L-50 wire, diameter 0.125 in (3.2 mm). The flux used was Lincolnweld 980 flux with basicity index of 0.6 (EM13K and F7A2 respectively, in AWS 5.17). The contact tip to workpiece distance (CTWD) was kept constant at 1.25 in (31.8 mm) for all the experiments. All welds were “bead on plate” with no weaving. All the experiments were made with program 58

(CC DC+ Steel 0.125 in.). The data acquisition of current, voltage and wire feed speed was done at 60 kHz using the embedded electronics of the power supply and WeldView software version 3.0.0.168.

The high-speed camera used was a Phantom V210. All videos have a frame rate of 10000 f/s and a resolution of 512 by 384 pixels. An 180-mm lens with a 99-mm extension was used to obtain desired magnification. An 850-nm long wave pass filter was used to block most of the light coming from the arc.

The welding parameters are listed in Table 3.1. The visible arc length (arc length above the plate surface) were calculated from frames A3.1. The electrode stickout was calculated by subtracting the visible arc length (arc length above the plate surface) from the CTWD. The voltage was varied with the intention of keeping a constant average visible arc length of 4.57 ± 0.22 mm (0.18 ± 0.009 in) (corresponding to an average electrode stickout of 27.18 ± 0.22 mm (1.07 ± 0.009 in)). The average visible arc length and hence, the average electrode stickout is reported with 95 % confidence interval determined with a t-test described in 3.14. Travel speed was varied aiming to keep a relatively uniform nominal heat input of 50.79 ± 0.64 kJ/in (1.99 ± 0.02 kJ/mm) in average. The heat input is reported with 95% confidence interval determined with a t-test described in 3.14. The important variation between welds is in the welding current varying between 500 A and 1000 A in 100 A intervals. The average values of the current, voltage and WFS are reported with a 95 % confidence interval determined with a t-test described in 3.14. The travel speed recorded was directly recorded from the gantry display.

3.3 Analysis of High-Speed Videos in DCEP polarity

Seven high-speed videos of metal transfer in SAW are uploaded as supporting online material [10]. The uploaded videos are rendered at 25 f/s which corresponds to a factor

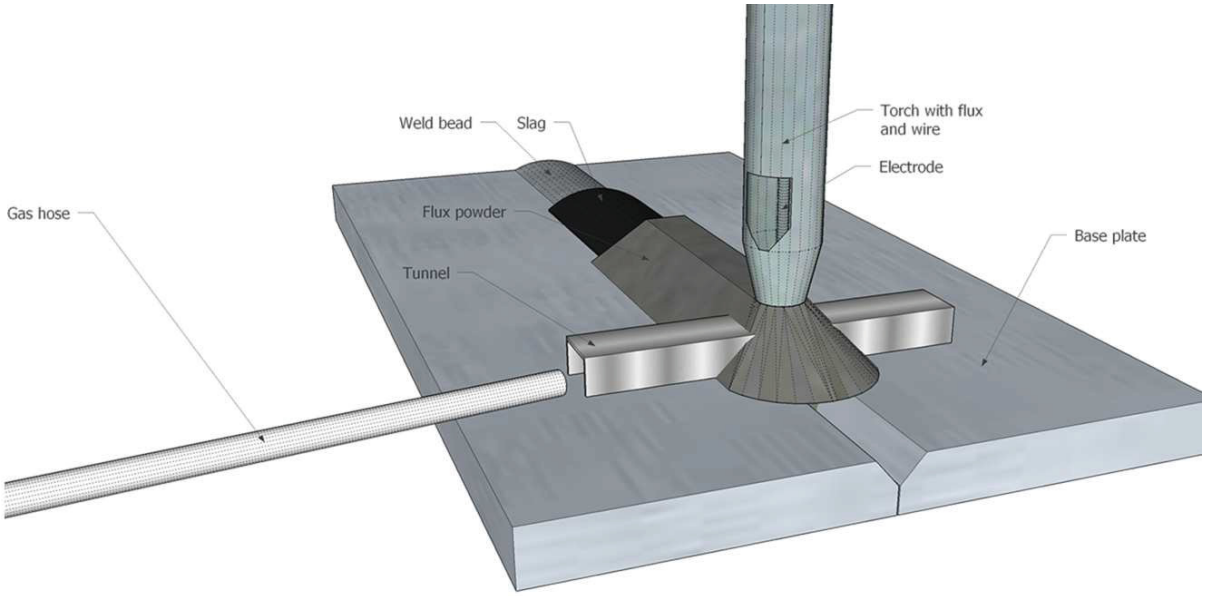

Figure 3.1: Experimental setup with modified tunnel adapted from Ref. [8]

Table 3.1: Parameters corresponding to high-speed videos of DCEP-SAW

Experiment	Video	Polarity	Average Current A	Average Voltage V	Average WFS m/min	Average WFS in./min	Travel Speed m/min	Travel Speed in./min
71	SOM1	DCEP	497.93 ± 0.206	30.03 ± 0.011	1.56 ± 0.002	61.33 ± 0.091	0.457	18
68	SOM2	DCEP	619.31 ± 0.149	32.84 ± 0.011	2.05 ± 0.005	80.74 ± 0.211	0.604	23.76
47	SOM3	DCEP	713.93 ± 0.234	35.99 ± 0.014	2.58 ± 0.004	101.57 ± 0.167	0.762	30
61	SOM4	DCEP	806.42 ± 0.197	38.17 ± 0.015	3.06 ± 0.003	120.46 ± 0.148	0.914	36
58	SOM5	DCEP	911.22 ± 0.242	40.00 ± 0.016	3.63 ± 0.003	142.98 ± 0.139	1.092	43
62	SOM6	DCEP	998.24 ± 0.311	42.07 ± 0.017	4.27 ± 0.007	168.03 ± 0.294	1.280	50.4
44	SOM7	DCEP	809.80 ± 0.827	38.10 ± 0.015	3.09 ± 0.003	121.55 ± 0.114	0.914	36

of 400 in the time dimension. Many more experiments were conducted but failed as the flux came in and blocked the camera view.

At 500 A, a chaotic globular droplet is observed at the wire tip. As the current increases, the electrode tip is seen to taper based on electromagnetic kink instability. The tapering of the electrode tip results in a "whipping tail" kind of detachment. The frames corresponding to the visual identification of droplet detachment for each experiment are listed in 3.11. The estimated detachment frequency was calculated and reported with a 95% confidence interval determined with a t-test and is described in 3.14 and represented in Figure 3.4. The average detachment frequency increases with current. The average droplet size based on detachment frequency, wire diameter, and wire feed speed is represented in Figure 3.5. The average droplet size was found to decrease with increasing current. At 500 A, the droplet diameter matches the wire diameter, and as current increases, droplets become smaller.

Video SOM1 corresponds to Experiment 71 (500 A). Fig. 3.2 summarizes frames 2610 to 3710 from the video at 100 frame intervals. From the beginning of the video, a large droplet is observed having an irregular shape. The metal transfer looks very similar to one observed by Mendez et al. [8]. The relatively small capillary forces compared to gravity forces in the large droplets are responsible for the irregular shape of the molten metal [8]. The video shows explosions at the droplet surface; similar explosions were observed in Ref. [8, 11]. The frequency of explosions is significantly higher than events such as droplet detachment. One such explosion can be seen in frame 6352. Fig. 2 captures evolution and detachment of a droplet. The detachment takes place between frames 3110 and 3210; the detached droplet flies to the left of the wire.

Video SOM2 corresponds to Experiment 68 (600 A). The video shows the molten metal at the electrode tip having an irregular shape. Explosions can be seen on a regular basis similar to Experiment 71 (500 A, DC). Careful observation shows that the electrode

tip tapers just before detachment. The weld pool under the arc is pressed down by the strong plasma jets produced at the high currents. A noticeable increase in penetration with current is seen in the cross-sections of the welds. As the steel tunnel was in electrical contact with the base plate, a stray arc occurs occasionally between the electrode and tunnel (e.g. starting at frame 1136 and lasting 8 frames, equivalent to 80 μs). The choice of a much thinner gage for the tunnel material compared to Ref. [8] (0.8 ms vs 6 ms) resulted in less frequent and much shorter stray arcs.

Video SOM3 corresponds to Experiment 47 (700 A). The detachment mechanism is based on the electromagnetic kink instability. Frames 3960 shows the development of a kink on the left side of the molten metal leading to detachment at frame 3983, with the remaining molten tail at the electrode tip moving to the right. The detached metal is oblate in shape and flies non-axially to the right of the wire. Frames 3178 to 3192 show the detached metal meeting the weld pool with high impact. Gases produced from evaporation and breakdown of the fluxes can be seen throughout the video.

Video SOM4 corresponds to Experiment 61 (800 A). The video shows more frequent detachments than under the lower currents. Frames 3421 to 3432 display a good example of the detachment mechanism. In frame 3421, a perturbation is seen to develop on the left side in the molten metal. By frame 3429, the perturbation develops into a kink finally leading to detachment of the molten metal at frame 3432. The detached metal flies to the left and down at a high speed towards the weld pool. The molten metal is deformed by the electromagnetic forces before detachment. Ref. [1] observes a similar mode of metal transfer. The weld pool is depressed under the action of strong plasma jets, and it is not visible in the video. A gouging penetration mechanism is expected at this current.

Video SOM5 corresponds to Experiment 58 (900 A). A smaller aperture was used to achieve a higher depth of field and to capture the phenomena taking place in background

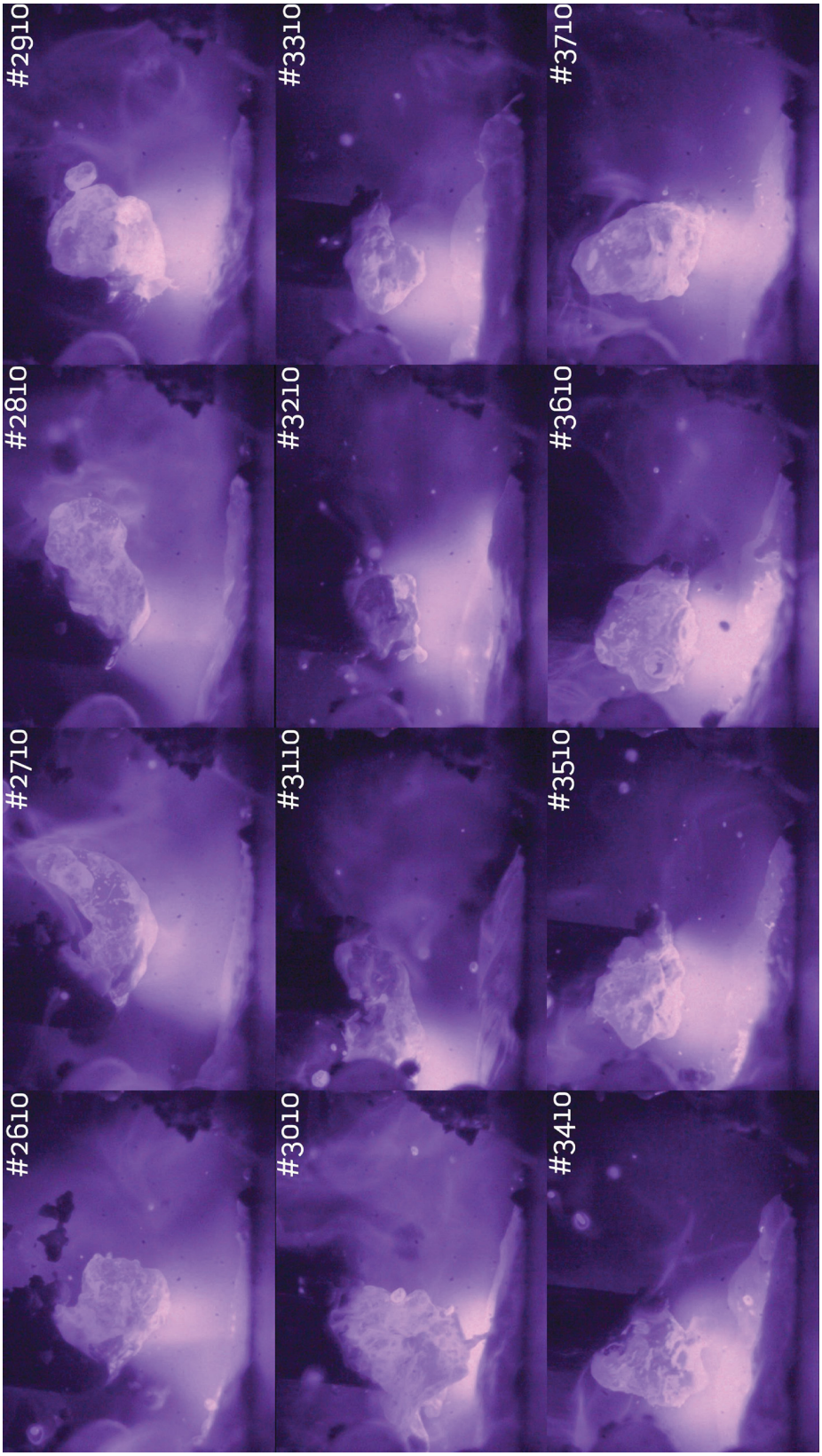

Figure 3.2: Metal transfer in SAW during Experiment 71 (500 A, 30 V). Time between frames is 1 ms (total time elapsed is 0.11 s). A droplet detachment takes place between frames 3110 and 3210. For reference scale, wire diameter is 3.2 mm (0.125 in).

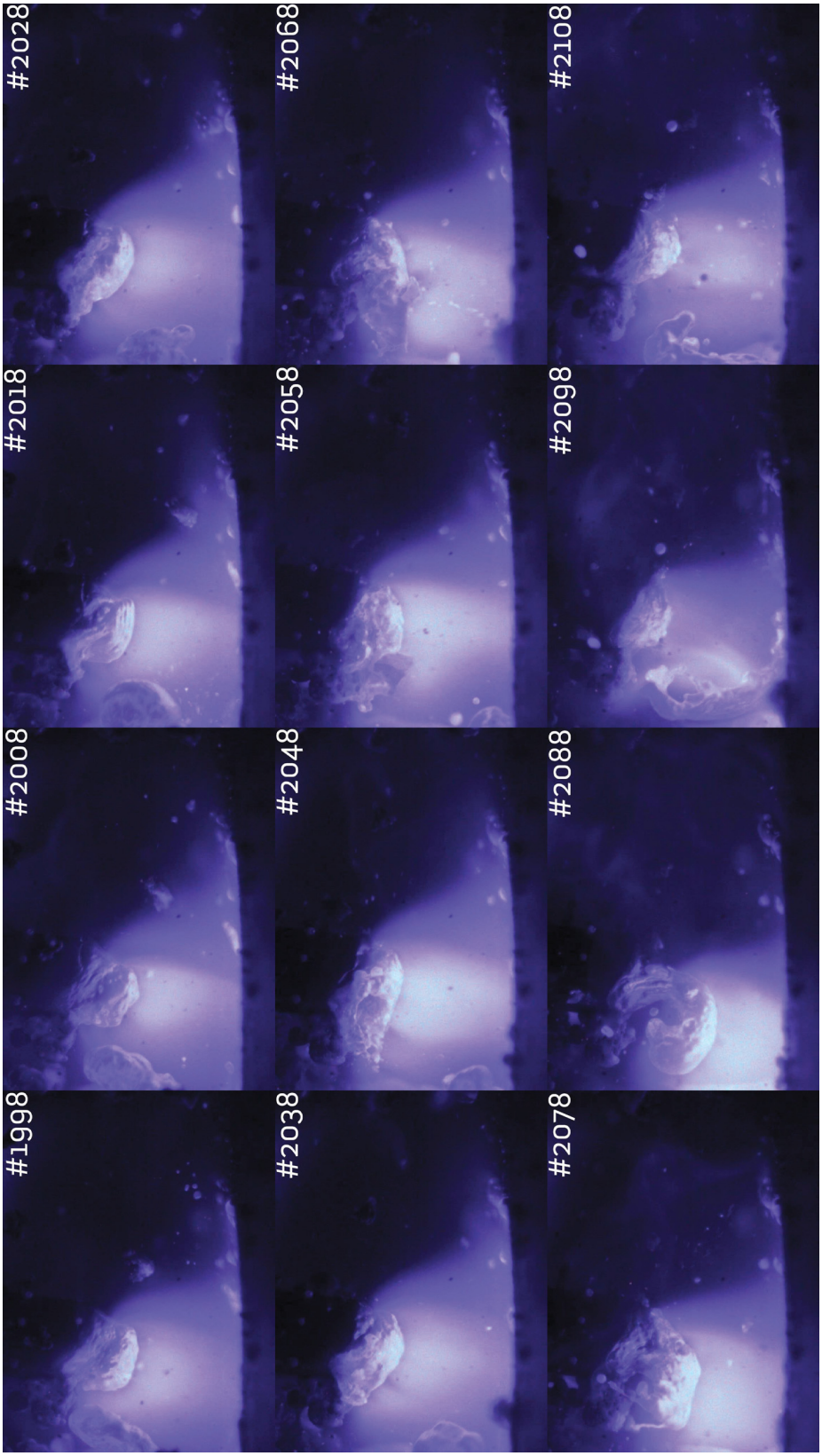

Figure 3.3: Metal transfer in SAW during Experiment 62 (1000 A, 42 V). Time between frames is 100 μs (total time elapsed is 0.011 s). A detachment event take place between frames 2088 and 2098 showing a tapering electrode tip ejecting a molten metal tail through a mechanism resembling electromagnetic kink instability. For reference scale, wire diameter is 3.2 mm (0.125 in).

addition to the metal transfer. The video shows similar features of metal transfer like Experiment 61 (800 A, DC). The metal transfer process is chaotic and frequent explosions can be observed in the melt. Frame 1530 onwards, the molten metal at the electrode tip is seen to move towards the left forming a kink leading to detachment at frame 1575. Frames 2100 and onwards show the flux granules falling from the top.

Video SOM6 corresponds to Experiment 61 (1000 A). Fig. 3.3 summarizes frames 1998 to 2108 at 10 frame intervals. From the beginning of the video onwards, the metal transfer shows the "whipping tail" phenomenon seen in previous experiments with much faster detachments. Frames 3571 shows the start of a kink formation with detachment at frame 3598. The ejected metal flies sideways and hits the flux wall at frame 3638 giving a good representative of the process taking place under the fluxes. Similarly, Fig. 3.3 shows a detachment event taking place between frames 2088 and 2098. The detached metal flies towards the left and down at high speed. The tapered electrode tip is more clearly visible than in Mendez et al. [8] due to the use of a higher voltage. Frames 2123 to 2354 and 3452 to 4222 shows direct contact of the flux with the molten electrode tip, suggesting the possibility of electrochemical reactions in SAW as reported by [12].

3.4 Analysis of Electrical Signal

The raw data acquisition of voltage, current and wire feed speed are supplied in a spreadsheet SOM8. The electrical signal for Experiment 71 is shown in Fig. 3.6. The signal looks noisy; the oscillations in the current and the voltage data are due to the changes in the WFS. The data acquisition and the gun travel are not synchronized; thus predicting the location of the tunnel from the data acquisition is challenging. Some short-circuit events are seen momentarily where the voltage drops to a very low value. A synchronized data acquisition set up is in a process to be built. The noise from the electronics

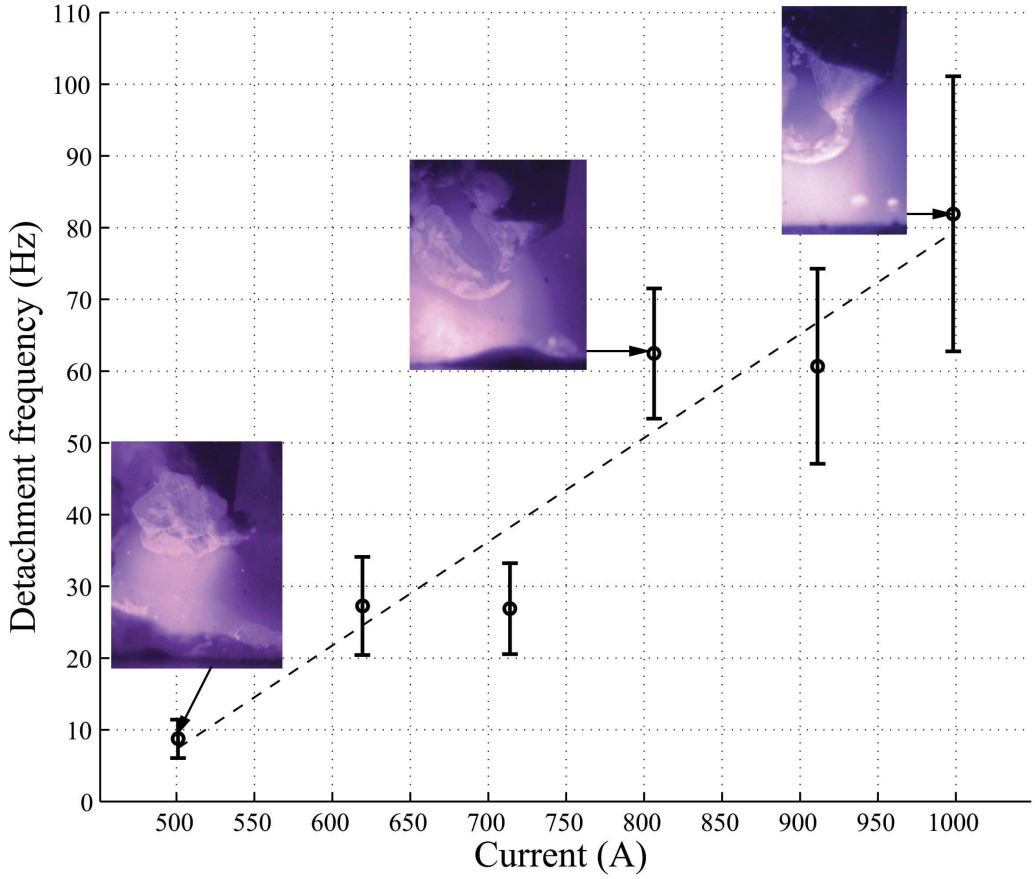

Figure 3.4: Detachment frequency for 3.20 mm (0.125 in) wire and 4.57 mm (0.18 in) visible arc length (corresponding to a electrode stickout of 27.18 mm (1.07 in)). Detachment frequency increases with current.

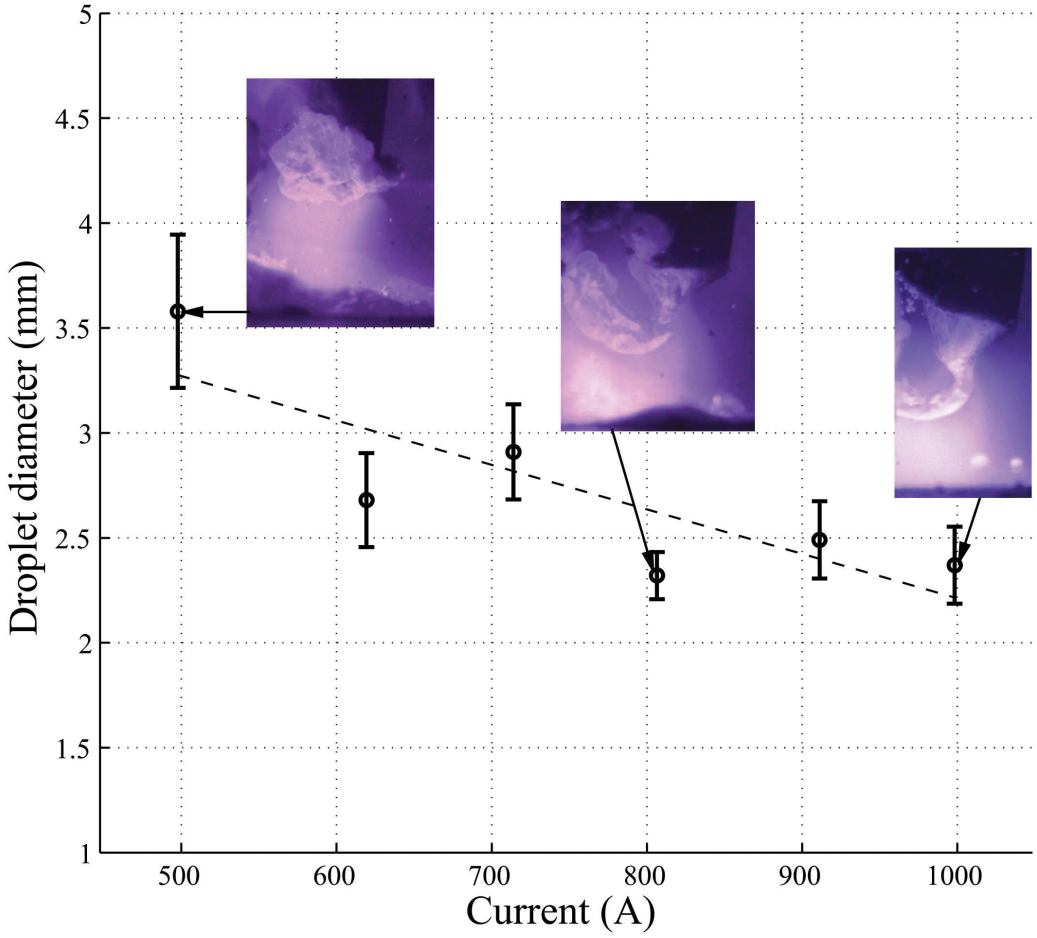

Figure 3.5: Droplet diameter for 3.20 mm (0.125 in) wire and 4.57 mm (0.18 in) visible arc length (corresponding to a electrode stickout of 27.18 mm (1.07 in)). Droplet diameter decreases with current.

is masking the features associated with the welding.

3.5 Analysis of Effect of External Gas

An external gas flow was used similar to Ref. [8] to blow away stray flux particles that blocked the camera view and to prevent the flux cavity from collapsing. Ref. [8] reported that the external gas used had a minimal effect on the metal transfer observed in the videos. The experiments show a strong ejection of gas while the wire penetrates the tunnel. The strong ejection should blow out the injected external gas, and it should not have any effect on the metal transfer. An experiment was attempted without the use of gas to check this hypothesis. Results obtained from the test is compared with an experiment conducted with same parameters but with the use of an external gas.

Experiment 44 was done in similar conditions as Experiment 61 (800 A, DC) but without using an external gas. Flux grains can be seen falling throughout the video ultimately blocking the view of the flux cavity completely by frame 5992. A tapered electrode is observed ejecting a molten tail by the mechanism of electromagnetic kink instability. The detachments are seen approximately at frames 2392, 2654, 3102, 3441, 3646, and 3811. The detachments are similar to the one observed for Experiment 61. The similar type of detachments observed in Experiment 44 and 61 suggests that the external gas used is not affecting the type of metal transfer, and the gas is needed to keep the cavity open. Also, a gas generated from the flux can be seen throughout the video, thus supporting the hypothesis that the gas seen in previous experiments are from the fluxes and not the external gas.

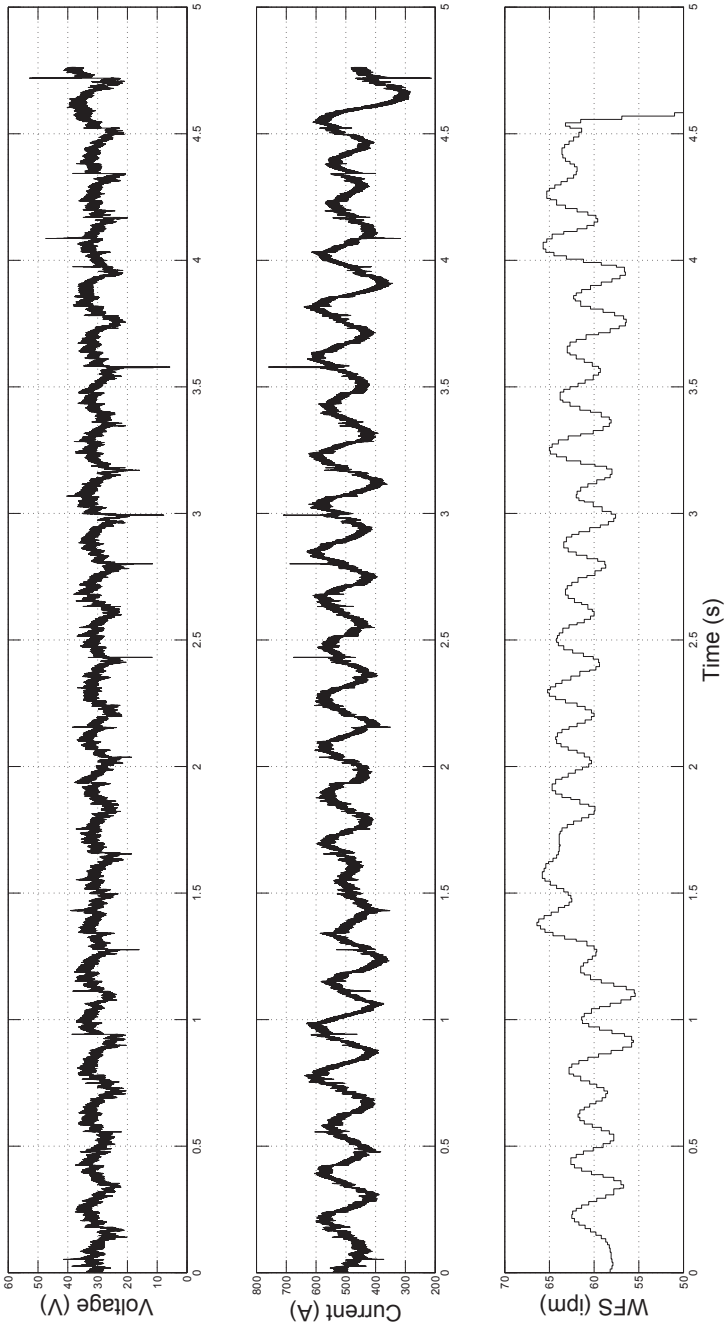

Figure 3.6: Electrical signal of Experiment 71 (500 A, 30 V, DC). No clear signal obtained representing droplet detachment.

3.6 Analysis of Weld Cross Sections

For all the welds discussed here, cross-sections were analyzed before, during and after the tunnel. Fig. 3.7 shows the cross-sections of welds, and Table A3.3 lists the measurements of the cross-sections before, during and after the tunnel for all welds. The cross sections for Experiment 71 (500 A, DC) is not carried out. The thickness of the plate was measured with a micrometer with 0.001 mm resolution and reinforcement, depth and width were measured counting pixels in images of 300 pixels per inch resolution giving an accuracy of measurements of the order of 0.1 mm (0.004 in). These measurements show that the tunnel has a small but measurable effect on the shape of the bead, with the welds being slightly wider and taller under the tunnel, but with less penetration. Figures 3.8 to 3.9 display the effect of current on penetration, and bead width.

In experiments at 700 A and above, the weld was stopped shortly after the exit of the tunnel (approximately 60 mm (2.36 in) or 5 s), while the trailing tail of the weld pool was still under the tunnel, affecting the measurements of cross sections under and after the tunnel because they did not reach steady state before they solidified. The cross sections at 700 A and above, the weld for "after tunnel" was stopped before the molten tail cleared the section. This is the reason for their relatively "flat top" profile. The undercut observed for 1000 A, "during tunnel" sample is a consequence of the experimental matrix used. Some parameters considered in these study do not apply to real-life situation, they were considered as part of complete study.

One possible explanation for the differences in cross sections inside and outside the tunnel is that the stray arcs shift the energy balance toward the electrode, increasing the amount of electrode melted (thus the larger cross-section), but reduce the amount of energy going to the plate (thus the lower penetration). As the stray arcs alternate with arcs to the plate, to maintain the same average voltage the arc to the plate is longer

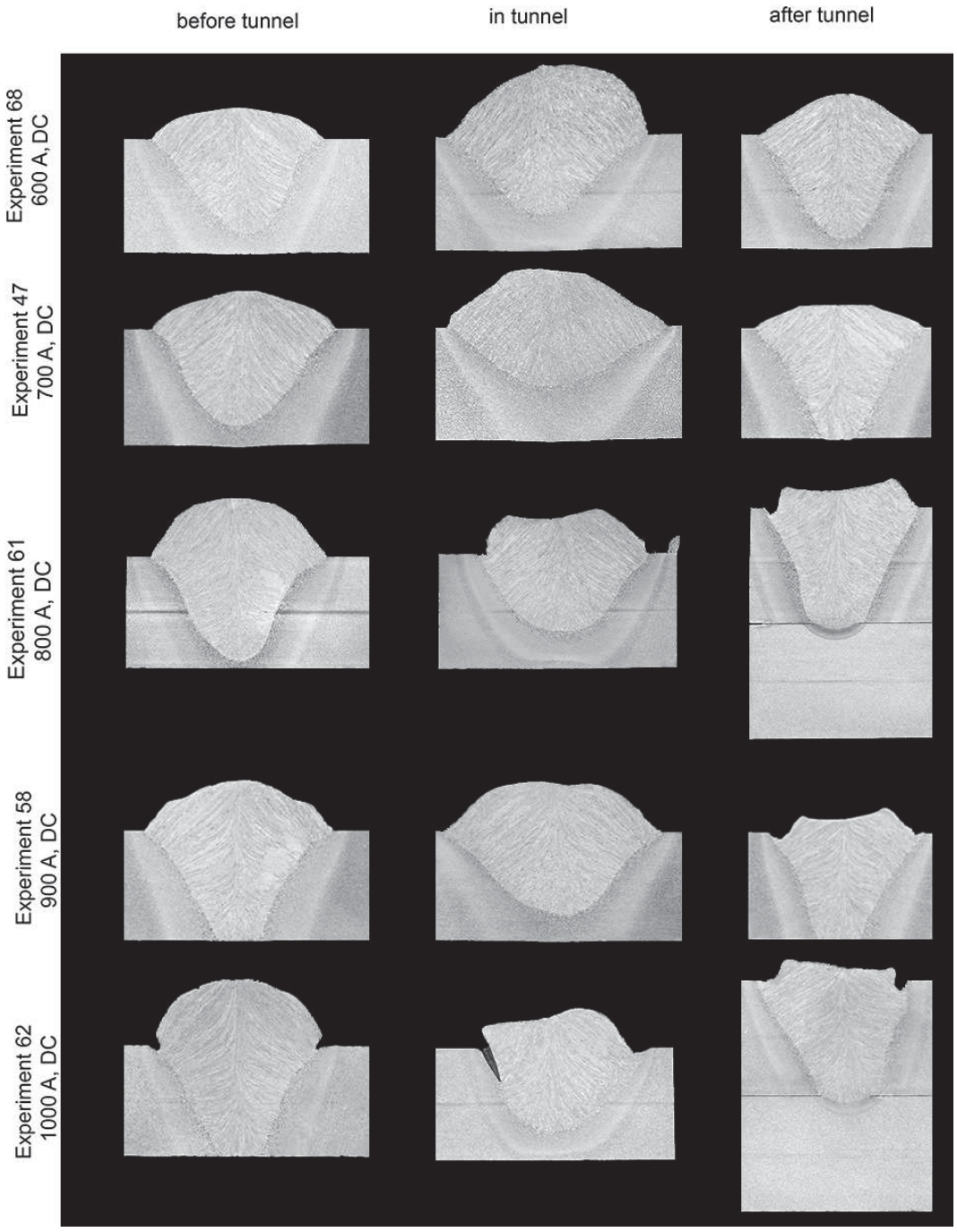

Figure 3.7: Cross-sections before, during and after the tunnel for welds done with DCEP. For reference of scale average thickness of substrate (single plate) is 9.64 mm (0.38 in). Average thickness of substrate (double plate) is 19.48 mm (0.77 in).

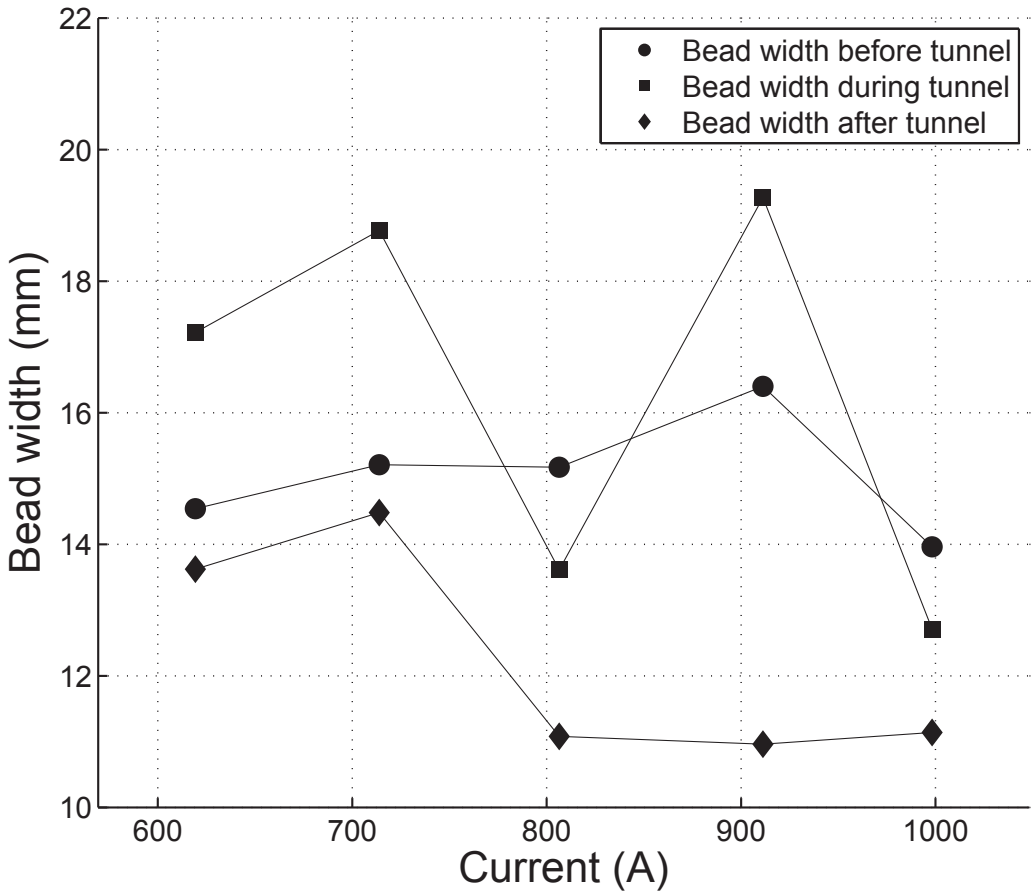

Figure 3.8: The effect of current on bead width. Bead is observed slightly wider during the tunnel except for cases when the solidifying molten tail ended inside the tunnel (at 800 A and 1000 A).

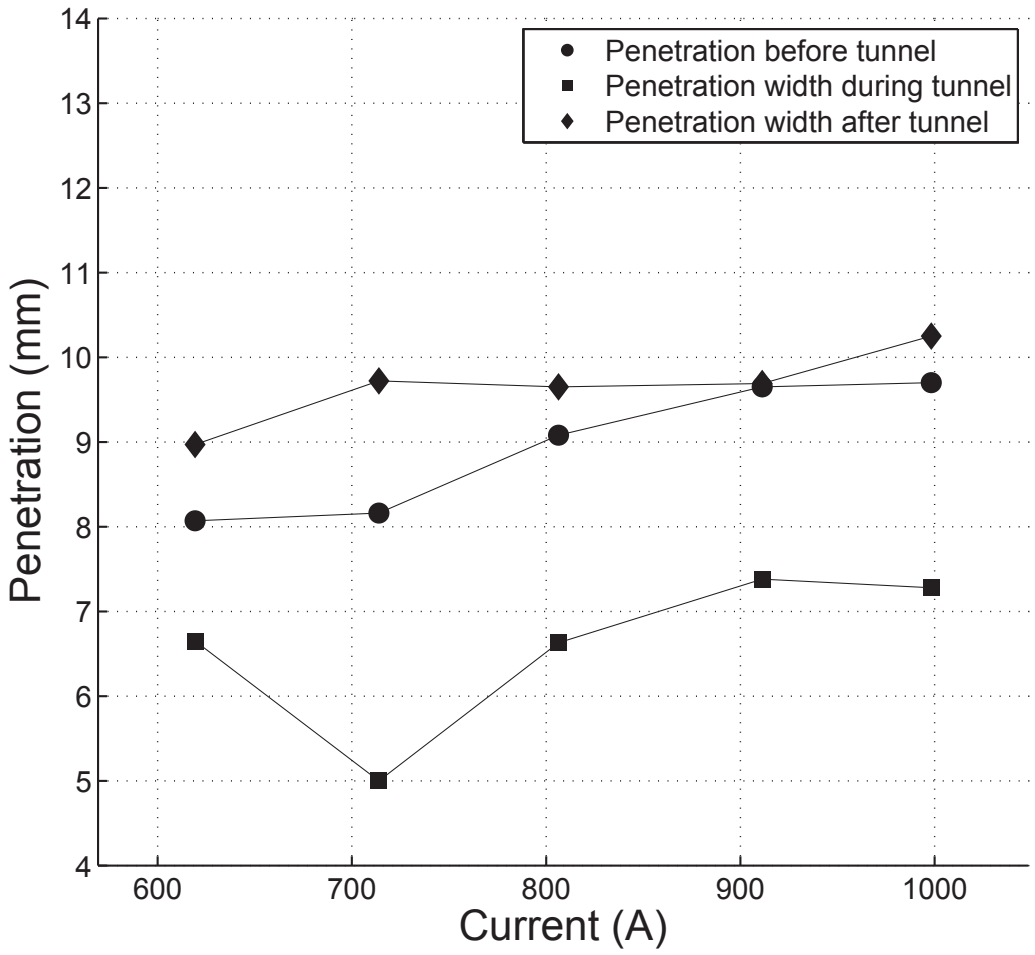

Figure 3.9: The effect of current on penetration. A gradual increase in penetration is observed, and between 700 A and 800 A molten metal meniscus is no longer seen, consistent with a change in penetration mode from recirculating flows to gouging penetration.

(thus the wider beads). Synchronized videos and data acquisition are needed to support or reject this hypothesis, and are the focus of ongoing work. An analysis of cross sections before and during the tunnel was performed excluding the cases in which the weld was stopped with the weld pool tail still under the tunnel (800 A and 1000 A). This analysis indicates that the cross section during the tunnel is on average 82% larger than before the tunnel. A similar analysis of cross sections of [8] results in increases of 109%. The fact that the difference in cross sections before and during the tunnel decreases with thinner steel for the tunnel is consistent with the explanation suggested.

For Experiment 68 (600 A), the weld bead during the tunnel is approximately 3 mm wider than that before the tunnel. The reinforcement is also higher (approximately 3.5 mm) than before the tunnel.

For Experiment 47 (700 A, DC), shows similar penetration like Experiment 68. Penetration during the tunnel is approximately 3 mm less than before the tunnel. The reinforcement during the tunnel is 2 mm higher than before the tunnel. The bead width is around 3 mm more during the tunnel compared to before the tunnel.

For Experiment 61 (800 A, DC), the penetration during the tunnel is approximately 2.5 mm less than before the tunnel. The width and reinforcement during the tunnel are approximately 2.5 mm and 1.5 mm lower than that observed before the tunnel.

For Experiment 58 (900 A, DC), the penetration is approximately 2 mm lower during the tunnel compared to before the tunnel. The reinforcement before and during the tunnel is almost identical. The bead is 3 mm wider during the tunnel compared to before the tunnel.

For Experiment 62 (1000 A, DC), the penetration during the tunnel is 2.5 mm less than before it. The reinforcement and bead width in the tunnel are 3 mm and 1 mm lower than that before the tunnel respectively.

3.7 Discussion

Direct observation of metal transfer in SAW indicates a strong influence of current in the metal transfer mode. This is consistent with similar processes like GMAW.

One of the most important finding of this paper is that the metal transfer mode observed in this work is consistent with that observed previously with non-invasive techniques and other methodologies. The present work and past work includes X-rays, optical techniques. The results obtained is in good agreement with five different researchers, shown in Fig. 3.11. Metal transfer is irregular shaped droplets; this is confirmed by the observations of [2, 4, 8, 13, 14]. Metal transfer mode does not show much effect of the wire diameter. The diameter of the droplet seems similar to the wire used.

For a 3 mm wire, the comparison is remarkably similar (Fig. 3.11b). However, Franz [4] used a fused calcium silicate flux (basicity index 1.0) compared to an aluminate flux (basicity index 0.60) used in the present study. Current experiments explore the effect of fluxes on metal transfer. The droplet observed in Fig. 3.11e is more deformed than compared to others. The possible reason for this can be the use of thinner wire (2 mm (0.08 in) diameter) for the experiments. The smaller diameter will lead to the increase of current density and hence the electromagnetic forces acting on the droplet and thus deforming its shape. Future work will explore the effect of wire diameter on the metal transfer in SAW.

A new metal transfer mechanism is reported for the first time. At higher current (600 A and above), a "whipping tail" kind of metal transfer is observed (Fig. 3.10). In this mechanism, the electrode tip tapers ejecting a molten tail through a mechanism resembling electromagnetic kink instability. Although Fig. 3.10 resembles the description of rotating transfer [15]; this mechanism is different. While in rotating transfer it rotates in this case no rotation. The kink instability formed leads to an asymmetric azimuthal

magnetic field which results in a stronger electromagnetic force on one side than the other and results to "whipping tail" kind of transfer.

Further comparison with X-rays at higher current (800 A) shows a good similarity in the metal transfer. The result obtained for 800 A is in good agreement with Grebelnik [1], shown in Fig. 3.12. The consistency in observed metal transfer in both at low current and transition to high current supports the validity of the methodology used in the present study. The identical contrast of the metal with the wire in Fig. 3.12a and Fig. 3.12b suggests the dark line as a stream of molten metal.

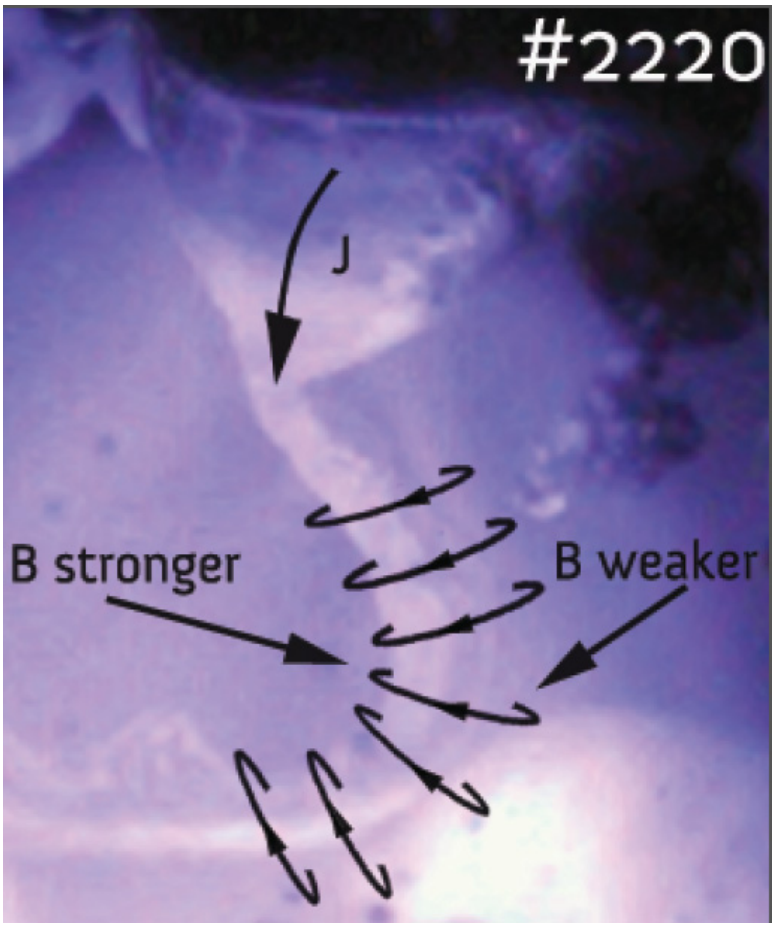

Figure 3.10: Phenomenon of kink instability observed in Experiment 61 explained by Blank [16]

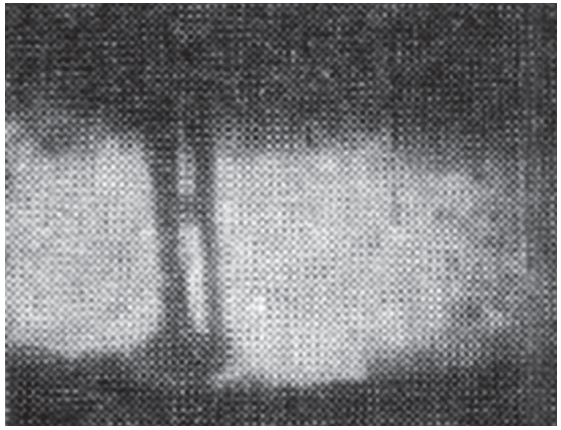

(a) 1964, Pokhodnya [2], 6 mm (0.24 in) wire 470 A, 29 V (X-ray)

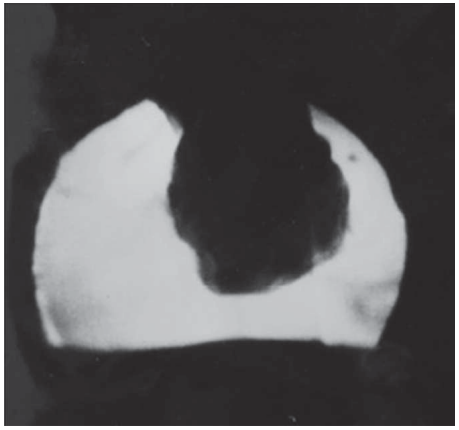

(b) 1965, Franz [4], 3 mm (0.12 in) wire 470 A, 31 V (optical)

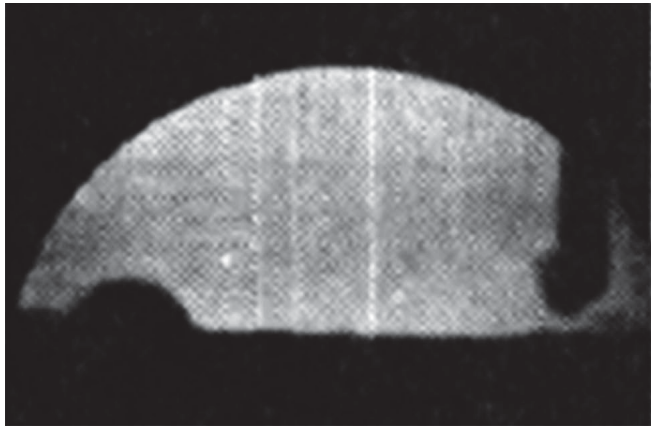

(c) 1981, Akahide et al. [13], 4.8 mm (0.19 in) wire 500 A, 40 V (X-ray)

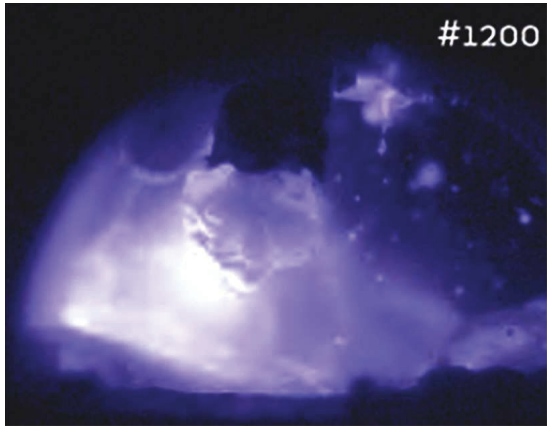

(d) 2013, Mendez et al. [7,8], 3.2 mm (0.12 in) wire 500 A, 30 V (optical)

(e) 2015, Reisgen et al. [14], 2 mm (0.08 in) wire 435 A, 28 V (optical)

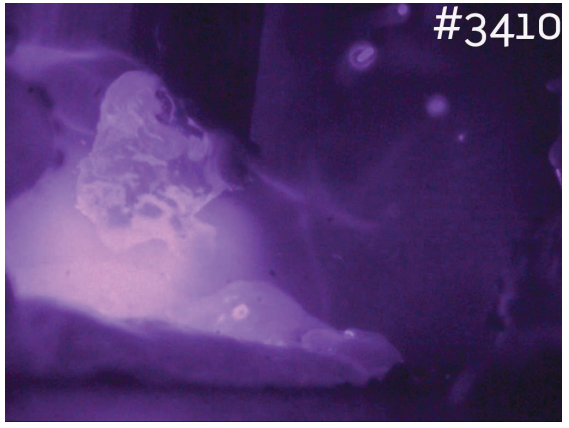

(f) 2016, Present work, 3.2 mm (0.12 in) wire 500 A, 30 V (optical)

Figure 3.11: Comparison of observations done by previous researchers at around 500 A. A large droplet with an irregular shape is typically observed. The diameter of the droplet is comparable to the wire.

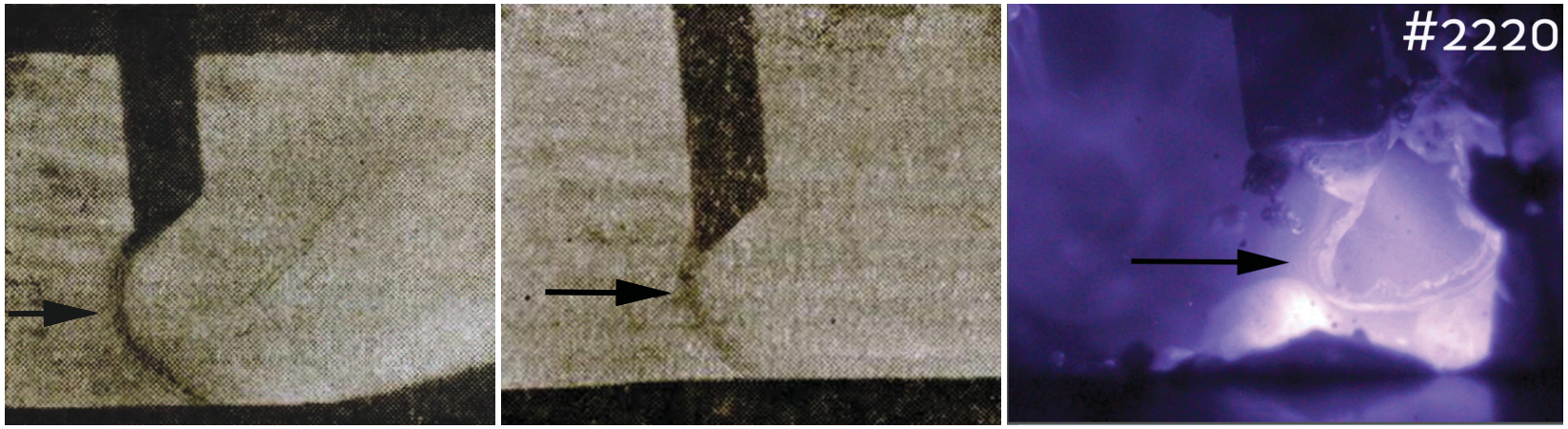

(a) 1950, Grebelnik [1], 800 A, 38 V, 41.6 cm/min (X-ray)

(b) 1950, Grebelnik [1], 800 A, 38 V, 66.6 cm/min (X-ray)

(c) 2015, Present study, 800 A, 38 V, 91.4 cm/min (flipped image) (optical)

Figure 3.12: Comparison of observations of metal transfer at 800 A with Ref. [1]. A characteristic "whipping tail" (indicated by arrows) was observed in X-ray imaging, consistent with the present study.

A noisy voltage and current signal is obtained and is consistent with the chaotic nature of the process. The current challenges in building a synchronized data acquisition is eliminating the noise at different frequencies. The use of a band pass filter to eliminate the noise is being currently explored. The detachment frequency increases between 500 A and 1000 A, this observation is consistent with processes like GMAW. The raw data acquisition of voltage, current and wire feed speed is included in Spreadsheet SOM8 for analysis by researchers interested in this field and compare the results with the detachment frequency obtained by a visual count of the droplets.

The metal transfer mode observed for an experiment done without an external gas is consistent with that of the experiment with gas under similar settings. The consistency in results suggests that the gas blown from the side has minimal effect on the metal transfer. The flux falling from the top quickly blocks the view of the cavity thus, suggesting the use of an external gas would be necessary for future experiments.

These small differences in the cross-sections under the tunnel are thought to be because of the stray arcs shift the energy balance toward the electrode, increasing the amount of electrode melted (thus the larger cross-section), but reduce the amount of energy going to the plate (thus the lower penetration). As the stray arcs alternate with arcs to the plate, to maintain the same average voltage the arc to the plate is longer (thus the wider beads). Synchronized videos and data acquisition are needed to support or reject this hypothesis, and are the focus of ongoing work.

The metal transfer observed at low currents resembles globular transfer [17, 18] but with a much more irregular droplet shape. At higher currents, the droplet size is smaller than the wire diameter, but the metal transfer mode does not resemble any of the classifications detailed in [17,18], and seems to be a new mode not observed until [8]. Recently, Gött et al. [9] reported the observation of the new mode of metal transfer at DCEP, 600 A.

For future experiments, a data acquisition system synchronized with the videos can be used to understand the effect of the tunnel on the current and voltage during the tunnel.

3.8 Conclusions

The effect of current on metal transfer in submerged arc welding has been captured in high-speed videos. Lincolnweld L-50 wire, 3.2 mm diameter and Lincolnweld 980 flux, basicity index of 0.6 was used for the experiments. At 500 A, a very chaotic irregular shaped droplet with chaotic, non-axial metal transfer is observed. A detachment frequency of approximately 9 Hz was observed for 500 A. Between 600 A and 1000 A, a tapering electrode tip was observed ejecting a molten tail through a mechanism resembling an electromagnetic kink instability. The electromagnetic kink instability results in a "whipping tail" kind of detachment of the molten metal as observed in the videos. Between 600 A and 1000 A, the detachment frequency increases approximately from 27 Hz to 82 Hz. No streaming or rotating spray type transfer as in GMAW was observed however can not be discarded for wires and fluxes different than those used in here. Future experiments will focus on different fluxes and wires.

A comparison of the observations with the one done by previous researchers using non-disruptive X-ray and other optical techniques shows excellent similarity in the metal transfer under similar conditions thus supporting the methodology utilized.

An external gas flow was used to blow away stray flux particles that block the flux cavity view and to prevent it from collapsing. An experiment conducted without external gas shows flux grains falling continuously and ultimately blocking the view of flux cavity. While observations were possible similar detachment characteristics were observed, thus indicating a negligible influence of the gas injected on metal transfer.

Optical analysis of the weld cross-sections shows similar features before, during and after the tunnel with small but measurable changes. Between 700 A and 800 A, a gradual increase in penetration is observed consistent with a change in penetration mode from recirculating flows to gouging penetration as seen in the videos. Understanding the effect of current on metal transfer in SAW will open doors for producing complex waveforms for the process tailored for particular wires and fluxes.

3.9 References

[1] P.G. Grebelnik. X-ray study of the process of automatic submerged arc welding (Russian). *Avtomatich. Svarka*, (6):18–29, 1950.

[2] I.K. Pokhodnya. A method of investigating the processes of melting and transfer of electrode metal during welding. *Automatic Welding*, (2):1–10, 1964.

[3] Von G. Tybus. Farbige Zeitlupenaufnahmen zur Beobachtung des Schweißbades beim UP-Schwhweißen. *Schweisstechnik*, 7(Hefte 3):68–71, 1957.

[4] U. Franz. Vorgänge in der Kaverne beim UP-Schweißen, Teil I (Processes in the cavern during submerged arc welding, Part I). *Schweisstechnik*, 15(4):145–150, 1965.

[5] U. Franz. Vorgänge in der Kaverne beim UP-Schweißen, Teil II (Processes in the cavern during submerged arc welding, Part II). *Schweißtechnik*, 16(9):400–404, 1966.

[6] Van Th. J. Adrichem. Metal transfer in submerged-arc welding. In *International Institute of Welding Document Number 212-78-66*, Nijmegen, Holland, 1966.

[7] Patricio F. Mendez, Gregor Goett, and Stuart D. Guest. High Speed Video of Metal Transfer in Submerged Arc Welding. In *International Institute of Welding Document Number 212-1345-14*, Seoul, South Korea, 2014.

[8] Patricio F. Mendez, Gregor Goett, and Stuart D. Guest. High Speed Video of Metal Transfer in Submerged Arc Welding. *Welding Journal*, 94(October):326–333, 2015.

[9] G. Gött, A. Gericke, K.M. Henkel, and D. Uhrlandt. Optical and Spectroscopic Study of a Submerged Arc Welding Cavern. *Welding Journal*, (December):491–499, 2016.

[10] http://www.ualberta.ca/∼ccwj/Publications/WJ_ECMT_DCSAW/
SOM1: ccwj_000035.016.mp4

SOM2: ccwj_000035.015.mp4
SOM3: ccwj_000035.002.mp4
SOM4: ccwj_000035.009.mp4
SOM5: ccwj_000035.005.mp4
SOM6: ccwj_000035.010.mp4
SOM7: ccwj_000035.017.mp4
SOM8: ccwj_000035.018.xlsx.

[11] P. C. Gupta, D. Rehfeldt, and F. Erdmann-Jesnitzer. Influence of Current Pulses During Submerged Arc Welding. *Welding Research Supplement*, (November):377–380, 1976.

[12] J.H. Kim, R H Frost, D L Olson, and M Blander. Effect of Electrochemical Reactions on Submerged Arc Weld Metal Compositions. *Welding Journal*, (December):446–453, 1990.

[13] Kozo Akahide, Teruo Ukibe, and Junichiro Tsuboi. Correlation between Arc Phenomena and Welding Parameters in Submerged-Arc Welding. *Journal of the Japan Welding Society*, 50(5):520–524, 1981.

[14] Uwe Reisgen, Konrad Willms, Rahul Sharma, and Johannes Schaefer. Diagnostic process analysis of the submerged-arc by welding high-strength fine-grained structural steels. In *International Institute of Welding Document Number 212-2205-15*, Helsinki, Finland, 2015.

[15] J. F. Lancaster. *The Physics of Welding*. 1986.

[16] Hugo J De Blank. MHD Instabilities in Tokamaks. *Transactions of Fusion Science and Technology*, 57(2):124–138, 2010.

[17] Américo Scotti, Vladimir Ponomarev, and William Lucas. A scientific application oriented classification for metal transfer modes in GMA welding. *Journal of Materials Processing Technology*, 212(6):1406–1413, 2012.

[18] John Norrish. A Review of Metal Transfer Classification in Arc Welding. *IIW Doc. XII-1769-03*, pages 1–15, 2003.

3.10 Appendix 3.1: Frames corresponding to visible arc length measurements, used to calculate electrode stickout

Table A3.1: Frames used to measure visible arc length and then to obtain the electrode stickout for DCEP-SAW

Experiment	Frames used to measure visible arc length
71 (500 A, DC)	1563, 3216, 4973, 6534, 3681
68 (600 A, DC)	664, 2641, 4417, 5237, 6579
47 (700 A, DC)	1798, 1968, 2400, 4025, 6289
61 (800 A, DC)	1722, 2231, 3654, 3125, 2543
58 (900 A, DC)	1144, 1394, 1931, 2614, 3655
62 (1000 A, DC)	1218, 1815, 2396, 3063, 3187

3.11 Appendix 3.2: Detachment frames corresponding to the high-speed videos

Table A3.2: Detachment frames corresponding to the high-speed videos

Experiment	**Detachment frames**
71 (500 A, DC)	261, 1143, 2062, 3157, 4530, 5989, 6145, 7079
68 (600 A, DC)	292, 577, 816, 1561, 1841, 2087, 2598, 32, 3933, 4371, 4603, 4854, 5047, 5231, 56, 5845, 6202, 6526
47 (700 A, DC)	784, 1337, 1932, 2387, 2547, 2745, 2864, 3189, 3985, 4536, 4650, 5366, 5731, 5855, 6287, 6371
61 (800 A, DC)	647, 791, 923, 1249, 1455, 1631, 1816, 1975, 2133, 2222, 2431, 2541, 2671, 2827, 3003, 3168, 3343, 3432, 3636, 3831, 4023, 4102, 4291, 4351
58 (900 A, DC)	257, 358, 490, 550, 591, 777, 874, 1040, 1306, 1342, 1576, 1814, 2071, 2279, 2385, 2487, 2667, 2875, 3163, 3388
62 (1000 A, DC)	778, 901, 1038, 1104, 1191, 1260, 1286, 1368, 1435, 1476, 1499, 1517, 1762, 1959, 2093, 2239, 2375, 2533, 2799, 2971, 3140, 3341
44 (800 A, DC)	2392, 2654, 3102, 3441, 3646, 3811

3.12 Appendix 3.3: Measurements of cross-sections

Table A3.3: Measurements of cross-sections of Fig. 3.7. Similar features observed before, during and after the tunnel with small changes

Experiment	Location relative to tunnel	Thickness of plate (mm)	Bead Width (mm)	Penetration (mm)	Reinforcement (mm)	Cross section (mm^2)
68	before	9.699	14.54	8.07	2.68	28.65
(600 A, DC)	during	9.697	17.22	6.65	6.10	75.44
	after	9.668	13.62	8.97	3.46	29.73
47	before	9.589	15.21	8.16	3.14	33.80
(700 A, DC)	during	9.556	18.77	5.00	4.81	60.24
	after	9.581	14.48	9.72	1.91	20.89
61	before	9.623	15.17	9.08	5.05	56.33
(800 A, DC)	during	9.688	13.61	6.63	3.48	39.80
	after	19.403	11.08	9.65	2.02	17.47
58	before	9.608	16.40	9.65	4.42	49.04
(900 A, DC)	during	9.579	19.27	7.38	4.53	61.22
	after	9.582	10.96	9.69	1.83	15.90
62	before	9.662	13.96	9.70	5.70	65.49
(1000 A, DC)	during	9.645	12.71	7.28	2.75	32.56
	after	19.563	11.14	10.25	1.66	14.33

3.13 Appendix 3.4: Detachment frequency and droplet diameter for DCEP-SAW experiments

Table A3.4: Detachment frequency and droplet diameter corresponding to DCEP-SAW experiments

Experiment	Average detachment frequency (Hz)	Average droplet diameter (mm)
71 (500 A, DC)	8.73 ± 2.69	3.58 ± 0.36
68 (600 A, DC)	27.27 ± 6.84	2.68 ± 0.22
47 (700 A, DC)	26.89 ± 6.34	2.91 ± 0.27
61 (800 A, DC)	62.46 ± 9.08	2.32 ± 0.11
58 (900 A, DC)	60.68 ± 13.60	2.49 ± 0.18
62 (1000 A, DC)	81.94 ± 19.17	2.37 ± 0.18

3.14 Appendix 3.5: Procedure used for reporting average values with calculated error

Average data acquisition values and error reported in Table 3.1

The data acquisition of current, voltage and WFS was done at 60kHz. The average current, voltage, and WFS are calculated from the data. The standard deviation in the current, voltage and WFS readings is calculated. A Student's t value is obtained from the t table corresponding to the number of data points. The error in the reported values is calculated by multiplying the t value and standard deviation divided by square root of the number of data points. The average value is then reported with the calculated error.

Average visible arc length, electrode stickout, and corresponding error in the measurement

Table A3.1 summarizes the frames used to measure the visible arc length. Assuming a constant contact tip to work piece distance (CTWD) of 31.75 mm (1.25 in), the electrode stickout is calculated by subtracting the visible arc length from the CTWD. The visible arc length and electrode stickout is calculated for each current, then an average electrode stickout is reported. Then the standard deviation of the data points is calculated. Based on the number of data points a 't' value is obtained from a Student's t table for 95% confidence interval using a two-tailed curve. The error in the average visible arc length and electrode stickout is calculated by multiplying the 't' value and respective standard deviation divided by square root of the number of data points.

Average nominal heat input with corresponding error in the measurement

The nominal heat input is calculated from the current, voltage and travel speed by the formula:

$$HI = \frac{60VI}{v_t} \tag{3.1}$$

where, HI is the nominal heat input in kJ/in., V is the voltage in Volts, I is current in Amperes, and v_t is the travel speed in in./min.

The average nominal heat input is calculated. Then the standard deviation of the data points is calculated. Based on the number of data points a 't' value is obtained from a Student's t table for 95% confidence interval using a two-tailed curve. The error in the average nominal heat input is calculated by multiplying the 't' value and standard deviation divided by square root of the number of data points.

Average detachment frequency and corresponding error in values shown in Fig. 3.4

The detachment frames for each current is obtained from the videos and are reported in Table A4.2. The difference in corresponding frames are calculated to determine the duration between the detachments. The corresponding time between detachments is calculated by dividing the difference in frames by 10000. Then average time interval (t) is calculated. Then the standard deviation of the data points is calculated. Based on the number of data points a t value is obtained from a Student's t table for 95% confidence interval using a two tailed curve. The error in the average time values (δ t) is calculated by multiplying the t value and standard deviation divided by square root of the number of data points. The average detachment frequency is the reciprocal of the average time values. The error in average detachment frequency (δ f) is calculated by error propagation, in which the formula for average detachment frequency i.e., f = 1/t is differentiated w.r.t. to t and then the result is multiplied by δ t.

Average droplet diameter and error in values shown in Fig. 3.5

The detachment frequency with error is calculated based on the detachment frames

reported in Table A4.2 by the procedure explained above. Assuming a spherical droplet the droplet diameter can be calculated by:

$$d_d = \left(\frac{3V_f d_e^2}{2f_d}\right)^{\frac{1}{3}} \tag{3.2}$$

where d_d is the droplet diameter in m, V_f is the wire feed speed in m/s, d_e is electrode diameter in m, and f_d is the detachment frequency in Hz.

Now the error in the detachment frequency and V_f for each current is calculated above. Assuming the electrode diameter is constant. We have to carry out an error propagation w.r.t. to f_d and V_f to estimate the error in the droplet diameter. The error in the droplet diameter by carrying out an error propagation of errors in WFS and detachment frequency is given by:

$$e_d = K\sqrt{\left(\left(\frac{\partial d_d}{\partial V_f}\right)\delta V_f\right)^2 + \left(\left(\frac{\partial d_d}{\partial f_d}\right)\delta f_d\right)^2} \tag{3.3}$$

On carrying out the respective derivatives we get,

$$e_d = K\sqrt{\left(1/3 f_d^{1/3} V_f^{-2/3}\delta V_f\right)^2 + \left(-1/3 V_f^{1/3} f_d^{-4/3}\delta f_d\right)^2} \tag{3.4}$$

where, K = 0.025

The error hence calculated is shown in the Fig. 3.5

Chapter 4

Effect of Current on Metal Transfer in Submerged Arc Welding. Part 2: AC Polarity

4.1 Introduction

The physical phenomena in submerged arc welding (SAW) takes place under a flux bed and is not visible directly. The AC polarity has a limited use in gas metal arc welding (GMAW) but it is commonly used in the case of SAW. Modern hardware to produce square waveforms and AC in SAW is also capable of producing more sophisticated waveforms. However, due to lack of understanding of the metal transfer in SAW, this capability is seldom used.

In the literature, very limited work has been reported on metal transfer in AC polarity in SAW. The Chapter 3 of this thesis discusses all the relevant literature available related to this topic. Among all the researchers, Adrichem [1] and Mendez et al. [2] has only reported to carry out metal transfer studies in AC SAW. Adrichem used a 3.2 mm wire and studied the metal transfer between 300 A and 600 A with AC polarity. The work reports the observations of metal transfer in SAW but nothing in specific was mentioned related to AC SAW. Mendez used a 3.2 mm wire and reported that for 500 A, the metal

transfer in AC is similar to DCEP. Mobile cathode area were observed on the droplet surface in the EN cycle. Gött et al. [3] carried out experiments by inserting a thin-gauge steel into the flux bed. They did experiments at 600-A AC and reported movement of cathode spots all over the droplet surface during the EN cycle.

The present work explores the effect of current on the metal transfer mode in SAW between 500 A and 1000 A with the use of high-speed videos captured at 10000 f/s for a 3.2 mm wire in AC polarity. The cross-sections before, during and after tunnel are compared for all currents. The electrical signal is analysed for an experiment.

4.2 Experimental Setup

The experimental setup, camera setting, and consumables are explained in Chapter 3. All experiments were made by program 59 (CC Square Wave Steel 0.125 in.) with a frequency of 60 Hz and balance of 50 % electrode positive (EP) and 50 % electrode negative (the EN) cycle. The offset was kept at 0% to maintain the same current during the EP and the EN polarities. The data acquisition was carried similar to that in Chapter 3.

The welding parameters are listed in Table 4.1. The voltage was varied with the intention of keeping a constant visible arc length of 4.85 ± 0.22 mm (0.19 ± 0.009 in) (corresponding to an electrode stickout of 26.90 ± 0.22 mm (1.06 ± 0.009 in). The frames used to measure the visible arc length are reported in Table A4.1. Travel speed was also increased aiming to keep a relatively uniform nominal heat input of 51.45 ± 1.00 kJ/in (2.03 ± 0.04 kJ/mm). The important variation between welds is in the welding current varying between 500 A and 1000 A in 100 A intervals. The travel speed recorded was directly recorded from the gantry display. The procedure to estimate all the related errors has been explained in Chapter 3.

4.3 Analysis of High-Speed Videos in AC polarity

Six high-speed videos of metal transfer in SAW are uploaded as supporting online material [4]. The uploaded videos are rendered at 25 f/s which corresponds to a factor of 400 in the time dimension. Many more experiments were conducted but failed as falling flux blocked the camera view.

Droplet detachment is much affected by current and polarity. At 500 A, the metal transfer is by the formation of a chaotic, irregular shaped droplet. At 600 A and above, the detachment morphology is often different in the EP and EN cycle. The metal transfer in the EP cycle is based on electromagnetic kink instability giving it a "whipping tail" kind of detachment. In the EN cycle, the detachment typically takes place through explosions. An instance of the effect of polarity on droplet detachment can be seen in video SOM12 (800 A, AC). Frames 4520 to 4580 of Video SOM12 shows an EP cycle with a detachment event based on electromagnetic kink instability taking place between frames 4550 and 4565. Frames 4430 to 4490 of video SOM12 shows an EN cycle with a detachment event based on explosions taking place between frames 4460 and 4475. A lot of spatter is generated in the EN cycle. The frames corresponding to the visual identification of droplet detachment for each experiment are listed in 3.11.

The detachment frequency is reported with a 95% confidence interval determined with a t-test described in 3.14 and represented in Fig. 4.1. The average detachment frequency increases with current. Table A4.4 summarizes the detachment frequency and droplet diameter for all currents. The average detachment frequency based on the frames was calculated and shown in Fig. 4.1. The average droplet size based on detachment frequency, wire diameter and average wire feed speed is represented in Fig. 4.2. Up to 800 A, the weld pool meniscus is visible in the videos; beyond this weld pool is below the plate surface and not visible. Most detachments (approximately 72%) takes place in

Table 4.1: Parameters corresponding to high-speed videos of AC-SAW

Experiment	Video	Polarity	RMS Current A	RMS Voltage V	Average WFS m/min	Average WFS in./min	Travel Speed m/min	Travel Speed in./min
60	SOM9	AC	530.50 ± 0.364	30.13 ± 0.020	2.04 ± 0.002	80.5 ± 0.0087	0.457	18
66	SOM10	AC	622.29 ± 0.462	32.83 ± 0.020	2.66 ± 0.002	104.7 ± 0.0100	0.604	23.76
55	SOM11	AC	720.19 ± 0.347	36.02 ± 0.023	3.19 ± 0.001	125.59 ± 0.0065	0.762	30
67	SOM12	AC	813.50 ± 0.418	37.8 ± 0.024	3.63 ± 0.001	142.9 ± 0.0119	0.914	36
57	SOM13	AC	920.53 ± 0.770	39.11 ± 0.031	4.19 ± 0.004	164.9 ± 0.0188	1.092	43
64	SOM14	AC	1011.60 ± 0.882	41.89 ±0.033	4.82 ± 0.005	189.96 ± 0.0200	1.280	50.4

the EP cycle.

Video SOM9 corresponds to Experiment 60 (500 A, AC). It was run with similar conditions to Experiment 71 (500 A, DC) but with AC polarity. For the balance, frequency and video parameters used, the electrode positive (EP) cycle lasts approximately 85 frames (3.4 s in rendered video) and the electrode negative (EN) cycle lasts approximately 80 frames (3.2 s in rendered video). The light from the arc dims-out during the polarity switch. Frame 3464 shows the start of the EN cycle, the droplet is observed to be irregular in shape due to the mobile cathode area. The EN cycle lasts till frame 3545 and then the EP cycle starts. Frame 3678 captures a moving cathode area (bright spot on the droplet) at the left surface of the droplet and then moves to the center by frame 3686. Explosions are observed similar to DCEP experiments.

Video SOM10 corresponds to Experiment 66 (600 A, AC). It was run in similar conditions to Experiment 68 (600 A, DC) but with AC polarity. For the balance, frequency and video parameters used the EP cycle lasts for approximately 78 frames (3.1 s in rendered video) and the EN cycle lasts for approximately 78 frames (3.1 s in rendered video). The switch between the EP and the EN cycles can be seen similar to Experiment 60 except when the weld pool blocks the view. Frame 4470 captures a cathode area in the right corner of the droplet which then moves to the center by frame 4480 and then to the left by frame 4489. It is mobile till the cycle ends at frame 4533 and gives the molten metal an irregular shape. Frames 5875 to 5901 shows the tapering of the electrode and then

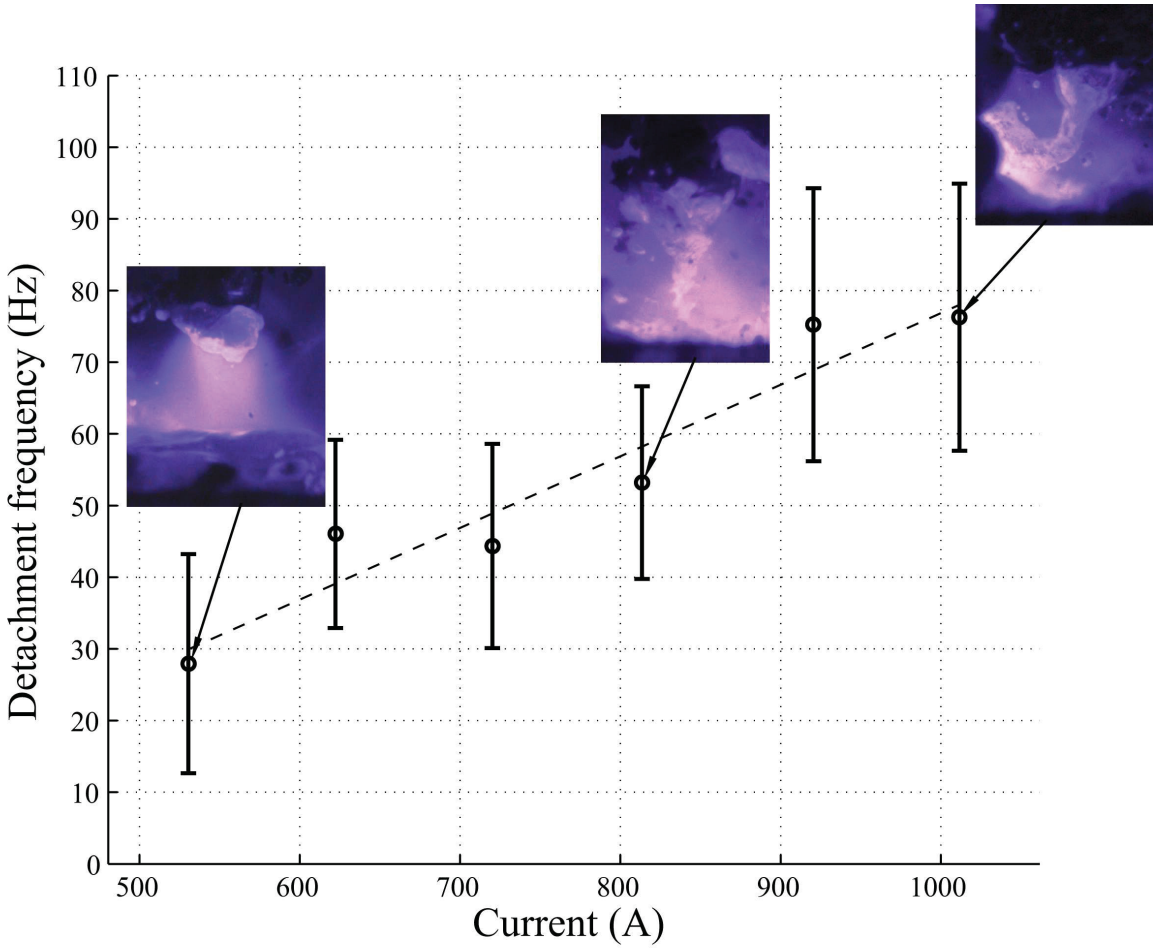

Figure 4.1: Detachment frequency for 3.2 mm wire and 4.85 mm (0.19 in) visible arc length (corresponding to 26.90 mm (1.06 in) electrode stickout). Detachment frequency increases with current.

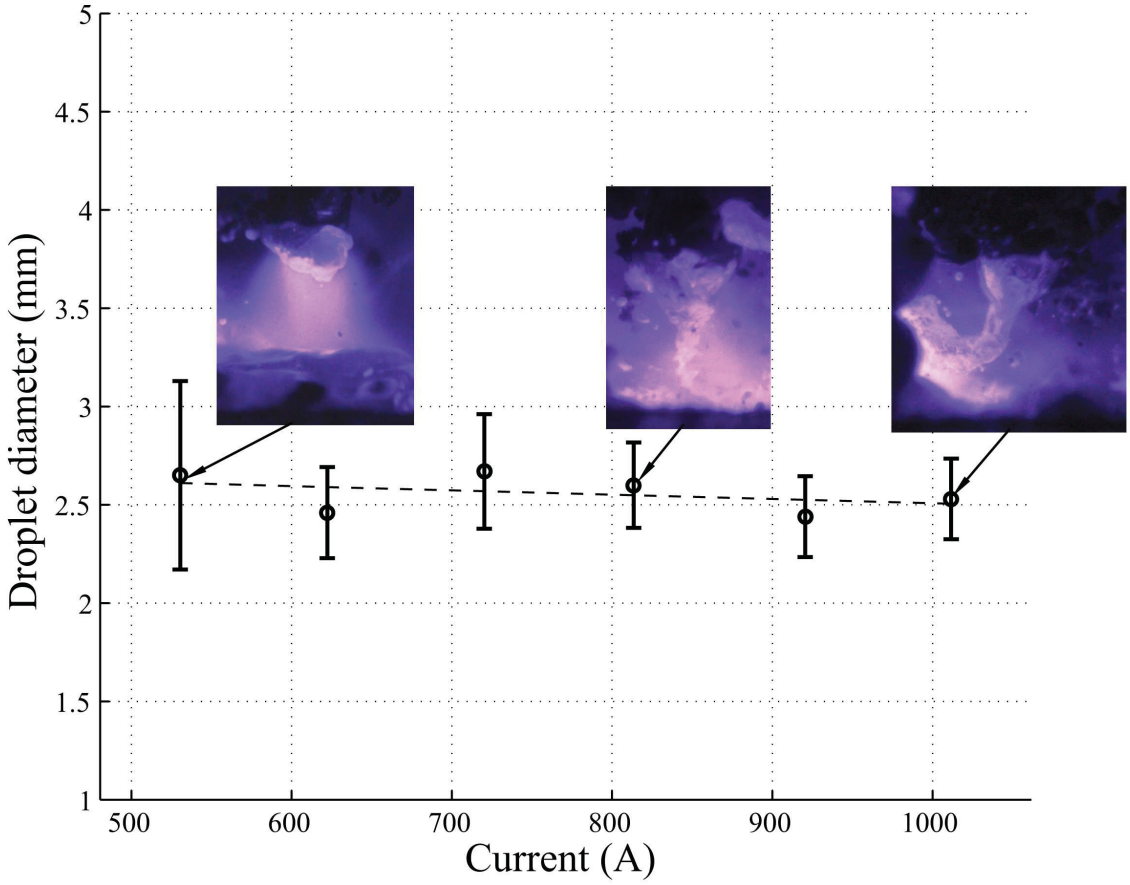

Figure 4.2: Droplet diameter for 3.2 mm wire and 4.85 mm (0.19 in) visible arc length (corresponding to 26.90 mm (1.06 in) electrode stickout)

detachment similar to one observed for Experiment 68 (600 A, DC). The molten metal explodes into fine drops in the EN cycle which spread randomly in all directions. One such explosion can be seen in frame 6339.

Video SOM11 corresponds to Experiment 55 (700 A, AC). It was run with similar conditions to Experiment 47 but with AC polarity. For the balance, frequency and video parameters used the EP cycle lasts approximately 85 frames (3.4 s in rendered video) and the EN cycle lasts approximately 79 frames (3.2 s in rendered video). Frame 1947 (in the EN cycle) captures a cathode area (bright area) which is at the bottom of the molten metal moves to the left by frame 1953 and then to right by frame 1957. Between frames 3590 to 3601 a detachment event takes place; the molten metal detaches forming a characteristic "whipping tail". The molten metal in the EN cycle is observed to be irregular in shape. Frames 4982 to 6605 shows electrode surrounded by the flux grains falling from the top giving a good representative of the process under fluxes. The detachment frequency is found to be higher than that observed with DC experiment done with same parameters. One possible reason for that is the erratic nature of the arc in the EN cycle leading to faster detachments. Gases produced from the fluxes similar to all the experiments before can be seen throughout the video.

Video SOM12 corresponds to Experiment 67 (800 A, AC). It was run with similar conditions to Experiment 61 but with AC polarity. For the balance, frequency and video parameters used the EP cycle lasts for approximately 80 frames (3.2 s in rendered video) and the EN cycle lasts for approximately 80 frames (3.2 s in the rendered video). Frames 4552 to 4559 shows the formation of a kink in the molten tail and then detachment. At frame 4569 (in the EN cycle) a cathode area (bright area) appears on the bottom left of the droplet. It is mobile throughout the cycle giving the molten metal an irregular shape. The cathode area is moving too fast, and it is difficult to quantify its location. Frame 2267 onwards flux grains can be seen falling from the top. The flux grains falling

near the wire are pushed to the side by the erratic arc in the negative cycle. Frames 6994 to 9192 captures the molten pool behind the arc (towards left of welding direction in the video) thus giving a good representation of molten pool phenomena in SAW as reported by Mori and Horii [5].

Video SOM13 corresponds to Experiment 57 (900 A, AC). It was run with similar conditions to Experiment 58 (900 A, DC) but with AC polarity. For the balance, frequency and video parameters used the EP cycle lasts for approximately 86 frames (3.4 s in rendered video) and the EN cycle lasts for approximately 82 frames (3.3 s in rendered video). From the first frame of the video, a tapered electrode is observed ejecting a molten tail. Detachments seem faster when compared to previously conducted experiments with AC at lower currents. Many of similar features are observed in Experiment 58 are present. Frames 1004 to 1031 shows the formation of a tapered electrode finally ejecting a molten tail. The ejected molten metal flies sideways, where it meets the flux and moves down into the weld pool.

Video SOM14 corresponds to Experiment 64 (1000, AC). It was run with similar conditions to Experiment 62 (1000 A, DC) but with AC polarity. For the balance, frequency and video parameters used the EP cycle lasts for approximately 77 frames (3.1 s in rendered videos) and the EN cycle lasts for approximately 81 frames (3.2 s in rendered videos). The EP cycle shows similar detachments as seen in Experiment 64. Frames 450 to 475 shows a tapered electrode ejecting a molten tail by a mechanism of electromagnetic kink instability. Frames 1738 to 1773 shows the formation of a molten tail which does not detach, a possible reason for this can be insufficient electromagnetic force necessary for detachment. After the experiment, the tunnel top surface on the right side of welding direction shows a hole which is made by the spatter because of explosions; this shows the importance of the flux in this welding, especially at high currents.

4.4 Analysis of Electrical Signal

A square wave AC waveform was used for the experiments with a 50% balance and 0% offset. The electrical data was recorded at a frequency of 60 kHz. Fig. 4.3 shows the electrical signal between 1.684 s to 2.086 s of Experiment 60 (500 A, AC). The square wave nature of both current and voltage signals is appreciated from the figure. It is interesting to note that the voltage is a bit higher than the target voltage of 30 V for both the EP and EN cycles. However, the RMS voltage calculated for the whole data neglecting that of the weld start lies around the target voltage of 30 V. The oscillations in the voltage and current signals is due to the changes in the average WFS.

4.5 Analysis of Weld Cross Sections

For all the welds discussed here, cross-sections were analyzed before, during and after the tunnel. Fig. 4.6 shows the cross-sections of welds, and Table A4.3 lists the measurements of the cross-sections before, during and after the tunnel for all welds. These measurements show that the tunnel has a small effect on the shape of the bead, with the welds being slightly wider and taller under the tunnel, but with less penetration. Figs. 4.4 and 4.5 display the effect of current on the bead width, and penetration.

A possible explanation for the differences in cross sections inside and outside the tunnel is that the stray arcs shift the energy balance toward the electrode, increasing the amount of electrode melted (thus the larger cross-section), but reduce the amount of energy going to the plate (thus the lower penetration). As the stray arcs alternate with arcs to the plate, to maintain the same average voltage the arc to the plate is longer (thus the wider beads). Synchronized videos and data acquisition are needed to support or reject this hypothesis and are the focus of ongoing work.

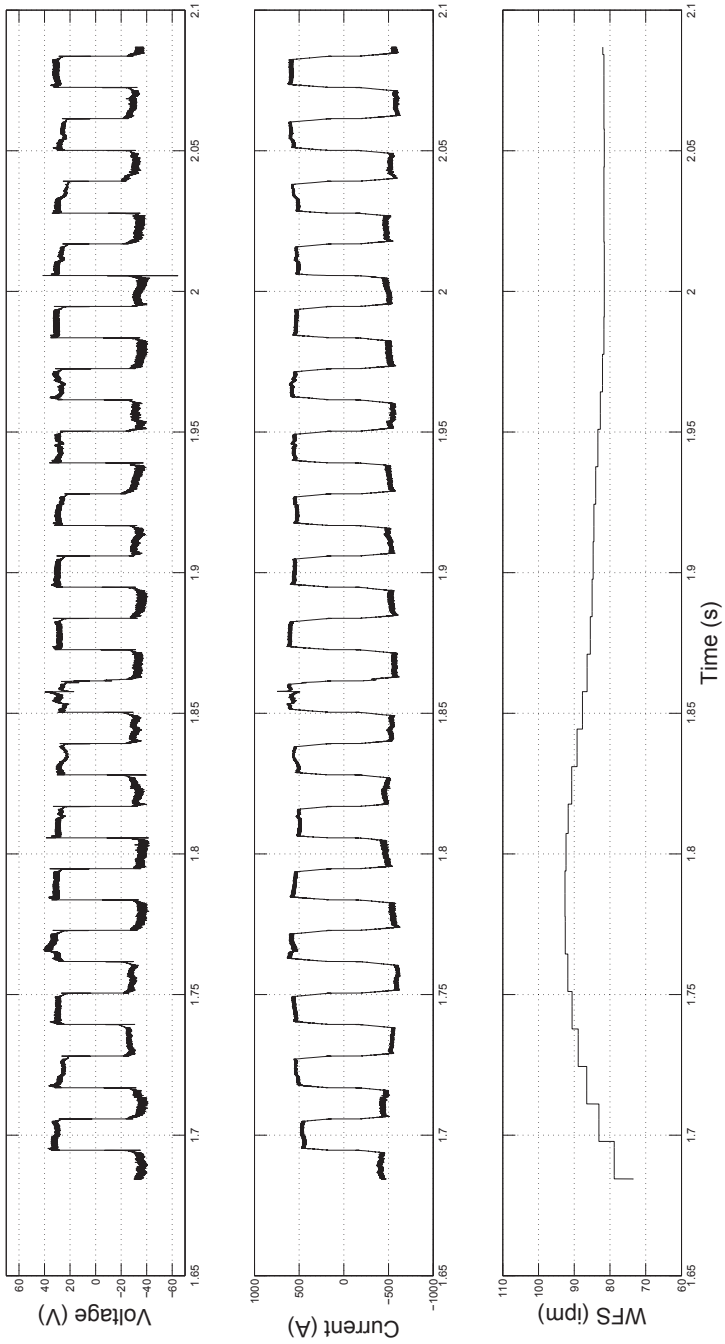

Figure 4.3: Electrical signal between 1.684 s to 2.086 s of Experiment 60 (500 A, AC).

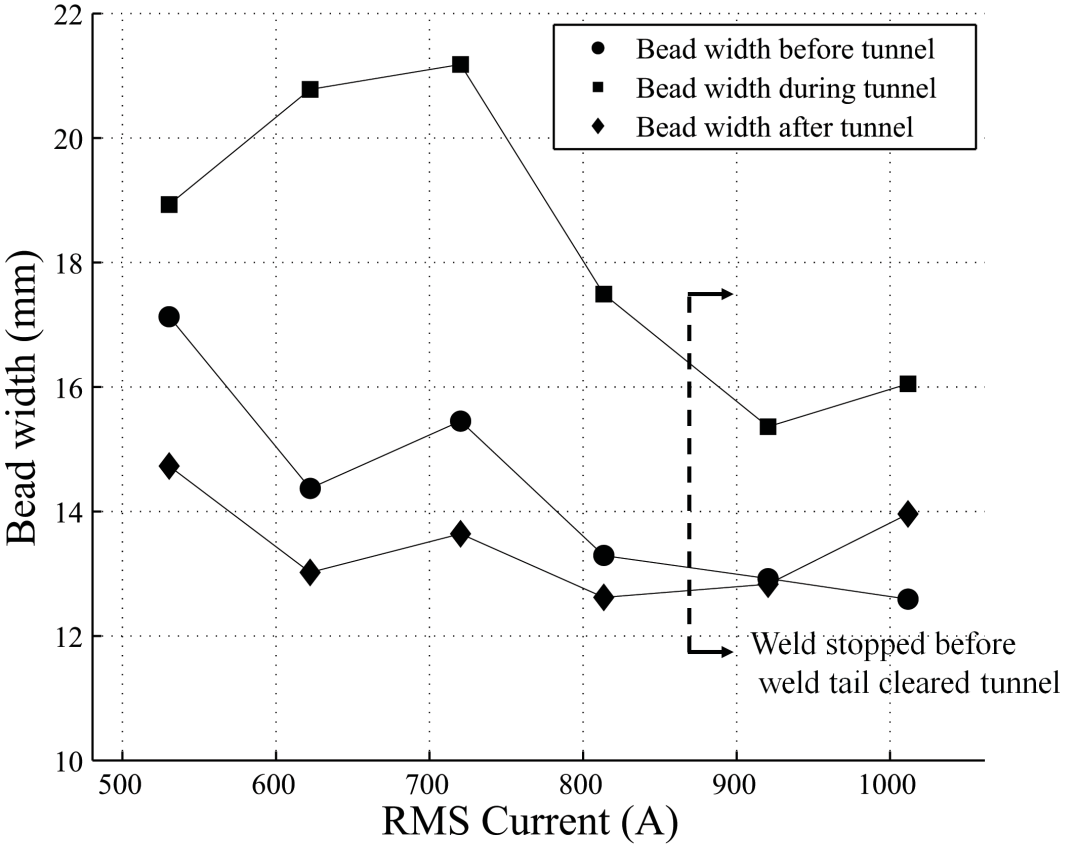

Figure 4.4: The effect of current on bead width in AC polarity. Bead is observed slightly wider during the tunnel except for cases when the solidifying molten tail ended inside the tunnel.

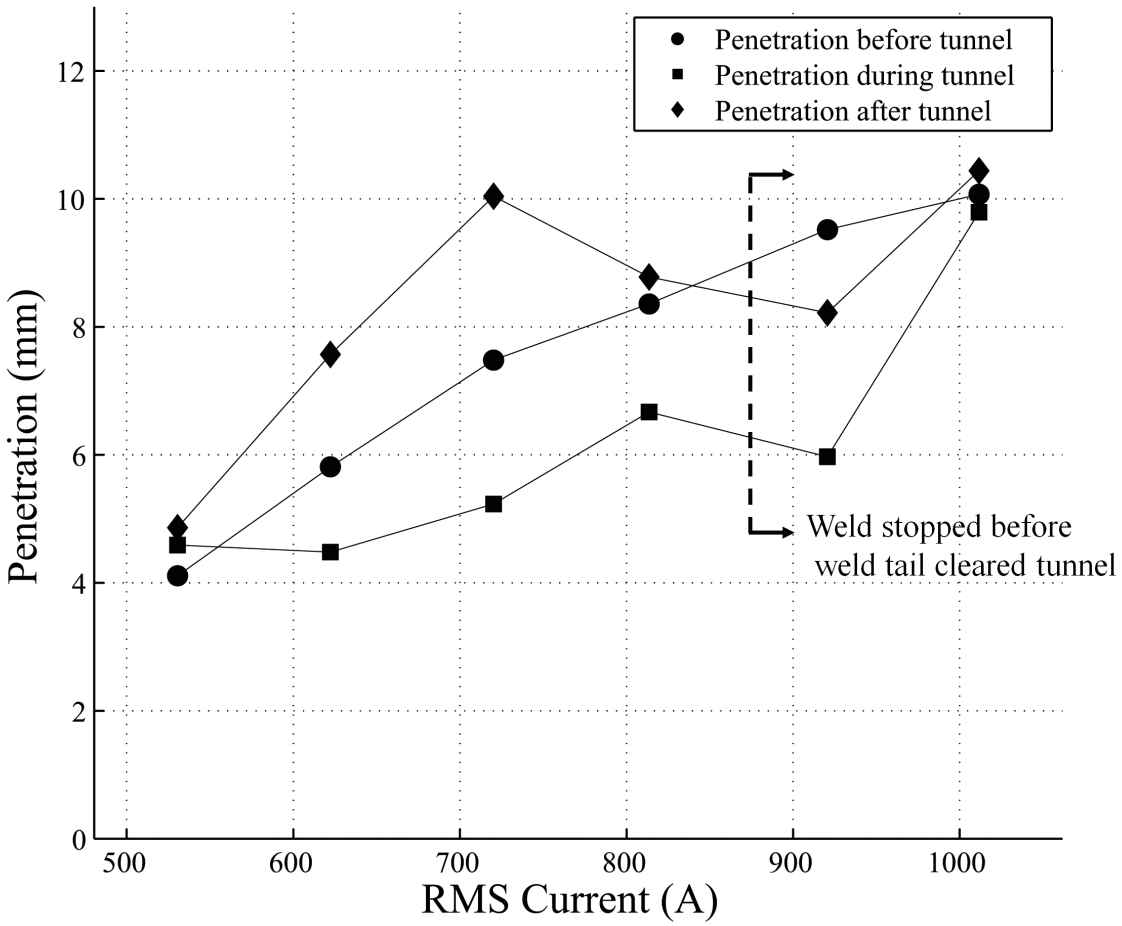

Figure 4.5: The effect of current on penetration. A gradual increase in penetration is observed, and between 800 A to 900 A molten metal meniscus is no longer seen, consistent with a change in penetration mode from recirculating flows to gouging penetration.

An analysis of cross sections before and during the tunnel indicates that the cross section during the tunnel is on average 62% larger than before the tunnel. A similar analysis of cross sections of [2] results in increases of 107%. The cross sections of experiments 57 and 64 were not included in this measurement as the molten tail ended inside the tunnel, thus, affecting the measurements. The fact that the difference in cross sections before and after the tunnel decreases with thinner steel for the tunnel is consistent with the explanation suggested.

The increase in the penetration with current is consistent with the observation of gouging penetration, observed clearly at 700 A and above despite constant heat input. The undercut observed for Experiment 64 (1000 A, AC) is due to the very fast travel speed chosen to maintain a constant nominal heat input for that current. The thickness of the plate was measured with a micrometer with 0.001 mm resolution and reinforcement, depth and width were measured counting pixels in images of 300 pixels per inch resolution giving an accuracy of measurements of the order of 0.1 mm.

Figs. 4.6 shows some artifacts resulting from the experimental setup. For Experiment 67 (800 A, AC), the tunnel did not get cut in a straight line, resulting into a bead an irregular shaped reinforcement for the during tunnel cross section. In experiments at 900 A and 1000 A, the molten tail of the weld pool become very long and the weld was stopped before the whole tail exited the tunnel (approximately 60 mm or 5 s) after the arc exited the tunnel, while the trailing tail of the weld pool was still under the tunnel, affecting the measurements of cross sections under and after the tunnel because they did not reach steady state before they solidified. The flat top observed for the during and after tunnel welds for 900 A and 1000 A is due to the trailing tail of the weld pool ending inside the tunnel.

The cross-sections of weld for Experiment 60 (500 A, AC), shows an increase of 1.8 mm in bead width between before and during the tunnel. An increase of 0.8 mm in

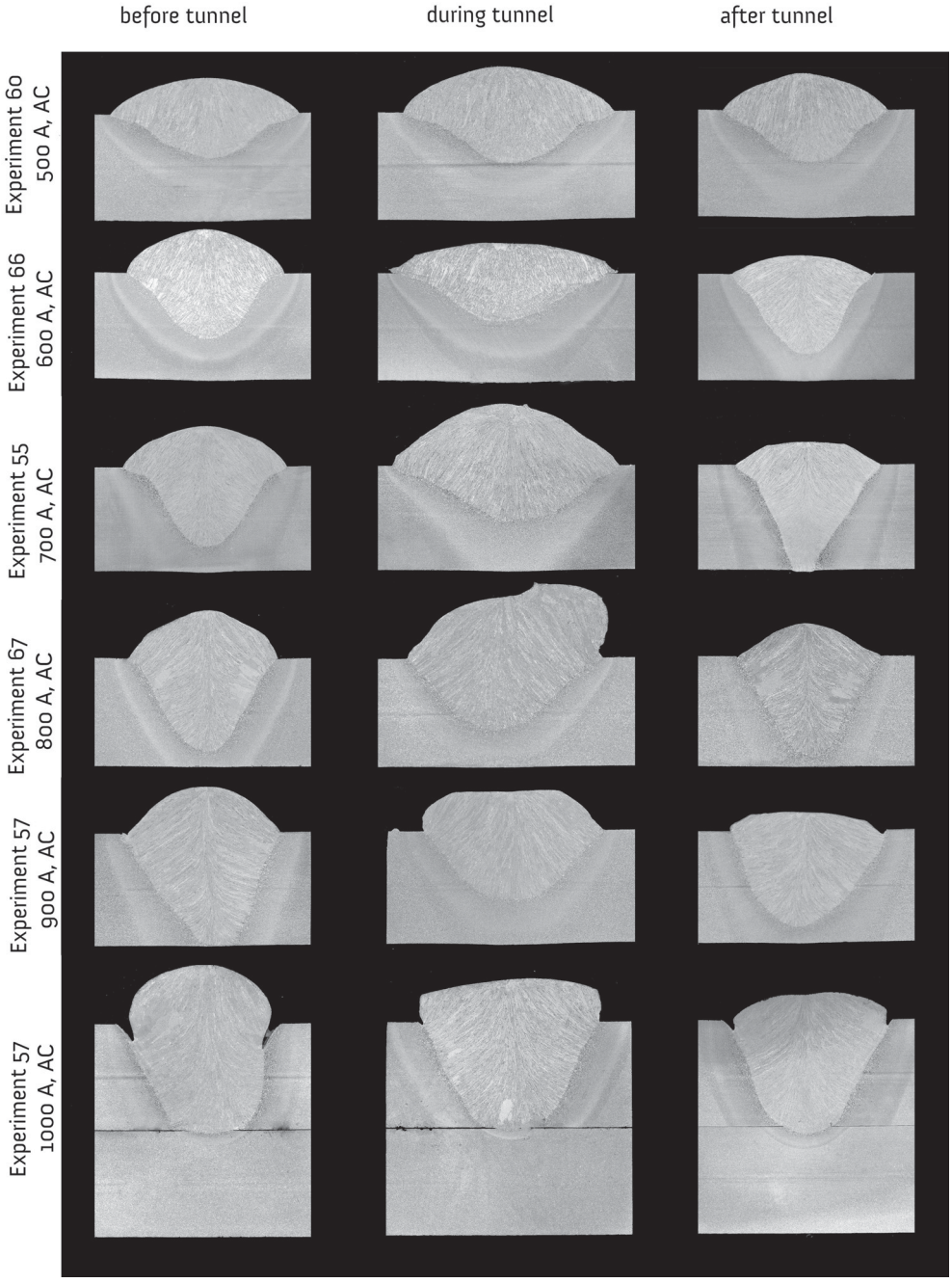

Figure 4.6: Cross-sections before, during and after the tunnel of the welds done with AC. For reference of scale, average thickness of the substrate is 9.65 mm (single plate) and 19.32 mm (two plates).

reinforcement is observed during the tunnel compared to before the tunnel. The difference in penetration is small, with a variation of 0.48 mm before and during the tunnel.

The cross-sections of weld for Experiment 66 (600 A, AC), shows the penetration is approximately 1.5 mm less during the tunnel compared to before the tunnel. The bead is approximately 6 mm wider during the tunnel than before the tunnel. The reinforcement during the tunnel is 1.5 mm lower than that before the tunnel.

The cross-sections of weld for Experiment 55 (700 A, AC), shows an increase in penetration compared to previous AC experiments; this is consistent with the gouging region penetration mechanism. The penetration during the tunnel is approximately 2 mm less than that before the tunnel. The bead width is approximately 2 mm more during the tunnel than before the tunnel. The reinforcement is approximately 5.5 mm more during the tunnel than before it.

The cross-sections of the weld of Experiment 67 (800 A, AC) shows the bead width during the tunnel is 4 mm more than that before the tunnel. The reinforcement during the tunnel is 2 mm more than that before the tunnel. Fig. 4.6 shows a different shape of reinforcement during and before the tunnel.

The cross-sections of the weld of Experiment 57 (900, AC) shows an increase in penetration compared to lower currents. The bead width during the tunnel is approximately 2 mm more than that before the tunnel. The penetration during the tunnel is approximately 3.55 mm lower than before the tunnel. The reinforcement is similar during and before the tunnel.

The cross-sections of the weld of Experiment 64 (1000 A, AC) shows an increase of bead width by 3.46 mm between before and during the tunnel. The reinforcement during the tunnel is 2.19 mm lower during the tunnel than before the tunnel. The penetration is similar during the tunnel than before.

4.6 Discussion

The metal transfer observed with this technique was found to be consistent with works of previous researchers and has been discussed in-depth in Part 1 of the paper. The key feature of the AC is the EN cycle and movement of the cathode area; this mobility of cathode area is in accord with Ref. [6].

The detachment frequency at 500 A, AC is found to be higher than that in DCEP. One possible reason for the higher detachment frequency for 500 A AC compared to DCEP experiments is the mechanical perturbations introduced by electromagnetic forces while switching polarity from EN to EP. The detachment frequency in this range (28 Hz) is of comparable order to the switching polarity (60 Hz). For the currents 600 A and 700 A, the higher detachment frequencies observed for AC compared to DCEP for an approximate constant droplet size indicates similar magnitude of capillary forces for both AC and DCEP, so the higher detachment frequencies is due to the higher amount of wire melted in AC. For example, the ratio of the detachment frequencies for 700 A for AC and DCEP is approximately 1.3 and the ratio of WFS is 1.24, almost the same magnitude. At higher currents (800 A to 1000 A), the detachments are governed by the electromagnetic forces, possibly causing the similar detachment frequencies in both AC and DCEP.

The weld pool flows observed in video SOM5 for Experiment 67 (800 A, AC) is consistent with previous non-disruptive experiments using radioactive tracers by Mori and Horii [5], shown in Figs. 4.7, shown in Figs. 4.7. The secondary pool is seen to be lifted above the original substrate surface and is in accord with Ref. [5]. The colour contrast of the weld pool is same as that of the molten metal at the tip of the wire thus, confirming that it is the molten pool and not molten slag. Researchers interested in this field are encouraged to analyze video SOM12.

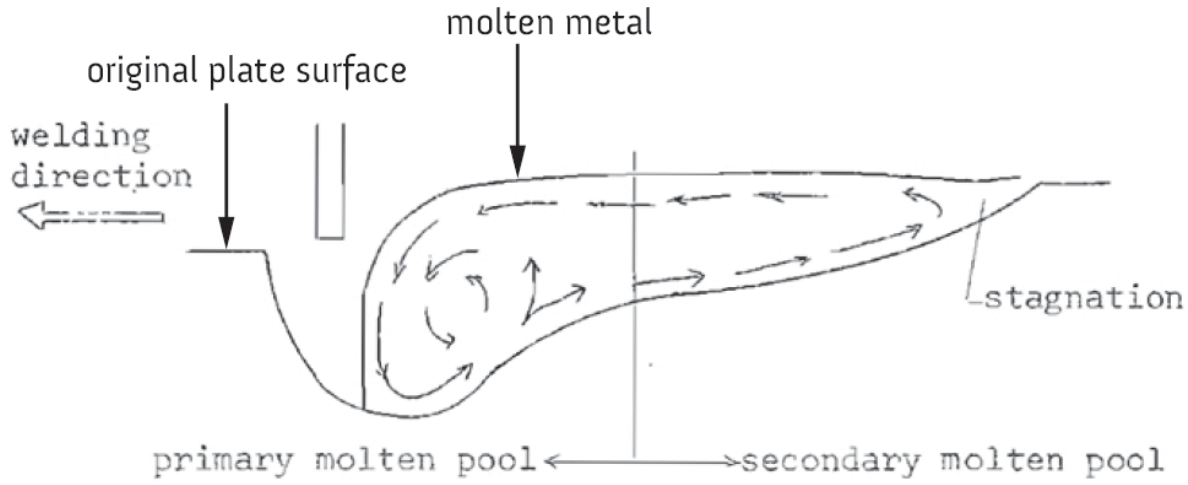

(a) 1970, Mori and Hori [5], Flow pattern in SAW

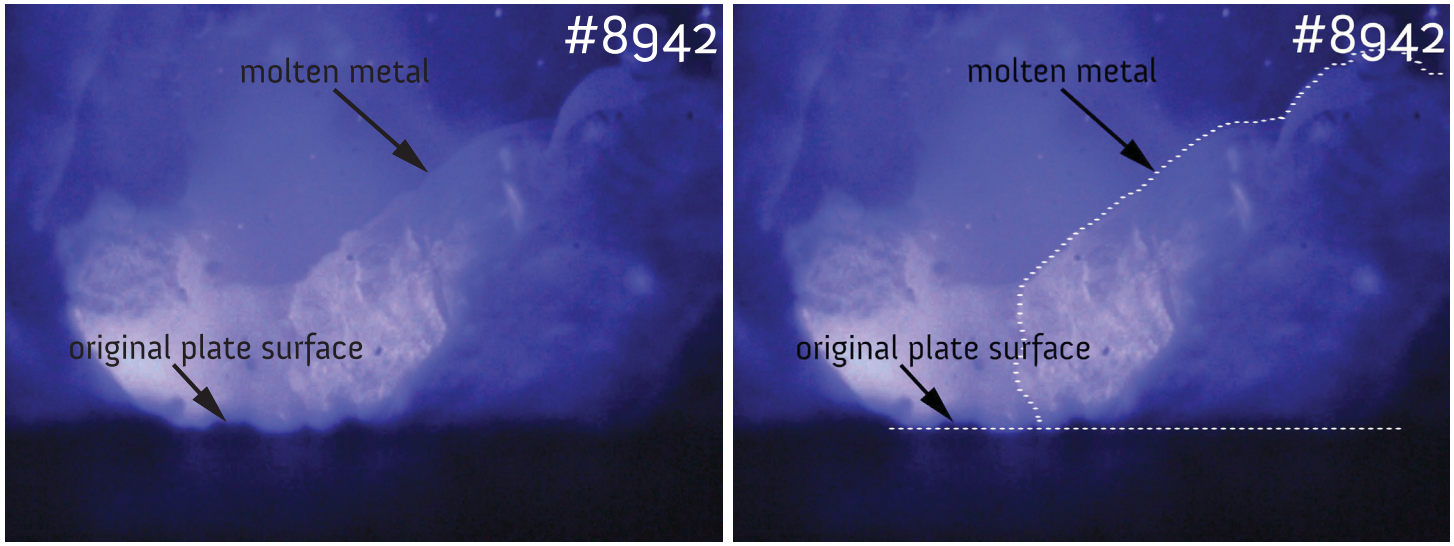

(b) 2015, Present study, Experiment 67 (flipped image)

Figure 4.7: Comparison of weld pool flows in SAW with Ref. [5]. The weld pool shows the regions of primary and secondary molten pool as observed by Ref. [5].

The small differences in weld width and penetration under the tunnel are thought to be because of the stray arcs shift the energy balance toward the electrode, increasing the amount of electrode melted (thus the larger cross-section), but reduce the amount of energy going to the plate (thus the lower penetration). As the stray arcs alternate with arcs to the plate, to maintain the same average voltage the arc to the plate is longer (thus the wider beads). Synchronized data acquisition is required to check this hypothesis. The reason for the full penetration observed for the before tunnel cross section of Experiment 57 (900 A, AC) and after tunnel cross section of Experiment 55 (700 A, AC) is not known.

4.7 Conclusions

The effect of current on metal transfer in submerged arc welding with AC polarity has been captured in high-speed videos. Lincolnweld L-50 wire, 3.2 mm diameter and Lincolnweld 980 flux, basicity index of 0.6 was used for the experiments. Many features observed in AC are similar to DCEP. The key feature for AC is the electrode negative (EN) cycle in which a very irregular shaped droplet is observed. A moving cathode area is seen on the droplet surface.

Droplet detachment is affected by current and polarity. The detachment frequency increased from 28 Hz at 500 A to 76 Hz at 1000 A. Most detachments (approximately 72%) are in EP cycle. The detachment morphology is often different in EP and EN cycle. At 500 A, the detachment in the EP cycle takes place without forming a tail. Between 600 A and 1000 A, the detachment in the EP cycle is based on the electromagnetic kink instability. The electromagnetic kink instability results in a "whipping tail" kind of detachment of the molten metal as observed in the videos. In the EN cycle, the detachment takes place through explosions.

The high-speed videos showed that penetration mode changes gradually from recir-

culating to gouging region penetration; this behavior is consistent with results of previous non-disruptive experiments using radioactive tracers. Analysis of the cross-sections showed that penetration increased with current. The presence of the tunnel had a small but measurable effect on the weld corss-sections, resulting in wider and shallower beads under the tunnel.

No streaming or rotating spray type transfer as in Gas Metal Arc Welding (GMAW) was observed; however, can not be discarded for wires and fluxes different than those used in here.

4.8 References

[1] Van Th. J. Adrichem. Metal transfer in submerged-arc welding. In *International Institute of Welding Document Number 212-78-66*, Nijmegen, Holland, 1966.

[2] Patricio F. Mendez, Gregor Goett, and Stuart D. Guest. High Speed Video of Metal Transfer in Submerged Arc Welding. *Welding Journal*, 94(October):326–333, 2015.

[3] G. Gött, A. Gericke, K.M. Henkel, and D. Uhrlandt. Optical and Spectroscopic Study of a Submerged Arc Welding Cavern. *Welding Journal*, (December):491–499, 2016.

[4] http://www.ualberta.ca/∼ccwj/Publications/WJ_ECMT_ACSAW/
SOM9: ccwj_000035.008.mp4
SOM10: ccwj_000035.013.mp4
SOM11: ccwj_000035.003.mp4
SOM12: ccwj_000035.014.mp4
SOM13: ccwj_000035.004.mp4
SOM14: ccwj_000035.011.mp4
SOM15: ccwj_000035.019.xlsx.

[5] Naomichi Mori and Yukihiko Horii. Molten pool phenomena in Submerged Arc Welding. In *IIW Doc. 212-188-70*, 1970.

[6] J. F. Lancaster. *The Physics of Welding*. 1986.

4.9 Appendix 4.1: Frames corresponding to visible arc length measurements, used to calculate electrode stickout

Table A4.1: Frames used to measure visible arc length and then to obtain the electrode stickout for AC SAW

Experiment	Frames used to measure visible arc length
60 (500 A, AC)	2266, 2591, 2801, 3073
66 (600 A, AC)	4556, 4670, 6264, 6548, 6722
55 (700 A, AC)	2259, 2654, 2913, 3659, 4248
67 (800 A, AC)	3124, 3517, 3691, 3933, 5594
57 (900 A, AC)	372, 529, 751, 2302, 2526
64 (1000 A, AC)	214, 280, 480, 878, 1118

4.10 Appendix 4.2: Detachment frames corresponding to the high-speed videos

Table A4.2: Detachment frames corresponding to the high-speed videos

Experiment	Detachment frames
60 (500 A, AC)	1935, 2166 (EN), 2783 (EN), 3043, 3143, 3420, 4083 (EN)
66 (600 A, AC)	2073, 2563, 2770, 3356 (EN), 3600, 3884 (EN), 3988, 4191, 4455, 4634, 4822, 5030 (EN), 5052, 5279, 5481 (EN), 5718, 5793, 5902, 6015, 6200
55 (700 A, AC)	107, 249, 426, 589, 773, 1054 (EN), 1095, 1121 (EN), 1575, 2213, 2543, 2585, 2898, 3383, 3600, 3761, 4015 (EN), 4205, 4237, 4448, 4616
67 (800 A, AC)	2674, 2750, 3086, 3282 (EN), 3462 (EN), 3664, 3960 (EN), 4133 (EN), 4241, 4472 (EN), 4560, 4737, 4937, 4967 (EN), 5289 (EN), 5494
57 (900 A, AC)	353, 402, 528, 568, 681, 717, 736, 773 (EN), 852, 993 (EN), 1031, 1218, 1389, 1513, 1531, 1684, 1791 (EN), 1928, 2128 (EN), 2289 (EN), 2420, 2611 (EN), 2783 (EN), 2895, 3177, 3456 (EN), 3613 (EN)
64 (1000 A, AC)	88, 377 (EN), 476, 597, 692 (EN), 846, 974, 1089, 1175, 1382, 1429,1504, 1595, 1888 (EN), 1952, 2198 (EN), 2261, 2402 (EN), 2434, 2523 (EN), 2717 (EN), 2886 (EN), 2972

4.11 Appendix 4.3: Measurements of cross-sections

Table A4.3: Measurements of cross-sections of Figs. 4.6. Similar features observed before, during and after the tunnel with small changes

Experiment	Location relative to tunnel	Thickness of plate (mm)	Bead Width (mm)	Penetration (mm)	Reinforcement (mm)	Cross section (mm^2)
60	before	9.657	17.13	4.11	3.28	40.77
(500 A, AC)	during	9.648	18.93	4.59	4.17	54.21
	after	9.622	14.73	4.86	3.32	33.76
66	before	9.678	14.37	5.81	4.04	40.82
(600 A, AC)	during	9.674	20.78	4.48	2.45	41.13
	after	9.698	13.02	7.57	1.62	16.08
55	before	9.720	15.45	7.48	3.91	42.05
(700 A, AC)	during	9.665	21.18	5.23	5.78	83.05
	after	9.689	13.64	10.04	2.15	21.27
67	before	9.636	13.29	8.36	4.32	40.51
(800 A, AC)	during	9.709	17.49	6.67	6.10	87.94
	after	9.652	12.62	8.78	2.90	22.91
57	before	9.559	12.92	9.52	3.93	35.78
(900 A, AC)	during	9.543	15.36	5.97	3.34	44.41
	after	9.555	12.83	8.22	1.76	18.30
64	before	19.321	12.59	10.07	5.57	57.46
(1000 A, AC)	during	19.334	16.05	9.79	3.88	58.16
	after	19.311	13.96	10.44	2.33	28.55

4.12 Appendix 4.4: Detachment frequency and droplet diameter for all AC-SAW experiments

Table A4.4: Detachment frequency and droplet diameter for all AC-SAW experiments

Experiment	**Average detachment frequency (Hz)**	**Average droplet diameter (mm)**
60 (500 A, AC)	27.93 ± 15.29	2.65 ± 0.48
66 (600 A, AC)	46.04 ± 13.12	2.46 ± 0.23
55 (700 A, AC)	44.36 ± 14.24	2.67 ± 0.29
67 (800 A, AC)	53.19 ± 13.44	2.60 ± 0.22
57 (900 A, AC)	75.23 ± 19.04	2.53 ± 0.20
64 (1000 A, AC	76.28 ± 18.64	2.52 ± 0.41

Chapter 5

Effect of Fluxes on Metal Transfer and Arc Length in Submerged Arc Welding

5.1 Introduction

In submerged arc welding (SAW) the welding takes place by formation of an arc cavity surrounded by a slag shell. The cavity atmosphere is partially determined by the welding flux used for the welding. The radiative heat from the plasma leads to the vaporization of the surrounding shell. Eagar [1] proposed breakdown of the oxides like SiO_2 into suboxides like SiO(g) under welding temperatures. The gases produced from the flux may influence the metal transfer and arc length in SAW thus, effecting the weld quality. The absence of innovative techniques to visualize the cavity of SAW has led to limited research in this field.

The prominent techniques used to study the metal transfer, and arc length in SAW are X-ray techniques and optical techniques. Sengupta and Mendez [2] has discussed the advantages and disadvantages of using one technique over the other. In 1947, Ostapenko and Medovar [3] used X-ray cinematography to study the arc cavity of SAW. The major findings of this study were that SAW takes place by forming an arc. The influence of

two different fluxes (AN-3 and OSC-45) on the arc length was studied. The arc length under OSC-45 flux was found to be shorter compared to AN-3 under same welding conditions. Ostapenko reports the lower stabilizing capabilities of OSC-45 flux leads to a shorter arc length. The effect of fluxes on the metal transfer was not studied. In 1950, Grebelnik [4] used the similar approach as Ostapenko and investigated the effect of fluxes on the arc length. Grebelnik did not observe a significant change in the arc length under different fluxes. In 1965, Franz [5] carried out innovative experiments using a ceramic tube to observe the arc cavity of SAW. The ceramic tube used penetrated the flux bed thus providing an opening to observe the phenomena taking place inside the cavity. He concluded that the flux composition has a minimal effect on the metal transfer.

In 1965, Peshak [6] used radiographic techniques to study the changes in arc length under different fluxes. An exhaustive research was carried out on the arc length in SAW. In 1966, Adrichem [7] used a similar technique as Franz and tried to study the effect of different fluxes on the metal transfer. He concluded that with the increase in surface activity of the flux results in lowering of the surface tension of the droplets hence increasing the detachment frequency.

Recently, Gött et al. [8] used a thin-gauge steel to penetrate the flux bed. They recorded high-speed videos at 5000 f/s, also spatially resolved spectroscopy was used to understand the cavity atmosphere in SAW. The flux used was Lincolnweld 8500 (basicity index of 2.9). A similar flux (Lincolnweld 880 M, basicity index of 3.3) is included in the present study. The results of the spectra show intense self-reversed lines of sodium (Na), calcium (Ca), and manganese (Mn). Iron (Fe) lines were also observed indicating the presence of metal vapors in the arc.

The present work explores the effect of fluxes on the metal transfer and arc length in SAW for a 3.2 mm wire between 500 A and 1000 A for both DCEP and AC polarities.

5.2 Experimental Setup

The experimental setup is explained in [2]. The wire used was Lincolnweld L-50 with diameter 0.125 in (3.2 mm). Five different fluxes were used for the experiments. Table 5.3 shows the fluxes with their chemical composition. Flux F1 and F3 are commercial SAW oxide fluxes. Flux F4 is a commercial SAW basic flux. Flux F2 is a commercial electroslag welding (ESW) flux. Flux F5 is an experimental flux with high fluoride content (85% CaF_2), developed by Lincoln Electric Company. The fluxes F2 and F5 with relatively high CaF_2 were chosen to test the possibility of SAW without the formation of an arc. All DCEP experiments were made by program 58 (CC Steel 0.125 in.). All AC experiments were made by program 59 (CC Square Wave Steel 0.125 in.) with a frequency of 60 Hz and balance of 50 % electrode positive (EP) and 50 % electrode negative (the EN) cycle. The offset was kept at 0% to maintain the same current during the EP and the EN polarities. The data acquisition of current, voltage and wire feed speed was done at 60 kHz using the embedded electronics of the power supply and WeldView software version 3.0.0.168.

The same camera, lens, extension tubes, and filter was used as in Chapter 3. For the experiments done between 500 A and 900 A, the videos were captured at 10,000 f/s at a resolution of 512x384. For experiments at 1000 A except with flux F3, the videos were captured at 20,000 f/s and at a resolution of 320 x 240 to study the fast dynamics of the process.

Tables 5.1 and 5.2 lists the parameters for DCEP and AC experiments respectively. The voltage was varied with the current to avoid the conditions of a "buried arc" at all currents and under all fluxes. The travel speed was increased to keep the nominal heat input at 50.737 $\pm$ 0.329 kJ/in (1.997 $\pm$ 0.013 kJ/mm). The average values of the welding current, voltage, WFS and heat input are reported with a 95% confidence interval determined by a Student t-test. The procedure to determine the errors is explained in

Chapter 3.

Table 5.1: Parameters corresponding to high-speed videos DCEP-SAW experiments under different fluxes

Experiment	Video	Polarity	Average Current A	Average Voltage V	Average WFS m/min	Average WFS in./min	Travel Speed m/min	Travel Speed in./min
F1.1	SOM1	DCEP	500.40 ± 0.188	29.89 ± 0.010	64.56 ± 0.014	1.64 ± 0.0003	18	0.457
F2.22	SOM2	DCEP	498.49 ± 0.298	29.98 ± 0.013	71.96 ± 0.020	1.83 ± 0.0005	18	0.457
F3.1	SOM3	DCEP	497.93 ± 0.206	30.03 ± 0.011	61.33 ± 0.009	1.56 ± 0.0002	18	0.457
F4.7	SOM4	DCEP	501.34 ± 0.144	29.99 ± 0.009	61.41 ± 0.012	1.56 ± 0.0003	18	0.457
F5.1	SOM5	DCEP	500.20 ± 0.242	30.01 ± 0.012	71.29 ± 0.015	1.81 ± 0.0004	18	0.457
F1.16	SOM6	DCEP	600.50 ± 0.077	33.01 ± 0.007	75.55 ± 0.010	1.92 ± 0.0002	23.76	0.604
F2.16	SOM7	DCEP	598.72 ± 0.219	33.02 ± 0.011	83.12 ± 0.014	2.11 ± 0.0004	23.76	0.604
F3.2	SOM8	DCEP	619.31 ± 0.150	32.84 ± 0.011	80.75 ± 0.021	2.05 ± 0.0005	23.76	0.604
F4.10	SOM9	DCEP	600.50 ± 0.097	33.01 ± 0.008	74.52 ± 0.011	1.89 ± 0.0003	23.76	0.604
F5.6	SOM10	DCEP	602.48 ± 0.143	32.99 ± 0.009	85.27 ± 0.011	2.17 ± 0.0003	23.76	0.604
F1.5	SOM11	DCEP	708.69 ± 0.175	36.18 ± 0.012	96.56 ± 0.015	2.45 ± 0.0004	30	0.762
F2.2	SOM12	DCEP	700.71 ± 0.193	36.01 ± 0.149	101.48 ± 0.017	2.58 ± 0.0004	30	0.762
F3.3	SOM13	DCEP	713.93 ± 0.234	35.99 ± 0.014	101.57 ± 0.017	2.58 ± 0.0004	30	0.762
F4.9	SOM14	DCEP	703.40 ± 0.135	36.01 ± 0.149	95.13 ± 0.007	2.42 ± 0.0002	30	0.762
F5.3	SOM15	DCEP	700.90 ± 0.121	36.02 ± 0.149	103.89 ± 0.006	2.64 ± 0.0001	30	0.762
F1.15	SOM16	DCEP	797.54 ± 0.227	38.10 ± 0.157	115.11 ± 0.012	2.92 ± 0.0003	36	0.914
F2.15	SOM17	DCEP	801.55 ± 0.237	38.00 ± 0.157	123.59 ± 0.014	3.14 ± 0.0003	36	0.914
F3.4	SOM18	DCEP	806.43 ± 0.197	38.17 ± 0.015	120.46 ± 0.015	3.06 ± 0.0004	36	0.914
F4.4	SOM19	DCEP	801.30 ± 0.145	38.03 ± 0.157	117.43 ± 0.007	2.98 ± 0.0002	36	0.914
F5.4	SOM20	DCEP	801.56 ± 0.154	38.11 ± 0.157	123.95 ± 0.007	3.15 ± 0.0002	36	0.914
F1.13	SOM21	DCEP	905.84 ± 0.205	39.93 ± 0.165	140.35 ± 0.010	3.56 ± 0.0003	43	1.092
F2.14	SOM22	DCEP	901.49 ± 0.164	40.03 ± 0.165	141.94 ± 0.008	3.61 ± 0.0002	43	1.092
F3.5	SOM23	DCEP	911.22 ± 0.242	40.00 ± 0.017	142.99 ± 0.014	3.63 ± 0.0004	43	1.092
F4.3	SOM24	DCEP	900.92 ± 0.193	40.04 ± 0.165	139.89 ± 0.011	3.55 ± 0.0003	43	1.092
F5.5	SOM25	DCEP	899.66 ± 0.155	40.04 ± 0.165	145.43 ± 0.007	3.69 ± 0.0002	50	1.280
F1.7	SOM26	DCEP	999.99 ± 0.182	42.10 ± 0.012	157.99 ± 0.023	4.01 ± 0.0006	50.4	1.280
F2.21	SOM27	DCEP	999.62 ± 0.176	42.06 ± 0.011	171.82 ± 0.008	4.36 ± 0.0002	50.4	1.280
F3.6	SOM28	DCEP	998.24 ± 0.312	42.07 ± 0.018	168.04 ± 0.029	4.27 ± 0.0007	50.4	1.280
F4.8	SOM29	DCEP	1003.44 ± 0.164	42.05 ± 0.011	159.96 ± 0.026	4.06 ± 0.0006	50.4	1.280
F5.17	SOM30	DCEP	995.29 ± 0.153	42.02 ± 0.010	174.20 ± 0.015	4.42 ± 0.0004	50.4	1.280

5.3 Analysis of metal transfer and arc length under different fluxes in DCEP

Sixty high-speed videos are uploaded in Ref. [9]. The results obtained under different fluxes is compared based on the detachment frequency, droplet diameter and arc length. Fig. 5.1 summarizes the detachment frequencies under all the fluxes between 500 A and 1000 A for DCEP polarity. The detachment events are noted from the high-speed videos;

Table 5.2: Parameters corresponding to high-speed videos for AC-SAW experiments under different fluxes

Experiment	Video	Polarity	RMS Current A	RMS Voltage V	Average WFS m/min	Average WFS in./min	Travel Speed m/min	Travel Speed in./min
F1.10	SOM31	AC	512.29 ± 0.233	30.09 ± 0.013	77.63 ± 0.008	1.97 ± 0.0002	18	0.457
F2.11	SOM32	AC	517.14 ± 0.505	31.18 ± 0.034	82.79 ± 0.055	2.10 ± 0.0013	18	0.457
F3.7	SOM33	AC	530.50 ± 0.365	30.13 ± 0.020	80.31 ± 0.009	2.04 ± 0.0002	18	0.457
F4.12	SOM34	AC	512.84 ± 0.279	30.16 ± 0.015	75.67 ± 0.050	1.92 ± 0.0013	18	0.457
F5.16	SOM35	AC	514.73 ± 0.280	30.31 ± 0.020	84.69 ± 0.053	2.15 ± 0.0013	18	0.457
F1.17	SOM36	AC	606.66 ± 0.324	33.25 ± 0.013	102.31 ± 0.063	2.60 ± 0.0016	23.76	0.604
F2.18	SOM37	AC	612.68 ± 0.424	33.36 ± 0.023	99.89 ± 0.063	2.54 ± 0.0016	23.76	0.604
F3.8	SOM38	AC	622.30 ± 0.438	32.83 ± 0.019	104.98 ± 0.010	2.67 ± 0.0002	23.76	0.604
F4.11	SOM39	AC	606.17 ± 0.337	33.23 ± 0.014	99.23 ± 0.061	2.52 ± 0.0015	23.76	0.604
F5.9	SOM40	AC	606.54 ± 0.384	33.36 ± 0.016	102.87 ± 0.064	2.61 ± 0.0016	23.76	0.604
F1.9	SOM41	AC	721.96 ± 0.579	36.14 ± 0.020	120.87 ± 0.004	3.07 ± 0.0001	30	0.762
F2.9	SOM42	AC	708.85 ± 0.448	36.17 ± 0.015	118.91 ± 0.072	3.02 ± 0.0018	30	0.762
F3.9	SOM43	AC	704.03 ± 0.522	36.00 ± 0.017	120.46 ± 0.122	3.06 ± 0.0031	30	0.762
F4.13	SOM44	AC	706.34 ± 0.456	36.27 ± 0.017	115.72 ± 0.070	2.94 ± 0.0017	30	0.762
F5.10	SOM45	AC	705.40 ± 0.443	36.35 ± 0.016	124.05 ± 0.074	3.15 ± 0.0019	30	0.762
F1.18	SOM46	AC	805.95 ± 0.614	38.30 ± 0.018	139.83 ± 0.083	3.55 ± 0.0021	36	0.914
F2.13	SOM47	AC	795.12 ± 0.601	38.52 ± 0.017	142.69 ± 0.079	3.62 ± 0.0020	36	0.914
F3.10	SOM48	AC	826.75 ± 0.817	37.87 ± 0.024	142.67 ± 0.012	3.62 ± 0.0003	36	0.914
F4.5	SOM49	AC	804.03 ± 0.621	38.34 ± 0.019	136.45 ± 0.083	3.47 ± 0.0021	36	0.914
F5.11	SOM50	AC	803.45 ± 0.605	38.33 ± 0.017	145.75 ± 0.084	3.70 ± 0.0021	36	0.914
F1.19	SOM51	AC	898.48 ± 0.793	40.37 ± 0.019	162.08 ± 0.094	4.12 ± 0.0024	43	1.092
F2.12	SOM52	AC	895.53 ± 0.790	40.51 ± 0.019	169.09 ± 0.095	4.29 ± 0.0024	43	1.092
F3.11	SOM53	AC	932.26 ± 1.312	39.11 ± 0.027	167.54 ± 0.034	4.26 ± 0.0008	43	1.092
F4.2	SOM54	AC	900.27 ± 0.814	40.46 ± 0.021	157.17 ± 0.091	3.99 ± 0.0023	43	1.092
F5.12	SOM55	AC	898.62 ± 0.804	40.54 ± 0.019	169.67 ± 0.097	4.31 ± 0.0025	43	1.092
F1.11	SOM56	AC	1002.27 ± 1.015	42.46 ± 0.022	181.33 ± 0.104	4.61 ± 0.0026	50.40	1.280
F2.20	SOM57	AC	999.54 ± 1.007	42.57 ± 0.021	188.01 ± 0.102	4.78 ± 0.0026	50.40	1.280
F3.12	SOM58	AC	1022.28 ± 1.340	41.66 ± 0.027	189.97 ± 0.010	4.83 ± 0.0003	50.40	1.280
F4.15	SOM59	AC	1002.57 ±1.025	42.50 ± 0.023	182.77 ± 0.102	4.64 ± 0.0026	50.40	1.280
F5.13	SOM60	AC	994.79 ± 1.005	42.67 ± 0.020	195.45 ± 0.106	4.96 ± 0.0027	50.40	1.280

Table 5.3: Composition of different fluxes used for the experiments*.

Flux	**%SiO_2**	**%MnO**	**%MgO**	**%CaF_2**	**%CaO**	**%Na_2O**	**%K_2O**	**%Al_2O_3**	**%TiO_2**	**%FeO**	**%ZrO_2**	**% Metal Alloys**
F1 (Lincolnweld 760M)	47	33	17	5	1	2	-	2	0.1	-	-	6
F2 (Lincoln ES200)	9.9	0.1	0.1	48.9	13.5	2.6	1.3	23	-	0.3	0.1	
F3 (Lincolnweld 980)	11	14	2	12	7	2	-	47	-	-	-	4
F4 (Lincolnweld 880M)	12	1	29	29	8	1	1	18	-	-	-	-
F5 (Experimental Flux)	5	-	-	85	5	-	-	5	-	-	-	-

* All values are in weight percentage

the frames used to calculate detachment frequencies are listed in Tables A5.1 and A5.2. Fig. 5.2 summarizes the droplet diameter under all the fluxes between 500 A and 1000 A for DCEP polarity. The droplet diameter is calculated based on detachment frequency, wire feed speed (WFS), electrode diameter and is explained in Chapter 3. Table A3.4 summarizes all the values of the detachment frequencies and droplet diameters for all the DCEP-SAW experiments.

Fig. 5.3 summarizes the average arc length measured at different power inputs under all the fluxes for DCEP polarity. The arc length is directly measured from the frames in the high-speed videos; the frames corresponding to these measurements are listed in Table A5.5. In this Chapter, the term "arc length" corresponds to the visible arc length (distance between the arc attachment at the wire and original plate surface). Some portion of the arc, especially at high currents, is below the original plate surface and is not visible with this technique. The values of detachment frequency, droplet diameter, arc length are reported with a 95% confidence interval determined by a Students t-test. The procedure to calculate the errors is explained in Chapter 3.

As discussed in Chapter 3 the droplet detachment in DCEP is much affected by the current. At low current (500 A), the videos show similar features characterized by a droplet of irregular shape at the tip of the wire under all the fluxes. The droplet under the oxide based fluxes (F1, F3) shows frequent explosions compared to fluxes with high CaF_2 (F2, F5). At high currents (600 A and above), under all the fluxes the detachment is based on electromagnetic kink instability. At low current, the detachment frequency is similar under all the fluxes. At higher currents, the detachment frequency for fluxes with high CaF_2 content is lower than that of the oxide based fluxes.

A larger droplet size was observed for the high CaF_2 fluxes (F2, F5) compared to the other fluxes (F1, F3, and F4). For fluxes F2 and F5, the droplet size does not change a lot with increasing current. Within experimental errors, fluxes F1, F3, and F4 shows a

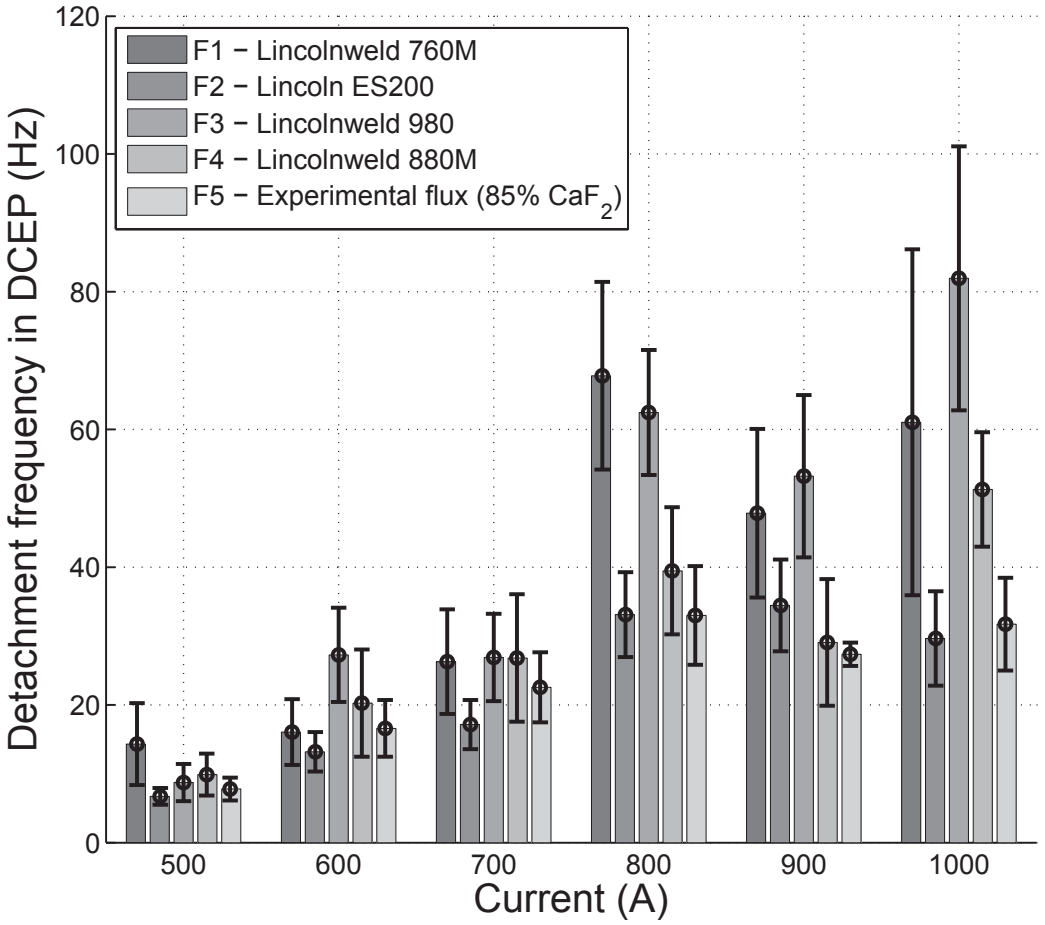

Figure 5.1: Detachment frequency vs current in DCEP-SAW under different fluxes. A low detachment frequency was observed for fluoride based fluxes (F2, F5) compared to the oxide based fluxes (F1, F3).

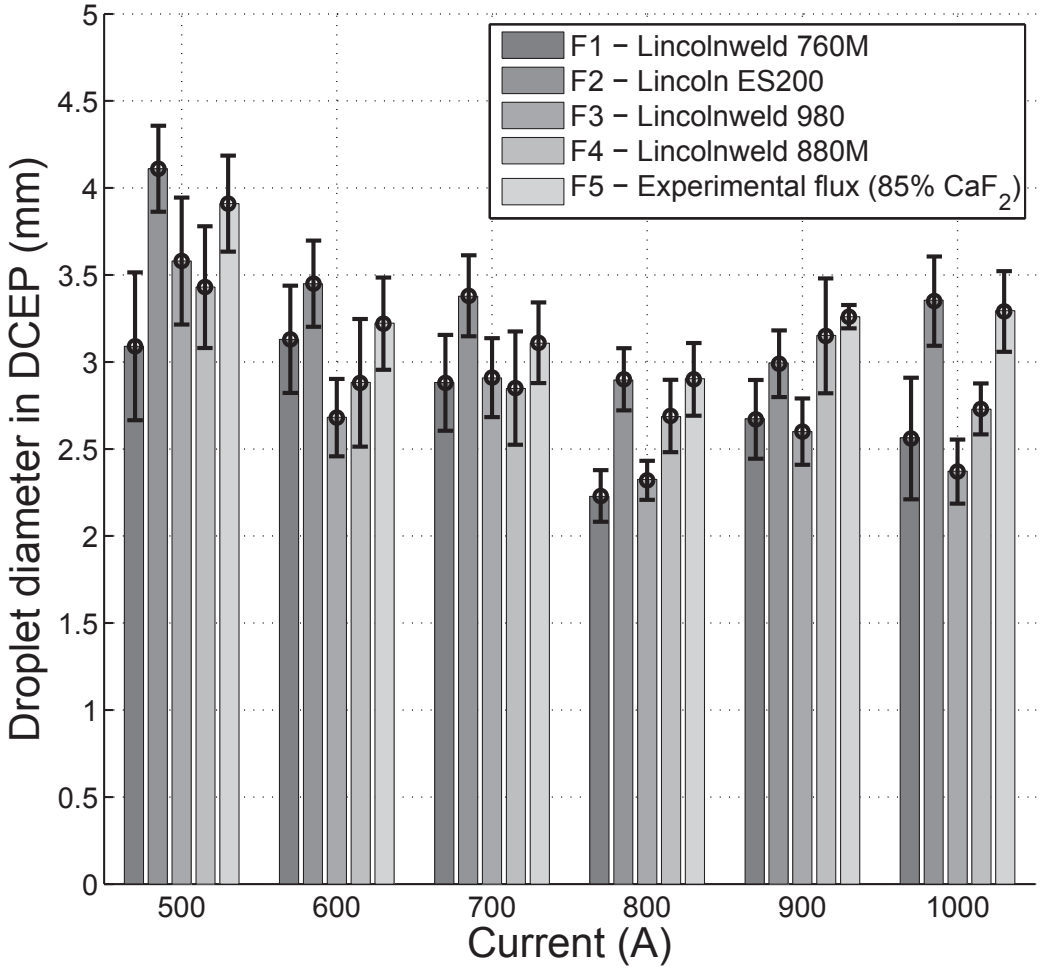

Figure 5.2: Droplet diameter vs current in DCEP-SAW for a 3.2 mm wire under different fluxes. A larger droplet is observed under the fluoride based fluxes (F2, F5).

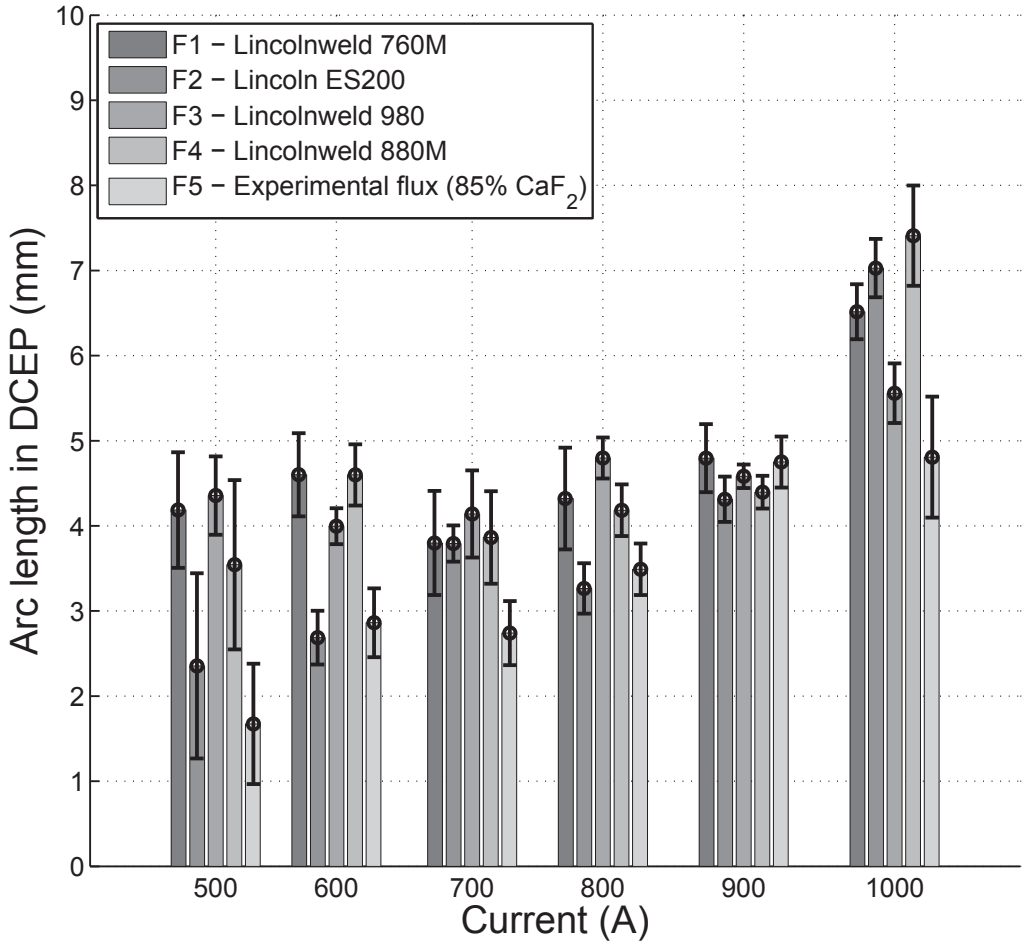

Figure 5.3: Arc length vs current in DCEP-SAW under different fluxes. A shorter arc was observed for fluoride based fluxes (F2, F5) compared to the oxide based fluxes (F1, F3).

decrease in droplet size with increasing current.

A shorter arc length was observed under the high CaF_2 fluxes (F2, F5). The arc length under these fluxes was found to be 2 mm shorter compared to the one observed for fluxes F1, F3, and F4. These observations clearly point to the fact that the plasma under the high CaF_2 is highly resistive in nature. The following paragraphs will summarize the key features observed in the videos corresponding to 500 A and 1000 A DCEP polarity.

5.3.1 Metal transfer and arc length observed at 500 A, DCEP

Fig. 5.4 summarizes the metal transfer observed under different fluxes at 500 A, DCEP. The figure captures a detachment event associated with each flux. The droplet is irregular in shape. The shorter arc can be appreciated for fluxes F2 and F5.

Video SOM1 corresponds to Experiment F1.1 (500 A, DC, F1) From the beginning of the video onwards chaotic explosions (frames 1159, 2164 etc.) are observed at the droplet surface. The frequent explosions lead to spatter which will eventually get caught by the surrounding slag shell in SAW. Throughout the video, the droplet moves in a chaotic manner before its detachment. The arc is attached to the droplet and is moving with the droplet movements. Frames 2406 to 3277 shows the development and then detachment of a droplet. Throughout these frames, the droplet is seen to move in all directions showing the reduced capillary forces under an oxide based flux. The arc does not cover the whole of the droplet and moves with it.

Video SOM2 corresponds to Experiment F2.22 (500 A, DC, F2). The video begins with showing a droplet attached to the wire with a short arc and flux particles falling in the background. In frame 62, the left corner shows a fluid mostly a mixture of slag and molten metal with flux particles sticking to it; this fluid is seen to cover the view of the droplet (for eg.: frame 335). Careful observations show the presence of froth on

the droplet surface and near the solid-liquid interface (frames 5290, 9334). Frame 2721 shows an arc length almost close to zero. The arc length is so short at times that the droplet short-circuits with the weld pool and surrounding molten slag/metal (frames 3068 to 3117) and these lead to chaotic detachments where the droplet explodes into small droplets (frames 3118 to 3189). Throughout the video, there is a noticeable variation in the arc length. Frames 4172 to 4721 shows that the falling flux particles stick to the droplet surface; thus, there is a possibility of electrochemical reactions at the droplet surface as proposed by Kim et al. [10].

Video SOM3 corresponds to Experiment F3.1 (500 A, DC, F3). Many features under this flux are similar to flux F1. A detachment event takes place at frame 260. The detached droplet flies to the right. Frequent explosions can be seen at the droplet surface. The spatter from the droplet surface flies in all directions. The arc length is longer than that in flux F2.

Video SOM4 corresponds to Experiment F4.7 (500 A, DC, F3). The video shows similar features as seen for SOM1 and SOM3. The droplet is irregular in shape. Around frame 2136 the arc becomes momentarily shorter resulting in a short-circuit event at frame 2160. Frames 2636 to 4143 shows the formation and detachment of a droplet. The detached droplet is seen to fly to the back of the wire.

Video SOM5 corresponds to Experiment F5.1 (500 A, DC, F5). The arc is attached to the bottom of the droplet and moves with its movement. Explosions at the droplet surface take place occasionally. The explosions observed under this flux are less frequent than the ones under the oxide fluxes. The detached droplets (frames 5940, 7302 etc.) travel down to meet the weld pool. The detached droplets (frames 5940, 7302) move down to meet the weld pool. Throughout the video, there is a noticeable variation in the arc length and the arc is completely out of sight in frames 8721 to 8809. The variation in the arc length is due to the absence of arc stabilizers in the flux.

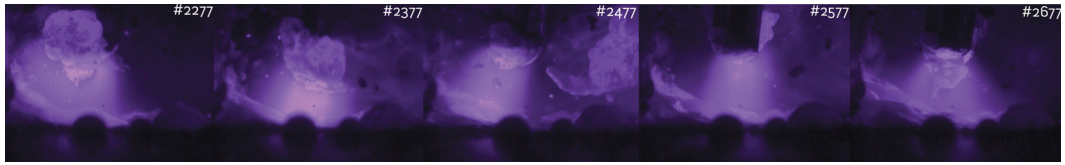

(a) Flux F1, a detachment event takes place between frames 2377 and 2477

(b) Flux F2, a detachment event takes place between frames 7287 and 7387

(c) Flux F3, a detachment event takes place between frames 4478 and 4578

(d) Flux F4, a detachment event takes place between frames 4123 and 4223

(e) Flux F5, a detachment event takes place between frames 7202 and 7302

Figure 5.4: Metal transfer at 500 A, DCEP for a 3.2 mm wire under five different fluxes. A spherical droplet is observed under all fluxes. The arc length under fluxes F2 and F5 is relatively shorter than fluxes F1, F3, and F4.

5.3.2 Metal transfer and arc length observed at 1000 A, DCEP

Fig. 5.5 summarizes the metal transfer observed under different fluxes at 1000 A, DCEP. The figure captures a detachment event associated with each flux. The metal transfer observed is based on electromagnetic kink instability.

Video SOM26 corresponds to Experiment F1.7 (1000 A, DC, F1). The video begins by showing the wire penetrating the tunnel. The video was recorded at 20,000 f/s, to capture the fast dynamics of the process. Under the action of high electromagnetic forces, a tapered electrode gets formed at this current. Frame 1442 shows an instance of the tapered electrode with the kinked molten tail. Frame 3662 shows the flux/slag layer on the left side surrounding the electrode. By frame 4040 the flux particles appear to be molten by the radiative heat from the arc.

Video SOM27 corresponds to Experiment F2.21 (1000 A, DC, F2). Frames 2871-3331 shows the evolution and detachment of the molten metal at the wire tip. Frames 2241 onwards show flux falling from the top and the side. Frame 3324 shows the development of a kink on the left side of the molten metal leading to detachment in frame 3331. The detached metal flies to the left and then comes below the wire in frame 3584 and then is pushed down to the weld pool. From Fig. 5.8 shows that the average arc length for this current is similar to the one observed under the oxide based fluxes.

Video SOM28 corresponds to Experiment F3.6 (1000 A, DC, F3). The video was recorded at 10,000 f/s and played at 25 f/s. The dynamics of the process will appear to be faster than other videos at 1000 A due to the use of the lower f/s to record the video. Frames 734 onwards a tapered electrode tip is observed. A detachment event takes place at frame 1191. Frame 2257 onwards flux grains are seen falling from the top and settling in the background.

Video SOM29 corresponds to Experiment F4.8 (1000 A, DC, F4). Many features

seen in this video are similar to the ones observed under fluxes F1, F2, and F3. Frame 1368 onwards captures the falling flux particles which move from left to right. Frame 1855 shows a detachment event. The detached metal is very irregular in shape and moves towards the left of the wire. Frame 1860 shows the falling flux particles coming in contact with the molten tip and getting melted. The molten flux particle is seen to move right of the wire.

Video SOM30 corresponds to Experiment F5.17 (1000 A, DC, F5). Frames 1322-2301 captures the evolution and detachment of the molten metal. The detached metal is pushed left and down to the weld pool. Fig. 5.3 shows that the average arc length under this flux is shorter when compared to the other fluxes.

5.4 Analysis of metal transfer and arc length under different fluxes in AC

The present section compares the metal transfer and arc length in AC polarity under different fluxes. Many features observed for the metal transfer and the arc length are similar to DCEP. The key feature under the AC polarity is the onset of the EN cycle and movement of the cathode area all over the droplet surface.

As discussed in Chapter 4, the droplet detachment in AC is affected by the current and the polarity. Fig. 5.6 shows the detachment frequency in AC under different fluxes. The frames corresponding to the detachments are listed in Tables A5.3 and A5.4. Unlike the DCEP experiments, the detachment frequency does not show a noticeable trend. At 500 A, the detachment takes place by formation of an irregular shaped droplet. For this current, all the detachments under the high-fluoride fluxes (F2, F5) are in the EP cycle. For the oxide fluxes (F1, F3) some detachments in the EN cycle are noted. From 600 A

(a) Flux F1, a detachment event takes place between frames 1737 and 1747

(b) Flux F2, a detachment event takes place between frames 3330 and 3340

(c) Flux F3, a detachment event takes place between frames 2967 and 2977

(d) Flux F4, a detachment event takes place between frames 3736 and 3746

(e) Flux F5, a detachment event takes place between frames 3037 and 3047

Figure 5.5: Metal transfer at 1000 A, DCEP for a 3.2 mm wire under five different fluxes. The metal transfer observed is based on electromagnetic kink instability.

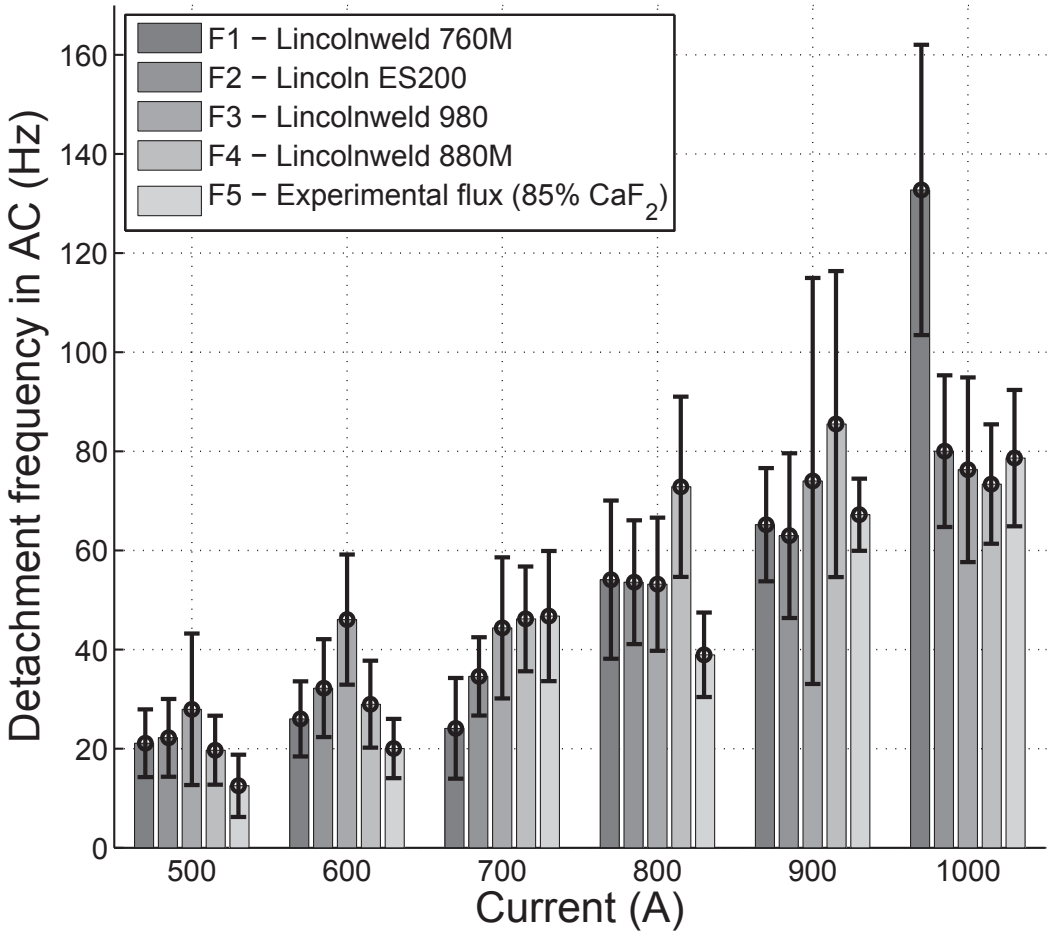

Figure 5.6: Detachment frequency vs current in AC-SAW under different fluxes. Unlike the DCEP experiments, a noticeable trend is not observed for the detachment frequency in the AC-SAW experiments.

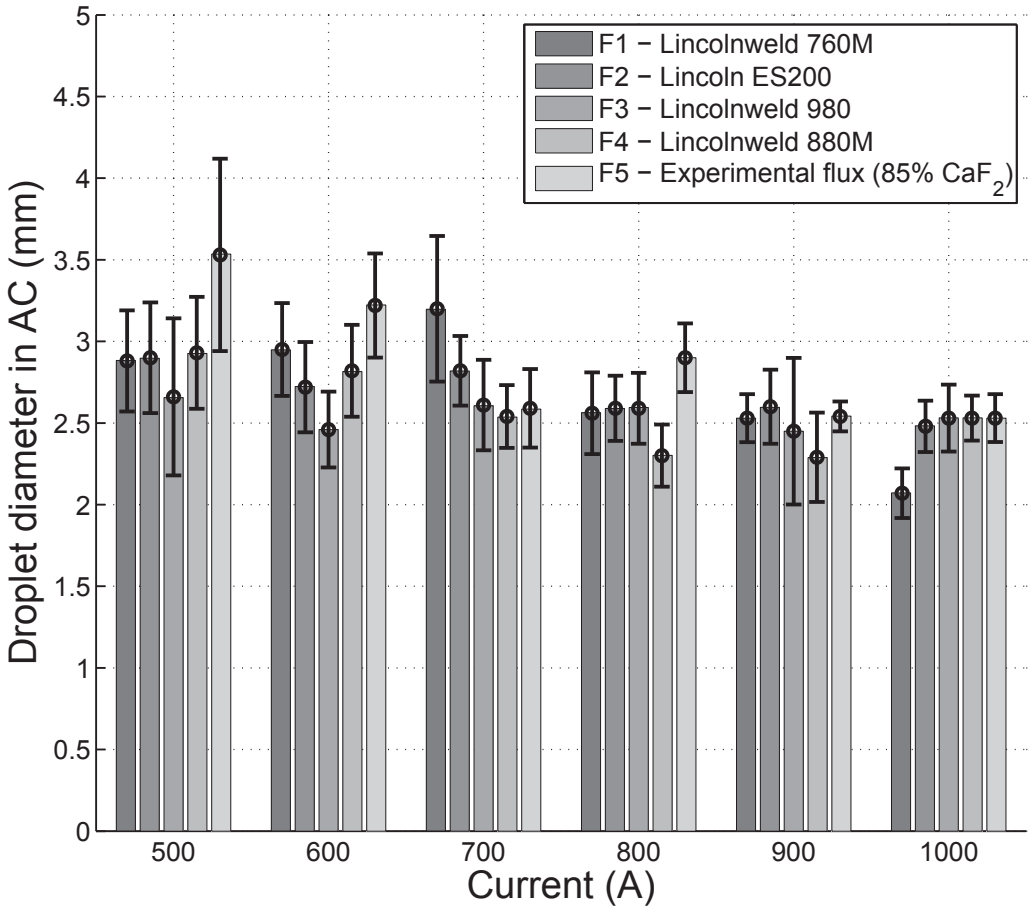

Figure 5.7: Droplet diameter under vs current in AC-SAW under different fluxes. Droplet diameter observed is similar under all the fluxes and decreases with increasing current.

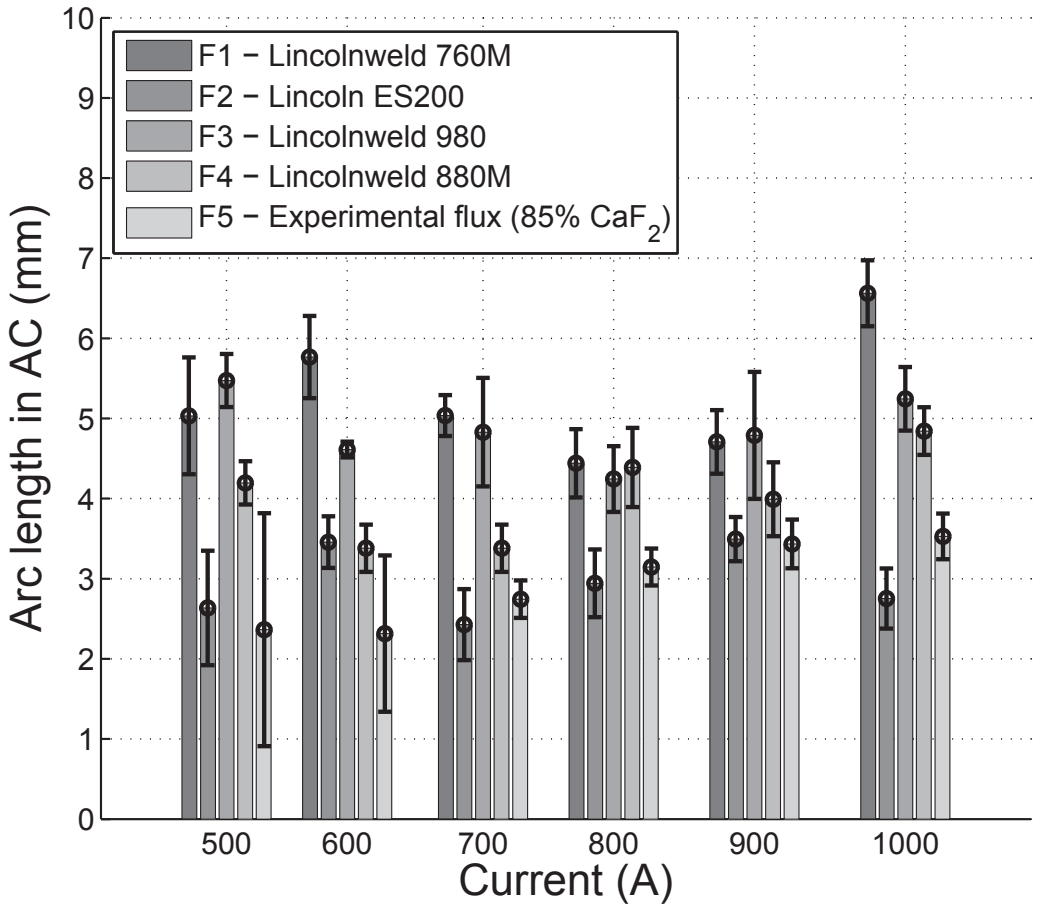

Figure 5.8: Arc length vs current in AC-SAW under different fluxes. A shorter arc was observed for fluoride based fluxes (F2, F5) compared to the oxide based fluxes (F1, F3).

and above the detachment morphology is often different under electrode positive (EP), and electrode negative (EN) cycle. Most of the detachments (approximately 74%) takes place in the EP cycle. Fig. 5.7 shows the droplet diameter in AC under different fluxes. The droplet diameter changes minimal with increasing current. Table A5.8 summarizes the detachment frequencies and droplet diameters for all the AC-SAW experiments.

Fig. 5.8 shows the arc length in AC under different fluxes. The frames corresponding to these measurements are listed in Table A5.6. The trend in arc length is similar to the DCEP experiments with a shorter arc under high CaF_2 fluxes.

5.4.1 Metal transfer and arc length observed at 500 A, AC

Video SOM31 corresponds to Experiment F1.10 (500 A, AC, F1). The video starts by showing a large droplet attached to the wire tip. Frequent explosions are seen on the droplet surface as seen in the DC experiments under this flux. The droplet is irregular in shape and has many modes of oscillations. The video shows an increased amount of weld pool compared to the DCEP experiments; this is due to the higher melting of the wire in the electrode negative (EN) cycle. Frame 3174 shows the moment of switching between electrode positive (EP) to EN cycle. The arc dims out and by frame 3179 a cathode area (bright spot) appears in the top left corner of the droplet. By frame 3181, the cathode area moves to the bottom right corner, then center and left by frame 3185. By frame 3191, it moves to the back of the droplet. The cathode area is mobile throughout the EN cycle.

Video SOM32 corresponds to Experiment F2.11 (500 A, AC, F2). It is done with similar settings as Experiment F2.22 (500 A, DC) but with AC polarity. Frame 2254 shows a switch between the EP and EN polarity. In frame 2258 a cathode area is seen at the bottom of the droplet. The cathode area moves all over the droplet; this movement

is very fast. Frame 2309 shows the highly deformed droplet moving towards the right. Frame 2319 shows a bend on the droplet surface (frame 2319) leading to detachment in frame 2347. Frame 3052 shows a short-circuit event. Frames 3357-3387 shows the slag/metal jets in the background. By frame 4049, the electrode tapers and detaches metal with having a small diameter.

Video SOM33 corresponds to Experiment F3.7 (500 A, AC, F3). Frame 3414 shows a detachment event. The detached droplet flies to the right. At frame 3629, a switch between the EP to EN cycle takes place. In frame 3635, a cathode area (bright spot) appears at the bottom of the droplet, this moves to the back of the droplet and reappears at the bottom left a corner of the droplet by frame 3646. The cathode area are mobile on the droplet throughout the EN cycle.

Video SOM34 corresponds to Experiment F4.12 (500 A, AC, F2). The features observed under this flux are similar to flux F1 and F3. Frame 5786 shows a detachment event in the EP cycle. Frames 5985-6040 captures the movement of the cathode area.

Video SOM35 corresponds to Experiment F5.16 (500 A, AC, F5). The video starts by showing the wire penetrating the tunnel. The arc is very short. The molten metal and slag mixture comes in front and hides the arc and electrode tip. Frame 2451 shows the arc almost buried under the molten metal and slag. It is not clear from the video whether this is a short-circuit or not. Frames 2497 onwards show the movement of the slag/metal jets to the right side of the wire. For the most part of the video, the tip of the wire is hidden by the slag cover. Thus, observing events like droplet detachments become challenging. Frame 12237 shows a detachment event the detached droplet moves down to the weld pool. The arc is not very stable due to the lack of arc stabilizers in the flux.

5.4.2 Metal transfer and arc length observed at 1000 A, AC

Video SOM56 corresponds to Experiment F1.11 (1000 A, AC, F1). Frame 1583 shows a highly tapered electrode tip. Frame 1868 shows a kink in the molten tail on the left side. The kink leads to a detachment at frame 1873. Frame 2649 shows the switch between the EP and the EN cycle. Under the force of the plasma jets, oxides from the plate surface are seen to fly upwards. Frames 5360 onwards, flux particles are seen to fall from the top and settle down near the wire. Frame 7810 gives a good view of the surrounding flux wall around the electrode. By frame 8517, the flux wall on the left side of the wire is completely molten.

Video SOM57 corresponds to Experiment F2.20 (1000 A, AC, F2). The metal transfer shows similar features as observed under flux F1. The EN cycle shows a less chaotic movement of the cathode area compared to the one under flux F1. Frame 3578 shows the arc completely out of sight; this phenomenon takes place often under this flux. A detachment event takes place at frame 6283, the detached metal flies towards the left side of the wire.

Video SOM58 corresponds to Experiment F3.12 (1000 A, AC, F3). The video was recorded at a lower frame rate (10,000 f/s) compared to 20,000 f/s as used in other 1000 A, AC experiments. Due to this, the features in this video appear to be faster. A detachment event takes place at frame 974. The EN cycle shows the characteristic mobile cathode area moving all over the droplet surface (frames 1332-1410). Flux particles are seen to be falling from the top.

Video SOM59 corresponds to Experiment F4.15 (1000 A, AC, F4). Frame 2459 captures the moment when the polarity switches from EP to EN. Frames 2480 to 2625 shows the EN cycle with cathode area moving all over the molten metal surface at very high speeds. Frame 2731 shows a detachment, a tapered electrode is observed after the

detachment. The arc length is comparable to the one observed under flux F1.

Video SOM60 corresponds to Experiment F5.13 (1000 A, AC, F5). The video shows many similar features as observed under flux F2. The mode of metal transfer in the EP cycle is based on electromagnetic kink instability. Frame 6436 onwards, flux particles are seen to be falling from the top. Frame 3867 shows froth on the molten metal surface near the solid-liquid interface; this froth has come from the flux. Frame 4119 shows a detachment with the metal flying towards the left side of the wire.

5.5 Analysis of voltage signal under different fluxes

The analysis of the voltage signal was carried out. Fig. 5.9 shows the voltage signal under different fluxes for DCEP, 500 A, and 30 V. The signals for the fluxes with a significant amount of CaF_2 (F2, F4, F5) shows events of short-circuiting. A similar trend is seen also for experiments done at 600 A, 33 V. Above 600 A, this phenomenon is not observed under all the fluxes. Under the high CaF_2 fluxes (F2, F5), the short-circuit can be between the wire tip and molten pool due to a less stable arc. The slag with high CaF_2 content is a good conductor in the molten state, thus, the slag can bridge between the wire tip and molten pool and cause the short-circuit.

5.6 Discussion

Direct observation of the metal transfer in SAW indicates a minimal influence of the fluxes in determining the mode of metal transfer. However, the observations indicated a strong effect of the fluxes on the arc length.

The decrease in the detachment frequency observed for DCEP experiments with increasing CaF_2 component of the flux is consistent with Ref. [11], shown in Fig. 5.10. The

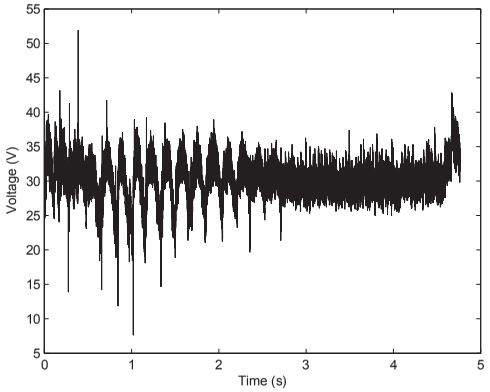

(a) Flux F1, Lincolnweld 760M.

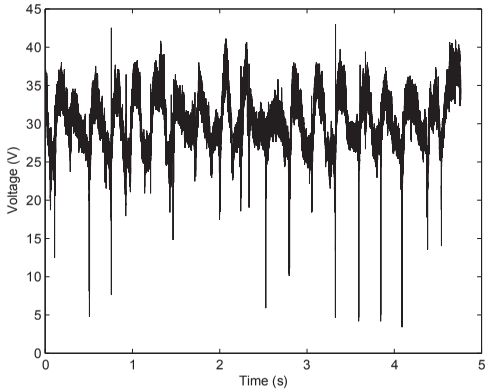

(b) Flux F2, Lincoln ES200.

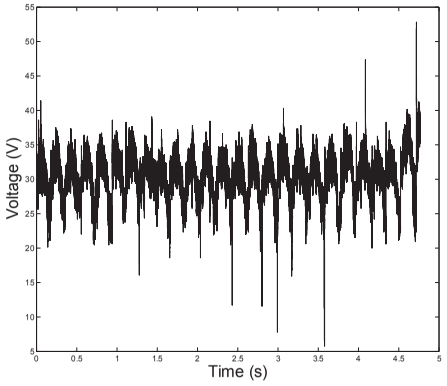

(c) Flux F3, Lincolnweld 980.

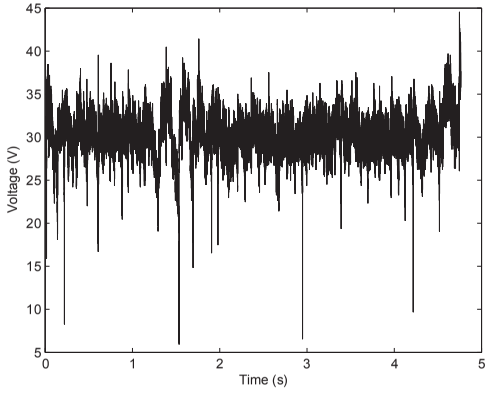

(d) Flux F4, Lincolnweld 880M.

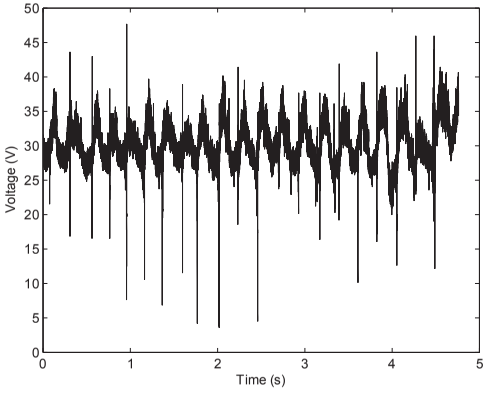

(e) Flux F5, Experimental flux (85% CaF_2).

Figure 5.9: Voltage signal under different fluxes for welds done at DCEP, 500 A, 30 V. The fluxes with significant amount of CaF_2 (F2, F4, F5) shows noticeable short-circuits, where the voltage drop to below 10 V.

comparisons were made for similar current density.

One possible reason for the higher detachment frequency in oxide based fluxes (F1, F3) compared to the fluoride based fluxes (F2, F4, F5) can be due to the decreased surface tension of the molten metal due to higher oxygen from the flux. The theory of higher oxygen in the arc cavity of the oxide flux is given by Eagar [1]. Mitra and Eagar [12] further proposed that the oxygen generated from the flux gets adsorbed on the droplet surface, thus, indicating that a reduction of surface tension can be achieved.

A significant trend is absent in the detachment frequency under different fluxes in AC polarity. One possible reason for this can be due to the less adsorption of oxygen at the droplet surface in AC. The adsorbed oxygen may be removed from the droplet surface by the mobile cathode area in the EN cycle. The lower oxygen at the droplet surface in AC will minimize the effect of surface tension on the detachment frequency.

The reduction in arc length under the fluxes with a significant amount of CaF_2 is consistent with Ref. [3], shown in Fig. 5.11. A shorter arc length is consistent for both DCEP and AC. One possible reason for the significant reduction in the arc length with very high CaF_2 (F2, F5) can be the presence of fluorine in the arc cavity. Fluorine has a high ionization potential, this increases the resistivity of the arc leading to the shorter arc for the same current and voltage.

One possible reason for the short-circuit events noted from the voltage signal for fluxes with high CaF_2 can be the low arc stability under these fluxes. Another possible reason for this phenomena can be the momentarily bridging of the conductive slag between the wire tip and molten pool, thus, causing the short-circuit.

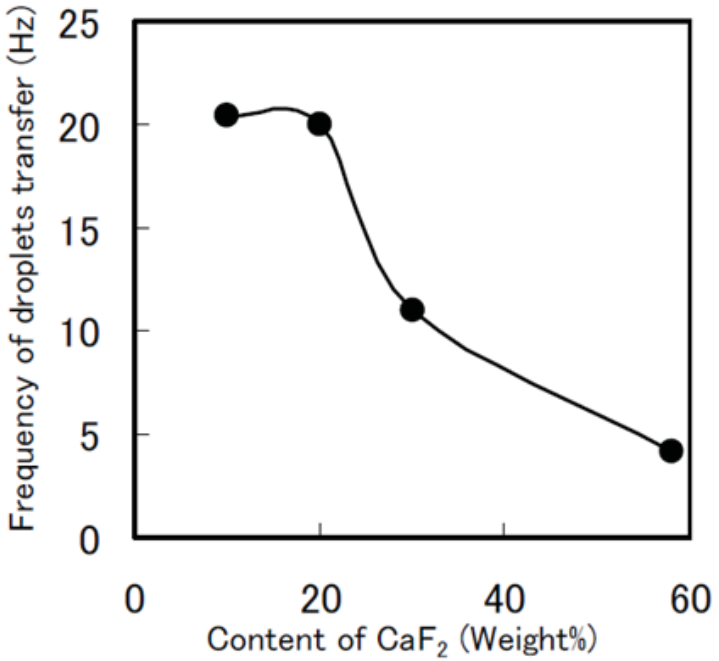

(a) Kasano et al. [11], 1.2 mm wire, 200 A

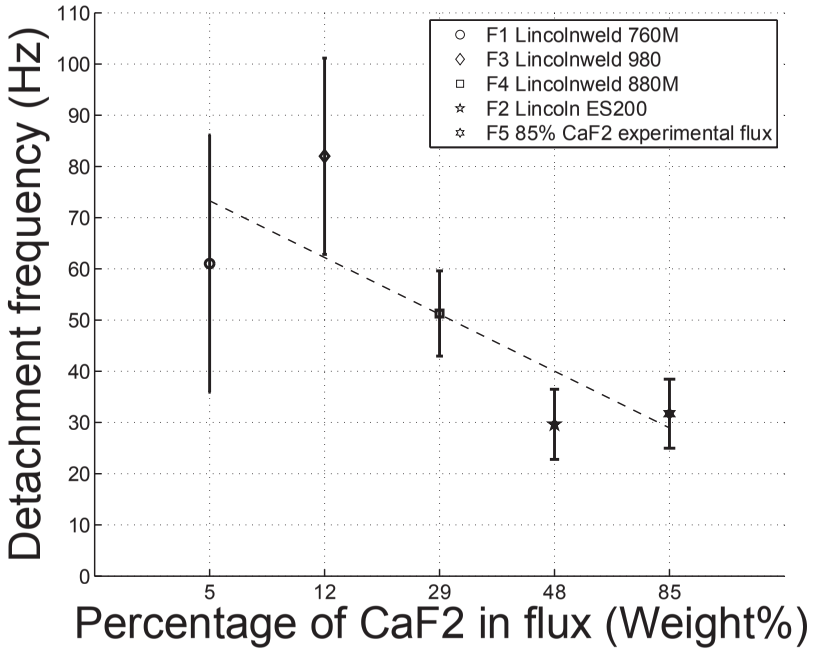

(b) Present study, 3.2 mm wire, 1000 A

Figure 5.10: Comparison of detachment frequency vs percentage of CaF_2 in flux with Kasano et al. [11]. Detachment frequency was found to decrease with increasing CaF_2 in the flux.

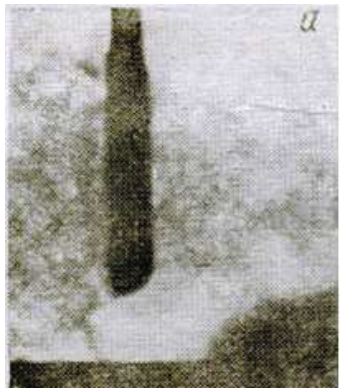

(a) Ostapenko [3], 5 mm wire, 800 A, 48 V, AN-3 (Russian) flux, arc length = 9 mm (X-ray)

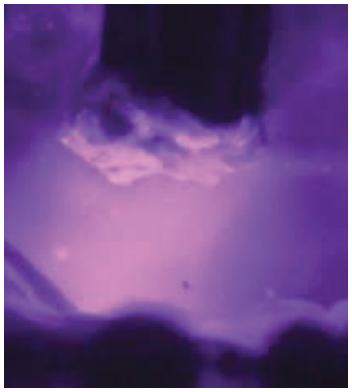

(b) Present study, 3.2 mm (0.19 in) wire, 500 A, 30 V, F1 flux, arc length = 3.72 mm (Optical)

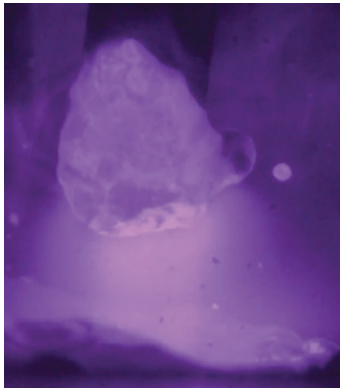

(c) Present study, 3.2 mm wire, 500 A, 30 V, F3 flux, arc length = 3.73 mm (Optical)

(d) Ostapenko [3], 5 mm (0.19 in) wire 800 A, 48 V, OSC-45 (Russian) flux, arc length = 3 mm (X-ray)

(e) Present study, 3.2 mm wire, 500 A, 30 V, F4 flux, arc length = 2.65 mm (optical)

(f) Present study, 3.2 mm wire, 500 A, 30 V, F2 flux, arc length = 2.35 mm (optical)

(g) Present study, 3.2 mm wire, 500 A, 30 V, F5 flux, arc length = 0 mm (optical)

Figure 5.11: Comparison of arc lengths observed under different fluxes with Ostapenko and Medovar [3]. A shorter arc length was observed with fluxes having fluorides compared to fluxes having oxides.

5.7 Conclusions

The effect of fluxes on metal transfer and arc length in submerged arc welding has been captured in high-speed videos. Five different fluxes (Lincolnweld 760, Lincoln ES200, Lincolnweld 980, Lincolnweld 880 M, Experimental flux (85% CaF_2)) was used with a Lincolnweld L-50 (3.2 mm) wire. The fluxes showed a minimal effect on determining the mode of metal transfer.

At 500 A, an irregular shaped droplet is observed under all the fluxes in DCEP. Frequent explosions are observed at the droplet surface with the oxide based fluxes compared to the fluoride based fluxes. Between 600 A and 1000 A DCEP, the metal transfer observed is based on the phenomena of electromagnetic kink instability. The AC experiments show similar features like the DCEP experiments. A mobile cathode area is seen under all fluxes in the EN cycle. Between 600 A and 1000 A AC, under all the fluxes, the detachment morphology is often different in EP and EN cycles of AC. . The detachment in the EP cycle is based on electromagnetic kink instability. In the EN cycle, the detachment takes by explosions. In AC, most of the detachments (approximately 74%) take place in the EP cycle.

In DCEP, the detachment frequency observed under the oxide based fluxes (F1, F3) was higher compared to the fluoride based fluxes (F2, F4, F5). In AC, unlike the DCEP experiments the detachment frequency does not show a noticeable trend. The detachment frequency was found to increase with increasing current under all the fluxes in both DCEP and AC polarities. In DCEP, the increase in the detachment frequency with the increase in current is more pronounced for the fluxes F1 and F3 compared to fluxes F2 and F5.

In DCEP, the droplet diameter was found to be larger under the fluxes F2 and F5 compared to fluxes F1, F3, and F4. In AC, the droplet diameter is comparable under all the fluxes. The droplet diameter decreases with increasing current in both the polarities.

In both DCEP and AC, the arc length was found to be shorter under the fluxes F2, F4, and F5 compared to the fluxes F1, F3. The voltage signal analysis for 500 A, 30 V DCEP showed more frequent short-circuit events under the fluxes F2, F4, and F5 compared to fluxes F1 and F3.

5.8 References

[1] T .W. Eagar. Sources of Weld Metal Oxygen Contamination During Submerged Arc Welding. *Welding Journal research supplement*, 2(March):76–80, 1978.

[2] V. Sengupta and P.F. Mendez. Effect of Current on Metal Transfer in Submerged Arc Welding. Part 1: Technique and DCEP polarity. *Unpublished research work*, 2016.

[3] N.G. Ostapenko and B.I. Medovar. X-ray analysis of submerged arc zone (Russian). *Avtogennoe Delo*, (11):16–20, 1947.

[4] P.G. Grebelnik. X-ray study of the process of automatic submerged arc welding (Russian). *Avtomatich. Svarka*, (6):18–29, 1950.

[5] U. Franz. Vorgänge in der Kaverne beim UP-Schweißen, Teil I (Processes in the cavern during submerged arc welding, Part I). *Schweisstechnik*, 15(4):145–150, 1965.

[6] Gary Martin Peshak. *A radiographic study of the plasma geometry in submerged arc process*. PhD thesis, The Ohio State University, 1965.

[7] Van Th. J. Adrichem. Metal transfer in submerged-arc welding. In *International Institute of Welding Document Number 212-78-66*, Nijmegen, Holland, 1966.

[8] G. Gött, A. Gericke, K.M. Henkel, and D. Uhrlandt. Optical and Spectroscopic Study of a Submerged Arc Welding Cavern. *Welding Journal*, (December):491–499, 2016.

[9] http://www.ualberta.ca/∼ccwj/Publications/WJ_EFMT_SAW/
SOM1: ccwj_000115.002.mp4
SOM2: ccwj_000115.018.mp4
SOM3: ccwj_000115.025.mp4
SOM4: ccwj_000115.043.mp4
SOM5: ccwj_000115.049.mp4
SOM6: ccwj_000115.003.mp4
SOM7: ccwj_000115.015.mp4

SOM8: ccwj_000115.026.mp4
SOM9: ccwj_000115.037.mp4
SOM10: ccwj_000115.055.mp4
SOM11: ccwj_000115.004.mp4
SOM12: ccwj_000115.017.mp4
SOM13: ccwj_000115.027.mp4
SOM14: ccwj_000115.045.mp4
SOM15: ccwj_000115.050.mp4
SOM16: ccwj_000115.010.mp4
SOM17: ccwj_000115.014.mp4
SOM18: ccwj_000115.028.mp4
SOM19: ccwj_000115.039.mp4
SOM20: ccwj_000115.051.mp4
SOM21: ccwj_000115.001.mp4
SOM22: ccwj_000115.013.mp4
SOM23: ccwj_000115.029.mp4
SOM24: ccwj_000115.041.mp4
SOM25: ccwj_000115.052.mp4
SOM26: ccwj_000115.011.mp4
SOM27: ccwj_000115.024.mp4
SOM28: ccwj_000115.030.mp4
SOM29: ccwj_000115.044.mp4
SOM30: ccwj_000115.053.mp4
SOM31: ccwj_000115.005.mp4
SOM32: ccwj_000115.019.mp4
SOM33: ccwj_000115.031.mp4
SOM34: ccwj_000115.048.mp4
SOM35: ccwj_000115.056.mp4
SOM36: ccwj_000115.007.mp4
SOM37: ccwj_000115.020.mp4
SOM38: ccwj_000115.032.mp4
SOM39: ccwj_000115.038.mp4
SOM40: ccwj_000115.057.mp4
SOM41: ccwj_000115.012.mp4
SOM42: ccwj_000115.016.mp4
SOM43: ccwj_000115.033.mp4
SOM44: ccwj_000115.046.mp4
SOM45: ccwj_000115.054.mp4
SOM46: ccwj_000115.008.mp4
SOM47: ccwj_000115.021.mp4
SOM48: ccwj_000115.034.mp4
SOM49: ccwj_000115.040.mp4

SOM50: ccwj_000115.058.mp4
SOM51: ccwj_000115.009.mp4
SOM52: ccwj_000115.022.mp4
SOM53: ccwj_000115.035.mp4
SOM54: ccwj_000115.042.mp4
SOM55: ccwj_000115.059.mp4
SOM56: ccwj_000115.006.mp4
SOM57: ccwj_000115.023.mp4
SOM58: ccwj_000115.036.mp4
SOM59: ccwj_000115.047.mp4
SOM60: ccwj_000115.060.mp4.

[10] J.H. Kim, R H Frost, D L Olson, and M Blander. Effect of Electrochemical Reactions on Submerged Arc Weld Metal Compositions. *Welding Journal*, (December):446–453, 1990.

[11] Kasano Kazuki, Matsunobu Shingo, Uchihara Masato, Hirata Hiroyuki, and Ogawa Kazuhiro. Study on Arc Phenomena of Submerged Arc Welding with Observation Method in Flux (Japanese). *Preprints of the National Meeting of JWS*, 2012s:102–103, 2012.

[12] U Mitra and T W Eagar. Slag-Metal Reactions during Welding : Part II. Theory. *Metallurgical Transactions*, 22B(February):65—-71, 1991.

[13] C. S. Chai and T.W. Eagar. Slag Metal Reactions in Binary CaF2 -Metal Oxide Welding Fluxes. *Welding Journal*, 61(7):S229–S232, 1982.

5.9 Appendix 5.1: Frames from the high-speed videos used to calculate the detachment frequency

The related tables are presented from next page.

Table A5.1: Detachment frames corresponding to high-speed videos (DCEP, 500 A - 700 A

Experiment	**Detachment Frames (DCEP, 500 A - 700 A)**
F1.1 (F1, 500 A, DC)	1184, 2050, 2456, 3292, 3632, 4040, 4694, 6098, 6485, 7471
F2.22 (F2, 500 A, DC)	250, 1396, 3129, 4736, 5748, 7239, 9195, 10653, 12428
F3.1 (F3, 500 A, DC)	261, 1143, 2062, 3157, 4530, 5989, 6145, 7079
F4.7 (F4, 500 A, DC)	765, 1080, 2638, 4155, 5882, 7455, 8628, 10001, 11276, 11693, 12604, 12845, 13486, 13922
F5.1 (F5, 500 A, DC)	3150, 4484, 4986, 5940, 7303, 8810, 10659, 12216, 13384, 14710
F1.16 (F1, 600 A, DC)	635, 1242, 1534, 2084, 3141, 3346, 4200, 4867, 5280, 6168, 6864
F2.16 (F2, 600 A, DC)	555, 1334, 1700, 2430, 2917, 3825, 4274, 5114, 5848, 6459, 6678, 7758, 8657, 9112, 10376, 11267, 12683
F3.2 (F3, 600 A, DC)	292, 577, 816, 1561, 1841, 2087, 2598, 3269, 3933, 4371, 4603, 4854, 5047, 5231, 5696, 5845, 6202, 6526
F4.10 (F4, 600 A, DC)	1219, 1720, 1943, 2405, 2976, 3206, 3292, 4102, 4661, 4731, 5791, 6695, 7142
F5.6 (F5, 600 A, DC)	3265, 3611, 4806, 5423, 6147,6678, 7339, 8039, 8896, 9212, 9671, 10409, 10605, 11101
F1.5 (F1, 700 A, DC)	155, 211, 452, 568, 1043, 1481, 1847, 2115, 2829, 3621, 3893, 4129, 4491, 4870, 5221, 5510, 5611, 5895
F2.2 (F2, 700 A, DC)	114, 384, 1060, 1508, 2010, 2625, 3448, 4156, 4456, 5319, 6083, 6792, 7109
F3.3 (F3, 700 A, DC)	784, 1337, 1932, 2387, 2547, 2745, 2864, 3189, 3985, 4536, 4650, 5366, 5731, 5855, 6279, 6361
F4.9 (F4, 700 A, DC)	3501, 3768, 4687, 4959, 5431, 5944, 6028, 6606, 7141, 7503, 7990, 8053, 8358, 8442, 8722
F5.3 (F5, 700 A, DC)	568, 978, 1747, 2164, 3240, 3861, 4386, 4741, 5505, 5836, 6358, 6398, 6998, 7397, 7720, 7931, 8001, 8446, 8750, 9022, 9386, 9758, 10046, 10766

Table A5.2: Detachment frames corresponding to high-speed videos (DCEP, 800 A - 1000 A)

Experiment	**Detachment Frames (DCEP)**
F1.15 (F1, 800 A, DC)	515, 662, 790, 893, 961, 1175, 1337, 1693, 1893, 2036, 2167, 2301, 2421, 2536, 2658, 2773, 2920, 3042, 3170
F2.15 (F2, 800 A, DC)	529, 760, 993, 1253, 1418, 1740, 2095, 2375, 2743, 3115, 3402, 3652, 3768, 4025, 4128, 4453, 4831, 5057, 5646, 6000, 6569
F3.4 (F3, 800 A, DC)	647, 791, 923, 1249, 1455, 1631, 1816, 1975, 2133, 2222, 2431, 2541, 2671, 2827, 3003, 3168, 3343, 3432, 3636, 3831, 4023, 4102, 4291
F4.4 (F4, 800 A, DC)	456, 699, 765, 992, 1338, 1544, 1637, 1766, 1879, 2061, 2160, 2236, 2703, 2965, 3542, 3810, 3955, 4154, 4445, 4823, 5193, 5409, 5868, 6284
F5.4 (F5, 800 A, DC)	3847, 4123, 4421, 4840, 5111, 5382, 5641, 6149, 6299, 6469, 6676, 6904, 7506, 7819, 8174, 8394
F1.13 (F1, 900 A, DC)	246, 413, 539, 664, 869, 998, 1056, 1173, 1218, 1428, 1644, 1818, 2020, 2316, 2361, 2428, 2892, 2995, 3128, 3564, 3792, 4332, 4745, 5075, 5135, 5480, 5722, 5890
F2.14 (F2, 900 A, DC)	844, 1045, 1246, 1656, 1818, 2002, 2202, 2667, 3064, 3554, 3874, 4088, 4325, 4547, 4707, 5144, 5428, 5780
F3.5 (F3, 900 A, DC)	442, 542, 707, 971, 1009, 1243, 1480, 1738, 1946, 2052, 2155, 2333, 2541, 2831, 3055, 3261, 3616
F4.3 (F4, 900 A, DC)	260, 441, 637, 775, 939, 1346, 1835, 2428, 2627, 3299, 3360, 3393, 3835, 4560, 4932, 5423, 5811, 6127, 6452
F5.5 (F5, 900 A, DC)	156, 509, 849, 1219, 1602, 1935, 2284, 2711, 3055, 3413, 3830, 4246, 4559, 4952, 5349, 5628
F1.7 (F1, 1000 A, DC)	619, 831, 1011, 1129, 1351, 1444, 1577, 1742, 2130, 2587, 3283, 4077, 4359, 4879, 5365
F2.21 (F2, 1000 A, DC)	659, 1085, 1200, 1635, 2389, 2837, 3332, 4511, 5284, 5683, 6358, 6867, 7324
F3.6 (F3, 1000 A, DC)	778, 901, 1038, 1104, 1191, 1260, 1286, 1368, 1435, 1476, 1499, 1517, 1762, 1959, 2093, 2239, 2375, 2533, 2799, 2971, 3140, 3341
F4.8 (F4, 1000 A, DC)	40, 456, 872, 1218, 1562, 1856, 2297, 2474, 2866, 3438, 3746, 3862, 4216, 4613, 4945, 5378, 5675, 6071, 6925, 7436, 7840
F5.17 (F5, 1000 A, DC)	532, 1321, 2312, 3046, 3639, 4321, 4886, 5520, 6062, 6228, 6689, 7467

Table A5.3: Detachment frames corresponding to high-speed videos (AC, 500 A - 700 A)

Experiment	Detachment Frames (AC)
F1.10 (F1, 500 A, AC)	472, 729 (EN), 1665, 1829, 2519, 2964, 3750 (EN), 4370 (EN), 5032, 5741, 6053 (EN), 6698, 7193, 8017, 8615
F2.11 (F2, 500 A, AC)	911, 1634, 1713, 2349, 2625, 3145, 3464, 3812, 4152
F3.7 (F3, 500 A, AC)	1935, 2166 (EN), 2738 (EN), 3043, 3143, 3420, 4083 (EN)
F4.12 (F4, 500 A, AC)	91 , 496, 597, 760, 982, 1585, 2198, 2883, 4207, 4547, 5785, 6494, 6581, 6739, 7419, 7728 (EN), 8091, 8731
F5.16 (F5, 500 A, AC)	9387, 9579, 10267, 10655, 11122, 12237, 13547, 14458, 16268 16590
F1.17 (F1, 600 A, AC)	240 (EN), 308, 345, 570 (EN), 613, 1151, 1531, 1824, 2026 (EN), 2369, 2676, 3250, 3635, 4450, 4733 (EN), 5312 (EN)
F2.18 (F2, 600 A, AC)	354, 683, 1654, 2320, 2668 (EN), 2973, 3270, 3597, 4087, 4562, 4805, 5156, 5272, 5486, 5805, 5994, 6477, 6921, 7150
F3.8 (F3, 600 A, AC)	2073, 2563, 2770, 3356 (EN), 3600, 3884 (EN), 3988, 4191, 4455, 4634, 4822, 5030 (EN), 5052, 5279, 5481 (EN), 5718, 5793, 5902, 6015, 6200 (EN)
F4.11 (F4, 600 A, AC)	775, 974, 2164, 2355, 2629 (EN), 2917, 3315, 3668, 4335, 4698, 4955 (EN), 5136 (EN), 5600, 6134, 6299 (EN), 6651, 6991, 7278 (EN), 7529, 7757, 7926, 8023
F5.9 (F5, 600 A, AC)	1941, 2160, 2871, 3150 (EN), 3965, 4536, 4978, 5489, 6506, 6821, 7122, 7670, 7938
F1.9 (F1, 700 A, AC)	2439 (EN), 2541, 2616, 2721, 3087, 3266, 4720, 4930, 5515 (EN), 6044, 6830 (EN), 6912, 7406, 7916 (EN), 8118 (EN), 8402, 8733, 9495 (EN)
F2.9 (F2, 700 A, AC)	345, 520 (EN), 758, 1001, 1138, 1329, 1730, 1885 (EN), 2350, 2540, 2741, 3181 (EN), 3701 (EN), 4205, 4380, 4525, 4746, 5100, 5550
F3.9 (F3, 700 A, AC)	107, 249, 436, 589, 773, 1054 (EN), 1095, 1121 (EN), 1575, 2213, 2543, 2585, 2898, 3383, 3600, 3761, 4015 (EN), 4205, 4237, 4448, 4616
F4.13 (F4, 700 A, AC)	280, 567, 666, 887, 957, 1209, 1415, 1568 (EN), 1801, 2113 (EN), 2250 (EN), 2547, 2797, 3084 (EN), 3230, 3397, 3567 (EN), 3798, 3949, 3994, 4610 (EN), 4736 (EN), 4914 (EN), 5259
F5.10 (F5, 700 A, AC)	390, 533, 856, 992, 1130, 1176, 1319, 1592, 1688, 1865, 1968 (EN), 2018, 2159 (EN), 2238, 2326 (EN), 2513, 2799 (EN), 2843, 3014, 3330 (EN), 3491 (EN), 3867, 4160 (EN) , 4389, 4537, 4891, 5237, 5402, 5677, 5893, 6807

Table A5.4: Detachment frames corresponding to high-speed videos (AC, 800 - 1000 A)

Experiment	Detachment Frames (AC)
F1.18 (F1, 800 A, AC)	261, 301, 416, 584, 730, 776, 896, 1099, 1263, 1394, 1584, 1756, 2018 (EN), 2276, 2511, 2712 (EN), 2864 (EN), 2906, 2983 (EN), 3109, 3349 (EN), 3578, 3817 (EN), 4015 (EN), 4745, 4974, 5136, 5267, 5437
F2.13 (F2, 800 A, AC)	985, 1141, 1281, 1700, 1909, 2103, 2322, 2432, 2579 (EN), 2681 (EN), 2858 (EN), 3037 (EN), 3197 (EN), 3350 (EN), 3500, 3556, 3762, 3873 (EN), 4114, 4531
F3.10 (F3, 800 A, AC)	2674, 2750, 3086, 3282 (EN), 3462 (EN), 3664, 3960 (EN), 4133 (EN), 4241, 4483, 4560, 4737, 4937, 4967, 5289, 5494
F4.5 (F4, 800 A, AC)	122, 279 (EN), 353, 417, 445, 503, 578 (EN), 630, 670, 785, 807, 829, 851, 932, 1071 (EN), 1112, 1260 (EN), 1493, 1656, 1828, 2047, 2311, 2504, 2630, 2799, 2992, 3226 (EN), 3634, 3769 (EN), 3938 (EN), 4240 (EN)
F5.11 (F5, 800 A, AC)	455, 790, 1280, 1490, 1935 (EN), 2102, 2386, 2626, 2686, 2784, 2968, 3053 (EN), 3293, 3438, 3722, 3943, 4169, 4323, 4723, 5316, 5542, 5849
F1.19 (F1, 900 A, AC)	127, 277, 396 (EN), 426, 554 (EN), 708 (EN), 785, 978, 1086, 1109, 1238 (EN), 1395 (EN), 1423, 1518 (EN), 1592, 1742 (EN), 1813, 1931, 2056 (EN), 2251 (EN), 2453, 2482, 2735 (EN), 2984, 3158, 3429, 3720, 4101, 4231 (EN), 4422
F2.12 (F2, 900 A, AC)	574, 623, 860, 1060 (EN), 1223 (EN), 1371, 1547, 1673, 1891 (EN), 2397 (EN), 2452, 2619, 2818, 2987, 3086 (EN), 3236 (EN), 3465, 3565 (EN), 3619, 3742 (EN), 3787, 3958, 4067 (EN)
F3.11 (F3, 900 A, AC)	948 (EN), 1006, 1111 (EN), 1177, 1223, 1348, 1388, 1504, 1539, 1561, 1601 (EN), 1674, 1814 (EN), 1855, 2040, 2211, 2355, 2481 (EN), 2508, 2620 (EN), 2751, 2945 (EN), 3115 (EN), 3242
F4.2 (F4, 900 A, AC)	508, 567, 664, 716, 742, 836 (EN), 875, 998, 1177, 1213, 1235, 1295 (EN), 1333, 1386, 1422, 1473 (EN), 1506, 1538, 1561, 1635 (EN), 1683, 1825 (EN), 1893, 1911, 2007, 2194, 2288 (EN), 2339, 2501 (EN) , 2669, 2827 (EN), 3208, 3423, 3558, 4275 (EN), 4525, 4603 (EN), 4835
F5.12 (F5, 900 A, AC)	47, 236, 417, 597, 761, 904, 1091, 1207, 1400, 1561, 1709, 1932, 2038, 2189 (EN) , 2342 (EN), 2385, 2490 (EN), 2718, 2905, 3077, 3216, 3352 (EN), 3403, 3521 (EN), 3656 (EN), 3742, 3942, 4092, 4208 (EN), 4351 (EN), 4510
F1.11 (F1, 1000 A, AC)	1184, 1237, 1290, 1510, 1591, 1655, 1873, 1928, 1992, 2296, 2538, 2616, 2671, 2770 (EN), 2900, 2943, 2977, 3118 (EN), 3241, 3275, 3306, 3452 (EN), 3546, 3763 (EN), 3871, 4028 (EN), 4122 (EN), 4180, 4377 (EN), 4442 (EN), 4848, 5101 (EN), 5175, 5441 (EN), 5597, 5891, 6287, 6608
F2.20 (F2, 1000 A, AC)	1612, 1814, 1936, 2115, 2687, 2958, 3213 (EN), 3624, 3936, 4282, 4504 (EN), 4620, 4808 (EN), 5063, 5221 (EN), 5501 (EN), 5809(EN), 5976, 6157 (EN), 6286, 6530 (EN), 6676, 6865 (EN), 6929, 7359
F3.12 (F3, 1000 A, AC)	88, 377 (EN), 476, 597, 692 (EN), 846, 974, 1089, 1175, 1382, 1429, 1504, 1595, 1888 (EN), 1952, 2198 (EN), 2261, 2402 (EN), 2434, 2523 (EN), 2717 (EN), 2886 (EN), 2972
F4.15 (F4, 1000 A, AC)	7 , 240 (EN), 511, 660, 887 (EN), 1251 (EN), 1415, 1522, 1908 (EN), 1985, 2268 (EN), 2588 (EN), 2732, 3050, 3432, 3793, 3979, 4260 (EN), 4549 (EN), 4884 (EN), 5228 (EN), 5335, 5717, 6051, 6635, 6842, 7092
F5.13 (F5, 1000 A, AC)	476, 762, 1183, 1397, 1627 (EN), 1814, 1890, 2082, 2396, 2489, 2761, 3012 (EN), 3124, 3377 (EN), 3923, 4120, 4364 (EN), 4683 (EN), 4960 (EN), 5067, 5385, 5682, 5854, 6082, 6451, 6834

5.10 Appendix 5.2: Frames from the high-speed videos used to calculate the arc length

The related tables are presented from next page.

Table A5.5: Frames used to measure arc length under different fluxes for DCEP-SAW experiments

Experiment	**Frames used to measure arc length**
F1.1 (F1, 500 A, DC)	575, 2100, 3654, 4100, 6829
F2.22 (F2, 500 A, DC)	2006, 2766, 2992, 3280, 4836, 7571
F3.1 (F3, 500 A, DC)	1563, 3216, 4973, 6534, 3681
F4.7 (F4, 500 A, DC)	120, 2323, 2818, 3478, 5058, 6646, 7622, 11086, 14459
F5.1(F5, 500 A, DC)	6516, 7418, 8546, 8702, 9047, 10323, 10533, 10844, 11435
F1.16 (F1, 600 A, DC)	1660, 2303, 3392, 4334, 5750
F2.16 (F2, 600 A, DC)	1537, 1808, 2508, 2998, 6011, 6885
F3.2 (F3, 600 A, DC)	664, 2641, 4417, 5237, 6579
F4.10 (F4, 600 A, DC)	1453, 3156, 3837, 4770, 6002
F5.6 (F5, 600 A, DC)	1895, 2186, 3789, 5039, 5491, 6245, 6787, 7432, 8112
F1.5 (F1, 700 A, DC)	303, 1942, 2071, 4021, 6568
F2.2 (F2, 700 A, DC)	1219, 1420, 1660, 2194, 4288, 5474
F3.3 (F3, 700 A, DC)	1798, 1968, 2400, 4025, 6289
F4.9 (F4, 700 A, DC)	3346, 3812, 4543, 5532, 7233
F5.3 (F5, 700 A, DC)	2820, 3423, 4080, 4560, 5093, 5794, 6473, 6702, 7778, 9450
F1.15 (F1, 800 A, DC)	42, 1571, 1978, 2346, 3689
F2.15 (F2, 800 A, DC)	420, 907, 1925, 4170, 4616, 5236
F3.4 (F3, 800 A, DC)	1722, 2231, 2543, 3125, 3654
F4.4 (F4, 800 A, DC)	884, 1979, 2773, 3295, 4549, 6369
F5.4 (F5, 800 A, DC)	3716, 4152, 5244, 5429, 6316, 6945, 7551, 8315
F1.13 (F1, 900 A, DC)	1536, 1874, 2384, 3080, 3280
F2.14 (F2, 900 A, DC)	928, 1092, 1396, 2076, 2595, 3167
F3.5 (F3, 900 A, DC)	1144, 1394, 1931, 2614, 3655
F4.3 (F4, 900 A, DC)	1189, 1911, 2694, 3507, 4660
F5.5 (F5, 900 A, DC)	1717, 2057, 2416, 2883, 3256, 3520, 3930, 4348, 4659, 5075
F1.7 (F1, 1000 A, DC)	1267, 1360, 1621, 1943, 2256
F2.21 (F2, 1000 A, DC)	1749, 2503, 3410, 4635, 5620
F3.6 (F3, 1000 A, DC)	1218, 1815, 2396, 3063, 3187
F4.8 (F4, 1000 A, DC)	119, 551, 1904, 2998, 4733, 6244
F5.17 (F5, 1000 A, DC)	599, 1528, 1883, 2431, 2781, 3192, 3878, 4481, 5228, 5744

Table A5.6: Frames used to measure arc length under different fluxes for AC-SAW experiments

Experiment	**Frames used to measure arc length**
F1.10 (F1, 500 A, AC)	421, 1968, 3921, 5610, 6106
F2.11 (F2, 500 A, AC)	189, 581, 693, 1352, 1876
F3.7 (F3, 500 A, AC)	2266, 2591, 2801, 3073
F4.12 (F4, 500 A, AC)	120, 629, 1072, 2610, 4286
F5.16 (F5, 500 A, AC)	1747, 9579, 10061, 10162, 11785
F1.17 (F1, 600 A, AC)	361, 1911, 1969, 3645, 3944
F2.18 (F2, 600 A, AC)	25, 758, 858, 1808, 5192
F3.8 (F3, 600 A, AC)	4556, 4670, 6264, 6548, 6722
F4.11 (F4, 600 A, AC)	845, 1394, 1689, 3494, 4476
F5.9 (F5, 600 A, AC)	2002, 2201, 2658, 4186, 5831
F1.9 (F1, 700 A, AC)	3825, 4148, 4542, 6210, 6421
F2.9 (F2, 700 A, AC)	364, 768, 2406, 2938, 4485
F3.9 (F3, 700 A, AC)	2259, 2654, 2913, 3659, 4248
F4.13 (F4, 700 A, AC)	151, 345, 591, 2291, 3828
F5.10 (F5, 700 A, AC)	439, 887, 1034, 2859, 4551
F1.18 (F1, 800 A, AC)	395, 1935, 2103, 2317, 2558
F2.13 (F2, 800 A, AC)	935, 1163, 1748, 1946, 3600
F3.10 (F3, 800 A, AC)	3124, 3517, 3691, 3933, 5594
F4.5 (F4, 800 A, AC)	538, 1087, 1743, 1948, 2132
F5.11 (F5, 800 A, AC)	2114, 2443, 2713, 3069, 4634
F1.19 (F1, 900 A, AC)	187, 2097, 2298, 2592, 2930
F2.12 (F2, 900 A, AC)	639, 921, 1388, 1621, 1908
F3.11 (F3, 900 A, AC)	372, 529, 751, 2302, 2526
F4.2 (F4, 900 A, AC)	763, 1030, 1300, 1931, 3714
F5.12 (F5, 900 A, AC)	1139, 1242, 1433, 2963, 3095
F1.11 (F1, 1000 A, AC)	2252, 2552, 2994, 3589, 3897
F2.20 (F2, 1000 A, AC)	2301, 2701, 2969, 3949, 4468
F3.12 (F3, 1000 A, AC)	214, 280, 480, 878, 1118
F4.15 (F4, 1000 A, AC)	731, 1337, 1550, 2020, 2346
F5.13 (F5, 1000 A, AC)	2113, 2518, 2779, 4416, 4771

5.11 Appendix 5.3: Detachment frequency and droplet diameter for all experiments

Table A5.7: Detachment frequency and droplet diameter for all DCEP-SAW experiments

Experiment	Average detachment frequency (Hz)	Average droplet diameter (mm)
F1.1 (F1, 500 A, DC)	14.32 ± 5.95	3.09 ± 0.42
F2.22 (F2, 500 A, DC)	6.73 ± 1.22	4.11 ± 0.25
F3.1 (F3, 500 A, DC)	12.31 ± 5.55	3.58 ± 0.36
F4.7 (F4, 500 A, DC)	9.88 ± 3.04	3.43 ± 0.35
F5.1(F5, 500 A, DC)	7.79 ± 1.66	3.91 ± 0.28
F1.16 (F1, 600 A, DC)	16.05 ± 4.78	3.13 ± 0.31
F2.16 (F2, 600 A, DC)	13.19 ± 2.86	3.45 ± 0.25
F3.2 (F3, 600 A, DC)	27.27 ± 6.84	2.68 ± 0.22
F4.10 (F4, 600 A, DC)	20.26 ± 7.79	2.88 ± 0.37
F5.6 (F5, 600 A, DC)	16.59 ± 4.12	3.22 ± 0.27
F1.5 (F1, 700 A, DC)	26.28 ± 7.59	2.88 ± 0.28
F2.2 (F2, 700 A, DC)	17.16 ± 3.57	3.38 ± 0.23
F3.3 (F3, 700 A, DC)	26.90 ± 6.34	2.91 ± 0.23
F4.9 (F4, 700 A, DC)	26.81 ± 9.26	2.85 ± 0.33
F5.3 (F5, 700 A, DC)	22.55 ± 5.08	3.11 ± 0.23
F1.15 (F1, 800 A, DC)	67.80 ± 13.63	2.23 ± 0.15
F2.15 (F2, 800 A, DC)	33.11 ± 6.17	2.90 ± 0.18
F3.4 (F3, 800 A, DC)	62.46 ± 9.08	2.32 ± 0.11
F4.4 (F4, 800 A, DC)	39.46 ± 9.23	2.69 ± 0.21
F5.4 (F5, 800 A, DC)	32.99 ± 7.17	2.90 ± 0.21
F1.13 (F1, 900 A, DC)	47.84 ± 12.24	2.67 ± 0.23
F2.14 (F2, 900 A, DC)	34.44 ± 6.66	2.99 ± 0.19
F3.5 (F3, 900 A, DC)	53.21 ± 11.78	2.60 ± 0.19
F4.3 (F4, 900 A, DC)	29.07 ± 9.20	3.15 ± 0.33
F5.5 (F5, 900 A, DC)	27.35 ± 1.70	3.26 ± 0.07
F1.7 (F1, 1000 A, DC)	61.03 ± 25.11	2.56 ± 0.35
F2.21 (F2, 1000 A, DC)	29.64 ± 6.85	3.35 ± 0.26
F3.6 (F3, 1000 A, DC)	81.94 ± 19.17	2.37 ± 0.18
F4.8 (F4, 1000 A, DC)	51.28 ± 8.32	2.73 ± 0.15
F5.17 (F5, 1000 A, DC)	31.72 ± 6.47	3.29 ± 0.23

Table A5.8: Detachment frequency and droplet diameter for all AC-SAW experiments

Experiment	**Average detachment frequency (Hz)**	**Average droplet diameter (mm)**
F1.10 (F1, 500 A, AC)	21.09 ± 6.84	2.88 ± 0.31
F2.11 (F2, 500 A, AC)	22.18 ± 7.84	2.90 ± 0.34
F3.7 (F3, 500 A, AC)	27.93 ± 15.29	2.66 ± 0.48
F4.12 (F4, 500 A, AC)	19.68 ± 6.97	2.93 ± 0.34
F5.16 (F5, 500 A, AC)	12.49 ± 6.29	3.53 ± 0.59
F1.17 (F1, 600 A, AC)	26.00 ± 7.58	2.95 ± 0.28
F2.18 (F2, 600 A, AC)	32.21 ± 9.88	2.72 ± 0.28
F3.8 (F3, 600 A, AC)	41.87 ± 10.15	2.46 ± 0.23
F4.11 (F4, 600 A, AC)	28.97 ± 8.76	2.82 ± 0.28
F5.9 (F5, 600 A, AC)	20.01 ± 5.98	3.22 ± 0.32
F1.9 (F1, 700 A, AC)	24.09 ± 10.15	3.20 ± 0.45
F2.9 (F2, 700 A, AC)	34.58 ± 7.90	2.82 ± 0.21
F3.9 (F3, 700 A, AC)	44.36 ± 14.24	2.61 ± 0.28
F4.13 (F4, 700 A, AC)	46.19 ± 10.57	2.54 ± 0.19
F5.10 (F5, 700 A, AC)	46.75 ± 13.14	2.59 ± 0.24
F1.18 (F1, 800 A, AC)	54.10 ± 15.96	2.56 ± 0.25
F2.13 (F2, 800 A, AC)	53.58 ± 12.48	2.59 ± 0.24
F3.10 (F3, 800 A, AC)	53.19 ± 13.44	2.59 ± 0.20
F4.5 (F4, 800 A, AC)	72.85 ± 18.19	2.30 ± 0.22
F5.11 (F5, 800 A, AC)	38.93 ± 8.53	2.90 ± 0.21
F1.19 (F1, 900 A, AC)	65.19 ± 11.44	2.53 ± 0.15
F2.12 (F2, 900 A, AC)	62.98 ± 16.64	2.60 ± 0.23
F3.11 (F3, 900 A, AC)	74.03 ± 40.96	2.45 ± 0.45
F4.2 (F4, 900 A, AC)	85.51 ± 30.88	2.29 ± 0.27
F5.12 (F5, 900 A, AC)	67.22 ± 7.28	2.54 ± 0.09
F1.11 (F1, 1000 A, AC)	132.74 ± 29.29	2.07 ± 0.15
F2.20 (F2, 1000 A, AC)	80.04 ± 15.30	2.48 ± 0.16
F3.12 (F3, 1000 A, AC)	76.28 ± 18.64	2.53 ± 0.21
F4.15 (F4, 1000 A, AC)	73.39 ± 12.05	2.53 ± 0.14
F5.13 (F5, 1000 A, AC)	78.64 ± 13.76	2.53 ± 0.15

Chapter 6

Conclusions and Future Work

6.1 Conclusions and Summary of Findings

A technique has been developed to capture the phenomena in the weld zone of SAW in high-speed videos. The technique involves penetrating the flux bed of SAW by a tunnel made of thin-sheet material. The videos are recorded at 10,000 and 20,000 frames per second. The thesis presents for the first time the effect of current on metal transfer in SAW for both DCEP and AC polarities. Additionally, the effect of five fluxes on metal transfer and arc length in SAW for both DCEP and AC polarities is presented for the first time.

The research began by carrying out an exhaustive literature review of the work done in understanding the weld zone in SAW for over 80 years. The review focused on the research into the metal transfer, the arc length, the arc cavity and slag shell, and the dynamics of the weld pool in SAW. The key findings of the review are as follows:

- **Metal transfer:** The metal transfer in SAW was found to be in free flight mode. Short-circuit metal transfer was not observed. Current has a significant effect on the metal transfer. At low current, the metal transfer was found to be chaotic globular. At high currents, a metal transfer based on electromagnetic kink instability was

reported. The voltage was found to have minimal effect on the metal transfer. It was found that on increasing voltage, the ratio of slag/free transfer increases. Also, the fluxes were found to have minimal effect on determining the metal transfer. Fluxes with high CaF_2 showed a lower detachment frequency compared to fluxes with oxides.

The reactions at the droplet attached to the wire were also studied. It was concluded that due to the high temperature of the droplet, the oxygen from the flux gets adsorbed at the droplet. The adsorbed oxygen prevents carbon and other elements from reaching the surface and react. Possibilities of electrochemical reactions at the droplet and the weld pool were also suggested.

- **Arc length:** SAW takes place by forming an arc. The increase in current was found to decrease the arc length for the same voltage. The increase in voltage was found to increase the arc length. The composition of the fluxes was found to have an effect on the arc length. A flux providing arc stabilizers increased the arc length.

- **Arc cavity and slag shell:** SAW takes place by forming an arc cavity which is surrounded by a slag shell. The cavity has a pressure which is higher than the atmospheric pressure. The atmosphere of the arc cavity is determined by the composition of the fluxes used. Gases like SiO_2, MnO, SiF_4, CO, HF, H_2, etc. has been reported. A unanimous conclusion on the atmosphere of the arc cavity was not reported. Most of the researcher except one believed that there is a slag shell surrounding the arc cavity.

- **Dynamics of weld pool:** For high heat input welding, the molten metal is seen to flow towards the tail of the pool. The molten metal then turns back to form a secondary surface flow towards the welding direction. For high-speed SAW, both

the surface and the bottom flows were found to be directed towards the end of the pool. The bottom flows turned upwards, and the surface flows turned downwards to combine into one center flow. There was no consistency on the magnitude of the velocity of the flows reported by different researchers.

The developed technique is used to capture the effect of current on metal transfer in SAW for a 3.2 mm wire with Lincolnweld 980 flux for both DCEP and AC polarities. For the DCEP experiments, At 500 A, a very chaotic irregular shaped droplet with chaotic, non-axial metal transfer is observed. Between 600 A and 1000 A, a tapering electrode tip was observed ejecting a molten tail through a mechanism resembling an electromagnetic kink instability. The electromagnetic kink instability results in a "whipping tail" kind of detachment of the molten metal as observed in the videos. A detachment frequency of approximately 9 Hz was observed for 500 A. Between 600 A and 1000 A, the detachment frequency increases approximately from 27 Hz to 82 Hz.

A comparison of the observations with the one done by previous researchers using non-disruptive X-ray and other optical techniques shows excellent similarity in the metal transfer under similar conditions thus supporting the methodology utilized.

The metal transfer in AC was found to be similar to the DCEP experiments. The key feature for AC is the electrode negative (EN) cycle in which a very irregular shaped droplet is observed. A moving cathode area is seen on the droplet surface. Droplet detachment is affected by current and polarity. The detachment frequency increased from 28 Hz at 500 A to 76 Hz at 1000 A. Most detachments (approximately 72%) are in EP cycle. The detachment morphology is often different in EP and EN cycle. At 500 A, the detachment in the EP cycle takes place without forming a tail. Between 600 A and 1000 A, the detachment in the EP cycle is based on the electromagnetic kink instability. The electromagnetic kink instability results in a "whipping tail" kind of detachment of

the molten metal as observed in the videos. In the EN cycle, the detachment takes place through explosions.

For both DCEP and AC experiments, the high-speed videos showed that penetration mode changes gradually from recirculating to gouging region penetration; this behavior is consistent with results of previous non-disruptive experiments using radioactive tracers. Analysis of the cross-sections showed that penetration increased with current. The presence of the tunnel had a small but measurable effect on the weld cross-sections, resulting in wider and shallower beads under the tunnel.

The effect of fluxes on metal transfer and arc length are captured in high-speed videos for both DCEP and AC polarities and between 500 A and 1000 A. Five different fluxes, Lincolnweld 760, Lincoln ES200, Lincolnweld 980, Lincolnweld 880 M, and an experimental flux (with 85% CaF_2) was used with a Lincolnweld L-50 (3.2 mm) wire.

At 500 A, an irregular shaped droplet is observed under all the fluxes in DCEP. Frequent explosions are observed at the droplet surface with the oxide based fluxes compared to the fluoride based fluxes. Between 600 A and 1000 A DCEP, the metal transfer observed is based on the phenomena of electromagnetic kink instability. The AC experiments show similar features like the DCEP experiments. A mobile cathode area is seen under all fluxes in the EN cycle. Between 600 A and 1000 A AC, under all the fluxes, the detachment morphology is often different in EP and EN cycles of AC. . The detachment in the EP cycle is based on electromagnetic kink instability. In the EN cycle, the detachment takes by explosions. In AC, most of the detachments (approximately 74%) take place in the EP cycle.

In DCEP, the detachment frequency observed under the oxide based fluxes (F1, F3) was higher compared to the fluoride based fluxes (F2, F4, F5). In AC, unlike the DCEP experiments the detachment frequency does not show a noticeable trend. The detachment frequency was found to increase with increasing current under all the fluxes in both DCEP

and AC polarities. In DCEP, the increase in the detachment frequency with the increase in current is more pronounced for the fluxes F1 and F3 compared to fluxes F2 and F5. In DCEP, the droplet diameter was found to be larger under the fluxes F2 and F5 compared to fluxes F1, F3, and F4. In AC, the droplet diameter is comparable under all the fluxes. The droplet diameter decreases with increasing current in both the polarities.

In both DCEP and AC, the arc length was found to be shorter under the fluxes F2, F4, and F5 compared to the fluxes F1, F3. The voltage signal analysis for 500 A, 30 V DCEP showed more frequent short-circuit events under the fluxes F2, F4, and F5 compared to fluxes F1 and F3.

Understanding the effect of current and fluxes on metal transfer and arc length in SAW will open doors for producing complex waveforms and alter flux formulations in the future.

6.2 Future work

- Understand the effect of balance in the AC waveform on the detachment frequency in the AC polarity.
- From the high-speed videos, study the droplet surface for slag patches or films.
- Understand the effect of different current densities on the metal transfer in SAW for DCEP and AC polarities. The different current densities can be obtained by using wires with different diameters.
- Developing custom waveforms for SAW.

Bibliography

[1] V.V. Podgaetskii. Reactions in arc atmosphere in submerged arc welding. *Avtomatich. Svarka*, (1):10–12, 1953.

[2] I.K. Pokhodnya. A method of investigating the processes of melting and transfer of electrode metal during welding. *Automatic Welding*, (2):1–10, 1964.

[3] U. Franz. Vorgänge in der Kaverne beim UP-Schweißen, Teil I (Processes in the cavern during submerged arc welding, Part I). *Schweisstechnik*, 15(4):145–150, 1965.

[4] Patricio F. Mendez, Gregor Goett, and Stuart D. Guest. High Speed Video of Metal Transfer in Submerged Arc Welding. In *International Institute of Welding Document Number 212-1345-14*, Seoul, South Korea, 2014.

[5] V. Sengupta and P.F. Mendez. Effect of Current on Metal Transfer in Submerged Arc Welding. Part 1: Technique and DCEP polarity. *Unpublished research work*, 2016.

[6] P.G. Grebelnik. X-ray study of the process of automatic submerged arc welding (Russian). *Avtomatich. Svarka*, (6):18–29, 1950.

[7] Gary Martin Peshak. *A radiographic study of the plasma geometry in submerged arc process*. PhD thesis, The Ohio State University, 1965.

[8] H Tanheim. Die physikalisch-chemischen Grundlagen des Ellira-Verfahrens. *Elektroschweißung*, 2:17–24, 1942.

[9] N.G. Ostapenko and B.I. Medovar. X-ray analysis of submerged arc zone (Russian). *Avtogennoe Delo*, (11):16–20, 1947.

[10] B.E. Paton. The process of melting the electrode in the automatic submerged arc welding (Russian). 1949.

[11] Friedrich Eichhorn and Arnold Engel. *Dynamisches Verhalten der Unterpulver-Schweißzone*. Number 2391. VS Verlag für Sozialwissenschaften, Wiesbaden, 1974.

[12] Arnold Engel. *Beitrag zur Prozeßanalyse beim Unterpulverschweißen mit Drahtelektrode*. PhD thesis, RWTH, Aachen, 1972.

[13] Uwe Reisgen, Konrad Willms, Rahul Sharma, and Johannes Schaefer. Diagnostic process analysis of the submerged-arc by welding high-strength fine-grained structural steels. In *International Institute of Welding Document Number 212-2205-15*, Helsinki, Finland, 2015.

[14] U Reisgen, J Schäfer, and K Willms. Analysis of the submerged arc in comparison between a pulsed and non-pulsed process. *Welding in the World*, 2016.

[15] V .G. Kuzmenko. Continuity of slag shell in submerged arc welding. *Avtomatich. Svarka*, 3:14–19, 1998.

[16] V .G. Kuzmenko. Integrity of the slag envelope in submerged-arc welding. *The Paton Welding Journal*, 10(3):119–124, 1998.

[17] Nishiyama Noboru Junichiro Tsuboi Terashima, Hisaei. Influence of Slag Basicity on Deoxidation in Submerged-Arc Welding. *Journal of the Japan Welding Society*, 46(3):57–63, 1977.

[18] G. Gött, A. Gericke, K.M. Henkel, and D. Uhrlandt. Optical and Spectroscopic Study of a Submerged Arc Welding Cavern. *Welding Journal*, (December):491–499, 2016.

[19] F. Eichhorn, P. Hirsch, and Holbach P. Physical and chemical processes taking place in the arc cavity and weld pool during the submerged arc welding of aluminium materials. In *International Conference London*, pages 311–321, London, 1980.

[20] V .G. Kuzmenko. On the Subject of Electric Submerged-Arc Welding. *The Paton Welding Journal*, (5):8–12, 2011.

[21] V .G. Kuzmenko, V.I. Galinich, and Tokarev V.S. Characteristic zones of the weld pool in submerged arc welding. *The Paton Welding Journal*, 9(5):24–27, 1997.

[22] Takeshi Nishi, Haruo Fujita, Sumichika Haseba, and Masahiro Ohara. Study on High Speed Submerged Arc Welding (Report 1) (Japanese). *Journal of the Japan Welding Society*, 51(8):686–692, 1982.

[23] Naomichi Mori and Yukihiko Horii. Molten pool phenomena in Submerged Arc Welding. In *IIW Doc. 212-188-70*, 1970.

[24] Patricio F. Mendez, Gregor Goett, and Stuart D. Guest. High Speed Video of Metal Transfer in Submerged Arc Welding. *Welding Journal*, 94(October):326–333, 2015.

[25] Hugo J De Blank. MHD Instabilities in Tokamaks. *Transactions of Fusion Science and Technology*, 57(2):124–138, 2010.

[26] Kasano Kazuki, Matsunobu Shingo, Uchihara Masato, Hirata Hiroyuki, and Ogawa Kazuhiro. Study on Arc Phenomena of Submerged Arc Welding with Observation Method in Flux (Japanese). *Preprints of the National Meeting of JWS*, 2012s:102–103, 2012.

[27] Van Th. J. Adrichem. Metal transfer in submerged-arc welding. In *International Institute of Welding Document Number 212-78-66*, Nijmegen, Holland, 1966.

[28] T .W. Eagar. Sources of Weld Metal Oxygen Contamination During Submerged Arc Welding. *Welding Journal research supplement*, 2(March):76–80, 1978.

[29] E.O. Paton. *Automatische LichtbogenschweiSSung*. VEB Carl Marhold Verlag, Halle (Saale), 1958.

[30] Bob Irving. Blockbuster Events (Welding's vital part in major American historical events). *Welding Journal*, 1999.

[31] http://paton.kiev.ua/en/about-us/history/884-gody 1934-1950.

[32] Slavyanov N.G. Electric casting of metals, a guide for equipment and practical application (Russian). Technical report, St. Petersburg, 1892.

[33] B.E. Paton. State of the art of automatic submerged arc welding as the result of development of N.G. Slavyanov's ideas (Russian). In *Sci.-Techn. Conf. of Welders, Dedicated to the 100th Anniversary of N.G. Slavyanov.*, Kiev, 1955. Mashgiz.

[34] E.O. Paton. Development of automatic submerged arc welding during 10 years (Russian). *Avtogennoe Delo*, (2):1–3, 1951.

[35] DA Dulchevskogo. Method of electric arc welding of copper, Soviet patent no. 10578, 1929.

[36] Boris S. Robinoff, Sumner E. Paine, and Wringnol E. Quillen. Method of welding, US Patent 1,782,316, 1930.

[37] Jones Lloyd Theodere, Kennedy Harry Edward, and Maynard Arthur Rotermund. Electric Welding US patent 2,043,960, 1936.

[38] Eugeniusz Turyk and Wojciech Grobosz. Beginnings of submerged arc welding. *Biuletyn Instytutu Spawalnictwa*, (3):15–24, 2014.

[39] R D Simonson. *The history of welding*. 1969.

[40] J F Lancaster. The physics of fusion welding Part 1 : The electric arc in welding. *IEE Proceedings*, 134(5):233–254, 1987.

[41] J F Lancaster. The physics of fusion welding Part 2 : Mass transfer and heat flow. *IEE P*, 134(6):297–316, 1987.

[42] Charles A Natalie, David L Olson, and Milton Blander. Physical and Chemical Behavior of Welding Fluxes. *Annual Review of Materials Science*, 16:389–413, 1986.

[43] BA Pokhodnya, IK and Kostenko. Fusion of electrode metal and its interaction with the slag during submerged arc welding. *Automatic Welding*, (10):16–22, 1965.

[44] BA Pokhodnya, IK and Kostenko. Research into kinetics of electrode melting during welding. *Automatic Welding*, (4):11–14, 1965.

[45] U. Franz. *Vorgänge in der Kaverne beim UP-Schweißen, Dipl.-Ing. dissertation.* PhD thesis, Technischen Hochschule Otto von Guericke, Magdeburg, 1965.

[46] U. Franz. Vorgänge in der Kaverne beim UP-Schweißen, Teil II (Processes in the cavern during submerged arc welding, Part II). *Schweißtechnik*, 16(9):400–404, 1966.

[47] Eichhorn F. and U. Dilthey. High-speed X-ray photography for submerged arc welding. *Metal Construction and British Welding journal*, 3(12):453–456, 1971.

[48] P. C. Gupta, D. Rehfeldt, and F. Erdmann-Jesnitzer. Influence of Current Pulses During Submerged Arc Welding. *Welding Research Supplement*, (November):377–380, 1976.

[49] Kozo Akahide, Teruo Ukibe, and Junichiro Tsuboi. Correlation between Arc Phenomena and Welding Parameters in Submerged-Arc Welding. *Journal of the Japan Welding Society*, 50(5):520–524, 1981.

[50] U. Reisgen. Unterpulver-Impulsschweißen zur Reduzierung des Wasserstoffeintrages beim Schweißen hochfester Feinkornbaustähle. *DVS, Annual Report 2014 Innovations*, pages 40–41, 2014.

[51] Gregor Goett, Andreas Gericke, and Dirk Uhrlandt. Optical study of a SAW cavern. In *IIW Doc. 212-1387-15*, Helsinki, Finland, 2015.

[52] R. Hazzard. Continuous radiography of the submerged arc welding process. *Research Bulletin of The Welding Institute (Cambridge)*, page 295, 1968.

[53] L.A. Gobarev, A.G. Mazel, and I.A. Shmeleva. Research into the submerged welding arc. *Automatic Welding*, (2):69–70, 1973.

[54] Johannes Schäfer, Konrad Willms, and Uwe Reisgen. Pulsed submerged arc welding in order to reduce the hydrogen input during the welding of high-strength fine-grained structural steels. *Welding and Cutting*, 14(4):228–233, 2015.

[55] Von G. Tybus. Farbige Zeitlupenaufnahmen zur Beobachtung des Schweißbades beim UP-Schwhweißen. *Schweisstechnik*, 7(Hefte 3):68–71, 1957.

[56] Masahiro Ohara, Haruo Fujita, Sumichika Haseba, and Takeshi Nishi. Study on High Speed Submerged Arc Welding (Report 2) Effect of Arc Heat Source Shape on the Occurrence of Undercutting. *Quarterly Journal of The Japan Welding Society*, 1(2):133–138, 1983.

[57] Dae-Won Cho, Woo-Hyun Song, Min-Hyun Cho, and Suck-Joo Na. Analysis of submerged arc welding process by three-dimensional computational fluid dynamics simulations. *Journal of Materials Processing Technology*, 213(12):2278–2291, dec 2013.

[58] U. Reisgen, O. Mokrov, O. Lisnyi, and R. Sharma. Investigation of a welded seam formation of submerged arc welding by CFD simulation of heat-mass transfer, electromagnetic and hydrodynamics processes supported with experimental researches. In *IIW Commission IV, XII / SG 212, Intermediate Meeting*, pages 1–30, Fronius, Wels, Austria, 2014.

[59] U Reisgen, A Schiebahn, O Mokrov, O Lisnyi, and R Sharma. The experimental analysis of the influence of submerged arc welding parameters on weld bead geometry formation. Technical report, RWTH Aachen University, ISF – Welding and Joining Institute, Aachen, Germany.

[60] V.A. Sudnik, V.A. Erofeev, A.V. Maslennikov, D.V. Slezkin, and R.V. Tsvelev. A mathematical model of the submerged-arc welding process and phenomena in the arc cavity. *Welding International*, 27(8):629–637, 2013.

[61] Rahul Sharma and Johannes Schäfer. Diagnosewerkzeuge Für Das Unterpulverschweissen. In *ISF, Welding and Joining Institute, RWTH Aachen University*, pages 19–22. Alpha Informationsges, Aachen, Germany, 2013.

[62] Manabu Tanaka, Masaya Shigeta, Fumikazu Miyasaka, and Kazuki Kasano. A Simplified Numerical Model of Submerged Arc Welding. *Preprints of the National Meeting of JWS*, 2014f:192–193, 2014.

[63] S. I. Rokhlin, A. C. Guu, and D. E. Applegate. In-Process Radiography of ARC Weld. In Donald O. Thompson and Dale E. Chimenti, editors, *Review of Progress in Quantitative Nondestructive Evaluation*, volume 7B, pages 1581–1588. Springer US, Boston, MA, 1988.

[64] T.H. North. The Distribution of Manganese between Slag and Metal during Submerged Arc Welding. *Welding Research Abroad*, 23(March):2–40, 1977.

[65] U. Mitra. *Kinetics of slag metal reactions during submerged arc welding of steel*. PhD thesis, MIT, 1984.

[66] T. Lau. *Oxygen contamination in submerged arc welding, PhD thesis*. PhD thesis, University of Toronto, 1983.

[67] N.N Potapov and K.V. Lyubavskii. Interaction between the metal and slag in the reaction zone during submerged arc welding. *Welding Production*, 18(July):9–11, 1971.

[68] N.N Potapov and K.V. Lyubavskii. Oxygen content of weld metal deposited by automatic submerged arc welding. *Welding Production*, 18(January):11–13, 1971.

[69] T.H. North, H.B. Bell, A. Nowicki, and I. Craig. Slag / Metal Interaction , Oxygen and Toughness in Submerged Arc Welding. *Welding Journal's Research Supplement*, 24(March):63–75, 1978.

[70] T. Lau, C. Weatherly, and A. Mc Lean. Gas/Metal/Slag Reactions in Submerged Arc Welding Using CaO-Al2O3 Based Fluxes. *Welding Journal's Research Supplement*, (February):31–38, 1986.

[71] T. Lau, G C Weatherly, and A. MC Lean. The Sources of Oxygen and Nitrogen Contamination in Submerged Arc Welding Using CaO-Al2O3 Based Fluxes. *Welding Journal's Research Supplement*, (December):343–347, 1985.

[72] U Mitra and T W Eagar. Slag-Metal Reactions during Welding : Part I . Evaluation and reassessment ofa existing theories. *Metallurgical Transactions*, 22B(February):65—-71, 1991.

[73] U Mitra and T W Eagar. Slag-Metal Reactions during Welding : Part II. Theory. *Metallurgical Transactions*, 22B(February):65—-71, 1991.

[74] J.H. Kim, R H Frost, D L Olson, and M Blander. Effect of Electrochemical Reactions on Submerged Arc Weld Metal Compositions. *Welding Journal*, (December):446–453, 1990.

[75] American Welding Society. *The welding handbook*. 1942.

[76] G.M. Tikhodeyev. Energy properties of the electric welding arc. *Izdatel'stvo Akademii Nauk USSR Moskva*, pages 1–254, 1961.

[77] G Hunter, G. B. Kenney, M Ring, B.A. Russell, and T.W. Eagar. Submerged arc welding of Titanium. Technical report no. 3. Technical report, 1978.

[78] V.V. Podgaetskii and T.P. Novikova. About emission of silicon fluoride in heating of flux during welding and drying. *Avtomatich. Svarka*, 87(6):19–22, 1960.

[79] V .G. Kuzmenko. Special features of the interaction between calcium fluoride and silicon dioxide at 800-1900 C. *Avtomatich. Svarka*, (6):33–35, 1980.

[80] C. S. Chai and T.W. Eagar. Slag Metal Reactions in Binary CaF2 -Metal Oxide Welding Fluxes. *Welding Journal*, 61(7):S229–S232, 1982.

[81] T W Eagar. Oxygen and Nitrogen Contamination during Arc Welding. In *Proc. of Weldments:Physical Metallurgy and Failure Phenomena*, pages 31–42, Bolton Landing, Lake George; N.Y, 1979.

[82] Leonid Zhdanov, Vladyslav Kovalenko, Nataliya Strelenko, and Yevgenia Chvertko. Peculiarities of thermal dissociation of oxides during submerged arc welding. *Soldagem & Inspeção*, 18(4):314–321, dec 2013.

[83] F. Eichhorn and A. Engel. Mass Transfer in the Welding pool. In *International Institute of Welding Document Number 212-201-70*, 1970.

[84] H Nomura, Y Sugitani, and H Nakagawa. Magnetic force in multi-electrode submerged-arc welding. In *International conference proceedings of Arc Physics and Weld Pool Behavior, London*, pages 311–323, 1979.

[85] H. Kihara, K. Masubuchi, Y. Ogura, O. Takagi, and M. Hamazaki. As to Arc Phenomenon of Multiple Electrode Submerged Arc Welding (Japanese). *Journal of the Japan Welding Society*, 27(11):647–652, 1958.

[86] Patricio F. Mendez, Gregor Goett, and Stuart D. Guest. High Speed Video of Metal Transfer in Submerged Arc Welding. In *International Institute of Welding Document Number 212-1345-14*, Seoul, South Korea, 2014.

[87] http://www.ualberta.ca/∼ccwj/Publications/WJ_ECMT_DCSAW/
SOM1: ccwj_000035.016.mp4
SOM2: ccwj_000035.015.mp4
SOM3: ccwj_000035.002.mp4
SOM4: ccwj_000035.009.mp4
SOM5: ccwj_000035.005.mp4
SOM6: ccwj_000035.010.mp4
SOM7: ccwj_000035.017.mp4
SOM8: ccwj_000035.018.xlsx.

[88] P. C. Gupta, D. Rehfeldt, and F. Erdmann-Jesnitzer. Influence of Current Pulses During Submerged Arc Welding. *Welding Research Supplement*, (November):377–380, 1976.

[89] J. F. Lancaster. *The Physics of Welding*. 1986.

[90] Américo Scotti, Vladimir Ponomarev, and William Lucas. A scientific application oriented classification for metal transfer modes in GMA welding. *Journal of Materials Processing Technology*, 212(6):1406–1413, 2012.

[91] John Norrish. A Review of Metal Transfer Classification in Arc Welding. *IIW Doc. XII-1769-03*, pages 1–15, 2003.

[92] http://www.ualberta.ca/∼ccwj/Publications/WJ_ECMT_ACSAW/
SOM9: ccwj_000035.008.mp4
SOM10: ccwj_000035.013.mp4
SOM11: ccwj_000035.003.mp4
SOM12: ccwj_000035.014.mp4
SOM13: ccwj_000035.004.mp4
SOM14: ccwj_000035.011.mp4
SOM15: ccwj_000035.019.xlsx.

[93] http://www.ualberta.ca/∼ccwj/Publications/WJ_EFMT_SAW/
SOM1: ccwj_000115.002.mp4
SOM2: ccwj_000115.018.mp4
SOM3: ccwj_000115.025.mp4
SOM4: ccwj_000115.043.mp4
SOM5: ccwj_000115.049.mp4
SOM6: ccwj_000115.003.mp4
SOM7: ccwj_000115.015.mp4
SOM8: ccwj_000115.026.mp4
SOM9: ccwj_000115.037.mp4
SOM10: ccwj_000115.055.mp4
SOM11: ccwj_000115.004.mp4
SOM12: ccwj_000115.017.mp4
SOM13: ccwj_000115.027.mp4
SOM14: ccwj_000115.045.mp4
SOM15: ccwj_000115.050.mp4
SOM16: ccwj_000115.010.mp4
SOM17: ccwj_000115.014.mp4
SOM18: ccwj_000115.028.mp4
SOM19: ccwj_000115.039.mp4
SOM20: ccwj_000115.051.mp4
SOM21: ccwj_000115.001.mp4
SOM22: ccwj_000115.013.mp4
SOM23: ccwj_000115.029.mp4
SOM24: ccwj_000115.041.mp4
SOM25: ccwj_000115.052.mp4
SOM26: ccwj_000115.011.mp4
SOM27: ccwj_000115.024.mp4
SOM28: ccwj_000115.030.mp4
SOM29: ccwj_000115.044.mp4
SOM30: ccwj_000115.053.mp4
SOM31: ccwj_000115.005.mp4
SOM32: ccwj_000115.019.mp4

SOM33: ccwj_000115.031.mp4
SOM34: ccwj_000115.048.mp4
SOM35: ccwj_000115.056.mp4
SOM36: ccwj_000115.007.mp4
SOM37: ccwj_000115.020.mp4
SOM38: ccwj_000115.032.mp4
SOM39: ccwj_000115.038.mp4
SOM40: ccwj_000115.057.mp4
SOM41: ccwj_000115.012.mp4
SOM42: ccwj_000115.016.mp4
SOM43: ccwj_000115.033.mp4
SOM44: ccwj_000115.046.mp4
SOM45: ccwj_000115.054.mp4
SOM46: ccwj_000115.008.mp4
SOM47: ccwj_000115.021.mp4
SOM48: ccwj_000115.034.mp4
SOM49: ccwj_000115.040.mp4
SOM50: ccwj_000115.058.mp4
SOM51: ccwj_000115.009.mp4
SOM52: ccwj_000115.022.mp4
SOM53: ccwj_000115.035.mp4
SOM54: ccwj_000115.042.mp4
SOM55: ccwj_000115.059.mp4
SOM56: ccwj_000115.006.mp4
SOM57: ccwj_000115.023.mp4
SOM58: ccwj_000115.036.mp4
SOM59: ccwj_000115.047.mp4
SOM60: ccwj_000115.060.mp4.